

General Disclaimer

One or more of the Following Statements may affect this Document

- This document has been reproduced from the best copy furnished by the organizational source. It is being released in the interest of making available as much information as possible.
- This document may contain data, which exceeds the sheet parameters. It was furnished in this condition by the organizational source and is the best copy available.
- This document may contain tone-on-tone or color graphs, charts and/or pictures, which have been reproduced in black and white.
- This document is paginated as submitted by the original source.
- Portions of this document are not fully legible due to the historical nature of some of the material. However, it is the best reproduction available from the original submission.

(NASA-CR-144177) DESIGN, FABRICATION, AND
TEST OF A GRAPHITE/EPOXY METERING TRUSS
Final Report, Feb. 1974 - Dec. 1975 (Boeing
Aerospace Co., Seattle, Wash.) 167 p HC
\$6.75

N76-18529

Unclass
18213

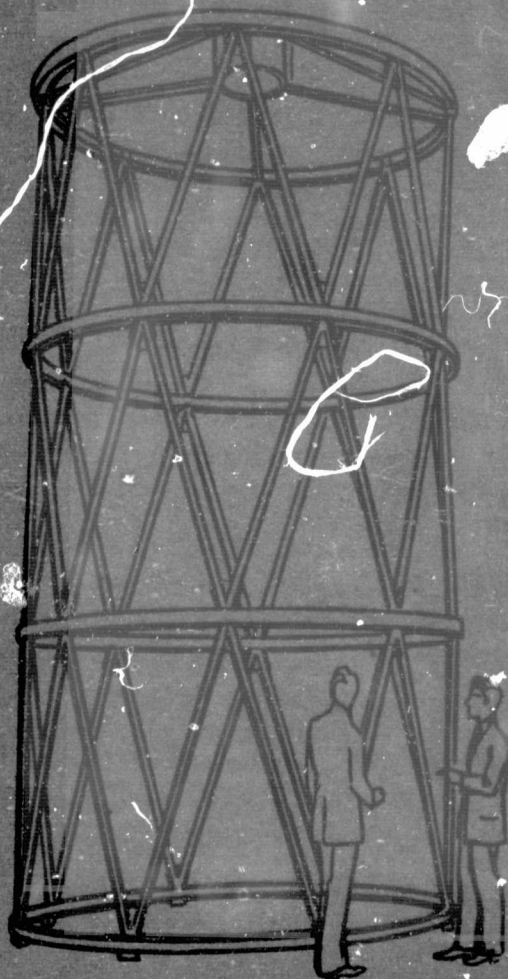
CSCI 20K G3/39

Report No.

Contract NAS 8-29825

D180-19335-1

Design, Fabrication, and Test of a Graphite/Epoxy Metering Truss



Final Report
February 1974
to
December 1975



BOEING AEROSPACE COMPANY

Report No. D180-19335-1

Contract NAS8-29825

Design, Fabrication, and Test of A
Graphite/Epoxy Metering Truss

Final Report

February 1974 to December 1975

by

S. OKEN and D. E. SKOUMAL

Prepared for

National Aeronautics and Space Administration

George C. Marshall Space Flight Center

Huntsville, Alabama

Prepared by

Boeing Aerospace Company

P.O. Box 3999

Seattle, Washington 98124

TABLE OF CONTENTS

Section		
1.0	SUMMARY	1
2.0	INTRODUCTION	5
3.0	DESIGN	10
3.1	DESIGN REQUIREMENTS	10
3.2	MATERIAL SELECTION	11
3.3	TRUSS DESIGN	15
4.0	ANALYSIS	23
5.0	ELEMENT TESTS	35
5.1	MICROYIELD TESTS	35
5.2	THERMAL EXPANSION TESTS	39
6.0	FABRICATION	57
6.1	DETAIL FABRICATION	57
6.2	SUBASSEMBLY FABRICATION	60
6.3	FULL-SCALE TRUSS ASSEMBLY	62
7.0	FULL-SCALE TESTS	88
7.1	STATIC LOAD TEST	88
7.2	DYNAMIC TEST	102
7.3	THERMAL-VACUUM TEST	111
7.4	TEST-ANALYSIS CORRELATIONS	138
8.0	CONCLUSIONS AND RECOMMENDATIONS	148
APPENDIX A - GRAPHITE/EPOXY METERING TRUSS		150
STRUCTURAL DAMPING TESTS		

LIST OF FIGURES

- 1-1 Metering Truss Configuration
- 2-1 LST Deployed from Space Shuttle Orbiter
- 2-2 Large Space Telescope
- 3-1 HMS ($0 \pm 45, 90$) Thermal Expansion
- 3-2 Thermal Expansion of ($0_2 \pm \theta$)_s Laminates
- 3-3 Schematic of UV Reflectometer
- 3-4 Typical Ring-Strut Joint
- 3-5 Typical Truss Joint
- 3-6A Graphite/Epoxy Metering Truss Assembly
- ↓
- 3-6G Graphite/Epoxy Metering Truss Assembly
- 4-1 Truss Model Geometry
- 5-1 Microyield Strain Test Equipment
- 5-2 Tubular Microyield Specimen with Extensometer Support Rings
- 5-3 Tubular Microyield Specimen with Linear Differential Transformer Extensometer Installed
- 5-4 Microyield Strain Ring (H-Section) Specimen
- 5-5 Microyield Strain Joint Specimen
- 5-6 Tubular Specimen ($0_2 \pm 65$)_s - Yield Strain vs Stress
- 5-7 Tubular Specimen ($0_2 \pm 65$)_s - Elastic Strain vs Stress
- 5-8 Ring Test Section - Yield Strain vs Stress
- 5-9 Tubular Specimen ($0_2 \pm 50$)_s - Yield Strain vs Load
- 5-10 CTE Test Setup Schematic
- 5-11 CTE Element Test Equipment
- 5-12 CTE Element Test - Laser Interferometer
- 5-13 CTE Element Instrumentation
- 5-14 Tube Growth vs Temperature

LIST OF FIGURES (Continued)

- 5-15 CTE Test Data/Design Comparisons
- 5-16 CTE Ring Element - Thermal Growth vs Temperature
- 5-17 CTE Tube Element - Thermal Cycling
- 5-18 Thermal Cycling Tube - Microcracks
- 6-1 Cure Schedule - 1334A (Fiberite Corp.)
- 6-2 Layup Configuration
- 6-3 Tubular Strut Ply Layup
- 6-4 Tubular Strut - End Trim
- 6-5 Tubular Strut - End Slotting
- 6-6 Tubular Strut - End Trim Complete
- 6-7 Graphite Fabric Gusset Fittings and Tooling
- 6-8 Graphite Fabric Truss Joint Details
- 6-9 Joint "T" Gussets
- 6-10 Graphite Fabric Ring Channel Layup
- 6-11 Graphite Fabric Ring Channel - Bagged and Ready for Cure
- 6-12 Truss Ring Chord Layup
- 6-13 Truss Ring Chord Laminates - Bagged and Ready for Cure
- 6-14 Strut Assembly - Slotted Tube Installed on Gusset
- 6-15 Strut Assembly - Joint Prefit
- 6-16 Strut Assembly - Joint Bonding
- 6-17 Strut Assembly - "T" Drilling
- 6-18 Completed Strut Assembly
- 6-19 Ring Assembly - Assembled Graphite Fabric Channels
- 6-20 Ring Assembly - Chord Installation

LIST OF FIGURES (Continued)

- 6-21 Ring Assembly - Template Drilling
- 6-22 Completed Ring Assembly
- 6-23 Spider Beam Assembly - Layup Tooling
- 6-24 Spider Beam Assembly - Bagged and Ready for Cure
- 6-25 Spider Cylinder Assembly - Cured Inner Skin
- 6-26 Spider Cylinder Assembly - Honeycomb Installation
- 6-27 Completed Spider Cylinder Assembly
- 6-28 Spider Assembly Installed on Top Truss Ring
- 6-29 Truss Assembly Sequence
- 6-30 First Bay Assembly
- 6-31 Second Bay Assembly Complete
- 6-32 Typical Truss Joint
- 6-33 Removal of Completed Truss from Tooling
- 6-34 Completed Truss Assembly
- 7-1 Static Load Test Setup - Schematic
- 7-2 Static Load Test Setup
- 7-3 Static Load Test - Base Attachment
- 7-4 Static Load Test - Base Attachment Close-up
- 7-5 Static Load Test - Load Introduction Fitting
- 7-6 Static Load Test - Load Actuator Pumps
- 7-7 EDI Reaction Structure and EDI Locations
- 7-8 Modal Survey Test Setup - Schematic
- 7-9 Modal Survey Test Setup
- 7-10 Modal Survey Test - Mass Plate and Instrumentation

LIST OF FIGURES (Continued)

- 7-11 Modal Survey Test - Support Equipment
- 7-12 Modal Survey Test - Accelerometer Locations
- 7-13 Thermal - Vacuum Test Setup - Schematic
- 7-14 Thermal - Vacuum Test - Truss Installation in
 Vacuum Chamber
- 7-15 Space Chamber - Schematic
- 7-16 Thermal - Vacuum Test - Support Ring Installation
- 7-17 Thermal-Vacuum Test - Nylon Block Supports
- 7-18 Truss and Fixturing Covered with Aluminized Mylar for Test
- 7-19 Truss in Space Chamber Prior to Test
- 7-20 Thermal-Vacuum Test - Distortion Measurement Geometry
- 7-21 Heater and Thermocouple Installation
- 7-22 Typical Resistant Heater Installation
- 7-23 Axial Temperature Perturbation - Control Zones
- 7-24 Radial Temperature Perturbation - Control Zones
- 7-25 Adjustment of Interferometer Pointing Mirrors
- 7-26 Test Temperature Distributions
- 7-27 Typical Condition I Temperature Distribution
- 7-28 Typical Condition II Temperature Distribution
- 7-29 Effect of Inner Spider Joint Stiffness on Static
 Axial Deflection

LIST OF TABLES

3-1	Graphite/Epoxy Metering Truss Materials
4-1	Graphite/Epoxy Truss Mass Distribution
4-2	Graphite/Epoxy Truss Properties
4-3	Modal Analysis Results
4-4	Truss Stiffness
5-1	CTE of Graphite/Epoxy Strut Elements
7-1	Static Side Load - Test Data
7-2	Static Torsion Load - Test Data
7-3	Static Axial Compression Load - Test Data
7-4	Modal Survey Test - Force Input Frequency and Damping Data
7-5	Modal Survey Test - Free Vibration Decay Frequency and Damping Data
7-6	Test Temperature Distributions
7-7	Thermal - Vacuum Test - Data Reduction Equations
7-8	Thermal - Vacuum Test - Truss Deflection Summary
7-9	Static Test - Analysis Correlations
7-10	Dynamic Test - Analysis Correlations
7-11	Thermal - Vacuum Test - Analysis Correlation
7-12	Spider Beam CTE vs Axial Truss Deflections
7-13	Spider Beam/Cylinder Joint Stiffness vs Axial Truss Deflection

FOREWORD

This report was prepared by the Boeing Aerospace Company under NASA contract NAS8-29825 and covers the work performed during the period from February 1974 to December 1975. The contracting officer's representative was Mr. Carl Loy from the George C. Marshall Space Flight Center.

This program was conducted in the Structural/Mechanical Research and Development organization which is under the direction of H. W. Klopfenstein. The program managers were J. W. Straayer and Hans Bjornestad. The technical leader was Sam Oken.

The authors wish to acknowledge the contributions of the following personnel:

J. M. Hearsey	}	Analysis
D. H. Merchant		
W. Sanders		Materials and Processes
R. Nelson	}	Manufacturing
D. Giesecking		
L. C. Lofgren		
D. Belvin		Static Test
R. Watanabe		Dynamic Test
S. Baber	}	Thermal-Vacuum Test
D. Jones		
J. Sparrow		
J. Jorgensen		
R. Pond		Laser Interferometer Measurements
W. W. Wood		Microyield Tests

1.0 SUMMARY

This report covers the investigations performed to evaluate a graphite/epoxy metering truss as applied to the Large Space Telescope (LST). A full-scale truss was designed, fabricated and tested. Tests included static limit loadings, a modal survey and thermal-vacuum distortion evaluation. The most critical requirement was the demonstration of the dimensional stability provided by the graphite/epoxy truss concept. Crucial to the attainment of this objective was the ability to make very sophisticated thermal growth measurements which was provided by a seven beam laser interferometer.

The full-scale truss was approximately 7.22 meters (23.7 feet) high and 3.35 meters (11 feet) in diameter. It consisted of a three bay configuration with a secondary mirror support assembly at the top (Figure 1-1). The truss was designed to minimize cost by standardization and repetitive use of its basic elements. All tubular struts were identical and all rings, spider beams and joints were the same. The designs of the basic truss elements were tuned to provide the high degree of dimensional stability and stiffness required by the truss. The struts and spider assembly were fabricated with Fiberite's AS/934 and HMS/934 broadgoods. The rings utilized T300 graphite fabricate with the same materials. The predicted performance of the truss was developed using the NASTRAN program. These results showed conformance with the critical stiffness and thermal distortion requirements and correlated well with the test results.

The predicted truss performance determined by the NASTRAN analysis was supported by substantial element testing. The inputs to the analysis were provided by highly sophisticated testing and measuring techniques. Microyield tests were performed to provide element strength and stiffness characterizations.

Measurements were made with matched linear differential transformers with the capability of measuring to 2.54×10^{-7} cm (10^{-7} inches). Coefficient of thermal expansion (CTE) tests were performed on 91.4 cm (36 inches) long truss elements. Measurements were made with a multi-beam laser interferometer with a 7.87×10^{-6} cm (3.1×10^{-6} inch) measurement resolution. Some of the truss element designs were finalized using the results of these tests for final tuning.

After fabrication, the full-scale truss was static tested. Limit loads were applied axially, in bending and in torsion. The truss carried these loads with little difficulty.

The truss was then dynamically tested. A secondary mirror mass simulation of 56.7 kg (125 lbs) was installed in the spider mounting assembly. The truss was fixed at its base and tested in the cantilevered configuration. A first mode resonant bending frequency of 16.2 Hz was measured. This was in excess of the 15 Hz minimum design requirement.

The final full-scale test consisted of a thermal-vacuum distortion test. The truss was instrumented using resistant heaters, thermocouples and a seven-beam laser interferometer and associated retroreflectors. The truss was placed in a vacuum chamber and allowed to stabilize under vacuum. Liquid nitrogen was

committed to the chamber shrouds and the resistance heaters were energized to establish an initial service temperature distribution. After the control thermocouples had attained target temperatures, the truss was allowed to soak several more hours until the interferometer readings stabilized. The truss temperatures were then raised 5.55°C (10°F). Truss dimensional changes resulting from the temperature change were obtained with the laser interferometer. An additional test in which the temperatures were perturbed laterally was performed using the same procedures. In all cases the truss dimensional changes were within the design despace, decenter and tilt budgets.

Primary units used in this report are in the international system of units which are followed by U.S. customary units in parenthesis.

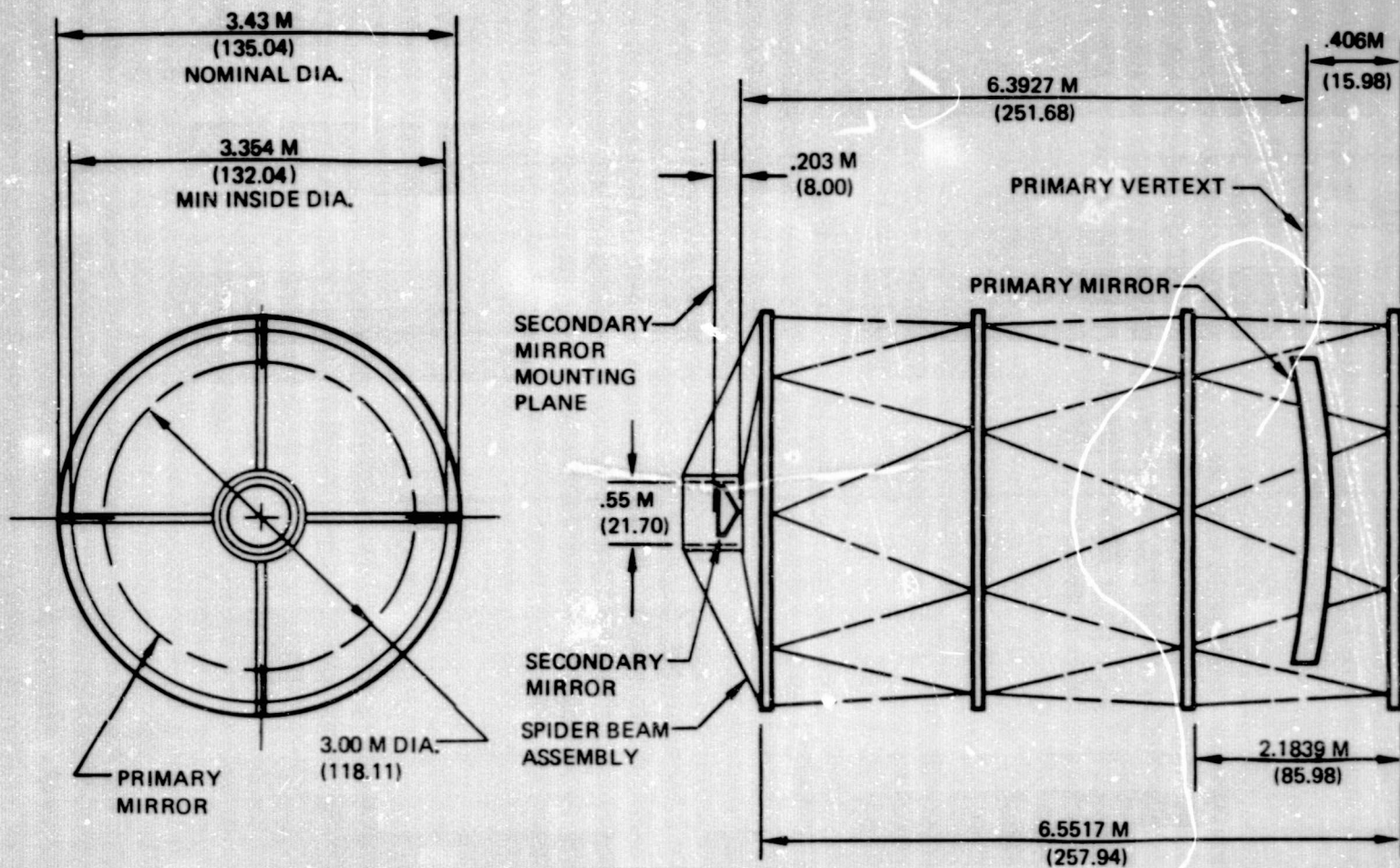


Figure 1-1. Metering Truss Configuration

2.0 INTRODUCTION

NASA-MSFC is developing a double mirror (Cassegrainian) Large Space Telescope (LST) to be placed in earth orbit by the Space Shuttle. Critical to the successful operation of this telescope is the dimensional stability of the structural assembly (metering structure) supporting the primary and secondary mirrors while undergoing mission temperature changes. Figure 2-1 pictorially shows the LST shortly after being released from the Space Shuttle and Figure 2-2 a cut-away view showing the location of the metering structure.

The objective of this program was to evaluate a metering structure design which utilized a graphite/epoxy truss concept. It was essential that this structure maintain an alignment of the telescope mirrors within extremely closed tolerances throughout the period of observation. During this period the telescope is subjected to significant temperature changes. This dictates the use of materials that can provide coefficients of thermal expansion (CTE) that are close to zero. The graphite/epoxy material systems can be designed to provide this unique characteristic. These materials are also ideal for this application since structural stiffness is critical. The truss configuration is one of the prime candidates for the metering structure. In addition to being structurally efficient its load paths are well defined and therefore it lends itself to accurate analysis. The majority of the parts were highly repetitive resulting in very cost effective manufacturing.

During the design phase of this program the LST optics were based on using a 3 meter diameter primary mirror. The metering truss evaluated in this program was also sized to support the same diameter mirror. A full size metering truss, approximately 7.2 m (24 ft) high and 3.3m (11 ft) in diameter, was

fabricated and tested. The full size geometry was selected because predicted associated fabrication and testing costs fell within a reasonable budget and this eliminated the use of complex scaling relationships. The full scale truss was tested and the results were applied directly in its evaluation.

This program was performed in four phases during the period from February 25, 1974 to December 31, 1975. The four phases were:

- Phase I - Design and Fabrication
- Phase II - Full-Scale Test and Evaluation
- Phase III - Cyclic and Creep Element Tests
- Phase IV - Reporting.

In Task I of Phase I several tasks were accomplished. Candidate graphite/epoxy truss materials were reviewed and a selection made early in the program. Several of the materials we felt could have successfully met the design requirements. Those selected from this group were those in which we had the largest Boeing in-house data base and also greatest amount of manufacturing experience. These materials were Fiberite 1334A (H-MS/934), Fiberite 1334C (A-S/934), Fiberite HMF330C/34 (graphite/epoxy fabric), and a room temperature curing adhesive, Lefkoweld Type 109. Several design investigations were performed. Several cross-section geometries were reviewed for both the struts and rings. A cylindrical tube was chosen for the struts to provide a design that could be made to close fabrication tolerances with repetitive properties. An "H" cross-section was selected for the rings because it was structurally efficient and was suitable for making strut ring attachments. In general, a truss design was developed that emphasized commonality of parts to minimize tooling and manufacturing costs.

Element tests were performed on specimens that were very representative of the truss details. They were performed using highly sophisticated measuring devices having resolutions that were capable of demonstrating compliance with stringent truss requirements. Tests were performed to determine microyield strain allowables and coefficient of thermal expansion (CTE) characteristics. Microyield strain measurements were made with matched linear differential transformers with the capability of measuring to 2.54×10^{-7} cm (1×10^{-7} in.). CTE measurements were made with a multibeam laser interferometer with the capability of measuring to 7.86×10^{-6} cm (3.1×10^{-6} in.) in a changing temperature environment. The results obtained from the elements tests were used to finalize the detail design of the truss.

In Task II of the first phase, a full scale truss was fabricated. The details were fabricated using conventional composite tooling and processes. Several methods for making the tubular struts were evaluated which included wet winding, winding with impregnated tow and tape winding. The latter was selected because material wastage was minimized and material placement, ply thickness and fiber orientation, was accomplished with the highest degree of accuracy. The truss was assembled on a tool one bay at a time. As each bay was completed it was placed on top of the tool and the lower bay was then assembled. This was repeated until the truss was completed.

In Phase II, full scale component tests were performed. These included static, dynamic and thermal-vacuum tests. In the static test, limit axial, limit bending and a selected torsion loads were applied. The truss carried these loads without any difficulty. The truss was tested dynamically in a cantilevered configuration. The truss was attached at its base and a 56.7 kg (125 lb) secondary mirror mass simulation installed at its top. Test results showed

that the first resonant bending frequency was beyond the design requirement of 15 Hz min. In the thermal-vacuum test the truss had resistant heaters and thermocouples installed on all its elements to control temperatures during test. The truss was then covered with one layer of aluminized mylar insulation to reduce thermal gradients. This configuration, resistant heaters and one layer of aluminized mylar, was developed by a series of thermal surveys performed on a tubular element. The thermally induced dimensional changes encountered during the test were measured with a seven beam laser interferometer. The interferometer was placed in its own environmentally controlled chamber mounted on the truss secondary mirror cylinder. The interferometer rays passed thru optical windows in the chamber cover to measure the movement of retro-reflectors mounted on the truss base ring. The instrumented truss was placed in a 500,000 ft³ vacuum chamber. Tests included first establishing representative service temperature distributions and perturbing these temperatures 5.55°C (10°F) axially and laterally. In these tests, all the truss deflections measured were within the design distortion budgets.

In Phase III load cycling, thermal cycling and creep element tests were performed. The specimens were tubular sections representative of the truss struts. In general, specimen characteristics changed very little as a result of the load cyclic and sustained load tests. Results obtained from thermal cycling tests indicated microcracking and a change in thermal growth characteristics below -32°C (-25°F).

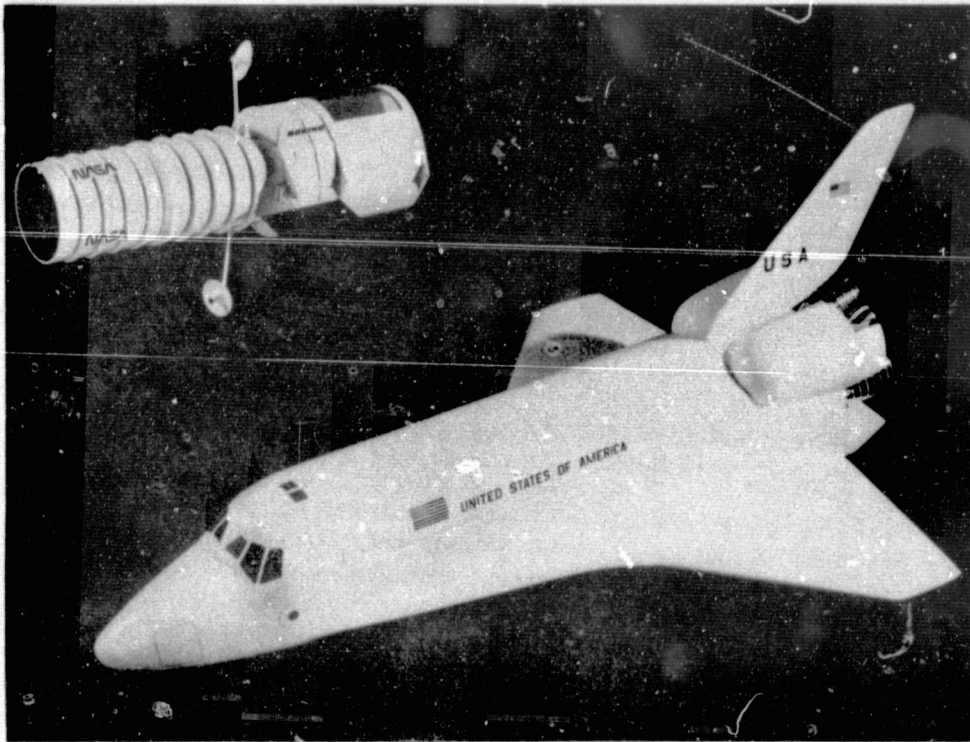


Figure 2-1. LST Deployed From Space Shuttle Orbiter

Large Space Telescope 3-Meter Aperture

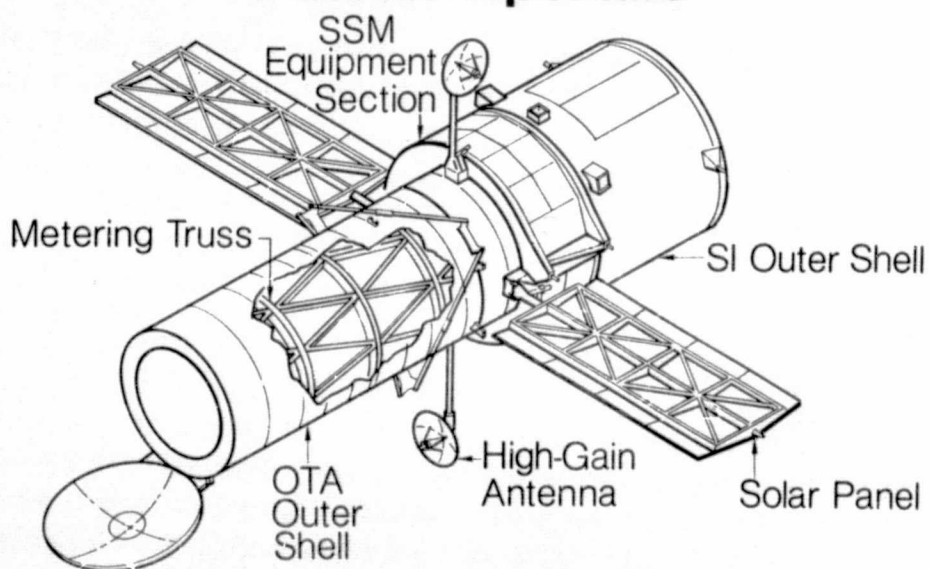


Figure 2-2. Large Space Telescope

3.0 DESIGN

A full-scale graphite/epoxy truss was designed for evaluation. This truss consisted of a three bay configuration with 16 tubular struts per bay and a spider assembly for supporting a secondary mirror at one end. The critical characteristics of main concern in developing this design were 1) the ability to meet dimensional stability requirements, 2) stiffness characteristics which provide a minimum resonant bending frequency of 15 Hz, and 3) costs. The truss elements were tuned to provide a low coefficient of thermal expansion, as well as the required stiffness. This was accomplished by the proper orientation and selection of fibers used in their laminates. To minimize costs, repetitive use of detail parts was emphasized. All 48 struts used in the design were identical. All rings, spider beams and joints between the struts and rings were the same.

3.1 DESIGN REQUIREMENTS

The metering structure design requirements are governed by the L.S.T. operational conditions. The materials must meet exceptionally low outgassing specifications and the structure must remain dimensionally stable while undergoing operational temperature changes to prohibit degradation of L.S.T. optical characteristics. The design must also comply with the structural static and dynamic requirements during the space shuttle launch and recovery. The specific requirements are listed below:

Alignment - Primary Mirror to Secondary for a 1.65°C (3°F)

Temperature Change

Despace = ± 2 Micrometers (80 Microinches)

Decenter = ± 10 Micrometers (400 Microinches)

Tilt = 4.9 Microradians (1 Arc Second)

Stiffness

Fixed-Base Minimum Natural Frequency = 15 Hz

Strength

Stress Level in all Components Below the Microyield Stress

Load Factors per JSC 07700, "Space Shuttle System Payload Accommodations"

Ultimate Factor of Safety of 1.4 or yield Factor of 1.1 whichever is more critical

Space-Environmental

Compliance with "Material Management Plan for L.S.T. Contamination Control" (Ref. 1)

3.2 MATERIAL SELECTION

The utilization of graphite/epoxy composites in the truss provided a materials system that had the unique properties and the flexibility to be designed to the specific properties required to comply with the specifications of the L.S.T. metering truss. By proper selection of the graphite fibers and their orientation, the required stiffness, as well as dimensional stability resulting from "near zero" CTE were attained.

At the initiation of this program several graphite/epoxy material systems were considered for use in this evaluation. It was recognized that several of these could meet the design requirements and a choice at that point in time may not represent the optimum selection. But to facilitate completion of the program in a timely manner, the materials used in the truss were selected early in the program.

Ref. 1 - Knowling, Ted. L., "Material Management Plan for LST Contamination Control," memo dated 3/74 S&E-ASTN(73-06) MFSC

Because of the large established data base developed in previous contractual and in-house work, Boeing selected the following graphite/epoxy material forms to be used in the metering truss design; 1) HM-S fiber with 934 epoxy resin (1334A)*, 2) "A-S" fiber with 934 epoxy resin (1334C)*, and 3) T300 graphite fabric with 934 epoxy resin (HMF 330C/34)*.

The unidirectional ply properties of the above composites were first established by test as summarized in Table 3-1. The ply properties were then used to develop theoretical laminate properties using a classical laminate analysis.

Analytical studies were conducted to determine laminate arrangements that would provide essentially zero coefficient of thermal expansion (CTE). Only symmetrical laminates were considered to avoid distortion during cure. Lamina families utilizing a single fiber type as well as hybrids of two or more were examined to establish a low sensitivity to CTE change due to manufacturing variables. These included variations in fiber volume (V_f), ply thickness and fiber orientation.

Carpet plots of laminates with varying fiber orientations were developed whose coefficients of thermal expansion were at or near zero. Candidate laminates which were within the CTE limits required to meet truss distortion requirements were selected from the carpet plots. These groups included laminates using only HM-S graphite fibers and others which used a mixture of HM-S and less costly graphite materials such as A-S fibers and graphite cloth. A typical plot for a $(0 \pm 45, 90)$ laminate of HM-S fiber is shown in Figure 3-1.

*Product designations of the Fiberite Corporation

Additional laminate families developed having near zero CTE's, one of which is shown in Figure 3-2. This figure shows the CTE characteristics of an 8-ply laminate family which uses HM-S fibers in the 0° direction and A-S fibers in the $\pm \theta$ directions. This laminate has the flattest slope in the near zero CTE region and therefore, would be more tolerant to fiber property and manufacturing variations. It is interesting to note that using A-S fiber, which has a positive CTE in the $\pm \theta$ directions, causes the hybrid laminate CTE to be more negative than the laminate made entirely with HMS fiber. Also the use of 50% A-S fiber provides a \$44/kg (\$20/lb.) cost saving over an all HM-S laminate.

The 8-ply laminate with HM-S fibers in the 0° direction and A-S fibers in the $\pm \theta$ directions was selected to be used in the design of the tubular truss struts. The near zero CTE and stiffness properties of the struts using this laminate were critical for meeting truss requirements and were the primary basis for this selection. The final selection of the direction of the orientated plies ($\pm \theta$) were developed using element tests.

The selected laminate designs were incorporated in structural elements representative of the details in the truss. These were tested using a laser interferometer to make thermal distortion measurements to the sensitivity required to demonstrate compliance with design requirements. This testing is covered in detail in Section 5.0.

In addition to providing physical and mechanical properties that meet design requirements the materials used on the LST must demonstrate the ability to meet rigid contamination control requirements.

The loss of matter by outgassing and by evaporation or sublimation is one of the most obvious effects of a thermal-vacuum environment on polymers used in the graphite/epoxy composites. Resins which are considered suitable for spacecraft usage are those which exhibit a minimum weight loss when exposed to the vacuum and thermal environments of space, and those which contain minimum polymers that vaporize at an elevated temperature in a vacuum and deposit an adjacent, cooler surfaces. The former is expressed as total weight loss. The latter is expressed as Volatile Condensible Materials or VCM. The 934 resin was tested in a facility which was patterned after the Goddard Space Flight Center Apparatus. Mylar standards were run simultaneously with the 934 sample to serve as controls and to verify that the test equipment functioned properly. The experiment was controlled to the following parameters: Sample bar temperature, $125 \pm 2^{\circ}\text{C}$ ($257 \pm 4^{\circ}\text{F}$); collection plate temperature, $23 \pm 2^{\circ}\text{C}$ ($72 \pm 4^{\circ}\text{F}$); a vacuum of 10^{-6} torr and an exposure time of 24 hours. The data shown on Table 3 shows 934 resin has per cent weight loss and vacuum condensible values which are less than 1% and 0.1%, respectively, and is therefore acceptable for most spacecraft usage.

An additional outgassing requirement for polymer materials used in and around optical systems which we considered for the metering truss, was degradation of optical performance, i.e., a change in specular reflectance of a mirror surface due to a coating of outgassing products. A specular reflectance test was performed with a specimen containing the 934 resin system in a UV-Reflectometer shown schematically in Figure 3-3. The specimen, 66mm x 66mm (2.6 in. x 2.6 in.) was placed in a vacuum chamber and held at 50°C (122°F) in the direct line of sight of a test mirror held at 25°C (77°F). The pressure in the chamber was held at less than 10^{-5} torr. Reflectance readings were taken periodically

over a spectrum range of 1000 Å to 3000 Å for 30 days. The reflectance change measured was slightly over 1%, which was well below the L.S.T. requirement of 5% maximum @ 1216 Å.

3.3 TRUSS DESIGN

Approach

The truss design consisted of an assembly of struts and rings which formed a three-bay configuration as shown in Figure 1-1. Structural configuration studies of the graphite/epoxy metering truss were performed to evaluate promising candidates. Studies included overall truss assembly configurations, as well as basic element concepts. Designs were evaluated with respect to strength, stiffness, geometric/thermal stability, manufacturing suitability and cost.

Candidate designs were developed which met the structural requirements of the truss without inhibiting the operational characteristics of the LST. In all designs, graphite/epoxy composites were used to the maximum extent possible. Special attention was given to provide geometrical/thermal stability. The graphite composite characteristics of the basic elements were tailored such that the overall truss was tuned to minimum growth in a changing temperature environment. This was accomplished by the proper selection and orientation of the graphite fibers.

The anisotropic characteristics of the composites required careful attention when considering the strength and stiffness requirements of the truss. These properties were balanced such as to provide a design which met all of the applicable requirements.

To study the various truss component concepts, the overall assembly was divided into critical design areas. The secondary mirror support structures was given special attention since it had to provide maximum support capabilities while causing minimum obscuration to the telescope. In the initial evaluation of truss designs, it was determined that a relatively large percentage of the truss deflection could occur in the spider region. The design selected utilized honeycomb stabilized sandwich construction to provide the maximum amount of stiffness with minimal frontal area. The top truss ring which supported the secondary mirror support structure also required special attention since concentrated loads introduced by the spider beams could cause large-inplane displacements under dynamic loading. Various ring geometries and cross sections were studied. A built-up "H" incorporating graphite fabric and graphite/epoxy broadgoods was selected. The fabric was used to provide the shape and the broadgoods used in the chord areas to tune the section to the proper physical and mechanical characteristics. Several strut designs were also investigated. These included round tubes made using wet and tape winding techniques, square tubes, and various built-up sections. The round tubular sections were selected on the basis of simplicity and costs. Techniques for attaching these struts to the truss rings were also studied. The relative merits of each concept was evaluated considering the ability to comply with structural and thermal L.S.T. requirements and favoring those concepts which had a high degree of part commonality to minimize tooling costs.

Detail Design

The metering truss configuration evolved to three, equal length bays, with sixteen strut members per bay. Four beams were used to attach the secondary mirror support structure to the upper ring member. The basic ring frame

consists of two channel sections bonded back-to-back to form an "H" section. The section properties required by the upper ring (at the secondary mirror end) were used to size all the rings. This provided common parts for all the rings and thereby minimized the tooling costs. The channel members were molded from graphite/epoxy fabric (330C/34) which provided a pseudo 0/90 fiber orientation with a modulus (E) of 72.4 GN/m^2 ($10.5 \times 10^6 \text{ psi}$) and a CTE that was positive $2.23 \text{ } \mu\text{E}/^\circ\text{C}$ ($1.24 \text{ } \mu\text{E}/^\circ\text{F}$). Cap strips made from GR/E tape were then bonded to the channels. By adjusting the cap thickness and ply orientations the ring was "tuned" to provide the required stiffness and a low CTE in the circumferential direction. The strut selection favored the one piece circular tube because it represented the most efficient structural shape and allowed the application of plies in a rapid and accurate manner. Identical diameters and wall thicknesses were used on all struts to minimize cost. The characteristics of the strut selected are summarized below.

Inside Diameter - 5.08 cm (2.0 inches)

HM-S A-S
Laminate - $(0_2 \pm 50)_s$

Effective Modulus - 108.3 GN/m^2 ($15.7 \times 10^6 \text{ psi}$)

Least Sensitive to Manufacturing and Material Variations

Low Cost - Minimum Plies

Minimum Material Cost

Semi-Automated Fabrication

A typical ring to strut joint is shown in Figures 3-4 and 3-5. Each pair of struts was bonded to a "zero" CTE gusset plate which was then bonded to the web of the ring. Mechanical fasteners were used to prevent peeling at the bondlines. This joint was used at all strut/ring intersections.

The secondary mirror support or spider consisted of an 45.72 cm (18.0 in.) long cylinder approximately 55.88 cm (22.0 in.) in diameter supported by four beams @ 90° spacing. The cylinder and support beams used honeycomb sandwich construction with GR/E skins designed to provide "zero" expansion in the circumferential direction of the cylinder and along the length of the beams.

The detail drawings of the truss are shown in Figures 3-6A thru 3-6G. All parts were assembled using room temperature bonding. All room temperature bonding was performed using Lefkowied - Type 109. This adhesive was selected because it provided the necessary mechanical properties, was qualified for space applications per 50M02442 (Ref. 1) and had successfully been used in other spacecraft.

Reference 1 - 50M02442 Revision W - ATM Material Control for Contamination Due to Outgassing, March 1, 1972, George C. Marshall Space Flight Center

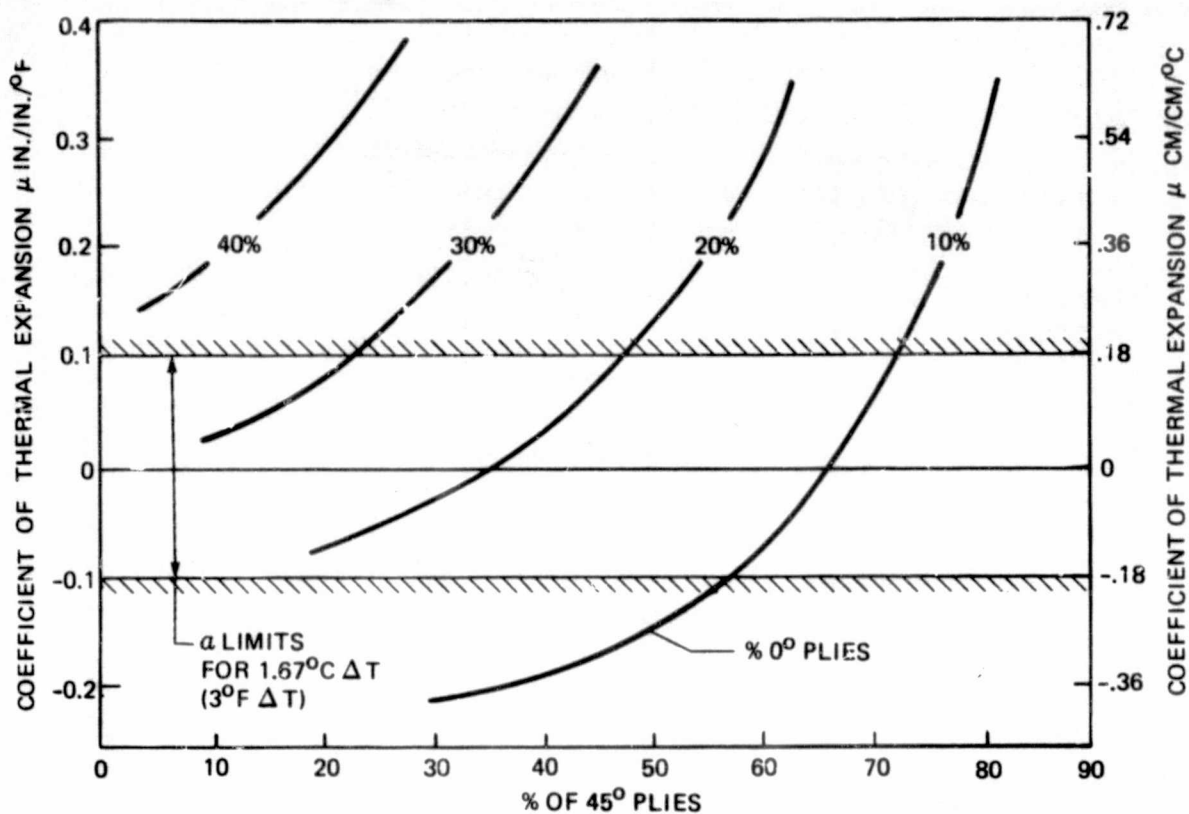


Figure 3-1. HMS (0 ± 45, 90°) Thermal Expansion

Table 3-1. Graphite/Epoxy Metering Truss Materials

Material	E_t $N/m^2 \times 10^9$ (psi $\times 10^{-6}$)	F_{tu} $N/m^2 \times 10^{-6}$ (psi $\times 10^{-3}$)	CTE @ RT $\epsilon \times 10^6/^\circ C$ ($\epsilon \times 10^6/^\circ F$)	Outgassing	
				% Weight loss	% Condensibles
HMS/934 (1334A) *	186.2 (27.0)	865.3 (125.5)	-0.54 (-0.3)	0.39	0.02
A-S/934 (1334C) *	127.6 (18.5)	1,689.3 (245)	+0.18 (+0.1)	↓	↓
G/E fabric (HMF 33C/34) *	72.8 (10.5)	620.6 (90)	+2.23 (+1.24)	↓	↓

*Product designations of the Fiberite Corporation

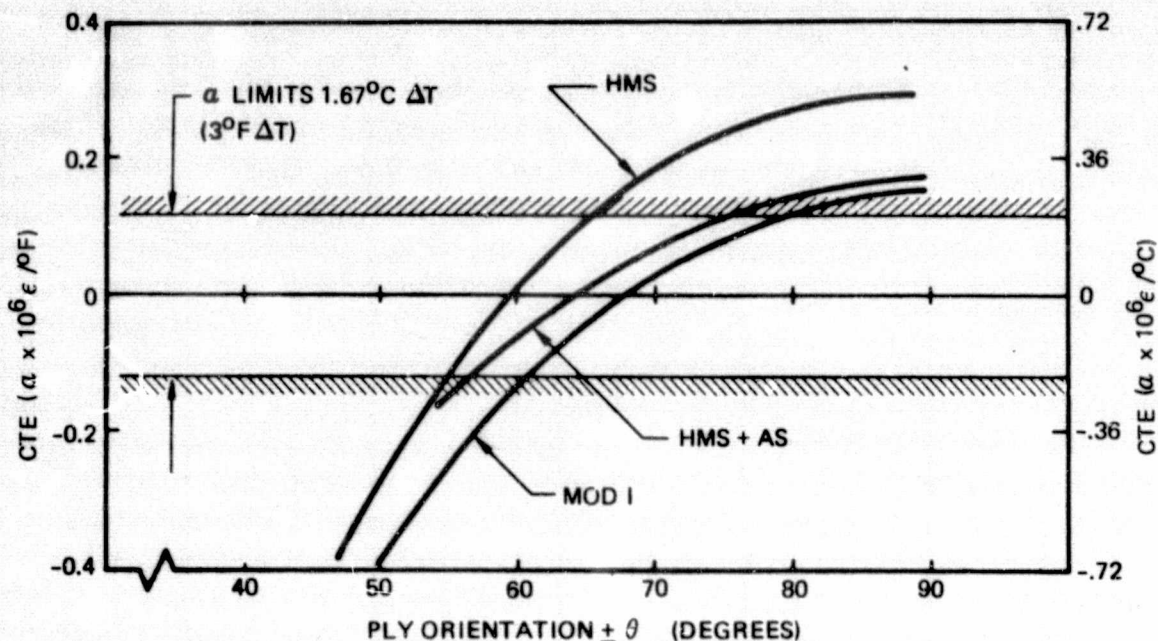


Figure 3-2. Thermal Expansion of $(0^\circ \pm \theta)$ S Laminates

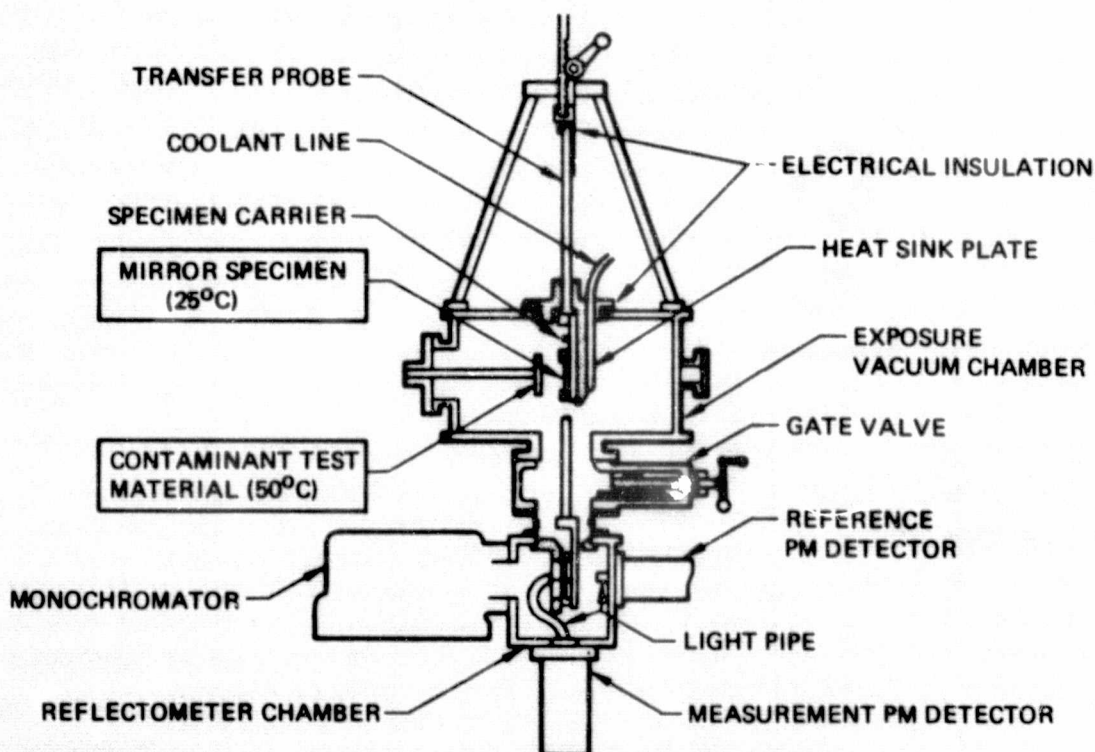


Figure 3-3. Schematic of UV Reflectometer

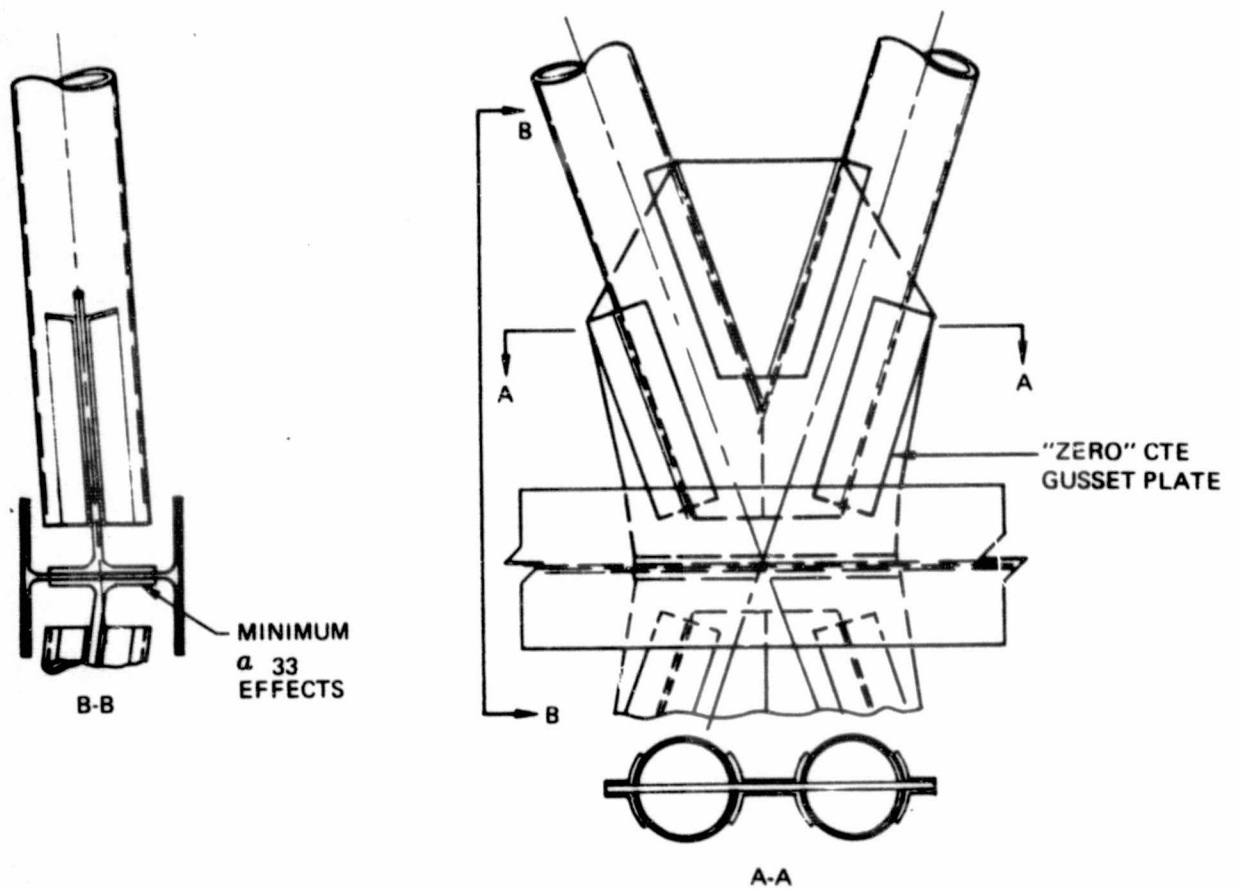


Figure 3-4. Typical Ring-Strut Joint

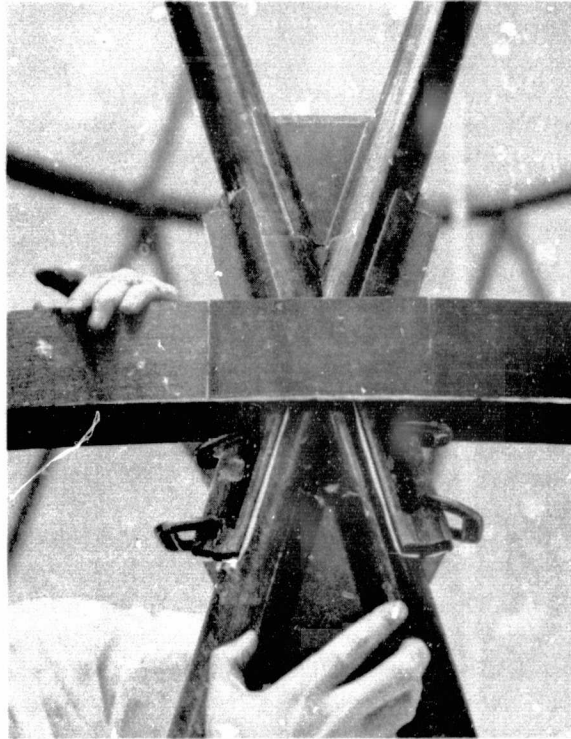
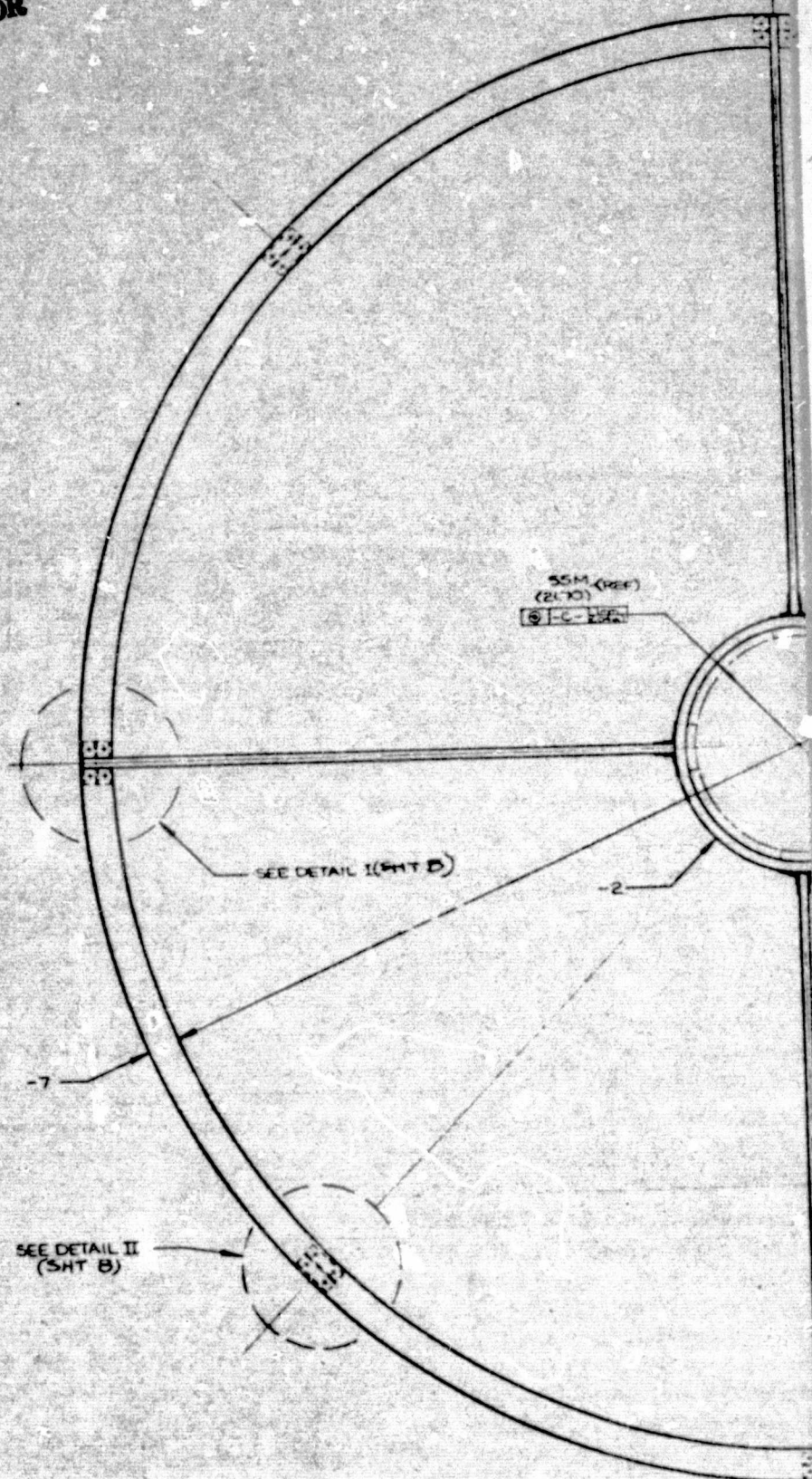
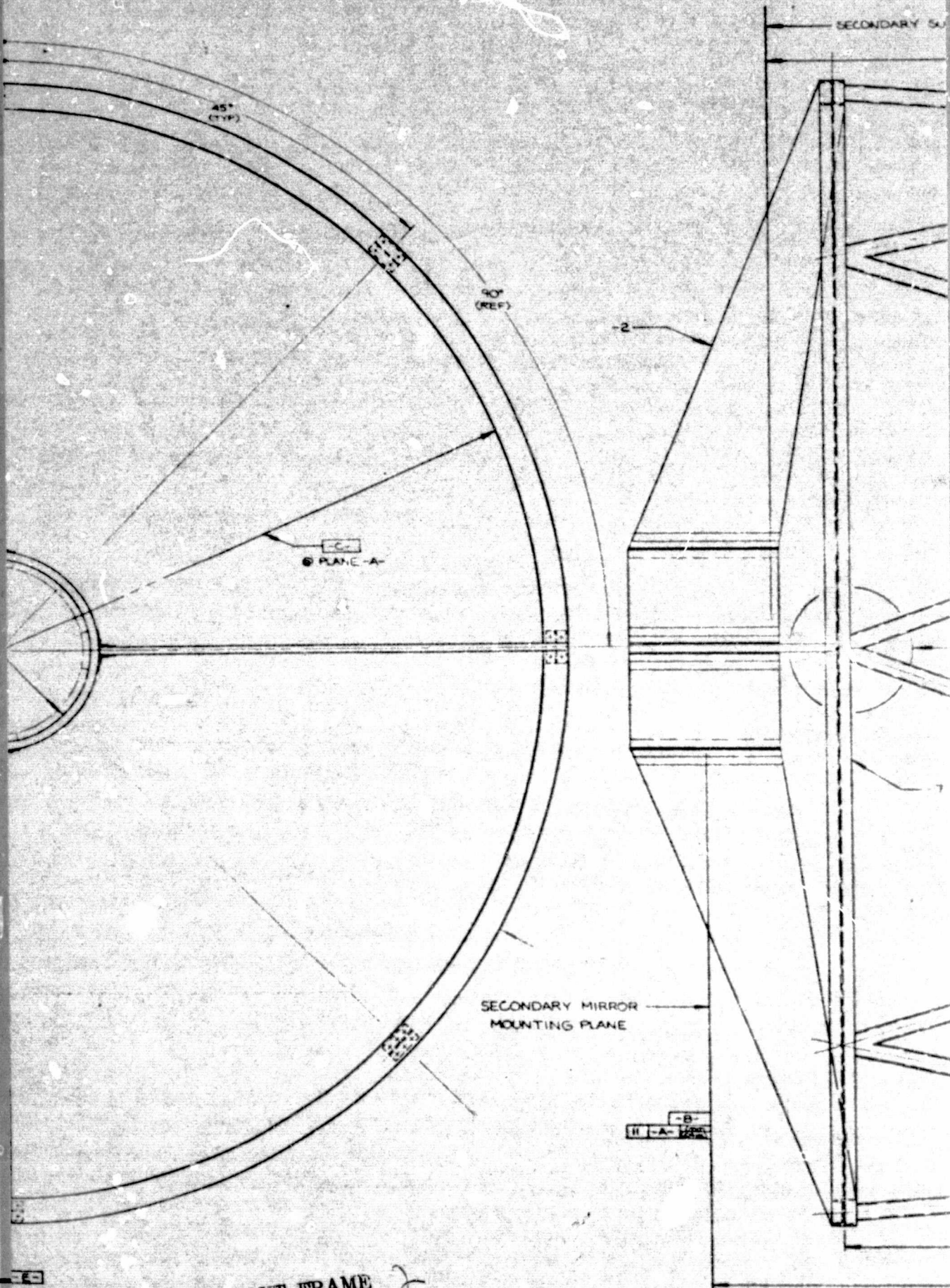


Figure 3-5. Typical Truss Joint

REPRODUCIBILITY OF THE
ORIGINAL PAGE IS POOR

FOLDOUT FRAME





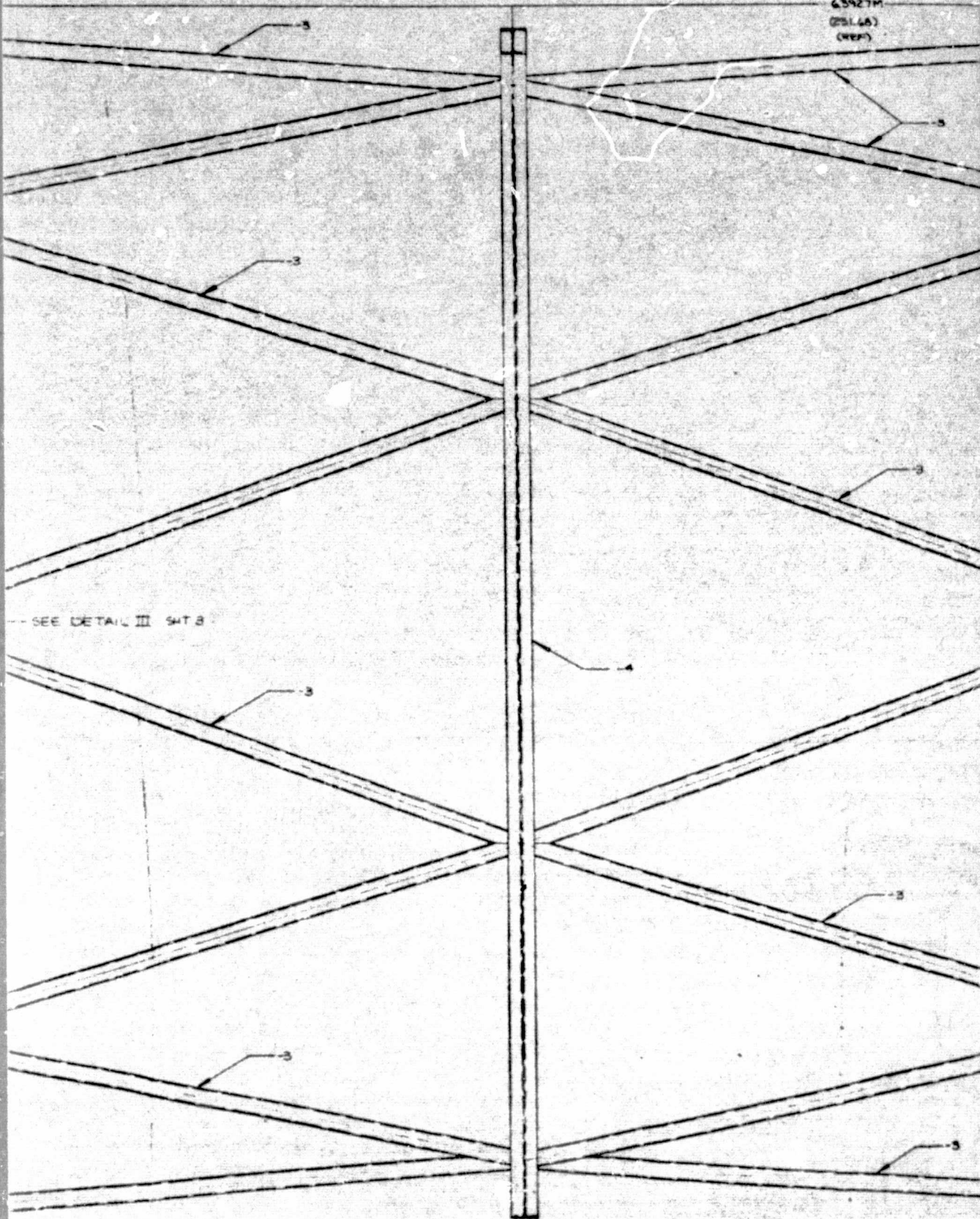
ESHT 4

FOLDOUT FRAME 2

REPRODUCIBILITY OF THE
ORIGINAL PAGE IS POOR

RFACE

63927M
(251.65)
(REF)



SEE DETAIL III SHIT 3

2160MM
(85.40)

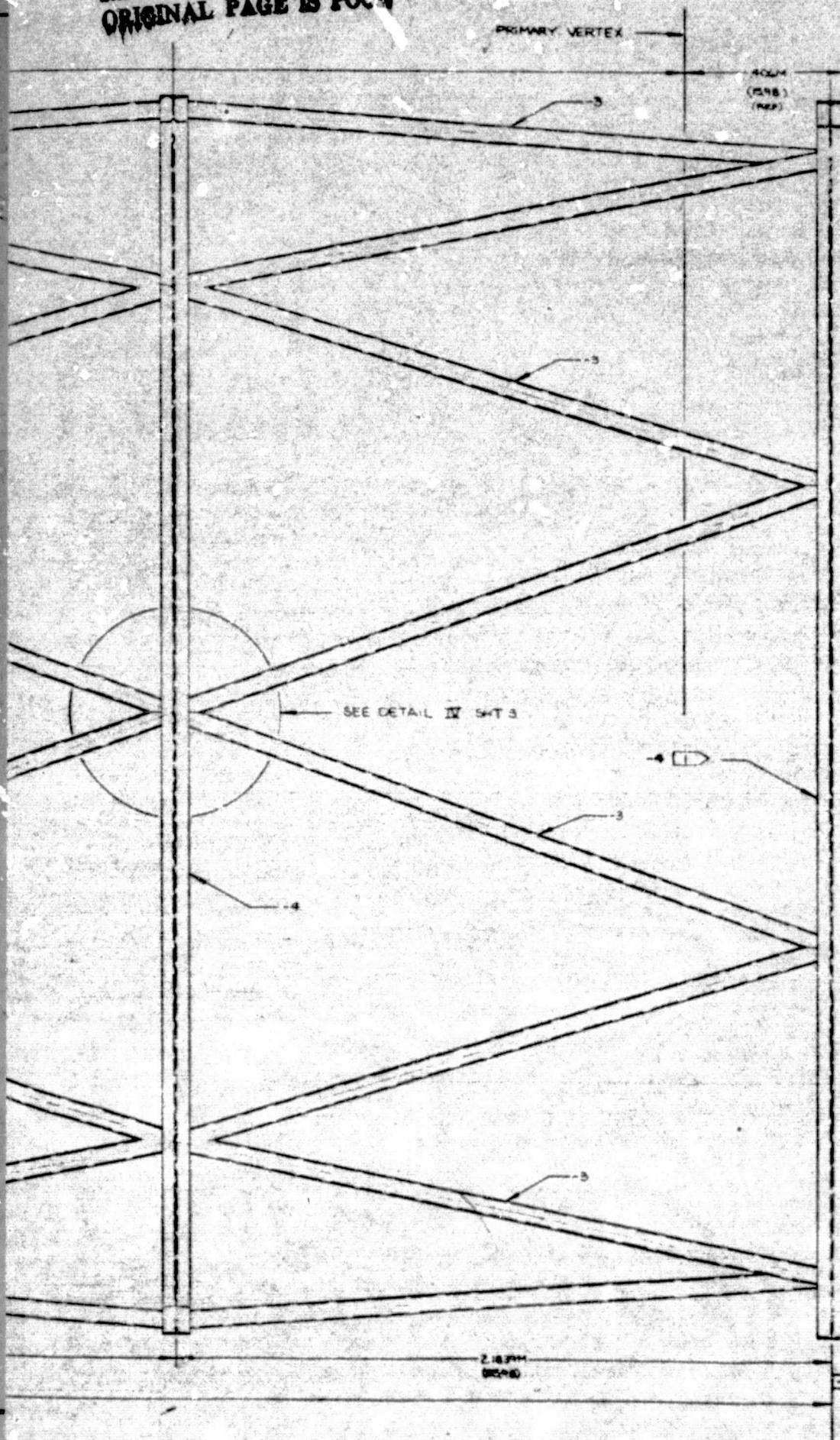
2160MM
(85.40)

100M
(39.37)

FOLDOUT FRAME 3

-1 ASSY
NO SCALE

REPRODUCIBILITY OF THE
ORIGINAL PAGE IS POOR



- 10 LAMINATE
- 9 LAMINATE
- 8 LAMINATE
- 7 LAMINATE
- 6 LAMINATE
- 5 HMF 3300/
- 4 1334 G PER
- 3 1334A PER
- 2 BOND WIT
- 1 BOND WIT
EXCEPT C
ASSYS A

BAKER-HUGHES 2
 PER ANNUAL TONAGE
 LOWEST OFFERED
 CONTRACTORS ARE
 TELEPHONICALLY
 THROUGH 220-
 REGULARLY 2001
 SWEET & SONS 2
 2001 2001 2
 1 2001 2001
 SWEET METAL CO.
 2001 2001 2

BOUYOT FRAMCE

4

ORIENTATION (0, 75%)

ORIENTATION (0, 20%)

ORIENTATION (0, 50%)

ORIENTATION (45, 45)

ORIENTATION (0, 90)

4 PER MB-0001

MB-0001

MB-0001

4 FM96 PER BAC 5514-570

4 LEFKOWELD TYPE 103

DO NOT BOND -4 RING TO -3

PLANE -A-

REPRODUCIBILITY OF THE
ORIGINAL PAGE IS POOR

[17] RADIUS FILLER (ENGR FURNISHED)

[16] TRIM -25 PRIOR TO RING ASSY

[15] SPLICE CORE WITH BMS 5-90 PER BAC 5514-590

[14] 80 F80 (5056) FLEXCORE, 2540mm (100) THICK

[13] 87-AC6-0X PERFORATED, 2540mm (100) THICK

[12] 81-516-10P (5052) PER MIL-C-7438C, 2540mm (100) THICK

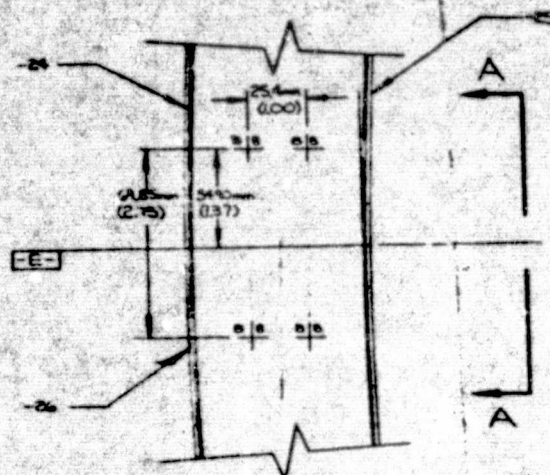
[11] LAMINATE ORIENTATION (0)

	AR	-40	CORE	[14]			
	AR	-39	CORE	[13]		6	
✓	4	-38	OPP -37	[5]	[7]	4	
✓	4	-37	ANGLE	[5]	[7]	4	
	AR	-36	CORE	[13]		6	
	1	-35	SKIN	[3]	[4]	[10]	4
	1	-34	SKIN	[3]	[4]	[10]	6
	1	-33	SKIN	[3]	[4]	[10]	2
	1	-32	SKIN	[3]	[4]	[10]	2
	1	-31	OUTER ANGLE	[3]	[4]	[8]	4
	1	-30	INNER ANGLE	[3]	[4]	[8]	4
	1	-29	CAP	[3]	[4]	[11]	4
	4	-28	DOUBLER	[3]	[4]		4
	8	-27	SPLICE	[3]	[4]	[9]	5
	4	-26	OUTER CAP	[3]	[4]	[9]	4
	4	-25	INNER CAP	[3]	[4]	[9]	4
	5	-24	CHANNEL	[5]	[6]		4
	2	-23	STRUT	[3]	[4]	[8]	5
✓	1	-22	MIRROR MOUNT				
✓	1	-21	CYL ASSY	[2]	[15]		6
✓	4	-20	BEAM ASSY	[2]			2
✓	8	-19	ANGLE	[5]	[6]		5
✓	16	-18	ANGLE	[5]	[6]		5
✓	4	-16	OPP -15	[5]	[6]		5
✓	4	-15	ANGLE	[5]	[6]		5
✓	4	-14	OPP -13	[5]	[6]		5
✓	4	-13	ANGLE	[5]	[6]		5
✓	4	-12	OPP -11	[5]	[6]		5
✓	4	-11	WEB GUSSET	[5]	[6]		5
✓	4	-10	OPP -9	[5]	[6]		5
✓	4	-9	WEB GUSSET	[5]	[6]		5
✓	4	-8	ANGLE	[5]	[7]		5
✓	1	-7	UPPER RING	[1]			4
✓	4	-6	CENTER GUSSET	[5]	[7]		5
✓	24	-5	TEE FITTING	[1]			3
✓	8	-4	RING	[1]			4
✓	24	-3	STRUT SUBASSEMBLY	[1]			5
✓	1	-2	SPIDER ASSEMBLY	[1]			2
✓	1	-1	TRUSS ASSEMBLY	[1]			1

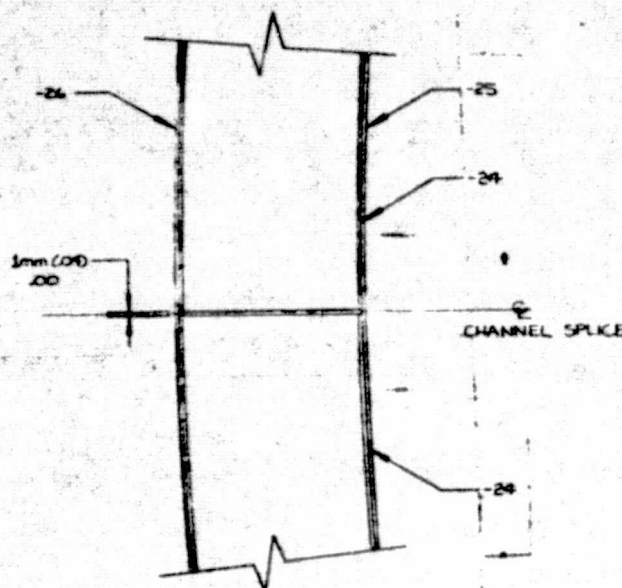
QTY	PART NO	DESCRIPTION	MATERIAL & SPECIFICATION
-----	---------	-------------	--------------------------

DATE RECEIVED		DRAWING NUMBER	
1/1/78		NASA-24825	
PROJECT		TASK	
GRAPHITE EPOXY		ENTERING TRUSS ASSY	
DATE		DATE	
1/1/78		1/1/78	
BY		BY	
J. H. HARRIS		J. H. HARRIS	
CHECKED		CHECKED	
J. H. HARRIS		J. H. HARRIS	
APPROVED		APPROVED	
J. H. HARRIS		J. H. HARRIS	
DATE		DATE	
1/1/78		1/1/78	
BY		BY	
J. H. HARRIS		J. H. HARRIS	
CHECKED		CHECKED	
J. H. HARRIS		J. H. HARRIS	
APPROVED		APPROVED	
J. H. HARRIS		J. H. HARRIS	
DATE		DATE	
1/1/78		1/1/78	
BY		BY	
J. H. HARRIS		J. H. HARRIS	
CHECKED		CHECKED	
J. H. HARRIS		J. H. HARRIS	
APPROVED		APPROVED	
J. H. HARRIS		J. H. HARRIS	
DATE		DATE	
1/1/78		1/1/78	
BY		BY	
J. H. HARRIS		J. H. HARRIS	
CHECKED		CHECKED	
J. H. HARRIS		J. H. HARRIS	
APPROVED		APPROVED	
J. H. HARRIS		J. H. HARRIS	
DATE		DATE	
1/1/78		1/1/78	
BY		BY	
J. H. HARRIS		J. H. HARRIS	
CHECKED		CHECKED	
J. H. HARRIS		J. H. HARRIS	
APPROVED		APPROVED	
J. H. HARRIS		J. H. HARRIS	
DATE		DATE	
1/1/78		1/1/78	
BY		BY	
J. H. HARRIS		J. H. HARRIS	
CHECKED		CHECKED	
J. H. HARRIS		J. H. HARRIS	
APPROVED		APPROVED	
J. H. HARRIS		J. H. HARRIS	
DATE		DATE	
1/1/78		1/1/78	
BY		BY	
J. H. HARRIS		J. H. HARRIS	
CHECKED		CHECKED	
J. H. HARRIS		J. H. HARRIS	
APPROVED		APPROVED	
J. H. HARRIS		J. H. HARRIS	
DATE		DATE	
1/1/78		1/1/78	
BY		BY	
J. H. HARRIS		J. H. HARRIS	
CHECKED		CHECKED	
J. H. HARRIS		J. H. HARRIS	
APPROVED		APPROVED	
J. H. HARRIS		J. H. HARRIS	
DATE		DATE	
1/1/78		1/1/78	
BY		BY	
J. H. HARRIS		J. H. HARRIS	
CHECKED		CHECKED	
J. H. HARRIS		J. H. HARRIS	
APPROVED		APPROVED	
J. H. HARRIS		J. H. HARRIS	
DATE		DATE	
1/1/78		1/1/78	
BY		BY	
J. H. HARRIS		J. H. HARRIS	
CHECKED		CHECKED	
J. H. HARRIS		J. H. HARRIS	
APPROVED		APPROVED	
J. H. HARRIS		J. H. HARRIS	
DATE		DATE	
1/1/78		1/1/78	
BY		BY	
J. H. HARRIS		J. H. HARRIS	
CHECKED		CHECKED	
J. H. HARRIS		J. H. HARRIS	
APPROVED		APPROVED	
J. H. HARRIS		J. H. HARRIS	
DATE		DATE	
1/1/78		1/1/78	
BY		BY	
J. H. HARRIS		J. H. HARRIS	
CHECKED		CHECKED	
J. H. HARRIS		J. H. HARRIS	
APPROVED		APPROVED	
J. H. HARRIS		J. H. HARRIS	
DATE		DATE	
1/1/78		1/1/78	
BY		BY	
J. H. HARRIS		J. H. HARRIS	
CHECKED		CHECKED	
J. H. HARRIS		J. H. HARRIS	
APPROVED		APPROVED	
J. H. HARRIS		J. H. HARRIS	
DATE		DATE	
1/1/78		1/1/78	
BY		BY	
J. H. HARRIS		J. H. HARRIS	
CHECKED		CHECKED	
J. H. HARRIS		J. H. HARRIS	
APPROVED		APPROVED	
J. H. HARRIS		J. H. HARRIS	
DATE		DATE	
1/1/78		1/1/78	
BY		BY	
J. H. HARRIS		J. H. HARRIS	
CHECKED		CHECKED	
J. H. HARRIS		J. H. HARRIS	
APPROVED		APPROVED	
J. H. HARRIS		J. H. HARRIS	
DATE		DATE	
1/1/78		1/1/78	
BY		BY	
J. H. HARRIS		J. H. HARRIS	
CHECKED		CHECKED	
J. H. HARRIS		J. H. HARRIS	
APPROVED		APPROVED	
J. H. HARRIS		J. H. HARRIS	
DATE		DATE	
1/1/78		1/1/78	
BY		BY	
J. H. HARRIS		J. H. HARRIS	
CHECKED		CHECKED	
J. H. HARRIS		J. H. HARRIS	
APPROVED		APPROVED	
J. H. HARRIS		J. H. HARRIS	
DATE		DATE	
1/1/78		1/1/78	
BY		BY	
J. H. HARRIS		J. H. HARRIS	
CHECKED		CHECKED	
J. H. HARRIS		J. H. HARRIS	
APPROVED		APPROVED	
J. H. HARRIS		J. H. HARRIS	
DATE		DATE	
1/1/78		1/1/78	
BY		BY	
J. H. HARRIS		J. H. HARRIS	
CHECKED		CHECKED	
J. H. HARRIS		J. H. HARRIS	
APPROVED		APPROVED	
J. H. HARRIS		J. H. HARRIS	
DATE		DATE	
1/1/78		1/1/78	
BY		BY	
J. H. HARRIS		J. H. HARRIS	
CHECKED		CHECKED	
J. H. HARRIS		J. H. HARRIS	
APPROVED		APPROVED	
J. H. HARRIS		J. H. HARRIS	
DATE		DATE	
1/1/78		1/1/78	
BY		BY	
J. H. HARRIS		J. H. HARRIS	
CHECKED		CHECKED	
J. H. HARRIS		J. H. HARRIS	
APPROVED		APPROVED	
J. H. HARRIS		J. H. HARRIS	
DATE		DATE	
1/1/78		1/1/78	
BY		BY	
J. H. HARRIS		J. H. HARRIS	
CHECKED		CHECKED	
J. H. HARRIS		J. H. HARRIS	
APPROVED		APPROVED	
J. H. HARRIS		J. H. HARRIS	
DATE		DATE	
1/1/78		1/1/78	
BY		BY	
J. H. HARRIS		J. H. HARRIS	
CHECKED		CHECKED	
J. H. HARRIS		J. H. HARRIS	
APPROVED		APPROVED	
J. H. HARRIS		J. H. HARRIS	
DATE		DATE	
1/1/78		1/1/78	
BY		BY	
J. H. HARRIS		J. H. HARRIS	
CHECKED		CHECKED	
J. H. HARRIS		J. H. HARRIS	
APPROVED		APPROVED	
J. H. HARRIS		J. H. HARRIS	
DATE		DATE	
1/1/78		1/1/78	
BY		BY	
J. H. HARRIS		J. H. HARRIS	
CHECKED		CHECKED	
J. H. HARRIS		J. H. HARRIS	
APPROVED		APPROVED	
J. H. HARRIS		J. H. HARRIS	
DATE		DATE	
1/1/78		1/1/78	
BY		BY	
J. H. HARRIS		J. H. HARRIS	
CHECKED		CHECKED	
J. H. HARRIS		J. H. HARRIS	
APPROVED		APPROVED	
J. H. HARRIS		J. H. HARRIS	
DATE		DATE	
1/1/78		1/1/78	
BY		BY	
J. H. HARRIS		J. H. HARRIS	
CHECKED		CHECKED	
J. H. HARRIS		J. H. HARRIS	
APPROVED		APPROVED	
J. H. HARRIS		J. H. HARRIS	
DATE		DATE	
1/1/78		1/1/78	
BY		BY	
J. H. HARRIS		J. H. HARRIS	
CHECKED		CHECKED	
J. H. HARRIS		J. H. HARRIS	
APPROVED		APPROVED	
J. H. HARRIS		J. H. HARRIS	
DATE		DATE	
1/1/78		1/1/78	
BY		BY	
J. H. HARRIS		J. H. HARRIS	
CHECKED		CHECKED	
J. H. HARRIS		J. H. HARRIS	
APPROVED		APPROVED	
J. H. HARRIS		J. H. HARRIS	
DATE		DATE	
1/1/78		1/1/78	
BY		BY	
J. H. HARRIS		J. H. HARRIS	
CHECKED		CHECKED	
J. H. HARRIS		J. H. HARRIS	
APPROVED		APPROVED	
J. H. HARRIS		J. H. HARRIS	
DATE		DATE	
1/1/78		1/1/78	
BY		BY	
J. H. HARRIS		J. H. HARRIS	
CHECKED		CHECKED	
J. H. HARRIS		J. H. HARRIS	
APPROVED		APPROVED	
J. H. HARRIS		J. H. HARRIS	
DATE		DATE	
1/1/78		1/1/78	
BY		BY	
J. H. HARRIS		J. H. HARRIS	
CHECKED		CHECKED	
J. H. HARRIS		J. H. HARRIS	
APPROVED		APPROVED	
J. H. HARRIS		J. H. HARRIS	
DATE		DATE	
1/1/78		1/1/78	
BY		BY	
J. H. HARRIS		J. H. HARRIS	
CHECKED		CHECKED	
J. H. HARRIS		J. H. HARRIS	
APPROVED		APPROVED	
J. H. HARRIS		J. H. HARRIS	
DATE		DATE	
1/1/78		1/1/78	
BY		BY	
J. H. HARRIS		J. H. HARRIS	
CHECKED		CHECKED	
J. H. HARRIS		J. H. HARRIS	
APPROVED		APPROVED	
J. H. HARRIS		J. H. HARRIS	
DATE		DATE	

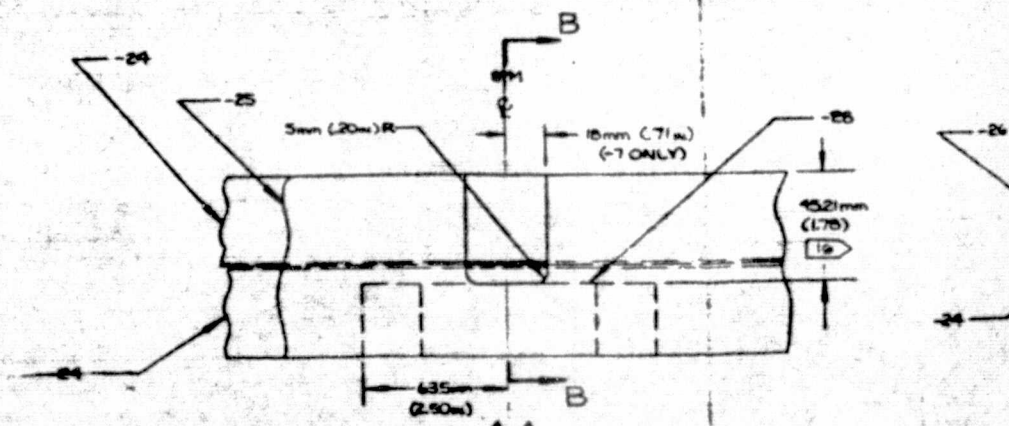
REPRODUCIBILITY OF THE
ORIGINAL PAGE IS POOR



DETAIL II
ROTATED 67 1/2° CW
FULL SCALE

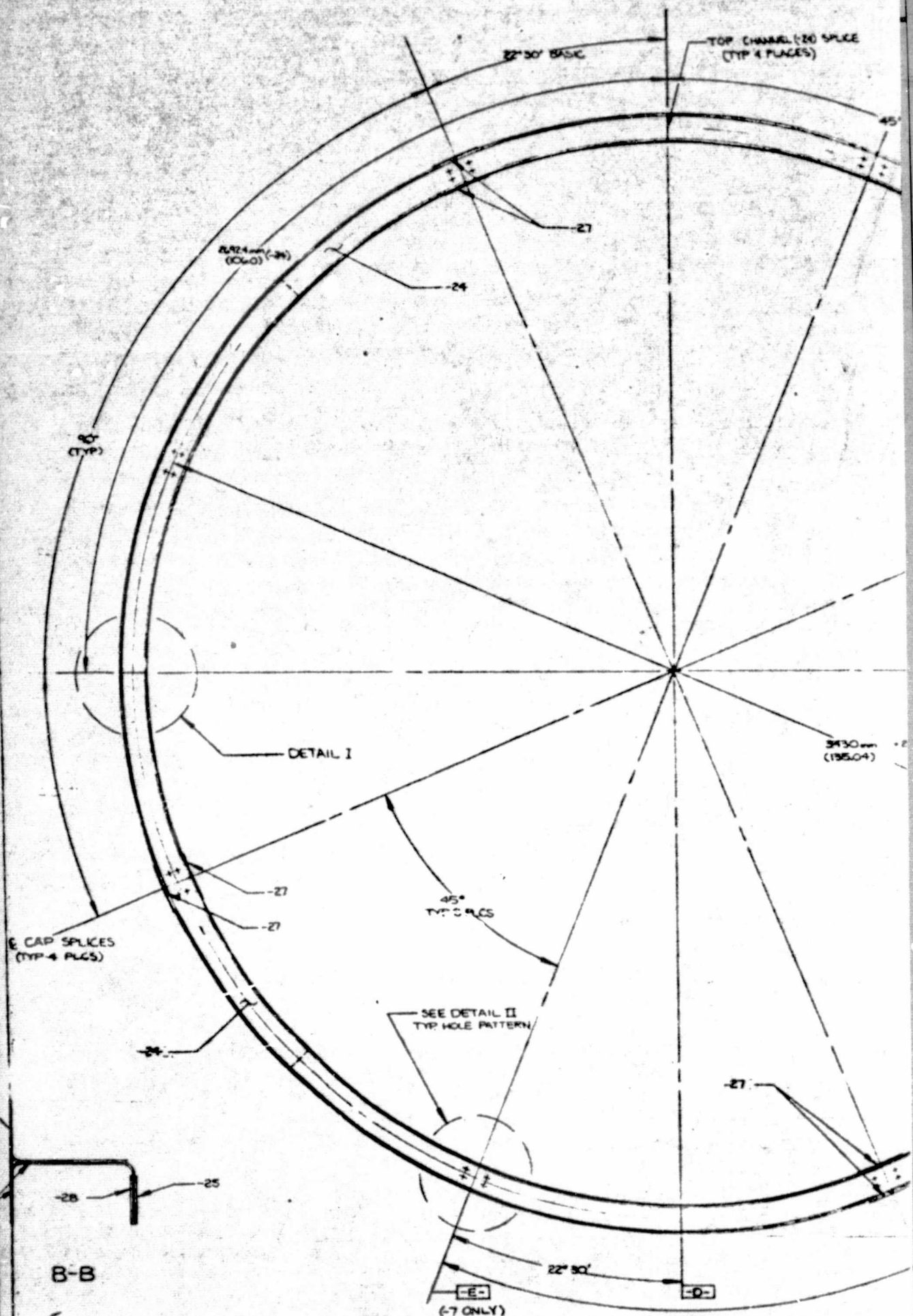


DETAIL I
FULL SCALE
TYP 8 PLACES



A-A
ROTATED 90° CW
FULL SCALE
TYP 4 PLACES

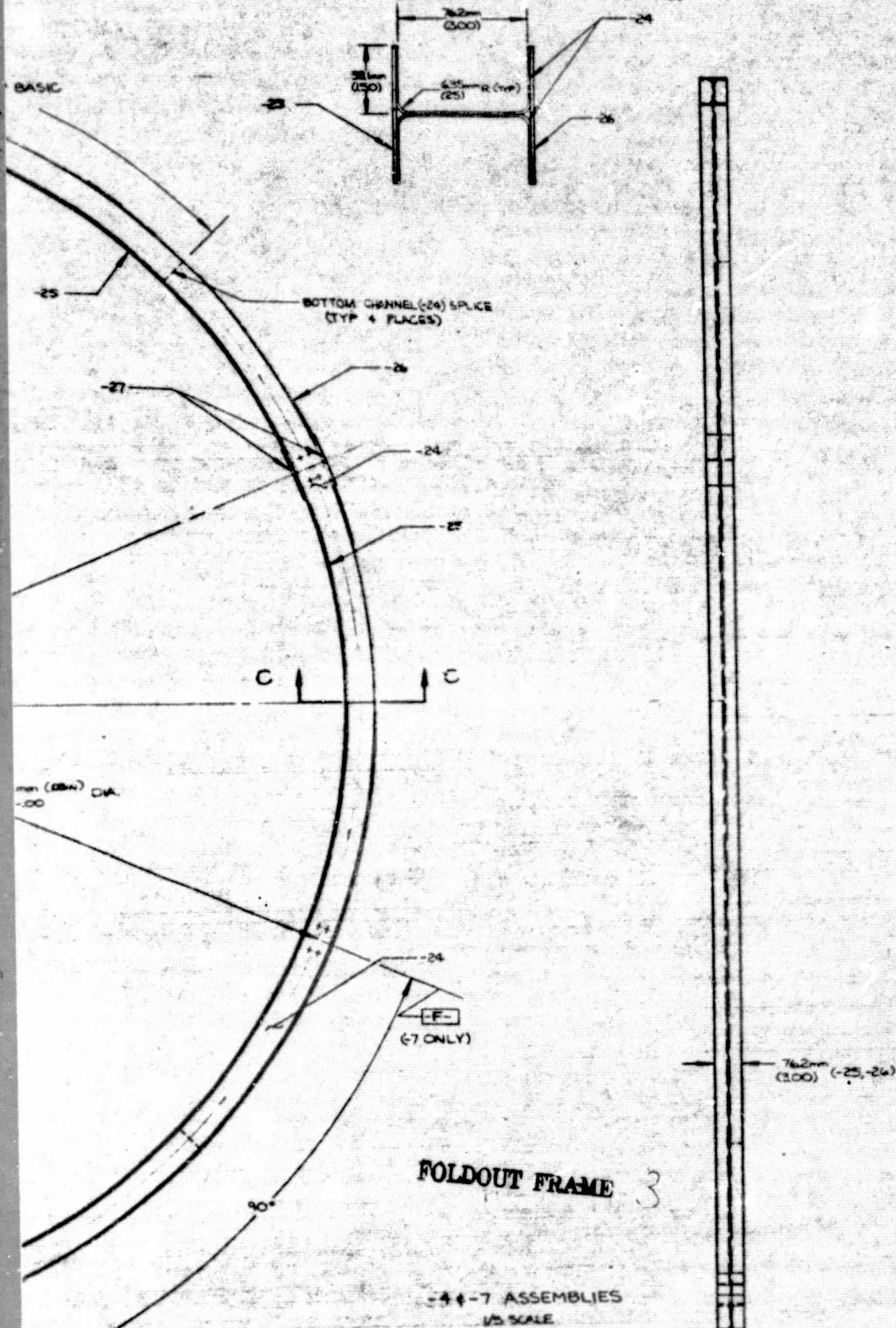
FOLDOUT FRAME



FOLDOUT FRAME

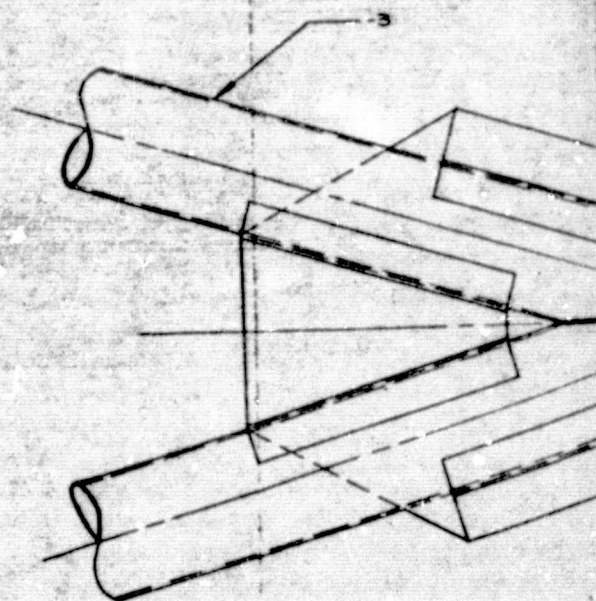
2

REPRODUCIBILITY OF THE
ORIGINAL PAGE IS POOR

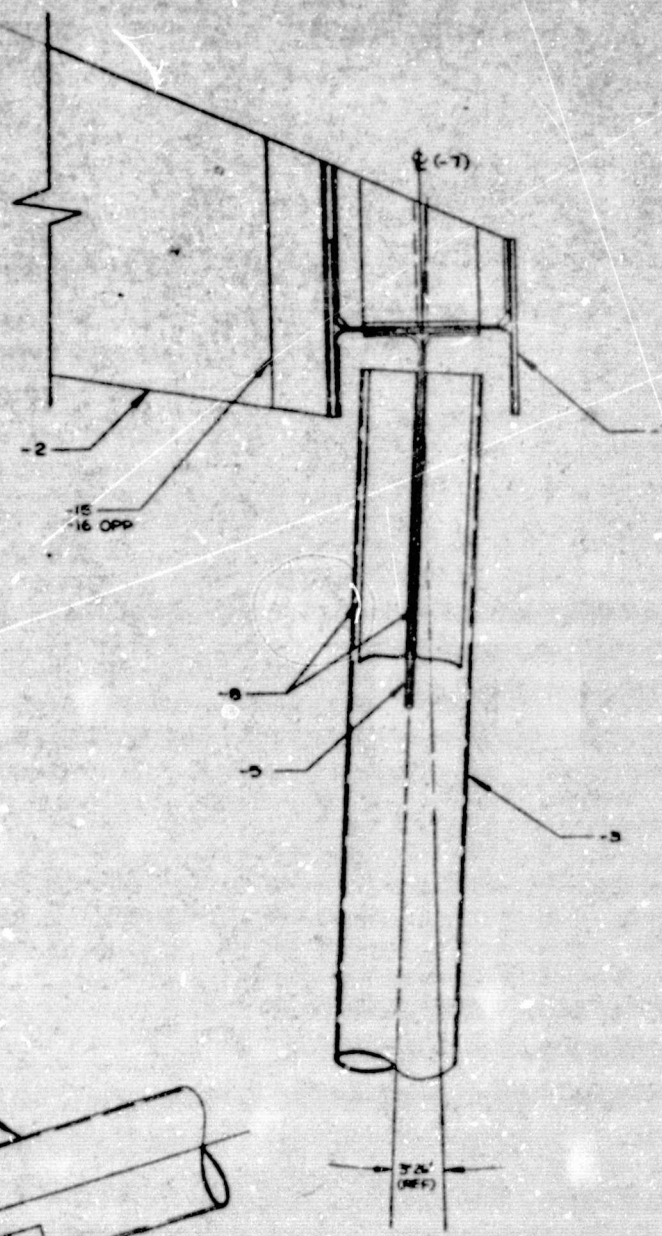


UNLESS OTHERWISE SPECIFIED DIMENSIONS ARE IN INCHES TOLERANCES ARE: DECIMALS .001 FRACTIONS 1/32 HOLE & SHAFT MOUNTING ARE 1/32 DIA. AND GREATER HOLE & SHAFT MOUNTING ARE 1/32 DIA. AND GREATER		DATA SHEET PROJECT: DATE: DRAWN BY: CHECKED BY: APPROVED BY: DATE: SCALE: SHEET NO. OF TOTAL SHEETS		CONTACT NUMBER NAS-22825 THE BOEING COMPANY CORPORATE OFFICES SEATTLE WASHINGTON 98106 GRAPHITE EPOXY METERING TRUSS ASSY SK-74003-GE SCALE: SHEET NO. OF TOTAL SHEETS	
--	--	---	--	---	--

Figure 3-6B.



FOLDOUT FRAME



2-7

2

15
16 OPP

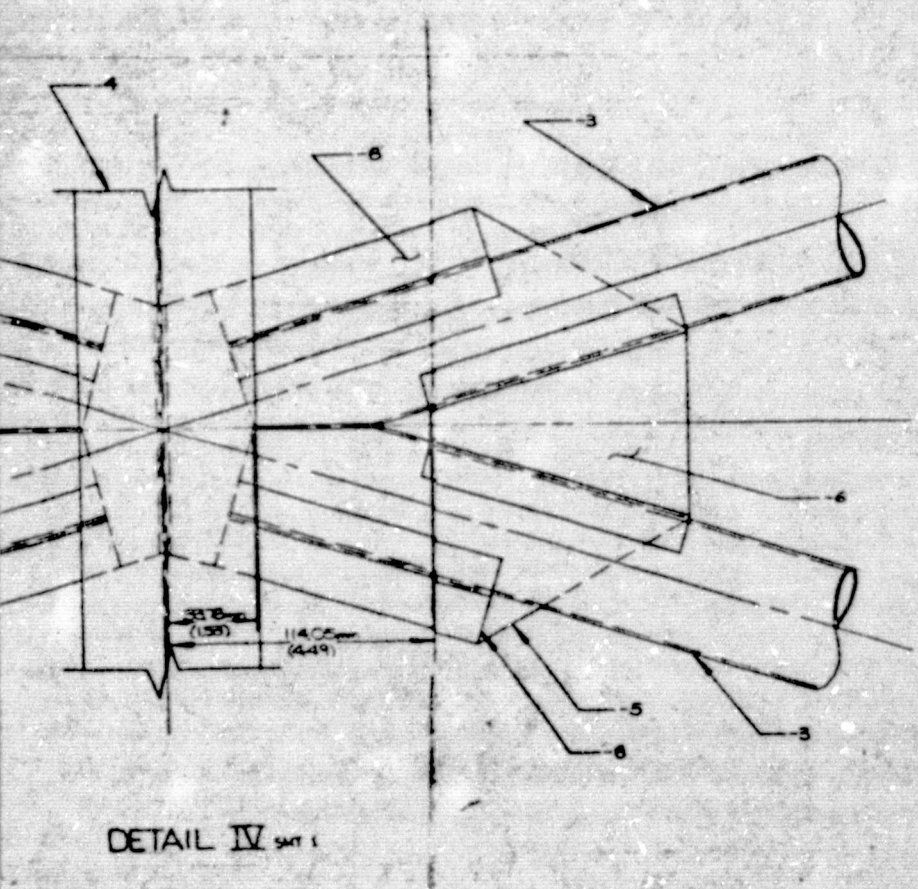
8

5

3

3.26
(REF)

A-A



DETAIL IV SWT 1

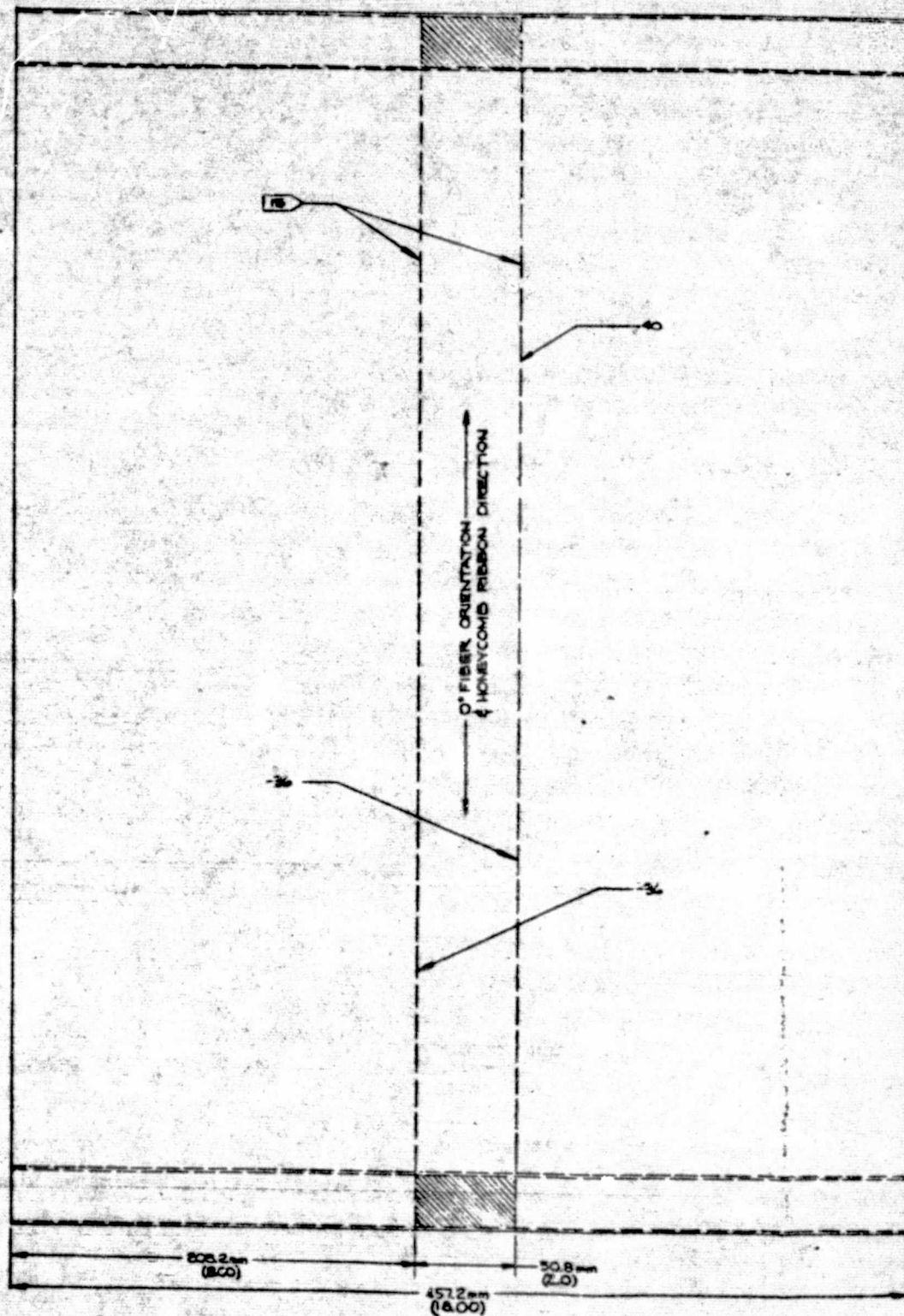
FOLDOUT FRAME

[illegible]

FOLDOUT FRAME

[illegible]

22 C

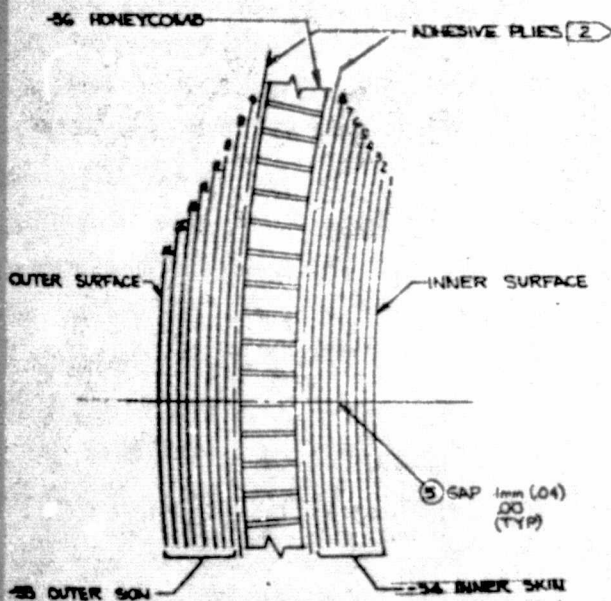
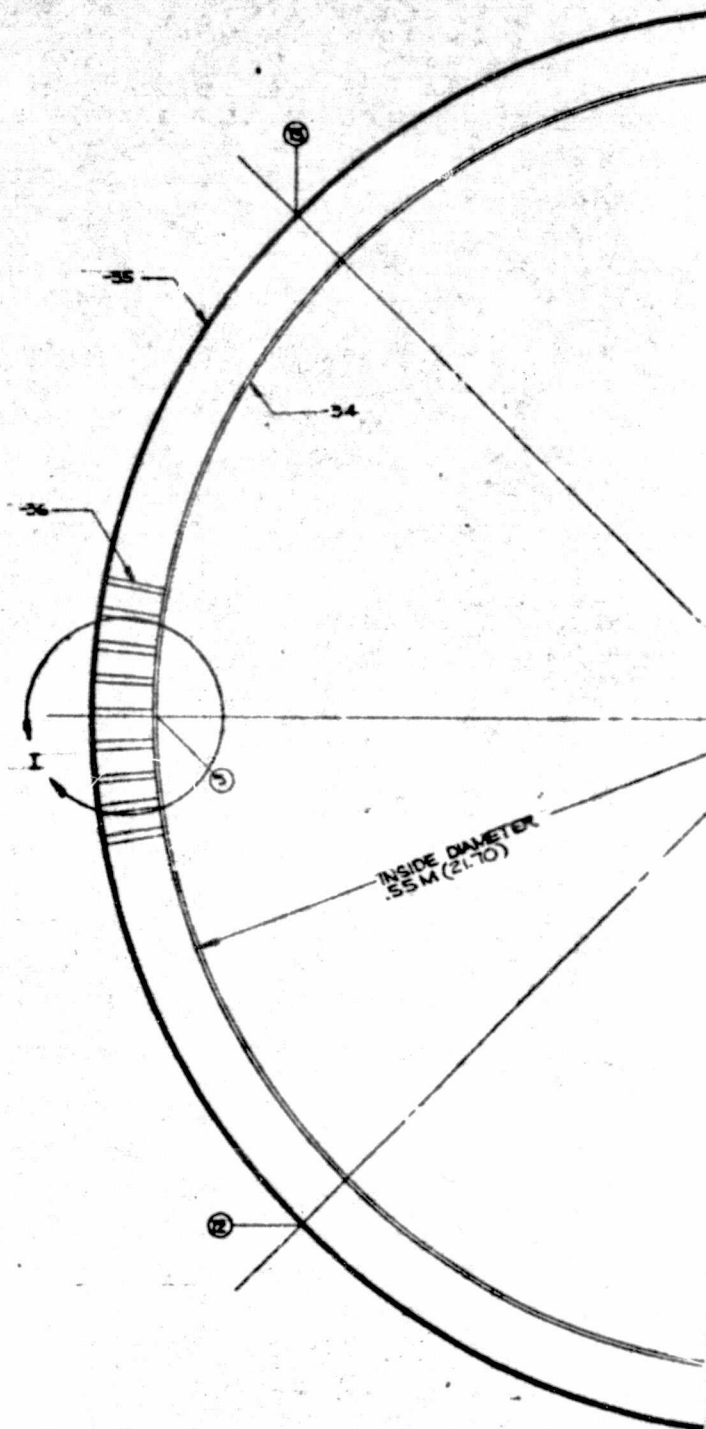


-21 ASSY SIDE VIEW
FULL SCALE

REPRODUCIBILITY OF THE
ORIGINAL PAGE IS POOR

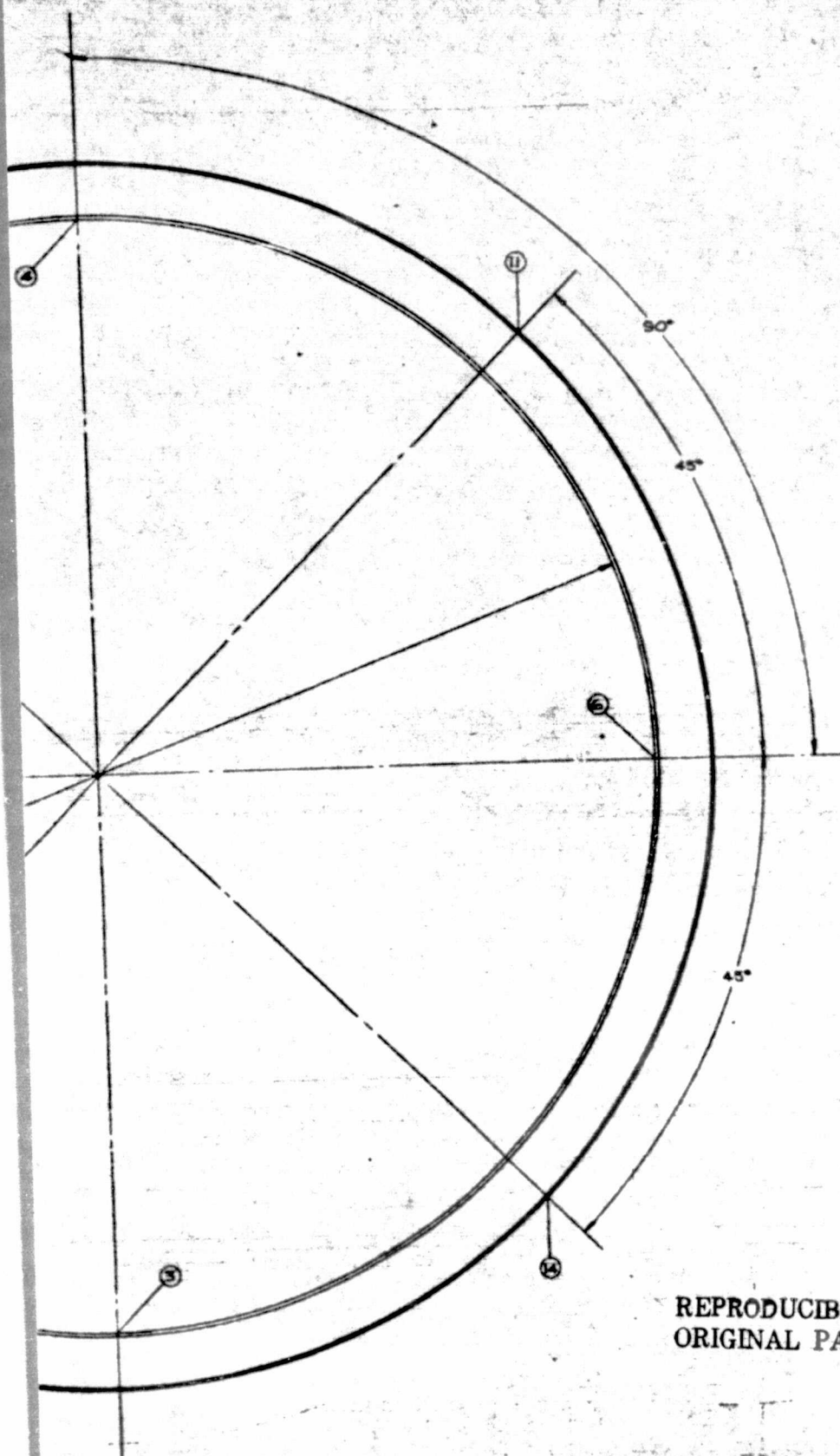
FOLDOUT FRAME

PLY NUMBER AND LOCATION		ORIENTATION (DEGREES)	SPLICE LOCATION (21 ASSY DESIG)
INNER SKIN		(31° TOL)	
INSIDE SURFACE	1	+75	-
	2	-75	-
	3	0	③
	4	0	④
	5	0	⑤
	6	0	⑥
	7	-75	-
	8	+75	-
OUTER SKIN	H/C		
	9	+75	-
	10	-75	-
	11	0	⑪
	12	0	⑫
	13	0	⑬
	14	0	⑭
	15	-75	-
OUTSIDE SURFACE	16	+75	-



DETAIL I
FLY LOCATIONS

FOLDOUT FRAME



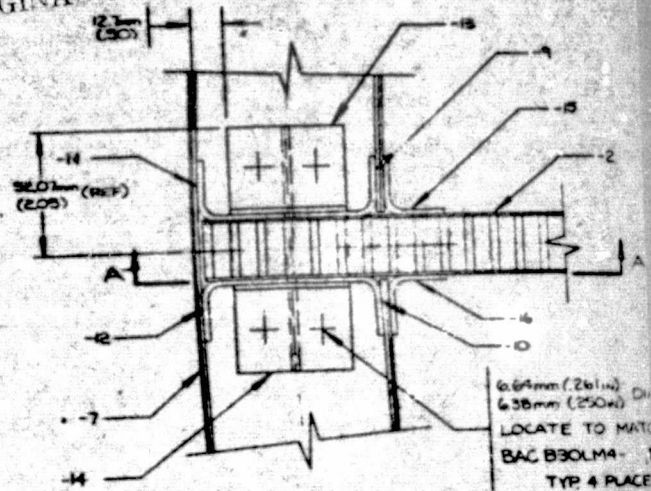
FOLDOUT FRAME 3

-21 CYLINDER ASSY.
FULL SIZE

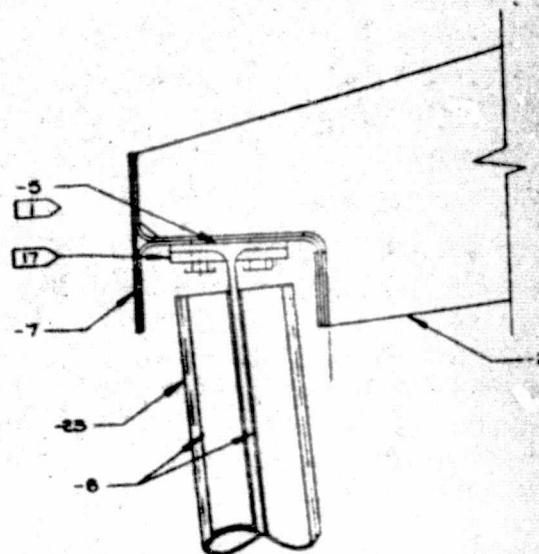
[illegible]

Figure 3-6D.

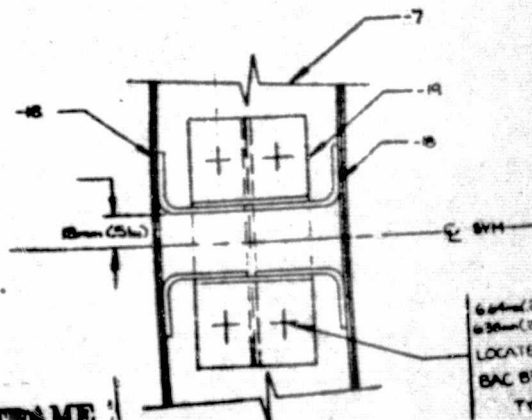
REPRODUCIBILITY OF THE
ORIGINAL PAGE IS POOR



DETAIL I
FULL SCALE
TYP 4 PLACES



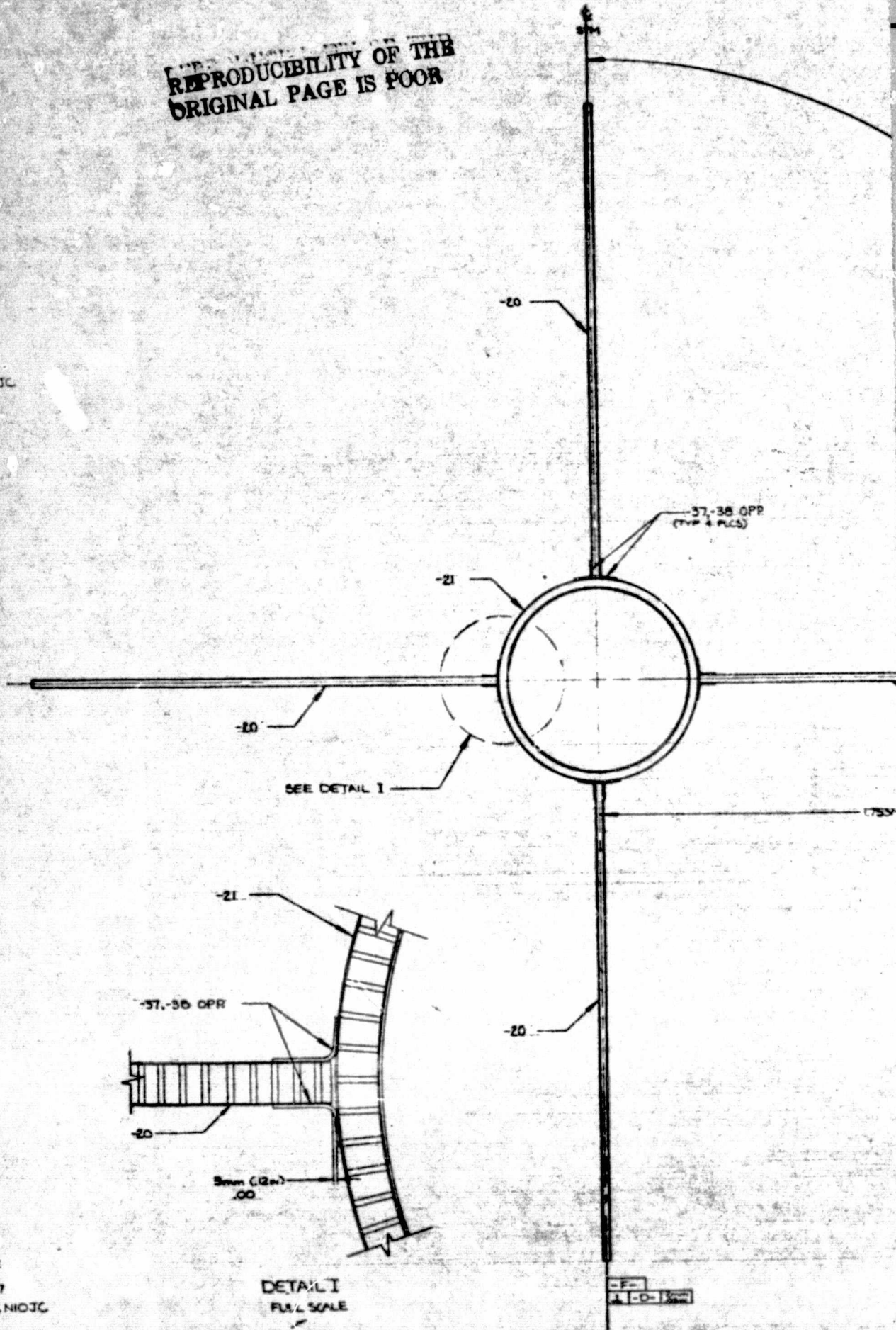
A-A
FULL SCALE



DETAIL II
ROTATED 45°
FULL SCALE

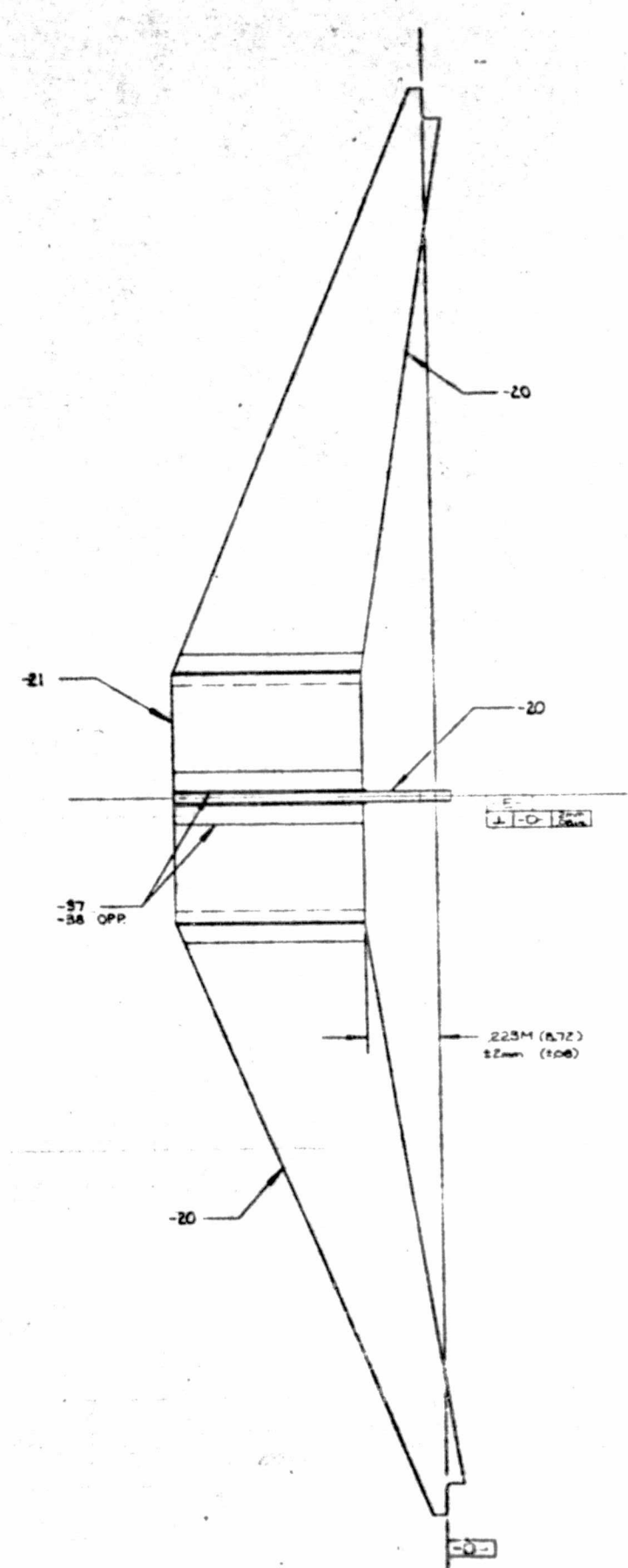
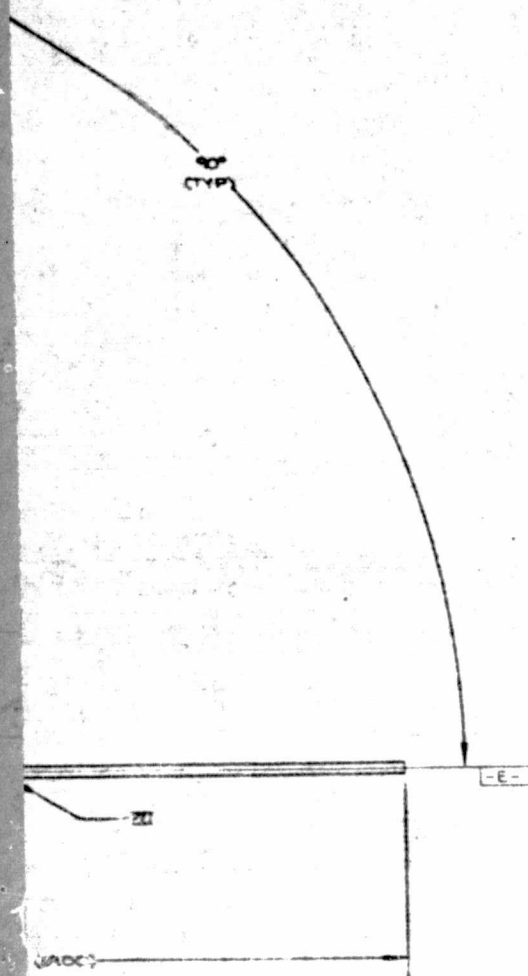
FOLDOUT FRAME

REPRODUCIBILITY OF THE
ORIGINAL PAGE IS POOR



FOLDOUT FRAME

TOP VIEW
-2 ASSY
VS SCALE



HOLDOUT FRAME

3

**SIDE VIEW
-2 ASSY
1/8 SCALE**

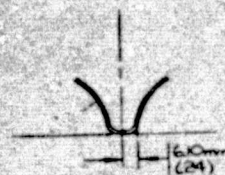
R



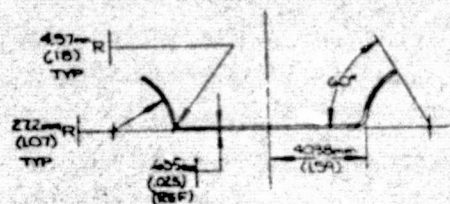
4

22 E

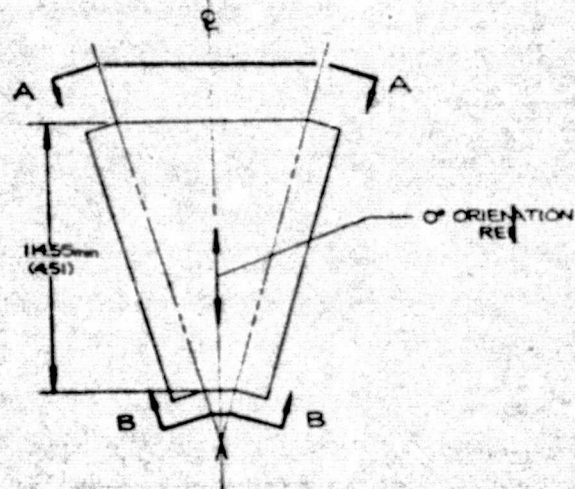
[illegible]



B-B

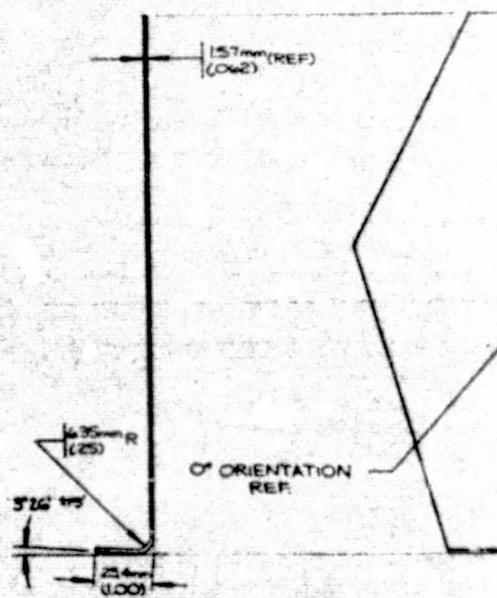
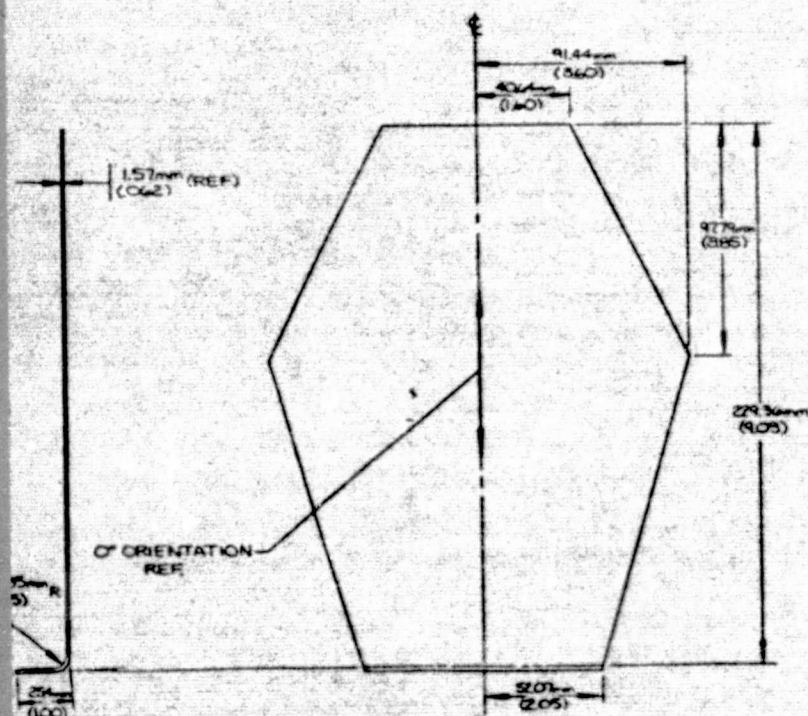
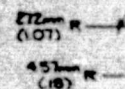
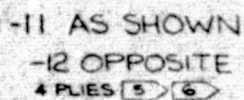
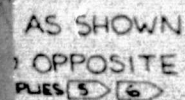


A-A



-6

REPRODUCIBILITY OF THE
ORIGINAL PAGE IS POOR



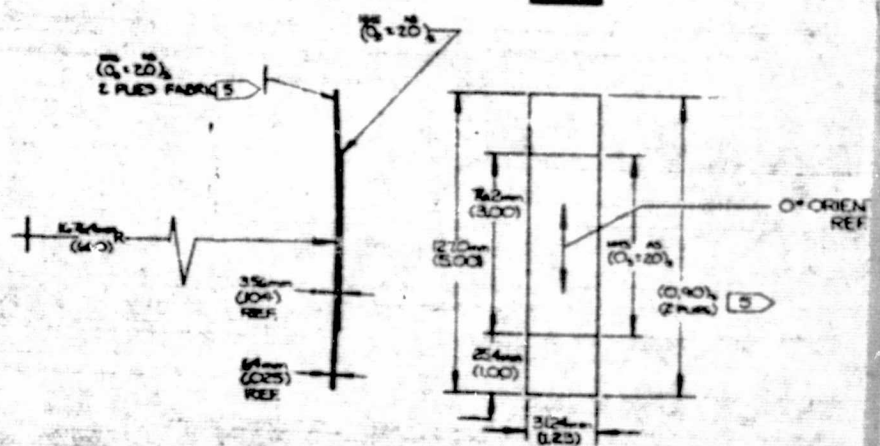
FOLDOUT FRAME

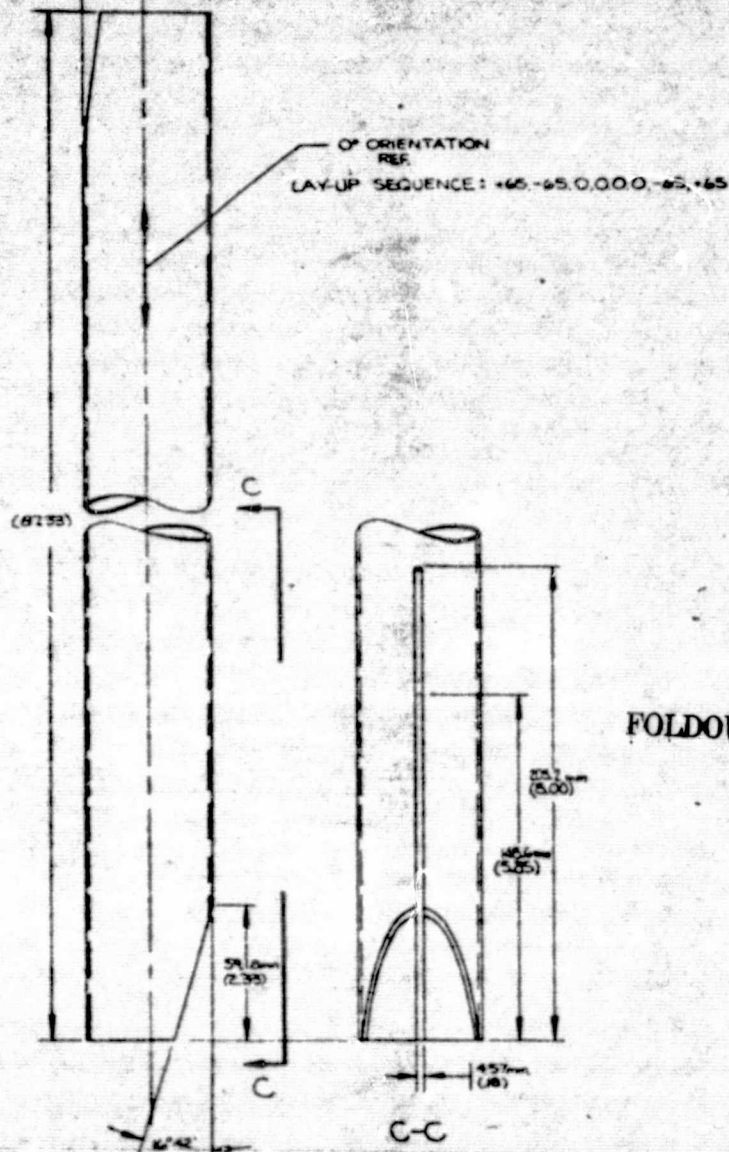
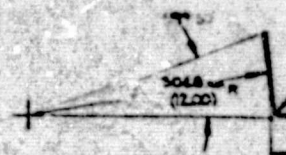
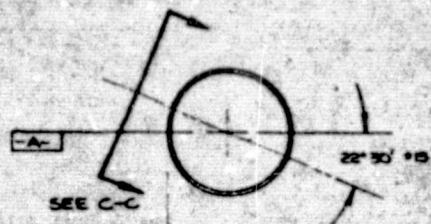
2



REPRODUCIBILITY OF THE
ORIGINAL PAGE IS POOR

FOLDOUT FRAME

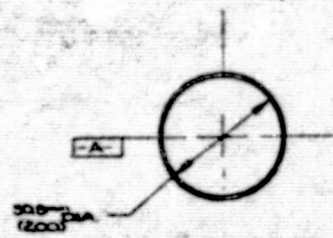




FOLDOUT FRAME 2

-37
-38
4 PL

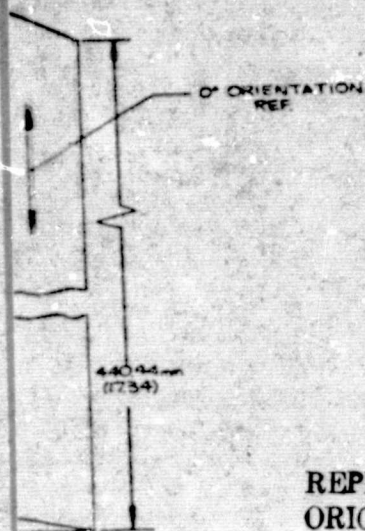
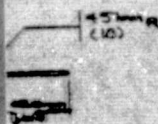
TATION



OF ORIENTATION REF.

45° (18)

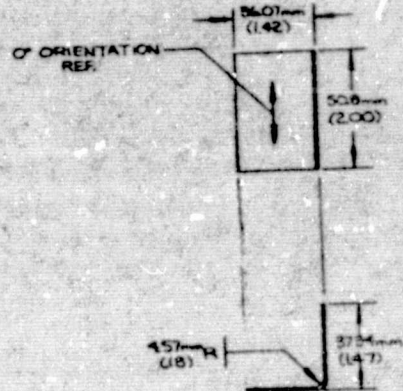
23511



AS SHOWN
OPPOSITE
B 5 6

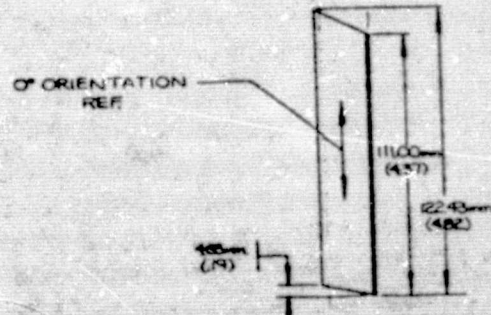
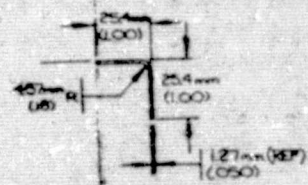


-18
B 5 6



-19
A PUES 5 6

FOLDOUT FRAME 3



-15 AS SHOWN
-16 OPPOSITE
A PUES 5 6

4.0 ANALYSIS

A NASTRAN finite element model of the metering truss, was used to perform static, dynamic and thermal distortion analysis. Several runs were made to determine the minimum EA and EI requirements for the truss elements. These were combined with the data obtained from the laminate analysis to establish the fiber orientations and laminate thicknesses used in the strut, and secondary mirror support structure designs.

The truss structure consists of a cylindrical configuration stabilized by four rings. The rings were modeled as octagons with eight NASTRAN CBAR elements. Each of the spider beams supporting the secondary mirror were modeled by three CBAR elements. Sixteen CBAR elements represented the tubular truss members in each bay.

The spider beams were constrained to move together with a common grid point representing the secondary mirror. This was achieved by use of the NASTRAN MPC capability.

In addition to the secondary mirror mass and moments of inertia, the spider beams, rings and truss members were assigned densities to establish an initial structural mass distribution. As new mass and element property data were developed the NASTRAN analysis was updated. The final dynamic and thermal deflection analysis was performed using actual scaled weights and properties obtained from elements that were representative of the fabricated truss details. Table 4-1 summarizes the truss mass distribution used in the analysis and Table 4-2 summarizes the truss properties. Figure 4-1 shows the model geometry.

Two types of stress and dynamics runs were performed. In both, the joints between the spider beams and the spider cylinder were fixed and the balance of the joints were assumed to be either moment resistant or pinned.

Modal Analysis Results

Frequencies and mode shapes were determined using NASTRAN Rigid Format 3 (Normal Mode Analysis) for the metering truss cantilevered from its base. The first five modes obtained for both fixed and pinned joints are described in Table 4-3. As shown, the first mode bending frequency for the structural model with pinned joints and the one with fixed joints are both in excess of the design requirement of 15 Hz minimum.

Stress Analysis

The stress analysis computed internal loads and deflections for the following conditions:

- 1) 453.6KG (1000 lb) applied at grid pt 10 (mirror CG) in the X direction.
- 2) 453.6KG (1000 lb) applied at grid pt 10 in the Y direction.
- 3) 453.6KG (1000 lb) applied at grid pt 10 in the Z direction.
- 4) 1152KG-cm (1000 lb-in) applied at grid pt 10 in the X axis.
- 5) 1152KG-cm (1000 lb-in) applied at grid pt 10 in the Y axis.
- 6) 1152KG-cm (1000 lb-in) applied at grid pt 10 in the Z axis.
- 7) 1g applied in the X direction.
- 8) 1g applied in the Y direction.

- 9) 1g applied in the Z direction.
- 10) Uniform temperature rise of 5.55°C (10°F).

NOTE: X & Y are mutually perpendicular axes in the lateral direction, Z is along the axis of the truss, positive from the base to the secondary mirror CG.

Structural Stiffness

The first six conditions were used to determine the stiffness of the structure due to unit loads applied at grid point 10 (CG of the secondary mirror). A summary of these results is shown in Table 4-4.

Component Maximum Stresses

The maximum stresses in the spider beams, strut members and ring members resulted from the LST crash load conditions. The latest revision to JSC 07700 Vol. XIV Rev. C (6/25/74) "Space Shuttle System Payload Accommodations" gives the ultimate load factors to be used with this condition as 9.0g (axial) and 4.5g (lateral), the factors to be applied separately.

The stresses resulting from 1g axial and 1g lateral loads are:

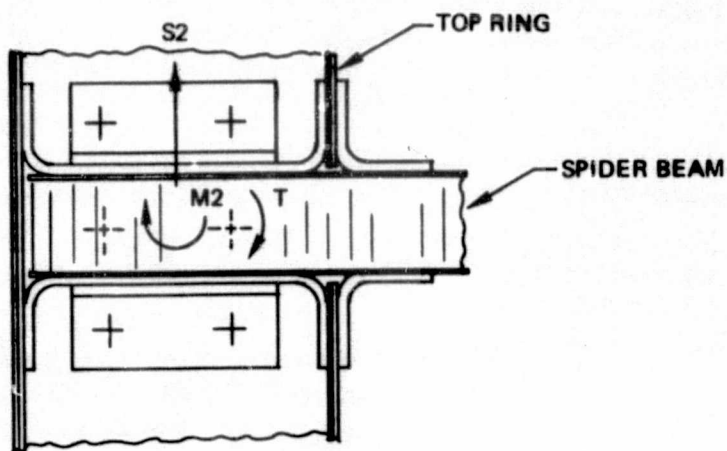
Component	Condition	Member Loading	Nominal Stress Level
Spider Beams	1G Axial	Bending	1.61 MN/m^2 (234 lb/in ²)
	1G Lateral	Axial Load	1.10 MN/m^2 (159 lb/in ²)
Rings	1G Axial	Bending	1.91 MN/m^2 (277 lb/in ²)
	1G Lateral	Bending	3.14 MN/m^2 (456 lb/in ²)
Lower Struts	1G Axial	Axial Load	$.37 \text{ MN/m}^2$ (53 lb/in ²)
	1G Lateral	Axial Load	2.99 MN/m^2 (433 lb/in ²)

The maximum ultimate member stresses based on the above design load factors are:

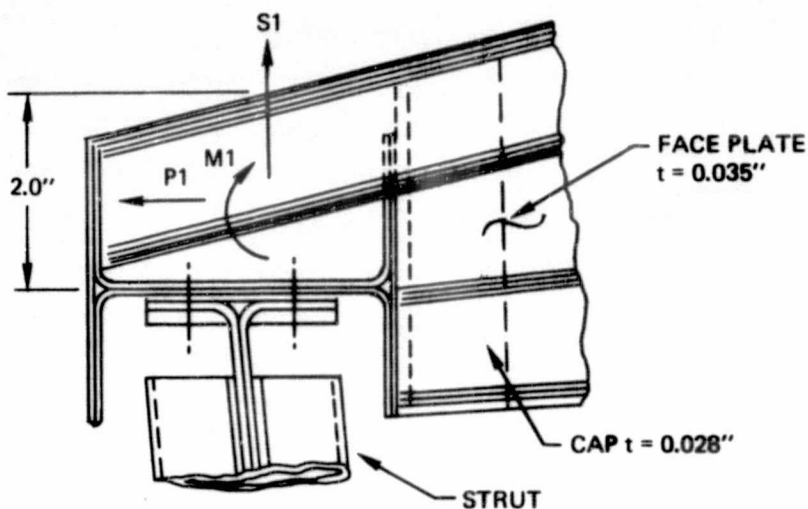
Component	Stress	Microyield Allowable	M.S.
Spider Beams	14.48 MN/m^2 (2100 lb/in ²)	-	High
Rings	17.17 MN/m^2 (2490 lb/in ²)	131 MN/m^2 (19,000 lb/in ²)	+ 6.6
Struts	13.45 MN/m^2 (1950 lb/in ²)	161.3 MN/m^2 (23,400)	+11.0

Joint Stresses

- 1) Spider Beam/top ring joint



Condition load	lg lateral load	lg axial load
S1 (1b)	- 8	-27
P1 (1b)	-55	24
M ₁ (1b.in)	-13	91
S ₂ (1b)	3	0
M ₂ (1b.in)	77	0
T (1b.in)	0	0



$$\text{Max spider beam stress (4.5g lateral)} = \left(\frac{13 \times 1}{.084} + \frac{77 \times .5}{.063} + \frac{55}{4 \times .063} \right) 4.5 = 4430 \text{ lb/in}^2$$

$$\text{Max spider beam stress (9g axial)} = \left(\frac{91 \times 1}{.084} + \frac{24}{4 \times .063} \right) 9.0 = 10,600 \text{ lb/in}^2$$

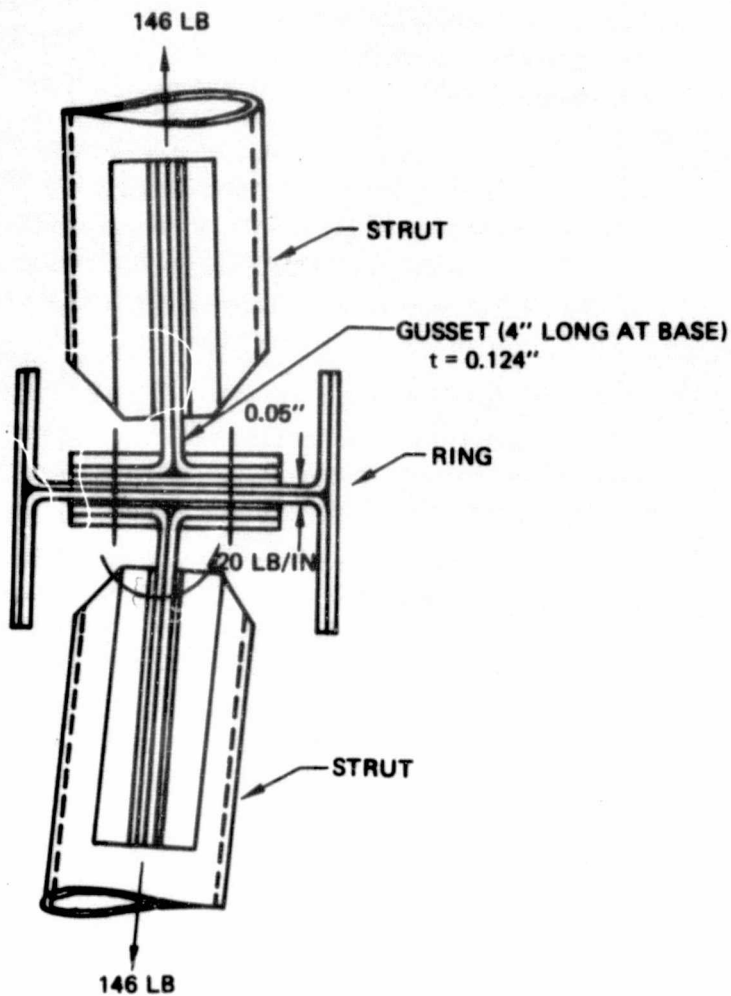
$$\text{Allowable stress } 25,000 \text{ lb/in}^2 \text{ MS } 1.35$$

$$\text{Max stress (adhesive)} = \frac{1.43 \times 91 \times 4.5}{2} + \frac{24 \times 4.5}{2 \times 1.25 \times 2.5} = 310 \text{ lb/in}^2$$

$$\text{Allowable adhesive stress} = 500 \text{ lb/in}^2 * \text{ MS } = +0.62$$

* Microyield strain allowable

2) Intersection of four strut members

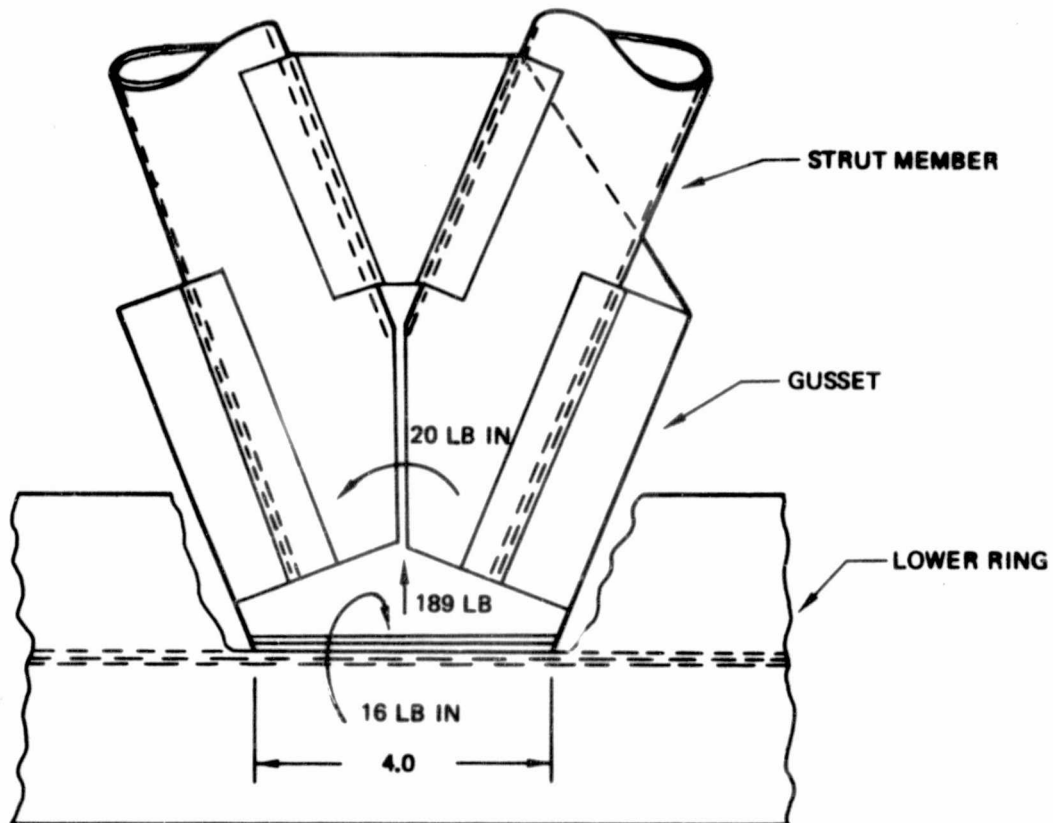


$$\text{Max gusset stress} = \left(\frac{20 \times 6}{4 \times 0.124^2} + \frac{146}{4 \times 0.124} \right) \times 4.5 = 10,000 \text{ lb/in}^2$$

$$\text{Ring Web Stress} = \frac{20 \times 5 \times 6}{3 \times 0.05^2 \times 3} \times 4.5 = 12,000 \text{ lb/in}^2$$

$$\text{Allowable stress} > 19,500 \text{ lb/in}^2 \quad \text{MS} > +0.62$$

3) Lower ring/strut joint



$$\text{Maximum gusset stress} = \left(\frac{16 \times 6}{4 \times 1.24^2} + \frac{189}{4 \times 1.24} \right) 4.5 = 8730 \text{ lb/in}^2$$

$$\text{Maximum ring web stress} = \left(\frac{16 \times 7.5 \times 6}{2.9 \times 4 \times 0.05^2} \right) 4.5 = 11,200 \text{ lb/in}^2$$

$$\text{Allowable stress } 19,500 \text{ lb/in}^2 * \quad \text{MS} \quad +0.74$$

$$\text{Adhesive stress (gusset/strut)} = \frac{174 \times 4.5}{4 \times 4.7} + \frac{14 \times 4.5}{1.75 \times 2 \times 4.7} = 46 \text{ lb/in}^2$$

$$\text{Allowable stress} = 500 \text{ lb/in}^2 * \quad \text{MS} = \text{High}$$

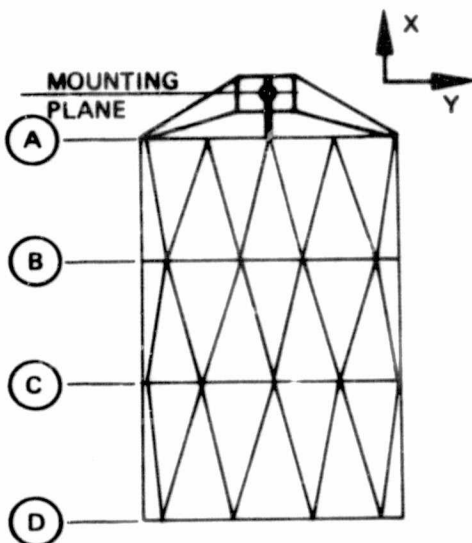
* Microyield stress allowable

Thermal Deflections

Deflections were determined using NASTRAN Rigid Format 1 (Static Analysis) for two thermal heating full-scale test conditions. The metering truss was supported at the secondary mirror grid point. The conditions were:

- 1) Uniform temperature rise of 5.55°C (10°F)
- 2) Uniform temperature rise of 5.55°C (10°F) on one-half of the truss

The calculated deflections are as follows:



Truss location	Condition (1) Axial (x) deflection	Condition (2) Lateral (y) deflection
Mounting plane	0	0
(A)	+21.87 E-5 cm (+8.61 E-5 in.)	+5.18 E-5 cm (+2.04 E-5 in.)
(B)	-2.49 E-5 cm (-0.98 E-5 in.)	-31.65 E-5 cm (-12.46 E-5 in.)
(C)	-26.80 E-5 cm (-10.55 E-5 in.)	-10.87 E-5 cm (-27.90 E-5 in.)
(D)	-51.10 E-5 cm (-20.12 E-5 in.)	-140.08 E-5 cm (-55.15 E-5 in.)

This analysis was originally made to predict the performance of the truss in the full-scale thermal vacuum test. In this test, resistance heaters were installed on all truss elements. In this configuration CTE element tests showed a $.072 \times 10^{-6} \text{ cm/cm/}^{\circ}\text{C}$ ($.04 \times 10^{-6} \text{ in/in/}^{\circ}\text{F}$) positive CTE effect on the struts. The above axial deflections have been adjusted for this effect.

Additional axial (X) deflection also result from the expansion of material thicknesses at the joints. The total through the thickness growth, using a CTE of 21.6×10^{-6} cm/cm/ $^{\circ}$ C (12×10^{-6} in/in $^{\circ}$ F), was 15.24×10^{-5} cm, (6.0×10^{-5} in.).

The total axial (X) movements for a ΔT of 1.67° C (3° F) applied to the structure was $[\frac{3}{10} (-201 - 60) \times 10^{-6}] = -1.99 \times 10^{-6}$ m (-78.3×10^{-6} inches). This is within the budget of $\pm 2 \times 10^{-6}$ m ($\pm 80 \times 10^{-6}$ inches) for a 1.67° C (3° F) change.

The results of the lateral deflection (decenter) analysis was 14×10^{-6} m (551.5×10^{-6} in.) which when ratioed for a 1.67° C (3° F) change is 4.2×10^{-6} m (165.4×10^{-6} in.). This is well within the despace budget of 10×10^{-6} m (394×10^{-6} in.).

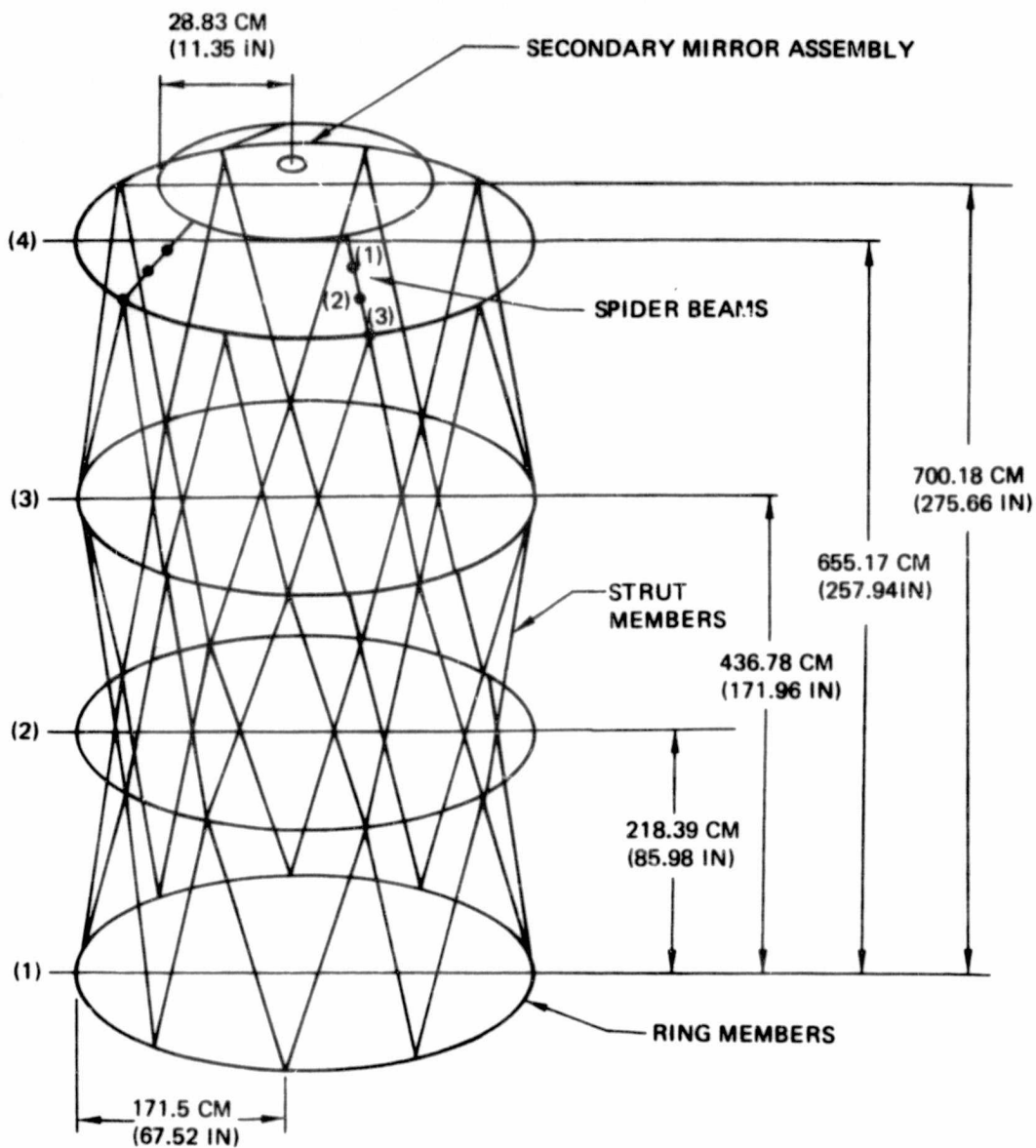


Figure 4-1. Truss Model Geometry

Table 4-1. Graphite/Epoxy Truss Mass Distribution

Description	kg	LB
Spider Cylinder	7.80	17.20
4 spider beams (with potting)	12.42	27.37
Top ring	10.75	23.71
8 top joints	2.30	5.06
1g. struts (bay 1)	16.46	36.29
8 joints	2.30	5.06
Ring	10.30	22.71
8 joints	2.30	5.06
16 struts (bay 2)	16.46	36.29
8 joints	2.30	5.06
Ring	10.30	22.71
8 joints	2.30	5.06
16 struts (bay 3)	16.46	36.29
8 joints	2.30	5.06
Bottom ring	10.30	22.71
Secondary mirror mass	56.70	125.00
Total	181.75	400.68

NOTE: ABOVE VALUES ARE ACTUAL WEIGHTS

Table 4-2. Graphite/Epoxy Truss Properties



	A $m^2 \times 10^4$ (in^2)	I_1 $m^4 \times 10^8$ (in^4)	I_2 $m^4 \times 10^8$ (in^4)	J $m^4 \times 10^8$ (in^4)	A_{S1}/A	A_{S2}/A	E_x $N/m^2 \times 10^{-9}$ ($PSI \times 10^{-6}$)	G_{xy} $N/m^2 \times 10^{-9}$ ($PSI \times 10^{-6}$)	cm/cm/ $^{\circ}C \times 10^6$ ($in/in/^{\circ}F \times 10^6$)
Strut members	2.68 (0.415)	8.91 (0.214)	8.91 (0.214)	17.81 (0.428)	(.050)	(0.50)	108.25 (15.7)	15.17 (2.2)	.31 (0.17) ①
Ring members	6.15 (0.954)	88.86 (2.135)	26.39 (0.634)	.062 (.0015)	(0.11)	(0.79)	107.56 (15.6)	7.52 (1.09)	.78 (.431) ①
Spider beams (1)	8.16 (1.265)	2,247.5 (54.00)	15.94 (0.382)	35.38 (0.850)	(0.84)	(0.25)	119.28 (17.3)	10.83 (1.57)	.088 (.049)
(2)	5.92 (0.917)	761.65 (18.30)	11.32 (0.272)	23.31 (0.560)	(0.78)	(0.23)	119.28 (17.3)	10.83 (1.57)	.088 (.049)
(3)	3.68 (0.570)	148.17 (3.560)	6.91 (0.166)	11.24 (0.270)	(0.66)	(0.20)	119.28 (17.3)	10.83 (1.57)	.088 (.049)


① Reflects full scale test configuration which includes effects of bonded resistance heaters.

Table 4-3. Modal Analysis Results

Mode	Fixed joints frequency (Hz)	Pinned joints frequency (Hz)	Description
1	16.76	16.47	1st bending (z)
2	16.76	16.47	1st bending (y)
3	32.93	30.69	Ovalization
4	36.26	35.96	Longitudinal
5	45.02	43.88	2nd bending (z)

Table 4-4. Truss Stiffness

		Kilogram/centimeter (Pound/inch)			Kilogram-cm/radian (Pound-in./radian)		
Condition number		1	2	3	4	5	6
Pinned joints		1,054 (5,900)	1,054 (5,900)	4,001 (22,400)	50.5×10^6 (43.8×10^6)	50.5×10^6 (43.8×10^6)	1.77×10^6 (1.52×10^6)
Fixed joints		1,089 (6,100)	1,089 (6,100)	4,661 (26,100)	55.1×10^6 (47.8×10^6)	55.1×10^6 (47.8×10^6)	2.59×10^6 (2.25×10^6)

 Strut/ring connections and spider assembly to upper ring joints

5.0 ELEMENT TESTING

Structural element tests were performed to obtain accurate data needed for analysis and predicting truss performance. The hardware tested was highly representative of the full-scale truss details. To show compliance with the very limiting design constraints, very accurate data was developed which required very sophisticated measuring and test techniques. Element tests were performed to determine:

- 1) the allowable microyield strain for tubular struts and a ring "H" section;
- 2) the effect of load cycling on the microyield strain of a tubular strut;
- 3) the creep of a tubular strut resulting from a 30 day loading at 80% of microyield;
- 4) the CTE of tubular struts and a ring "H" section; and
- 5) the effect of thermal cycling on the CTE of a tubular strut.

5.1 MICROYIELD TESTING

All microyield testing was performed on specimens 20.3 cm (8.0 inches) long with the microstrain test equipment shown in Figure 5-1. Measurements were made with differential transformer sensors which have the capability of measuring to 2.54×10^{-7} cm (1×10^{-7} inches) in the configuration used in these tests. Prior to test, the ends of the specimens were potted and ground flat and parallel to within .013 cm (.005 inches). Extensometer supports were cemented to the specimens with a filled thermosetting epoxy. Figure 5-2 shows the tubular microyield specimen with the extensometer support rings in-place.

Extensometer bodies were then cemented to the supports. Linear differential transformer (LVDT) sensors were then installed in the extensometer bodies and adjusted for clearance between core and bobbin. Figure 5-3 shows the tubular specimen with the LVDT sensors completely installed. The assembled specimen and extensometer were then installed in the loading machine and the sensors adjusted to within $\pm .25$ micrometers (± 10 microinches) of null. A double wall, two zone thermal control enclosure was then installed around the loading system. After one hour of thermal soak the enclosure was reopened and the sensors re-nulled as necessary. The thermal enclosure was then closed and thermal soak reactivated for a minimum of 16 hours. Temperature of the test specimen was maintained at 33°C (91°F) within a stability of $\pm .006^{\circ}\text{C}$ ($\pm 01^{\circ}\text{F}$) to minimize thermal expansion effects. The specimens were loaded in compression at increasing load increments. Loads were removed and the specimens permitted to relax after each load increment. Data was obtained on all four LVDT sensors and bending modes reduced to obtain axial deflections.

In addition to the tubular specimen shown in Figure 5-2, two additional micro-yield test specimen configurations were tested using the above procedure. Figure 5-4 shows the microyield ring specimen with the LVDT extensometer in-place. Figure 5-5 shows the microyield joint specimen prior to instrumentation.

The first tubular microyield specimen tested was fabricated with two plies of A-S/934 at $\pm 65^{\circ}$ on the inner and outer surfaces and four 0° plies of HM-S/934 at the center of the wall laminate. The outer plies were applied by filament winding which produced an .203 cm (.08 in) wall thickness. The truss struts were produced by tape winding the orientated plies which produced a thinner wall. Tubular tests of this design are discussed later in this section.

The data obtained from the first tubular microyield test was reduced and plotted to establish the microyield strain and effective modulus. Figure 5-6 shows a plot of the tube yield strain as a function of the applied stress. This data shows a microyield strain of 93.8 MN/m^2 (13.6 ksi).

Figure 5-7 shows a plot of elastic strain as a function of applied stress. This data shows an effective tube modulus of 80 GN/m^2 (11.6×10^6 psi). This effective tube modulus produced an axial stiffness (EA) of 26.5 N (5.947 lbs) that was within 1% of the theoretical EA of 26.7 N (6.002 lbs).

A microyield specimen representative of the truss rings was fabricated and tested. The section was fabricated by bonding two graphite fabric channels back-to-back to form an "H" and then adding graphite tape in the chord areas to obtain the proper thermal growth and stiffness characteristics. The materials, orientation, and section geometry were the same as the truss stiffening rings shown in Figure 3-6.

The microyield strain results obtained from the ring "H" section test are shown in Figure 5-8. The stress at microyield strain was 134.5 MN/m^2 (19.5×10^3 psi), which was well above the maximum stresses produced by critical loads in the truss. The effective modulus of the cross-section was $107.6 \times 10^9 \text{ N/m}^2$ ($15.6 \times 10^6 \text{ lb/in}^2$), which was 4% above the ring modulus used in the NASTRAN analysis.

The joint specimen tested produced a microyield strain which was very close to the tube microyield strain. This specimen was tested to failure and produced a bondline shear stress of 6.7 MN/m^2 (975 psi). This is well above the 3.45 MN/m^2 (500 psi) shear stress allowable used in the analysis.

Repetitive load cycles were applied to a tubular strut to determine the effect on microyield. This specimen was obtained by trimming one of the struts made for the truss and was therefore representative of the material and manufacturing processes used in building the truss. This specimen incorporated four plies of HM-S/934 at the center of the wall cross-section and two plies of A-S/934 at $\pm 50^\circ$ at the surfaces.

Upon installation in the microstrain test facility, the specimen was first allowed to stabilize. It was then subjected to microyield testing. The specimen was then loaded in steps to 0.8×10^{-6} yield strain which permitted extrapolation to a load value of 43.15 kN (9,700 lbs) for a compression microyield at 1.0×10^{-6} . A plot of yield strain vs. load is shown in Figure 5-9. A microyield stress of 23,373 psi is equivalent to the microyield strain at 1.0×10^{-6} .

Cyclic loads of 0 to 5337.6 N (1200 lbs) were applied to the specimen to calibrate the test set-up. The specimen was cycled 25 times, released for observation and cycled again. The introduction of cooling oil into the loading system caused transients in the thermal control system and caused an elongation indication. After three groups of 25 compression loadings, a steady test condition was judged to have been reached with an apparent load read-out error of 890 N (200 lbs). The compression load was then increased to an apparent 37.81 kN (8,500 lb) to simulate the 38.70 kN (8,700 lb) load experienced in the initial microyield test. After 200 cycles had been applied (in 25 cycle groups), no change in the compression yield was experienced.

The axial elastic stiffness (EA) was measured after each group of 25 cycles. A value of $28.9 \pm .5 \text{ MN/m}^2$ ($6.5 \pm .12 \times 10^6 \text{ lbs}$) was obtained at each measurement. The equivalent compression modulus of $107.98 \times 10^6 \text{ N/m}^2$ ($15.66 \times 10^6 \text{ psi}$) was used for the strut elements in the NASTRAN analysis.

A sustained load test was performed on a tubular strut specimen to determine its effect on microyield strain. This specimen was also trimmed from one of the struts made for the truss and incorporated the same laminate design described above for the lead cyclic specimen. Testing was performed in the microyield facility with the same techniques used in previous microyield testing.

The specimen was subjected to compression sustained load tests for periods of 1, 2 and 30 days. The load applied was 3946 kg (8.700 lbs) which corresponds to a yield strain of 0.8 $\mu\epsilon$. The specimen was placed in the chamber and allowed to stabilize as indicated by the LVDT sensors. Load was then applied for the required test periods. The loads were removed and the specimen allowed to recover. The gage length of the specimen after test was compared to the length prior to loading. Change in gage length from all load tests (1, 2 and 30 days) were within the long term stability limits of the test and no change in the microyield strain characteristic of the specimen was indicated.

5.2 THERMAL EXPANSION TESTING

Tests were performed to obtain the coefficient of thermal expansion (CTE) of tubes and "H" section elements. The CTE specimens 91.44 cm (36 in) long. They were placed in a vacuum chamber and permitted to stabilize for a minimum of 24 hours. Figure 5-10 shows a schematic of the test setup. As shown, the test part was suspended inside a thermal shroud located inside a vacuum chamber. The optical portion of a laser interferometer was installed beneath the vacuum chamber. Columnated beams, used to measure dimensional changes, were directed through an optical window located at the bottom of the chamber. The actual test setup is shown in the photo shown in Figure 5-11. A closeup of the laser optics is shown in Figure 5-12.

The tubular CTE test specimens were fabricated using HM-S in the zero degree directions and AS fiber in the $\pm\theta$ plies. Each specimen was instrumented with three thermocouples and four corner reflectors as shown in Figure 5-13. Laser interferometer data obtained on the movement of the four corner reflectors were used to establish thermal growth and to monitor tilt which was found to be insignificant. A reference reflector was mounted at the top of the tube and was used to nullify the effects of relative movement between the specimen and the laser interferometer.

The specimen was placed in the test chamber which was evacuated to below 1 torr, and allowed to stabilize for sixteen hours. The temperature of the specimen was then raised to 37.8°C (100°F) and then cooled. Thermal growth readings were taken every 2.8°C (5°F). At each 14°C (25°F) increment the temperature was stabilized and allowed to dwell for 30 minutes. This procedure was continued until -73.3°C (-100°F) was attained.

The thermal growth readings for a tube with $(0_2 \pm 50)_s$ lamination are shown in Figure 5-14. The overall average CTE was 7.2×10^{-8} cm/cm/°C (4×10^{-8} in/in/°F).

Figure 5-15 shows a comparison of the CTE's obtained with the tube elements tested. It illustrates the effectiveness of the orientated plies and the ability to design for specific characteristics with composite materials.

The test data shown in Figure 5-15 were developed from two tubes. Both had HM-S fibers at 0° and A-S fibers at $\pm\theta$. The curve developed using idealized

properties indicated the $(0_2 \pm 65)_s$ would produce a tube with a near zero CTE. During the initial development and evaluation of fabrication processes several methods of producing the tubular struts were tried. The tubes that were used in the initial CTE tests were made by wet winding the orientated $(+0)$ plies. This method produced tubes with wall thicknesses much larger than anticipated. As a result, the tube with the $\pm 65^\circ$ plies produced a CTE value higher than desired. When actual fabricated ply thicknesses were used in the analysis the theoretical CTE was much closer to the initial tube tested. As a result a second tube was fabricated in which the orientated plies were placed at $\pm 50^\circ$. This tube did demonstrate a "near zero" CTE, as shown in Figures 5-14 and -15.

A ring "H" section element was also tested to obtain its effective CTE. This specimen had the same cross-section as a truss stiffening ring, but was straight. It was 91.4 cm (36 inches) long and used the same materials and ply orientations as the truss ring. The test data produced during test is summarized in Figure 5-16. It shows an average CTE of $.74 \times 10^{-6}$ cm/cm/°F (0.411×10^{-6} in/in/°F). This value was within the range for the stiffening rings which allows the critical truss dimensional stability requirements to be met.

A third tubular strut element was tested to determine the effect of thermal cycling on CTE. This specimen was obtained from a strut that was built for the full-scale truss and, therefore, was representative of the materials and type of construction used in its fabrication. Prior to testing, two one-inch wide resistance heaters were installed along the length of the specimen to establish the same test configuration as the strut details in the full-scale thermal-vacuum (T-V) test. In the T-V test the heaters were energized and

used to control temperatures, but in the element test they were used only to develop the same influence on strut CTE as in the full-scale test. Temperature control of the element in the thermal cycling test was performed by the thermal shroud in the same manner as in previous tube tests.

The specimen was instrumented with 4 corner reflectors and 3 thermocouples. It was placed in the center of a cylindrical thermal shroud inside a vacuum chamber. The chamber was pumped down and the specimen allowed to dehumidify over a weekend. The specimen was then thermal cycled 208 times between +38°C and -74°C (+100°F and -100°F). Thermal deflection readings were taken at approximately 50 cycle intervals.* During the last cycle, readings were taken with the resistance heaters removed from the specimen.

The results of the thermal cycling test are shown in Figure 5-17. In the first cycle the CTE varied on a relatively constant slope from a value of $.23 \times 10^{-6}$ cm/cm/°C (0.13 24°C in/in/°F (+75°F) to $.36 \times 10^{-6}$ cm/cm/°C (0.20×10^{-6} in/in/°F) at -45°C (-75°F). In the following intervals the CTE readings followed the same slope up to -32°C (-25°F) and then fell-off sharply. It is strongly suspected this was caused by micro-cracking which was found after the completion of the cycling. The wall of the tube was sectioned, polished and photo enlargements were made. These enlargements (Figure 5-18) showed radial microcracks through the zero degree plies at approximately .38 cm (0.15 inch) spacing.

The drop in CTE shown as a result of increased cycling was probably due to the progressive delamination of the resistance heaters. The heaters were removed and CTE readings taken on an additional cycle (208th). This data

* These readings were taken at 28°C (50°F) intervals after allowing approximately 1 hour for laser stabilization (thermal equilibrium).

followed the CTE data of the 207th cycle made with the heaters in place, which indicated the heaters were totally ineffective (delaminated) by the end of cycling.

Prior to the test, theoretical calculations were made to determine the effect of the heaters on the CTE of the tube. These results predicted that the heaters would change the CTE values approximately the same magnitudes shown between the 1st and 208th cycle.

Table 5-1 summarizes the CTE test results for the various struts.

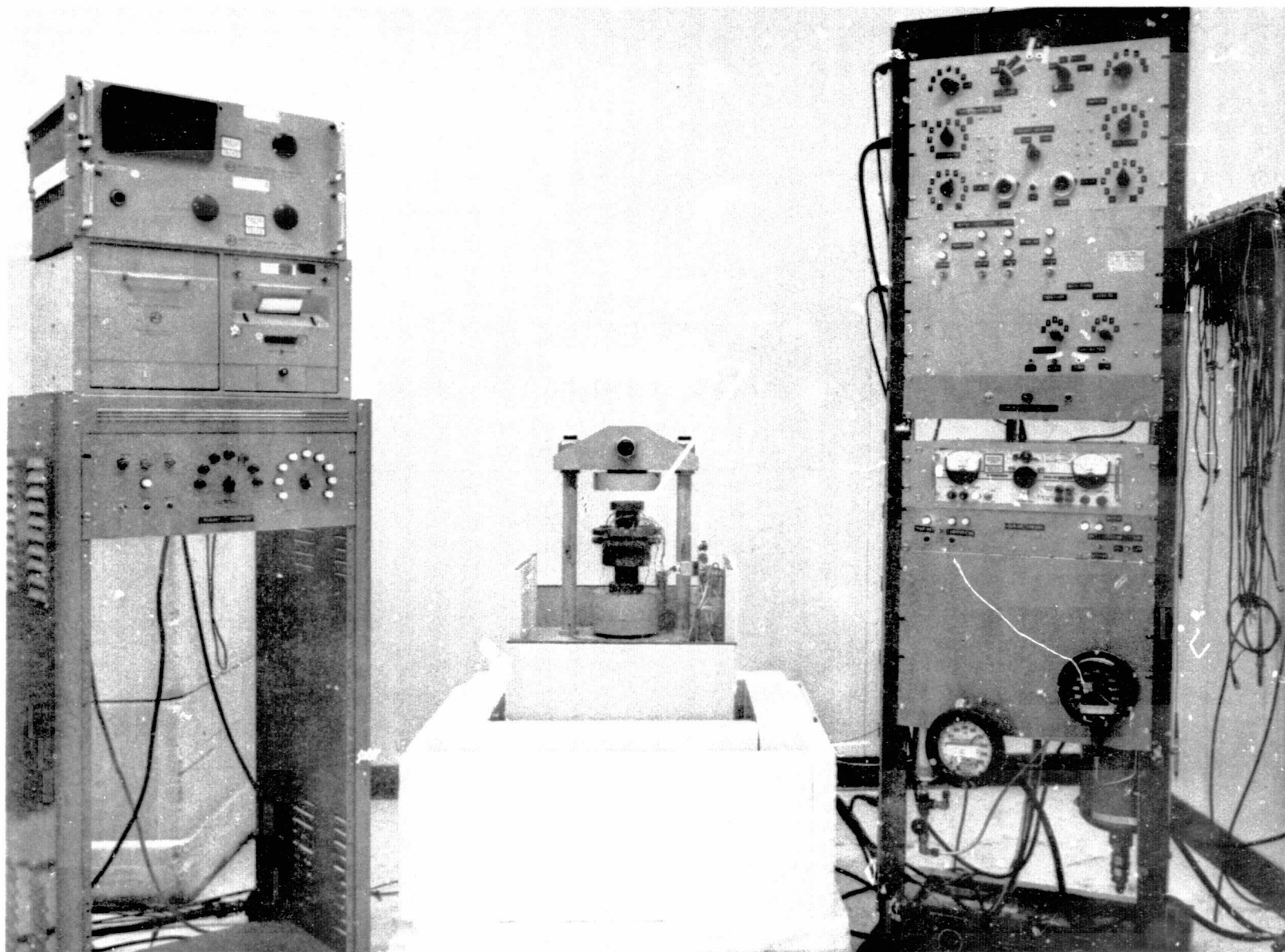


Figure 5-1. Microyield Strain Test Equipment

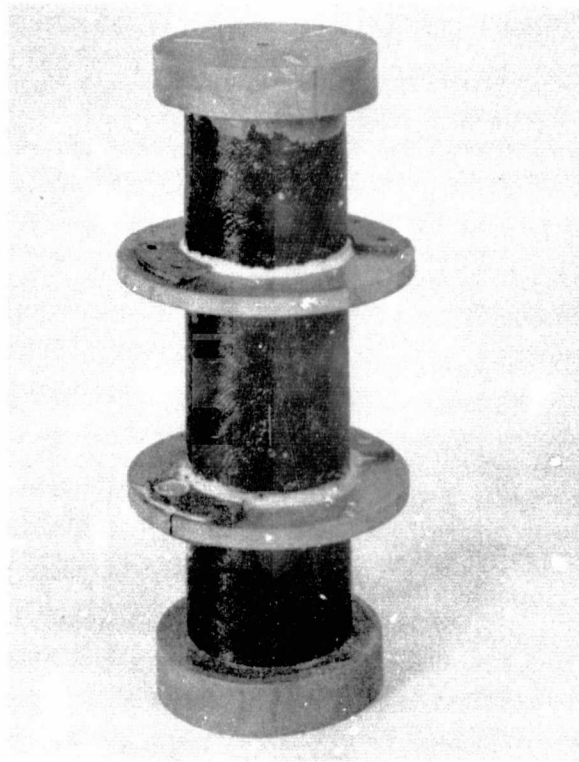


Figure 5-2. Tubular Microyield Specimen With Extensometer Support Range

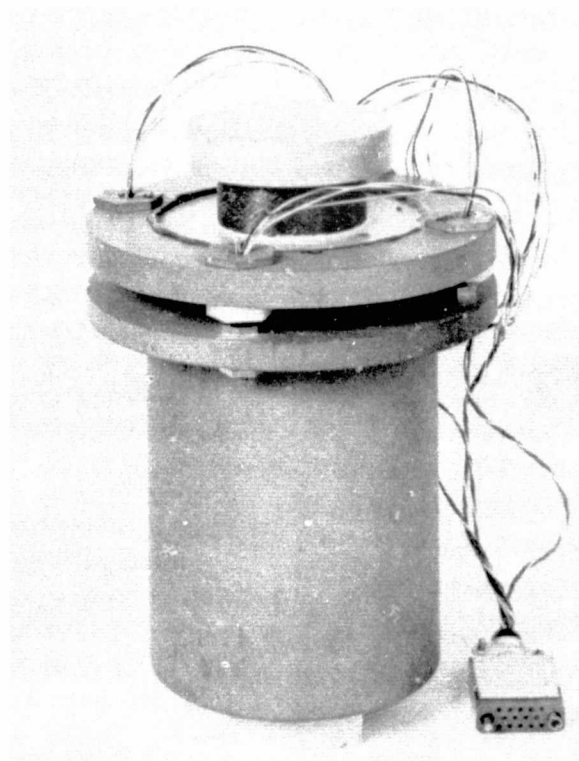


Figure 5-3. Tubular Microyield Specimen With Linear Differential Transformer Extensometer Installed

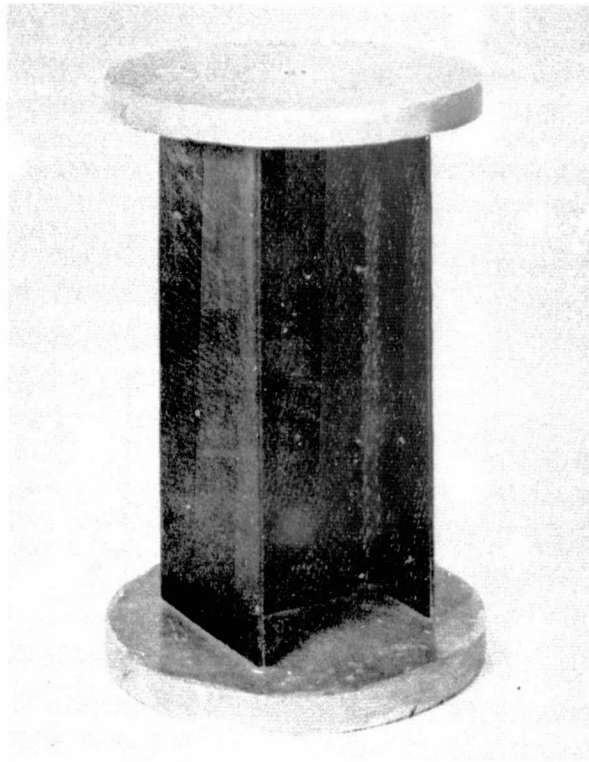


Figure 5-4. Microyield Strain Ring (H-Section) Specimen

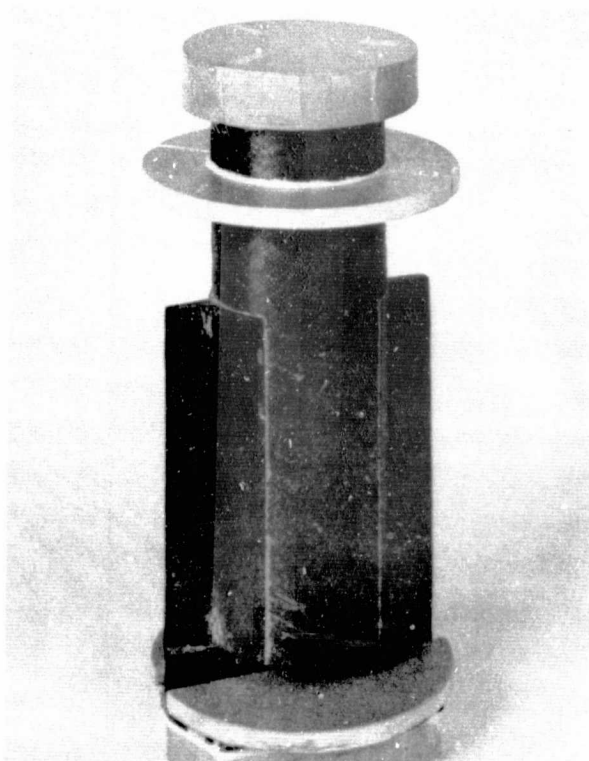


Figure 5-5. Microyield Strain Joint Specimen

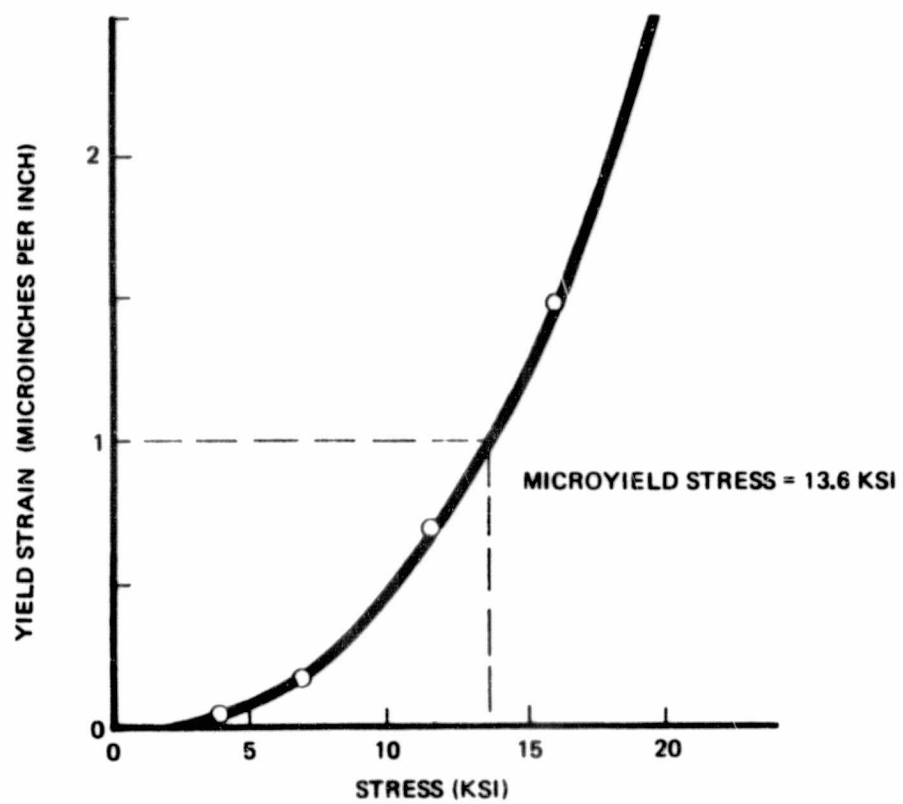


Figure 5-6. Tubular Specimen ($0_2 \pm 65$)₅ Yield Strain Versus Stress

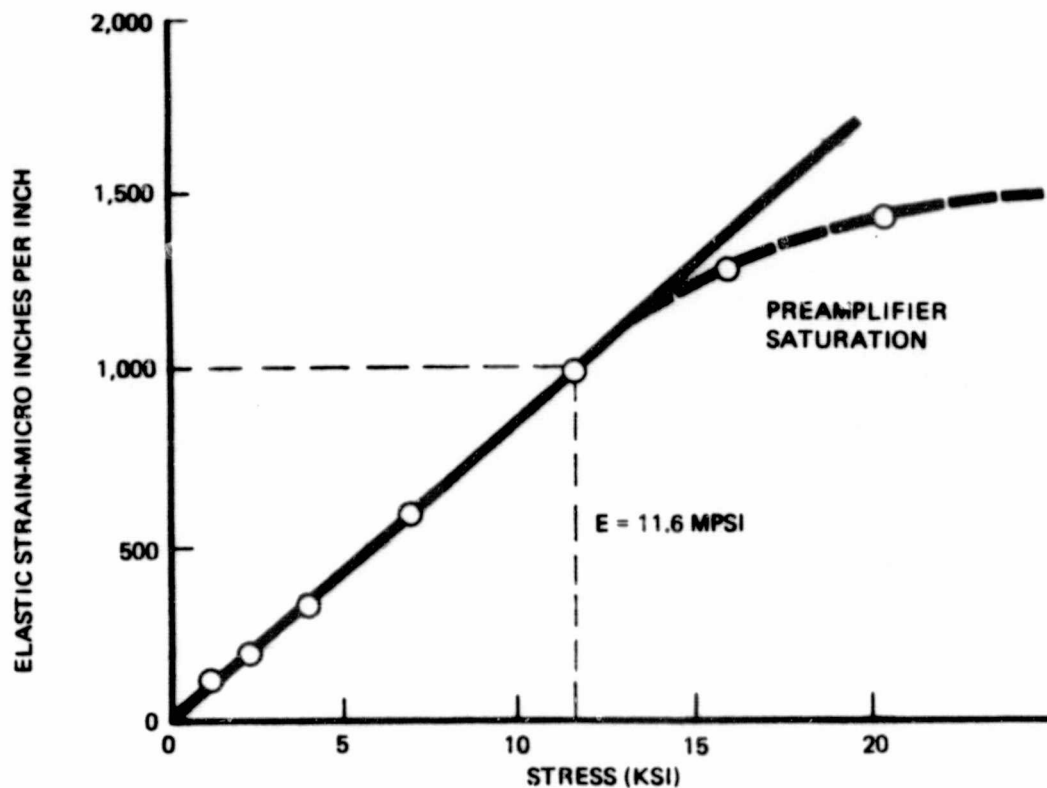


Figure 5-7. Tubular Specimen $(02 \pm 65)_S$ - Elastic Strain vs. Stress

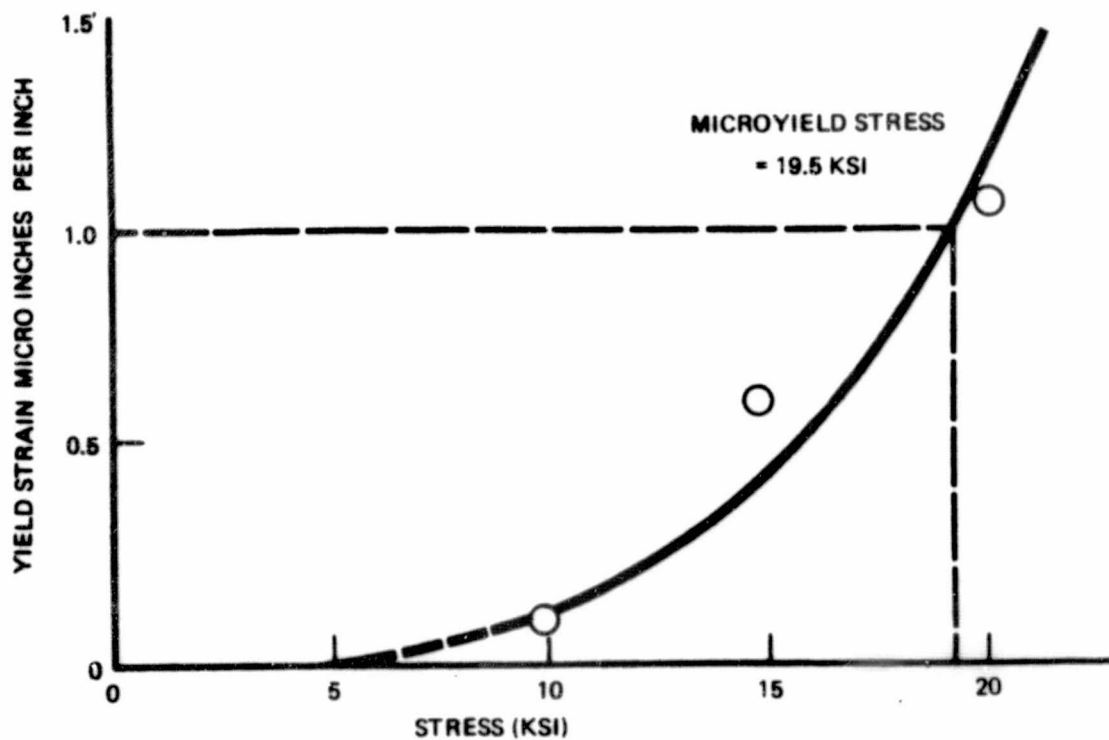


Figure 5-8. Ring Test Section Yield Strain vs. Stress

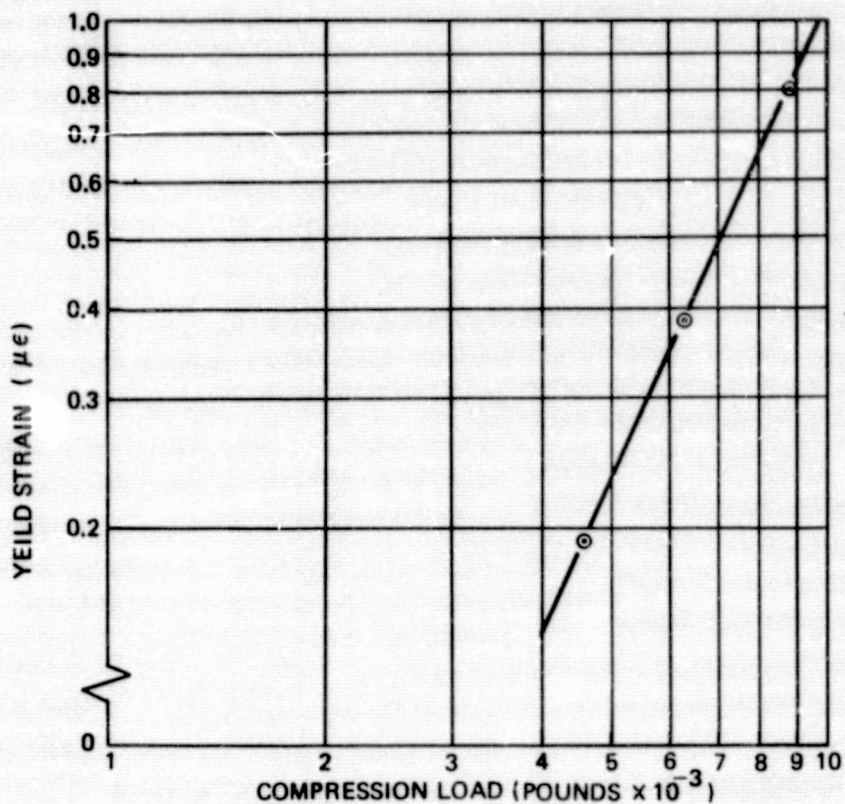


Figure 5-9. Tubular Specimen ($0_2 \pm 50$)_S – Yield Strain vs. Load

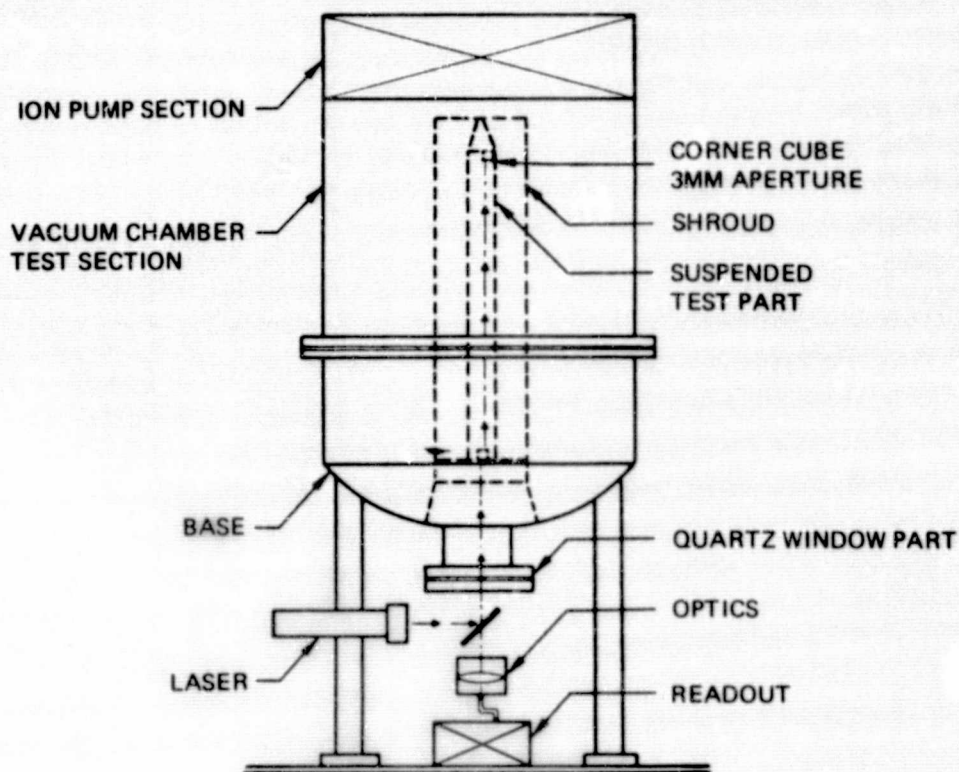
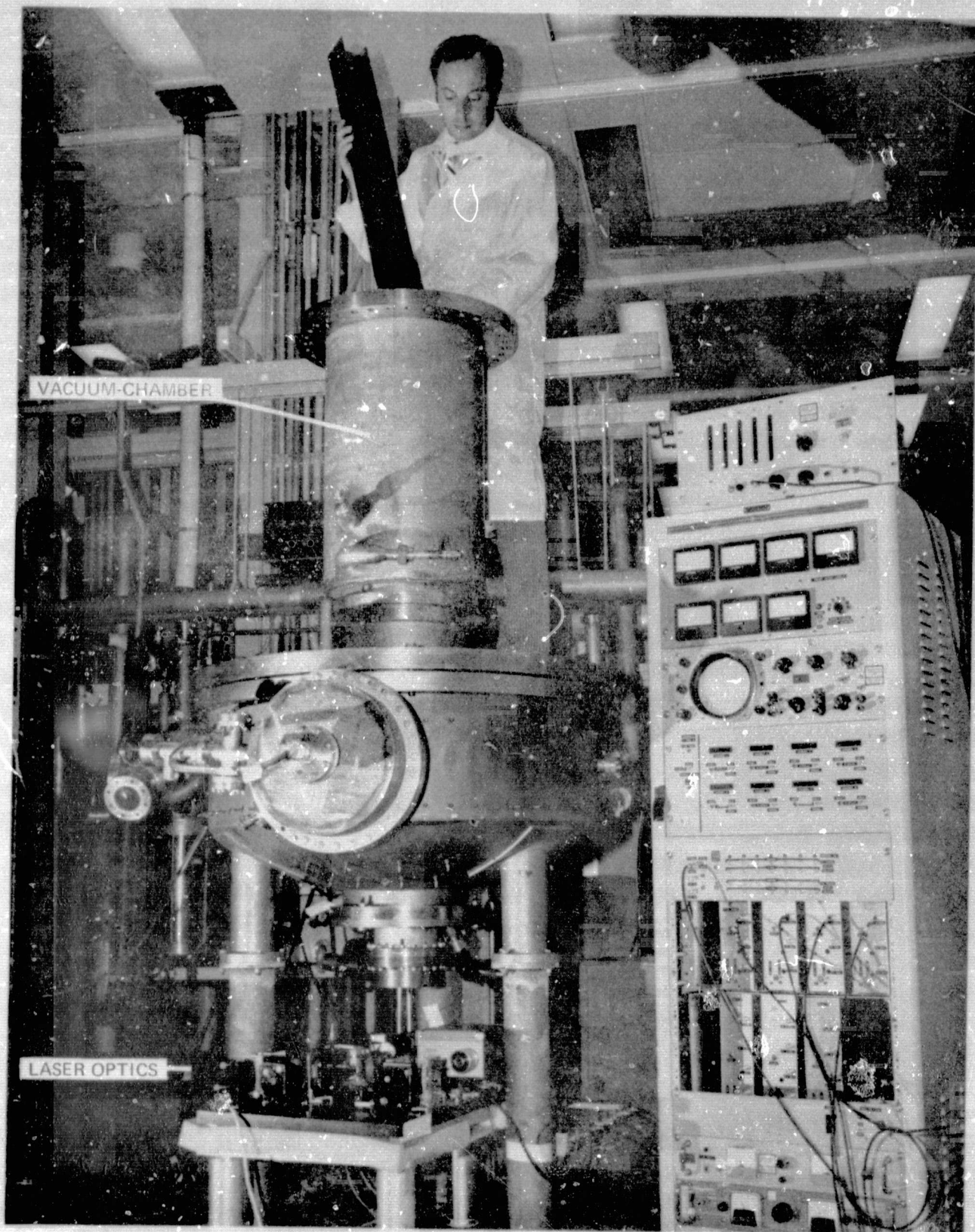


Figure 5-10. CTE Test Setup Schematic



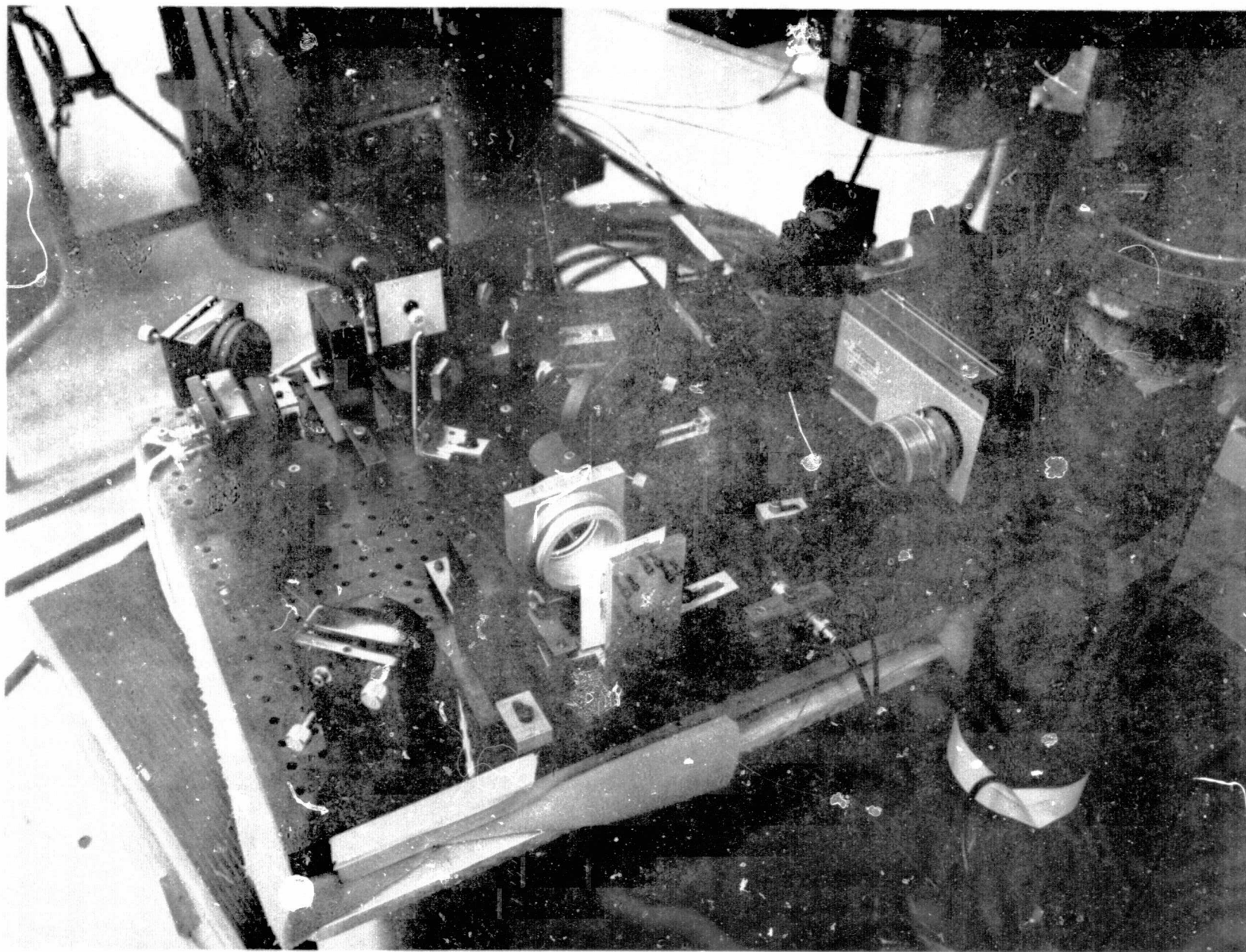


Figure 5-12. CTE Element Test - Laser Interferometer

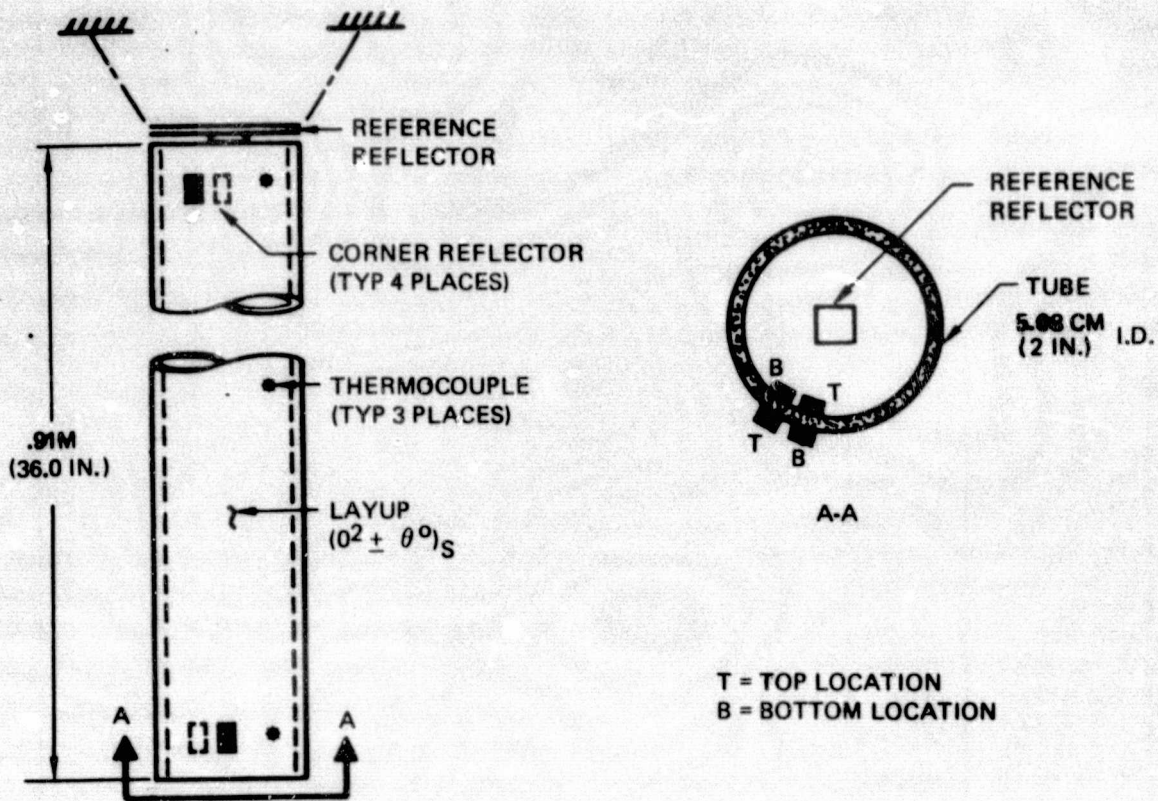


Figure 5-13. CTE Element Instrumentation

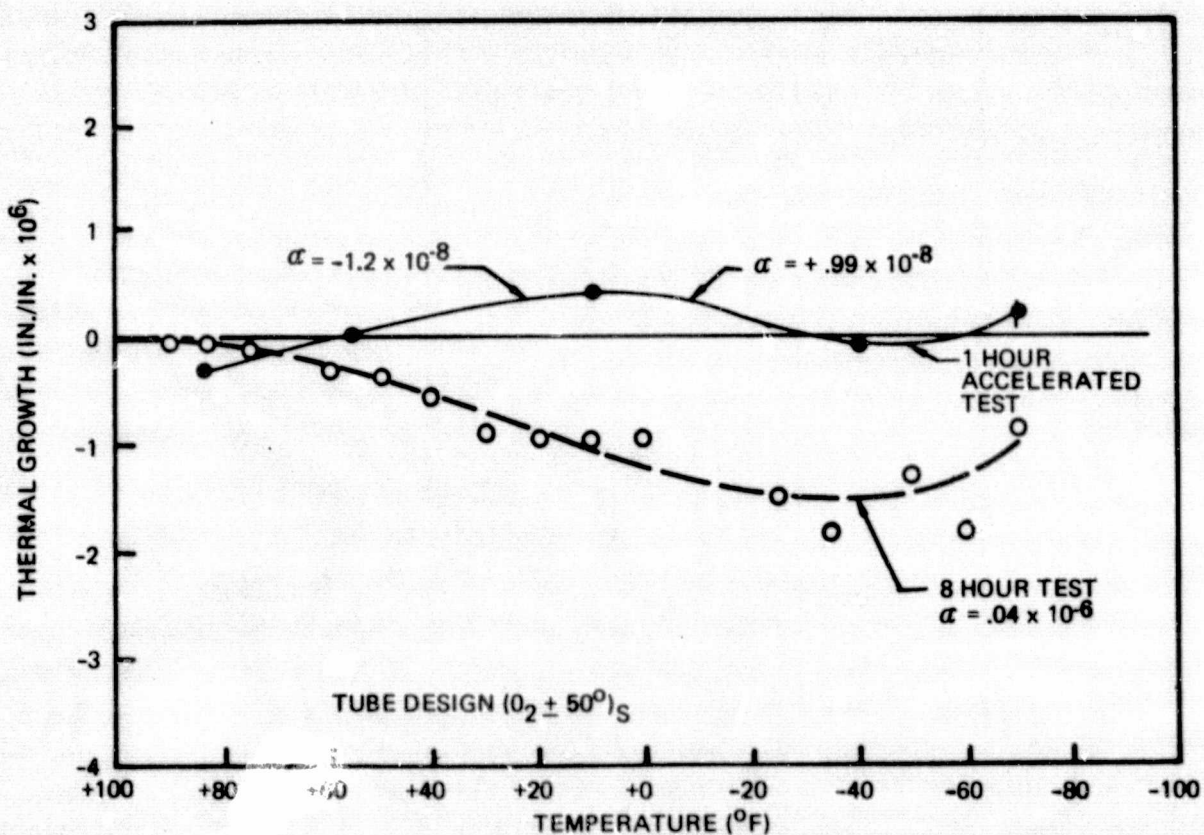


Figure 5-14. Tube Growth Vs Temperature

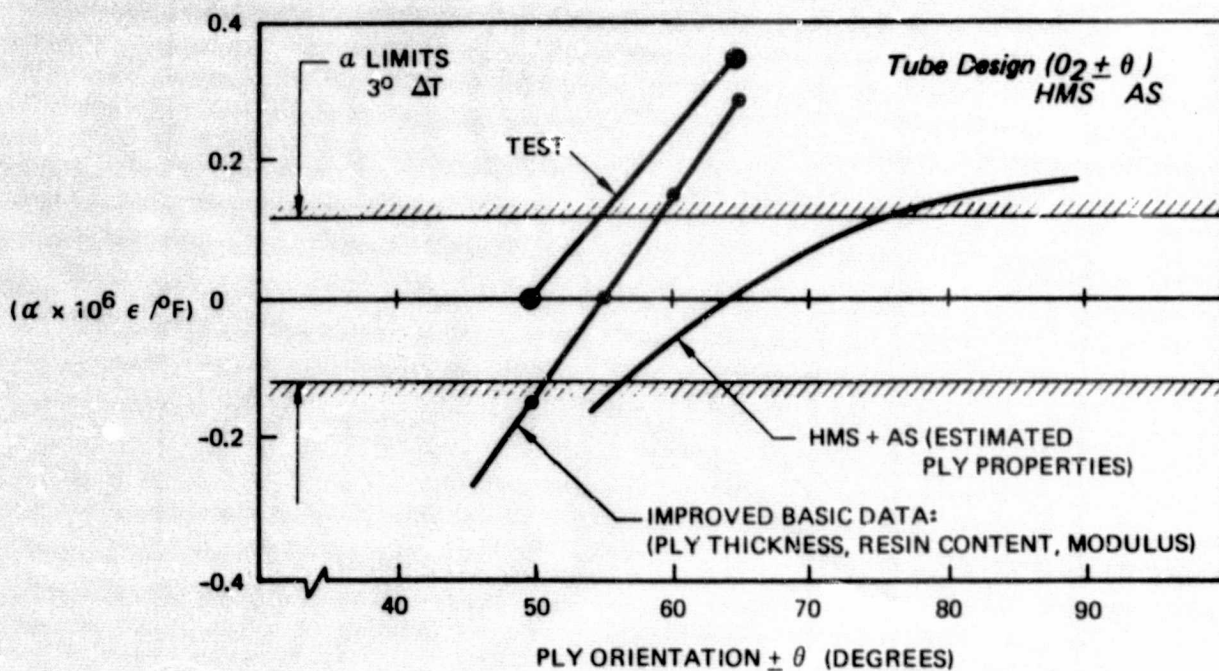


Figure 5-15. CTE Test Data and Design Comparisons,

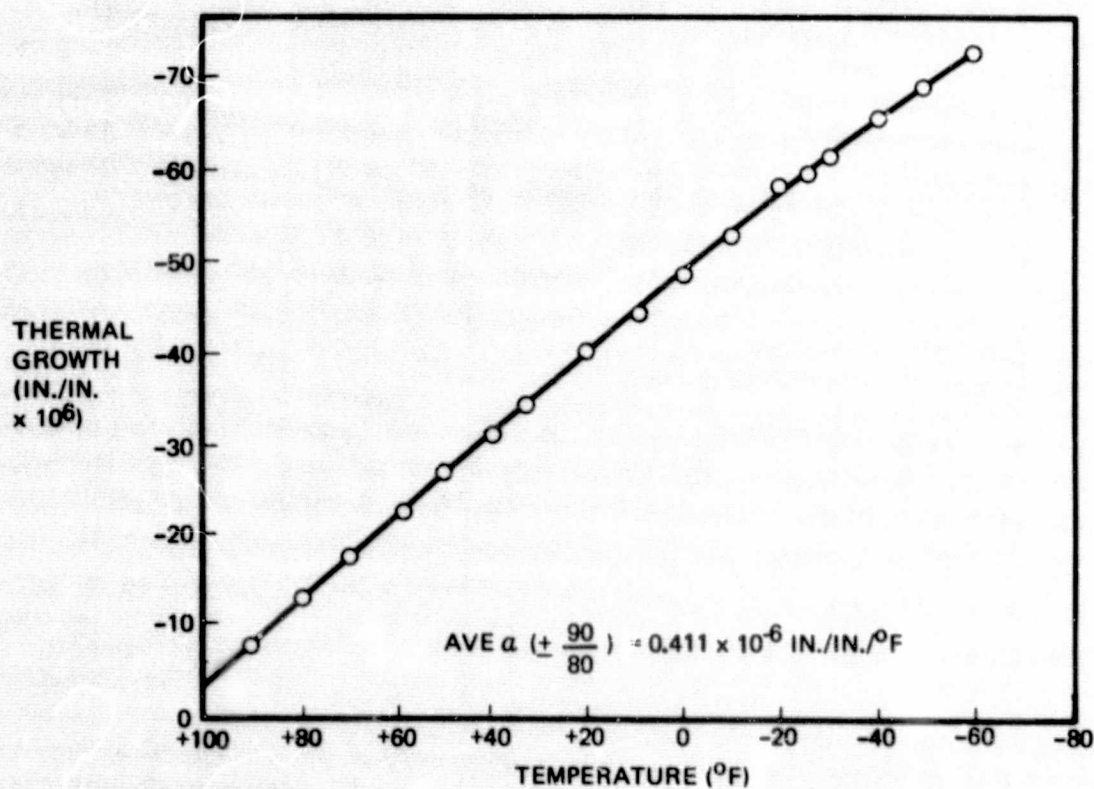


Figure 5-16. Thermal Growth vs. Ring Specimen Temperature

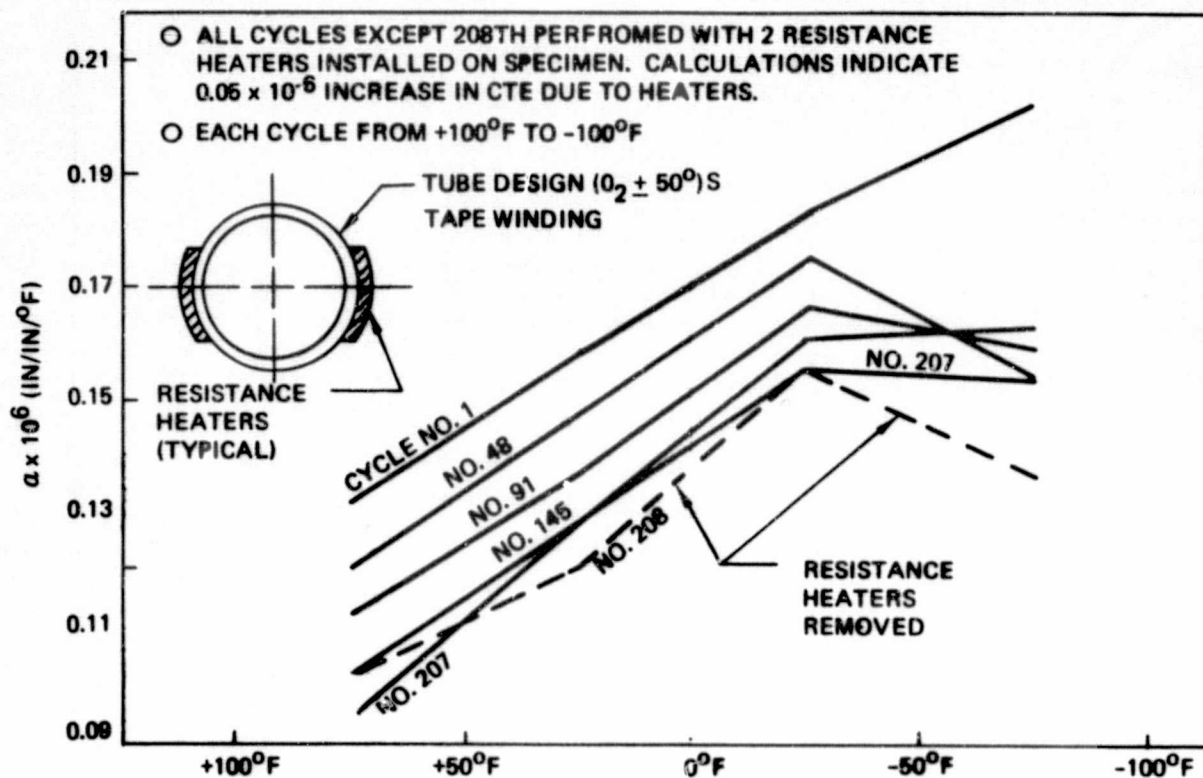


Figure 5-17. CTE Tube Element—Thermal Cycling

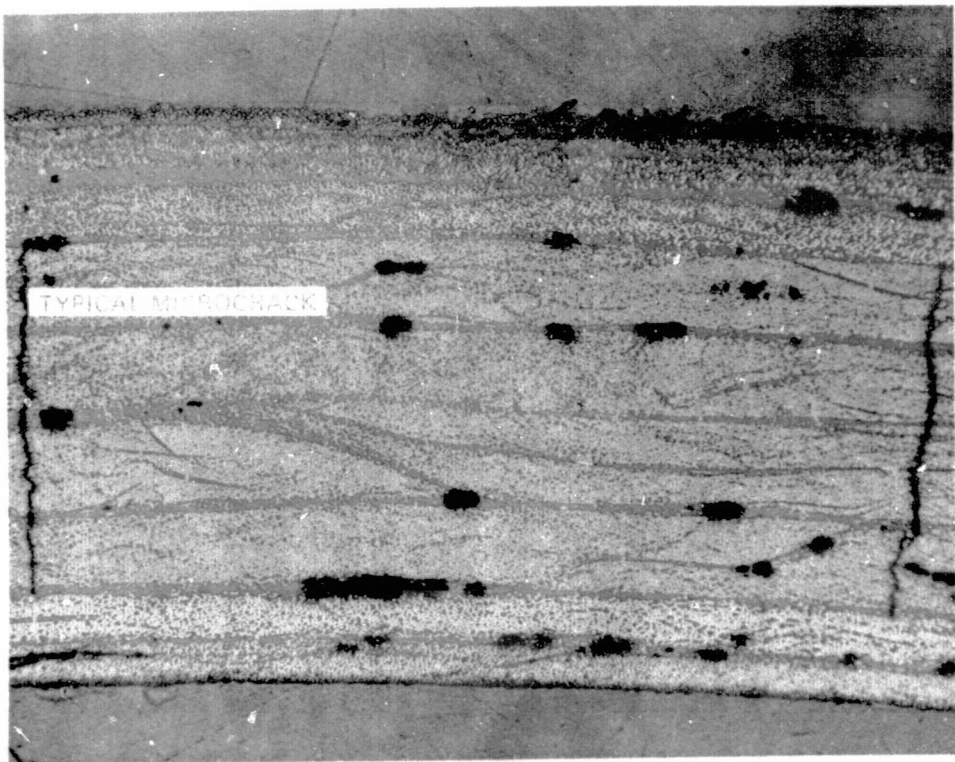


Figure 5-18. Thermal Cycling Tube-Microcracks

REPRODUCIBILITY OF THE
ORIGINAL PAGE IS POOR

Table 5-1. CTE of Gr/Ep Strut Elements

Laminate configuration	Assembly procedure	Wall thickness	Average CTE
$(0_2 \pm 65)_S$	Hand lay-up HMS plies Machine applied AS tow impregnated during wrapping	.20 cm (.08 in.)	1.8×10^{-7} cm/cm/ $^{\circ}$ C (3.3×10^{-7} in./in./ $^{\circ}$ F)
$(0_2 \pm 50)_S$	Hand lay-up HMS plies Machine applied preimpregnated AS tow	.20 cm (.08 in.)	$.22 \times 10^{-7}$ cm/cm/ $^{\circ}$ C ($.4 \times 10^{-7}$ in./in./ $^{\circ}$ F)
$(0_2 \pm 50)_S$	Hand lay-up HMS plies Machine applied preimpregnated AS tape (Selected production approach)	.16 cm (.064 in.)	$.76 \times 10^{-7}$ cm/cm/ $^{\circ}$ C (1.36×10^{-7} in./in./ $^{\circ}$ F)

6.0 FULL-SCALE TRUSS FABRICATION

Several approaches for producing the truss details were evaluated during the course of this program. The final processes and techniques selected and used will be described in this report.

All detail composite parts produced in this program incorporated Fiberite's 934 resin as the matrix. All parts except the struts were processed in an autoclave using the standard manufacturing procedures for this system. The standard 934 cure used is shown in Figure 6-1 and a standard layup configuration is shown in Figure 6-2. The strut laminates were layed up on a mandrel, covered with caul plates and then overwrapped with glass coverings. Since pressure was supplied by the glass overwrap an autoclave was not needed and curing was performed in an oven.

All parts, except those incorporating honeycomb construction, were assembled by room temperature bonding. This bonding was performed with Lefkoweld Type 109 adhesive.

6.1 DETAIL FABRICATION

Struts

A total of 48 struts were required for the truss assembly. They were approximately 8 ft (2.44 m) long with a two inch (5.08 cm) inside diameter and an eight ply wall. The wall laminate consisted of 4 plies of HM-S/934 at the center of 0 degrees and 2 plies of A-S/934 at each surface at ± 50 degrees.

The graphite/epoxy plies were layed up on an aluminum mandrel and cured. Part release was accomplished with little difficulty because of the large CTE difference and resulting shrinkage of the aluminum mandrel during cool down. The mandrel was coated with a baked on R671 Dow Corning release agent. The mandrel was also sprayed with a coat of Frekote 33 (Telex-Frekote) prior to each use. The plies were debulked at room temperature using shrink tape every two plies.

The orientation of the $\pm 50^\circ$ plies was established by laying tape to a reference line which was established by the feed control of the tape laying machine. The tape was placed by hand to this reference line. Initially a few struts were made with the tape one half the width required to cover the complete surface in a single layup as shown in Figure 6-3. The bulk of the struts were made with full width orientated plies layed down in a single pass. After completing the ply layup the lamination was covered with 10 mil aluminum caul sheets which were coated with Frekote 33. The assembly was then over-wrapped with "S" glass roving to provide pressure during cure. The completed layup was then placed horizontally in an oven and supported at several points along the length. The struts were cured in the oven for one hour at 350°F.

After removal from the mandrel, the struts were cut to size and the ends trimmed to the proper configuration. Figure 6-4 shows a strut end being cut to the proper angle with a band saw. Figure 6-5 shows the end being slotted with a carbide wheel. Figure 6-6 shows the completed trimmed strut end.

Graphite Laminate Details

The truss joints were designed to have a high degree of commonality of detail parts. A large portion of these details were made from graphite epoxy fabric (HMF 330C/34). All small details were layed-up on multi-part aluminum tooling such as the tools shown in Figure 6-7. These layups were then bagged and cured as shown in Figures 6-1 and -2. Figure 6-8 shows several types of fabric details that were used in the truss joints.

Joint "T's" were designed and fabricated to transfer loads from the struts to the adjacent structure. Initial angles were fabricated with the same material and orientations as the struts ($H_1-S; 0_2 A-S; \pm 50$)_S. These parts were layed up on steel tools and bagged and cured as described previously. The angles were then bonded back-to-back into "T"s at room temperature. They were then cut to the proper geometry and capped with 0° plies. Figure 6-9 shows the "T" details and the completed part.

Ring Details

The ring details included graphite fabric channels which were bonded back-to-back to form an "H" and graphite tape laminates for the ring caps.

Eight identical graphite fabric channels were required per ring. The fabric prepreg was layed up on steel tooling as shown for a trial part in Figure 6-10. These parts were then bagged as shown in Figure 6-11 and then cured in an autoclave.

The cap materials for the ring were made of ten plies orientated at $(0_3 \pm 20)$ _S. The plies were layed up on a steel tool as shown in Figure 6-12, bagged as

shown in Figure 6-13 and cured in an autoclave. The cured laminates which were approximately ten inches wide by 103 inches long and were cut into three inch wide cap strips,

6.2 SUBASSEMBLY FABRICATION

Several of the truss details were incorporated into subassemblies prior to the overall truss assembly. The subassemblies included, two strut assemblies, ring assemblies, spider beams, spider cylinder and spider assembly.

Strut Assembly

Two struts were combined by using a gusset joint, into a single subassembly. The slotted strut ends were slid over a "T" gusset which was clamped in an assembly fixture as shown in Figure 6-14. The balance of the graphite fabric details were then prefitted as shown in Figure 15. The parts were then disassembled, bonding surfaces cleaned and coated with Lefkowitz Type 109, reassembled and pressure pads placed and clamped as shown in Figure 6-16. Bond pressure was retained for a minimum of 24 hours after which pilot holes were drilled in the "T" base as shown in Figure 6-17. A completed strut subassembly is shown in Figure 6-18.

Ring Subassembly

A two piece circular aluminum tool was used for the ring assembly. This tool is shown assembled with some of the ring details in Figure 6-19. As shown, eight fabric channel sections were bonded into a continuous ring. The part ends were clocked at 45° angles to permit the upper and lower channel sections to be self-splicing. Pressure for bonding was provided by lead weights placed on wood filler blocks as shown in Figure 20. The assembly tool was shimmed to

provide a controlled in-plane web surface. The ring caps and splice plates were coated with adhesive and then put in place. Inner and outer steel pressure rings were then installed to provide pressure during cure. After the rings were assembled and cap splice plates installed, a drill template was used for drilling pilot holes in the rings at joint locations as shown in Figure 6-21. A completed ring is shown in Figure 6-22.

Spider Beam Subassembly

The spider beam designs employed aluminum honeycomb sandwich construction. GR/EP skins were first fabricated per the design shown in Section 3.0. The lower skins, adhesive, and aluminum honeycomb were then placed in an aluminum bonding frame as shown in Figure 6-23. After the adhesive and upper skin were placed the assembly was bagged for cure as shown in Figure 6-24. The adhesive used was FM-96 and cure was performed at 350°F.

Spider Cylinder Subassembly

The spider cylinder was fabricated in three stages. Initially the inner skin plies were laminated and cured on a steel mandrel as shown in Figure 6-25. A layer of FM-96 adhesive and honeycomb were placed over the skin as shown in Figure 6-26. Nine pound per cubic foot flexcore was used in attachment areas and three pound per cubic foot over-expanded core in the balance of the cylinder. Foaming adhesive was used to splice the honeycomb sections. The honeycomb was covered with caul sheets, bagged and bonded to the inner skin. The caul sheets were removed and the honeycomb splices sanded smooth. The honeycomb was then covered with adhesive and the outer skin layed in place. This was then covered with caul sheets, bagged and cured. The part was then

removed from the mandrel and trimmed. A complete spider cylinder with some of the attachment angles bonded in place is shown in Figure 6-27.

Spider Support Subassembly

The spider support assembly (cylinder, beams and top truss ring) were assembled as a single unit. The ring assembly tool was used to locate the top truss ring. A platform was optically placed and used to establish the height and location of the cylinder. The beams were then fitted to existing joint details to establish their location. All bonding was performed at room temperature using clamping pressure. Figure 6-28 shows the completed spider support assembly.

6.3 FULL-SCALE TRUSS ASSEMBLY

All detail parts and subassemblies were fabricated in a developmental plastics shop and shipped to the final assembly area. Final assembly was accomplished in the same building in which the full-scale tests were performed. This eliminated problems arising from shipping the large completed structure.

The final assembly was accomplished on a large steel tool designed to permit construction of a single bay. This tool located the upper and lower ring of each bay and held them in place as the strut assemblies were installed. As each bay was completed it was moved to the top of the fixture and the next lower bay was assembled. The assembly sequence is shown in Figure 6-29.

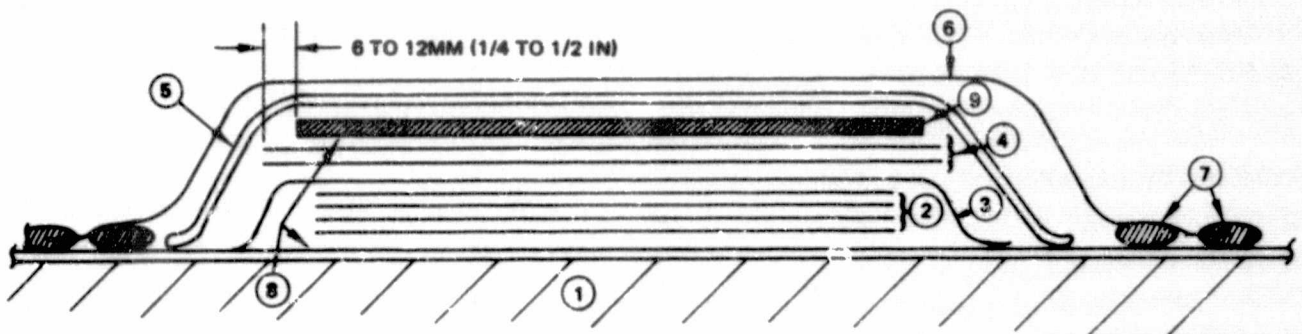
The top bay was assembled first. A truss ring was first located on the lower tooling surface and the spider assembly on the upper tooling surface. The connecting double strut assemblies and lower gussets were then temporarily

installed. The struts were then removed, bonding surfaces clear, coated with adhesive and reinstalled. Figure 6-30 shows the top bay propped off the upper tooling surface while the lower joints are being assembled. Note that the gussets for the middle bay below the lower ring have also been installed.

Figure 6-31 shows the middle bay being completed. The upper bay has been moved to the top of the assembly tool. The strut subassemblies have been installed. The connections have been assembled at the lower ring and are being completed at the upper ring. Figure 6-32 shows one of the joints being assembled.

The lower bay was assembled using the same sequence described above. Figure 6-33 shows the completed truss being removed from the assembly truss. Figure 6-34 shows the completed truss after being placed on the floor.

- | | |
|--|--|
| 1. TOOL SURFACE | 6. VACUUM BAG FILM |
| 2. GRAPHITE/EPOXY LAYUP | 7. SEALING TAPE |
| 3. PERFORATED PARTING FILM | 8. PARTING AGENT |
| 4. GLASS CLOTH BLEEDER
1 PLY BLEEDER FOR EACH 4 PLIES PREPREG | 9. PRESSURE PAD
(OPTIONAL FOR SMALL DETAIL PARTS) |
| 5. GLASS CLOTH BREATHER | |



NOTE:

WHERE SPLICING OF RESIN BLEEDER IS NECESSARY, USE BUTT SPLICES WITH MAXIMUM GAP OF 3MM (1/8 INCH).
WHERE SPLICING OF BREATHER IS NECESSARY, USE A MAXIMUM OVERLAP OF 25 MM (1 INCH).

Figure 6-2. Layup Configuration

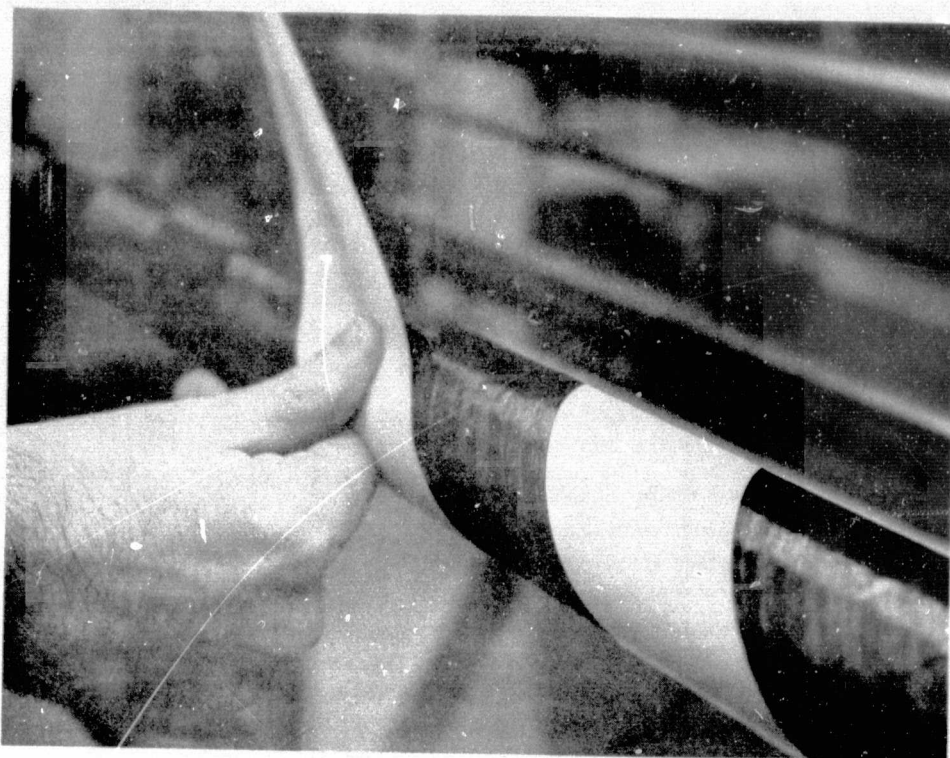


Figure 6-3. Tubular Strut Ply Layup

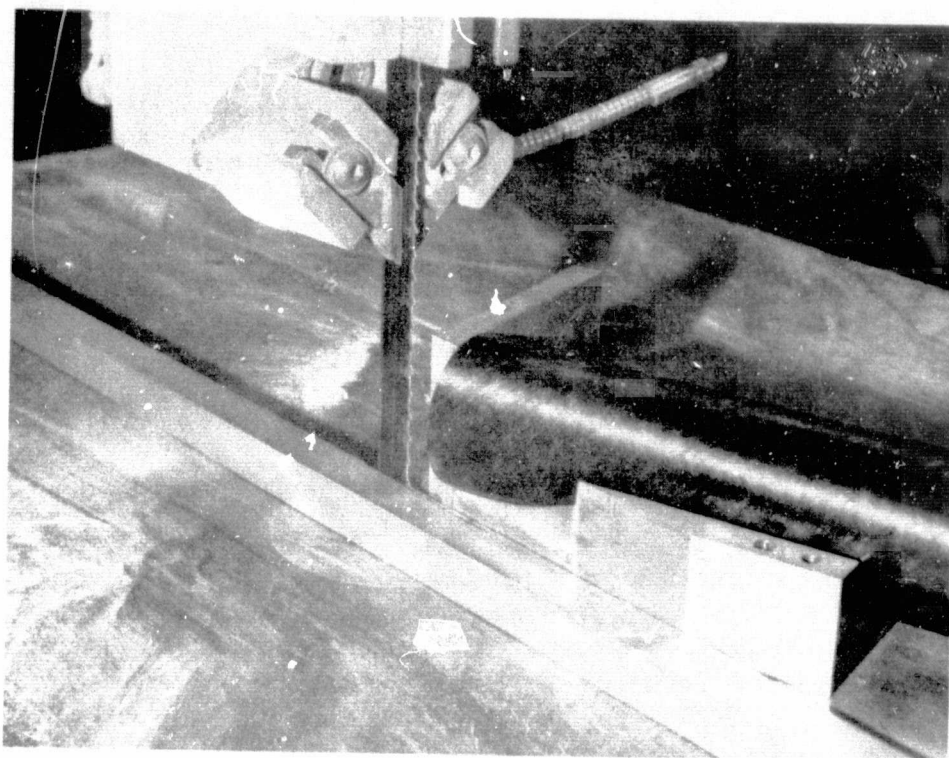


Figure 6-4. Tubular Strut—End Trim

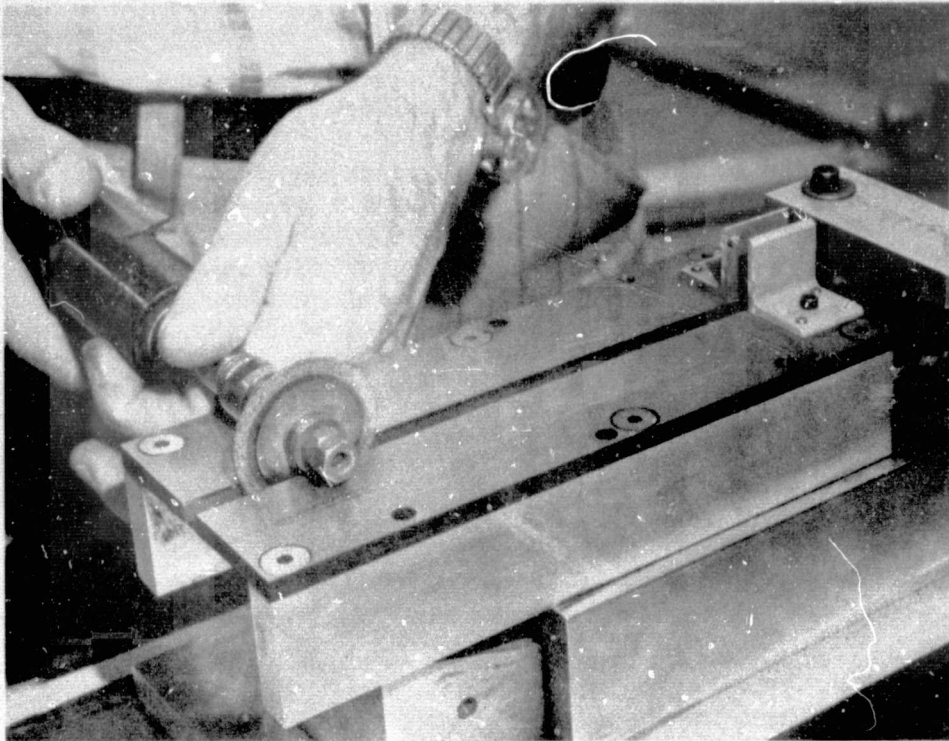


Figure 6-5. Tubular Strut—End Slotting

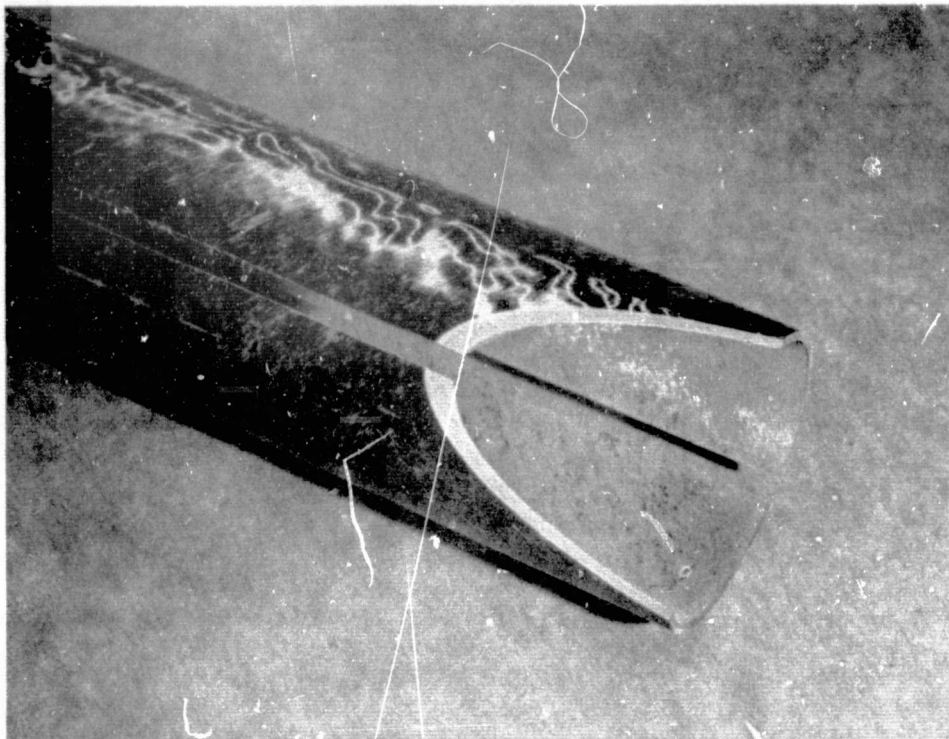


Figure 6-6. Tubular Strut - End Trim Complete

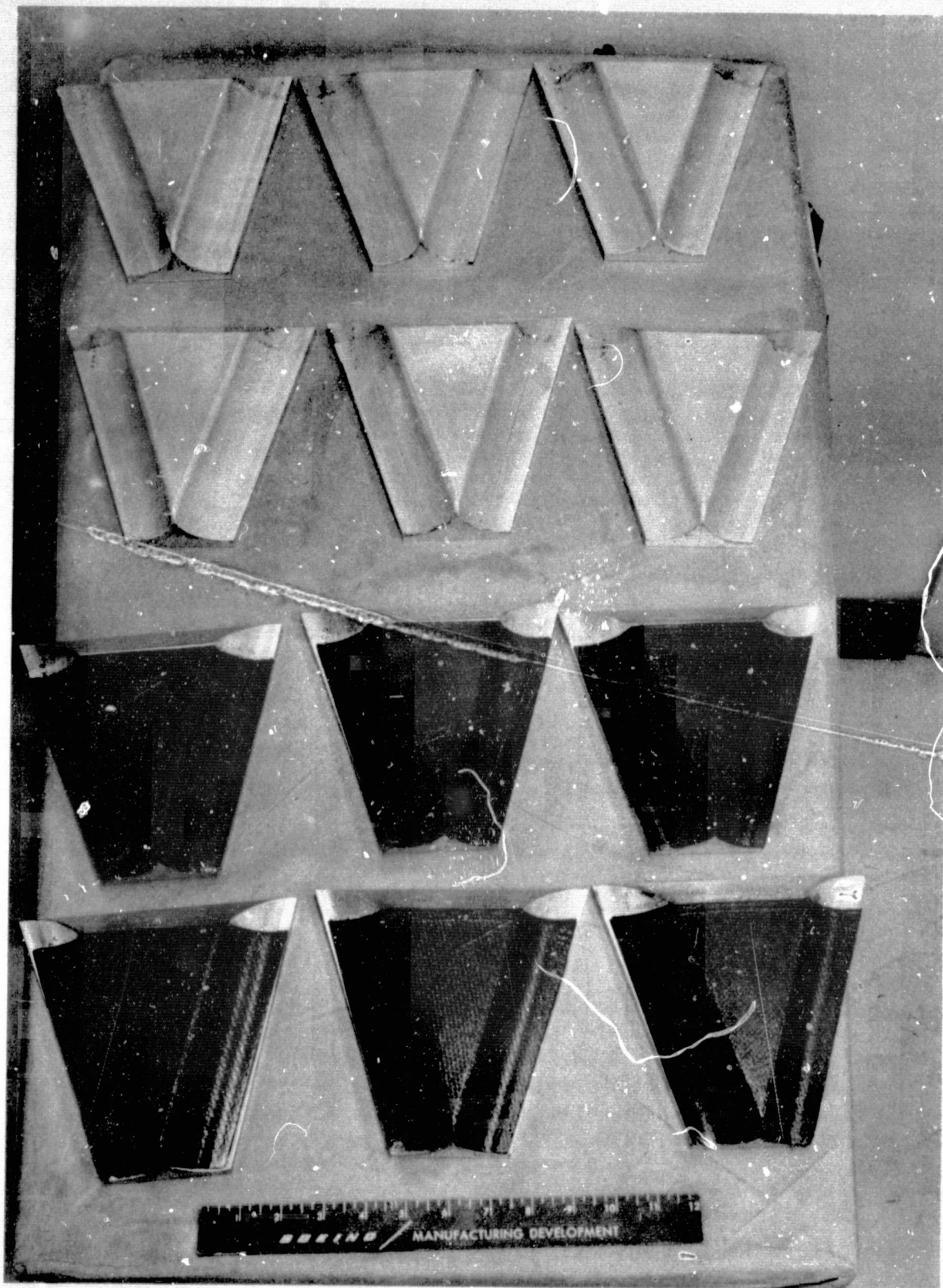


Figure 6-7. Graphite Fabric Gusset Fittings and Tooling

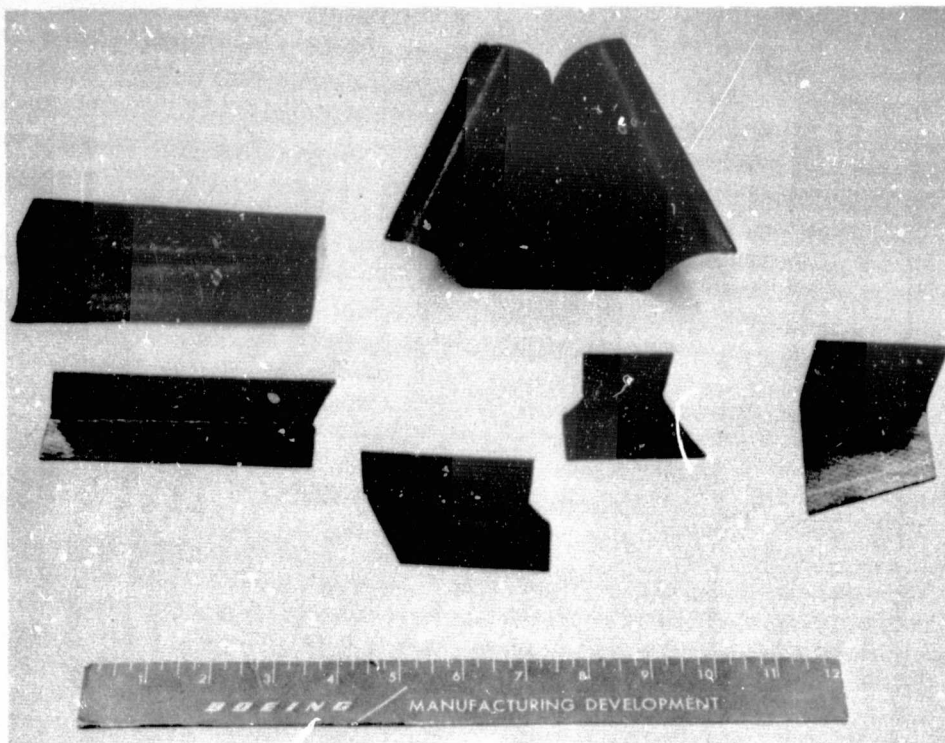


Figure 6-8. Graphite Fabric Truss Joint Details

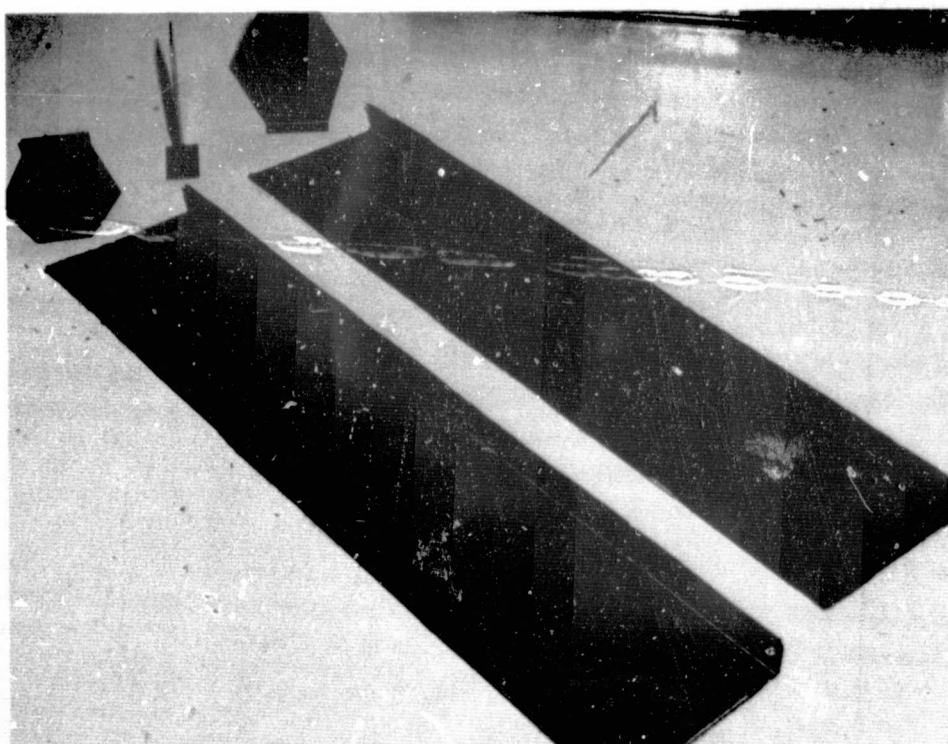


Figure 6-9. Joint "T" Gussets

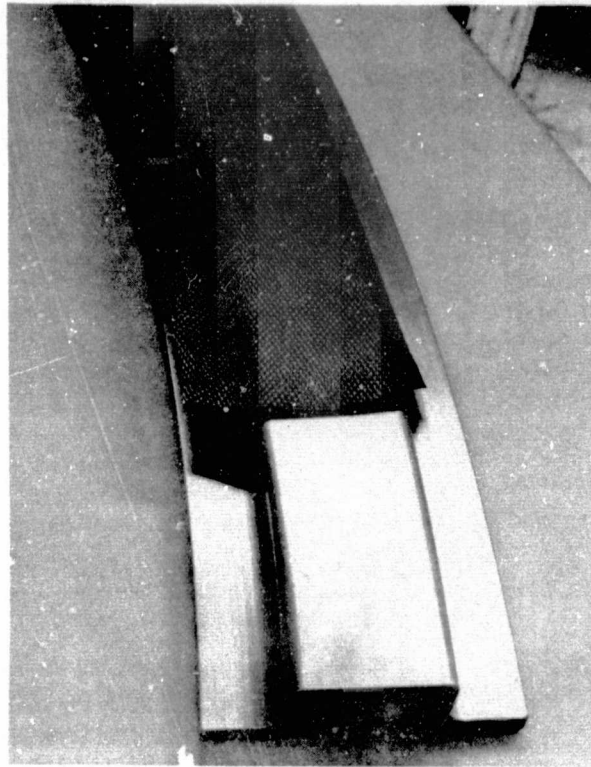


Figure 6-10. Graphite Fabric Ring Channel Layup

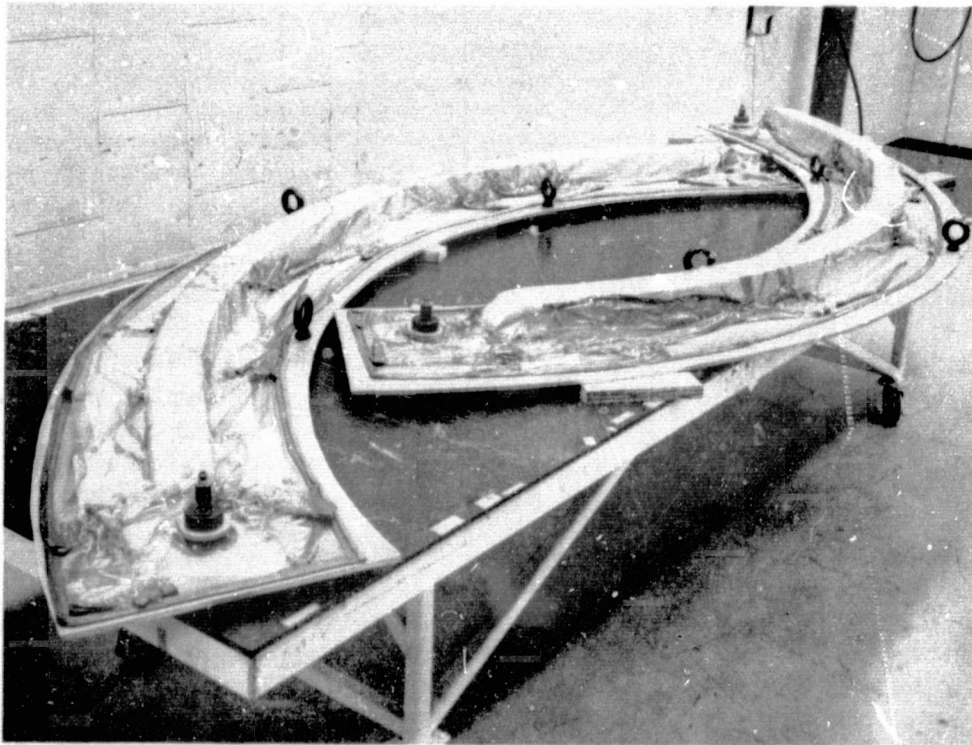


Figure 6-11. Graphite Fabric Ring Channel - Bagged and Ready for Cure

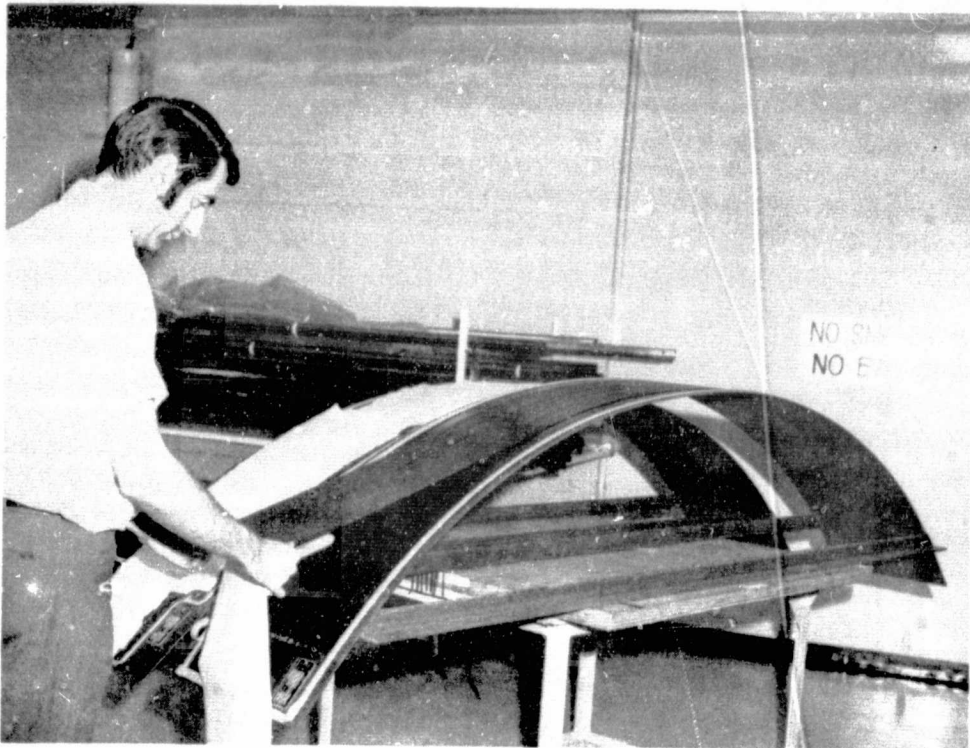


Figure 6-12. Truss Ring Chord Layup

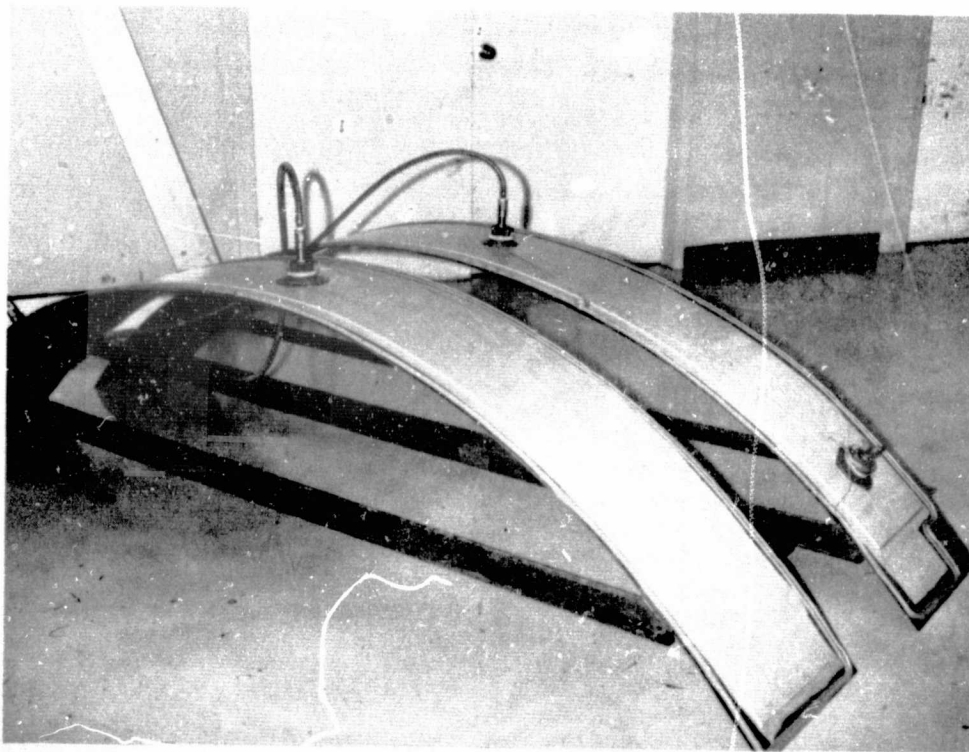


Figure 6-13. Truss Ring Chord Laminates - Bagged and Ready for Cure

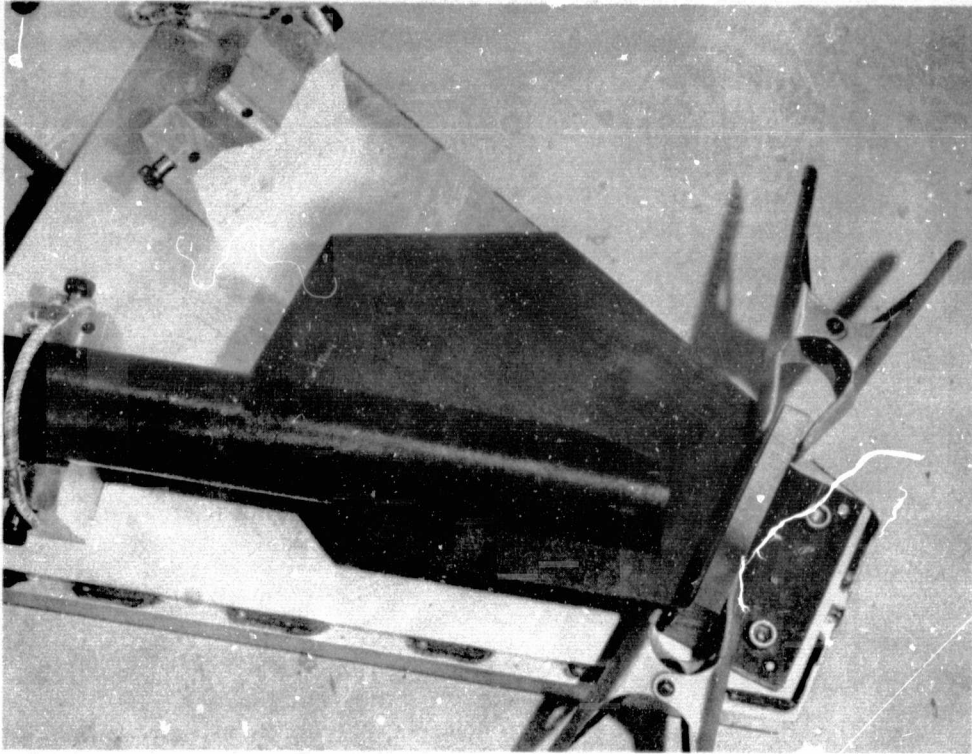


Figure 6-14. Strut Assembly - Slotted Tube Installed on Gusset

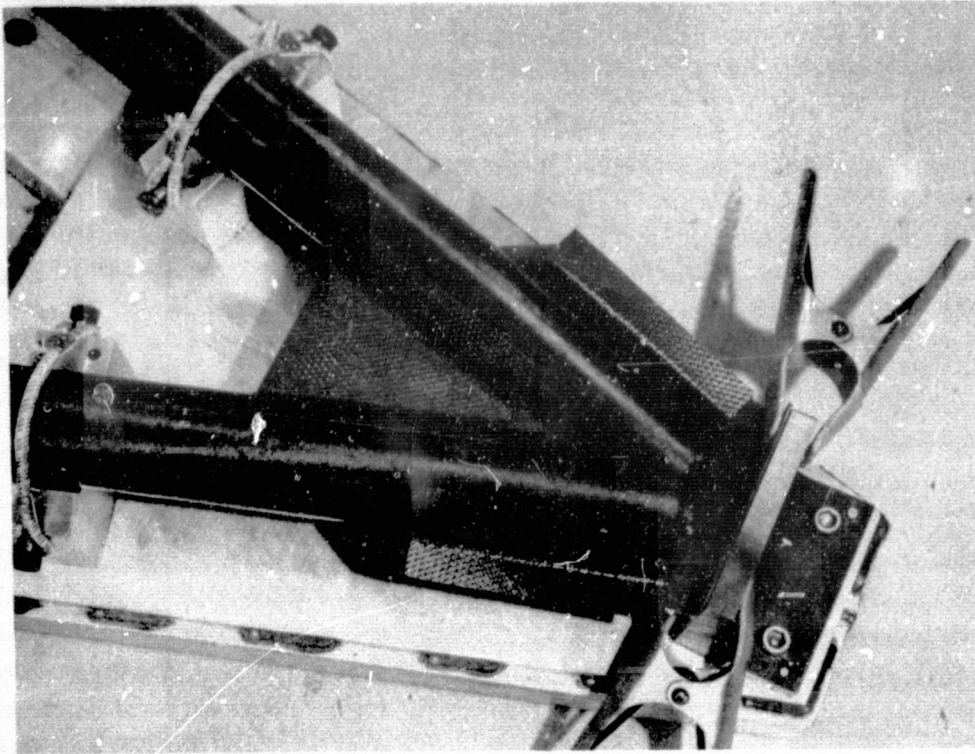


Figure 6-15. Strut Assembly - Joint Prefit

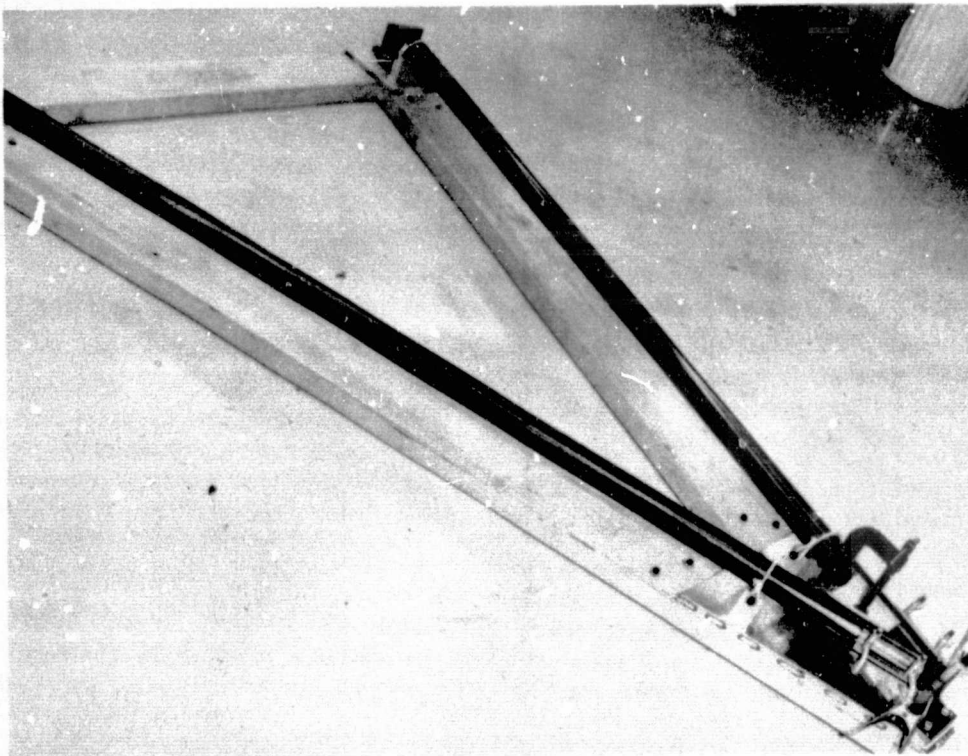


Figure 6-16. Strut Assembly - Joint Bonding

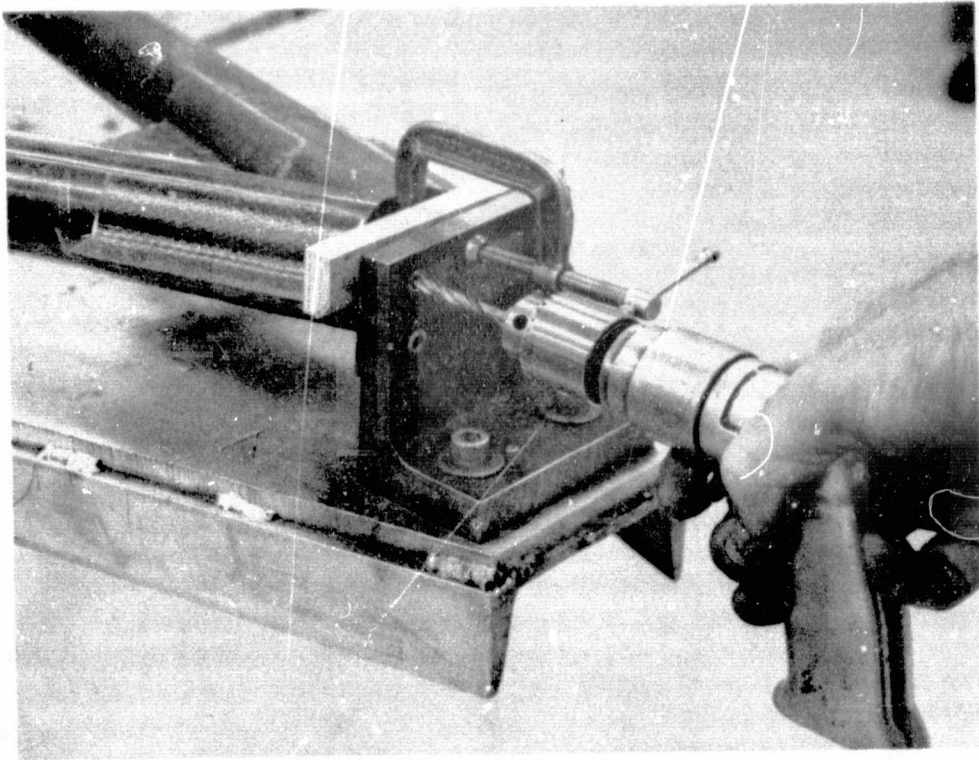


Figure 6-17. Strut Assembly - "T" Drilling

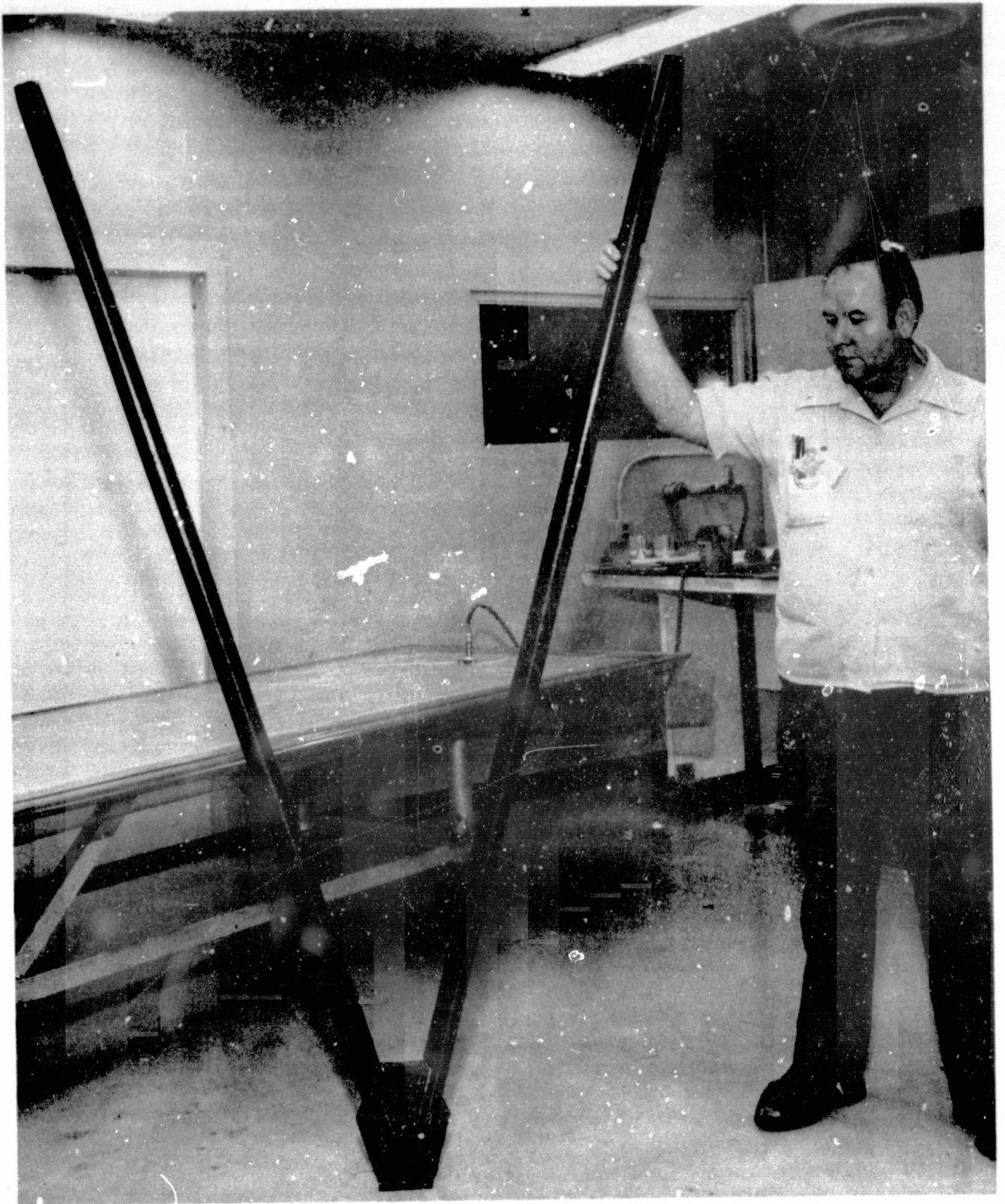


Figure 6-18. Completed Strut Assembly

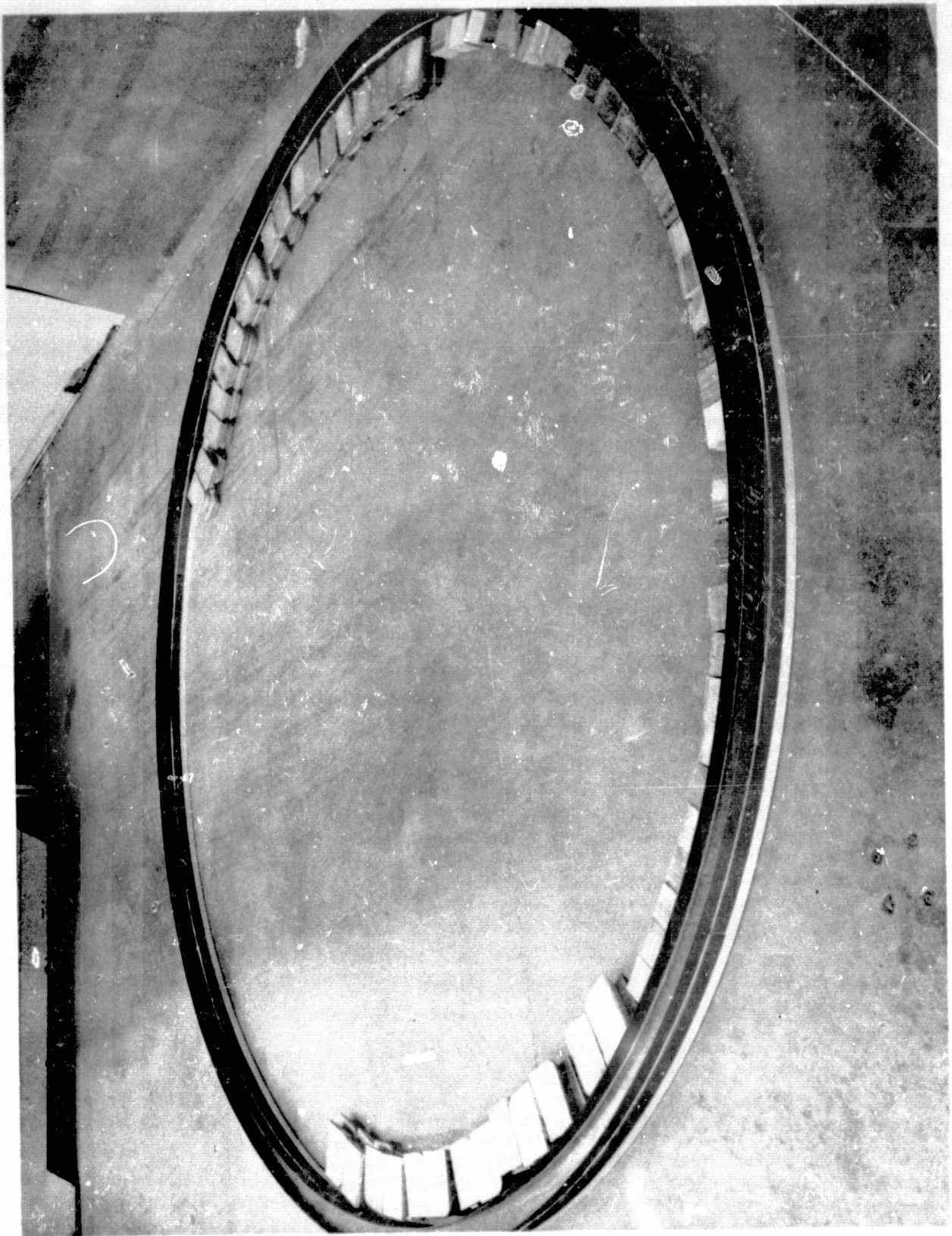


Figure 6-19. Ring Assembly - Assembled Graphite Fabric Channels

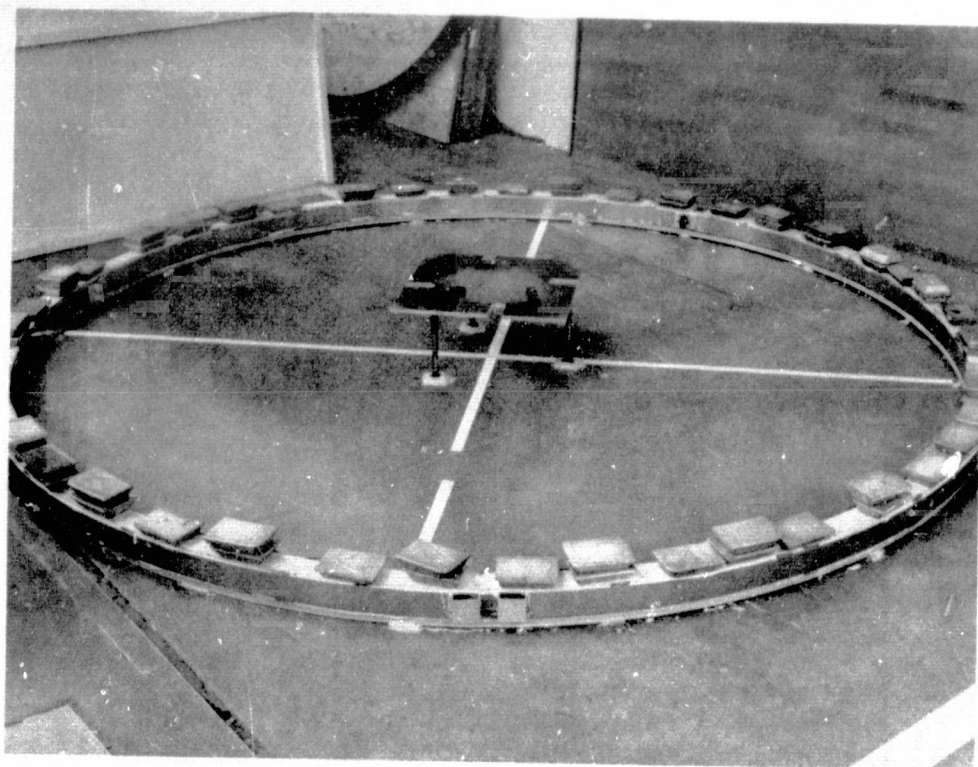


Figure 6-20. Ring Assembly - Chord Installation



Figure 6-21. Ring Assembly - Template Drilling

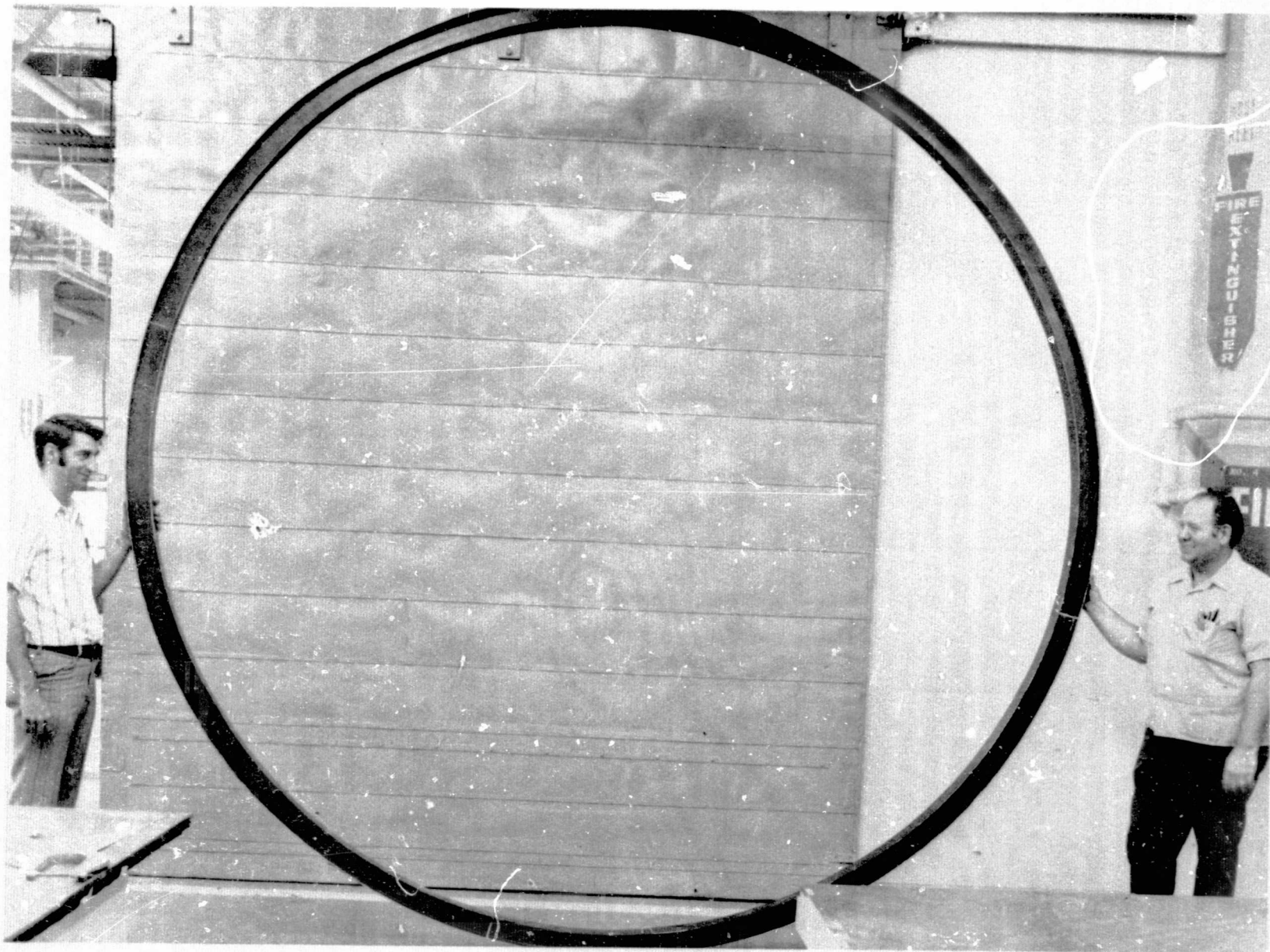


Figure 6-22. Completed Ring Assembly

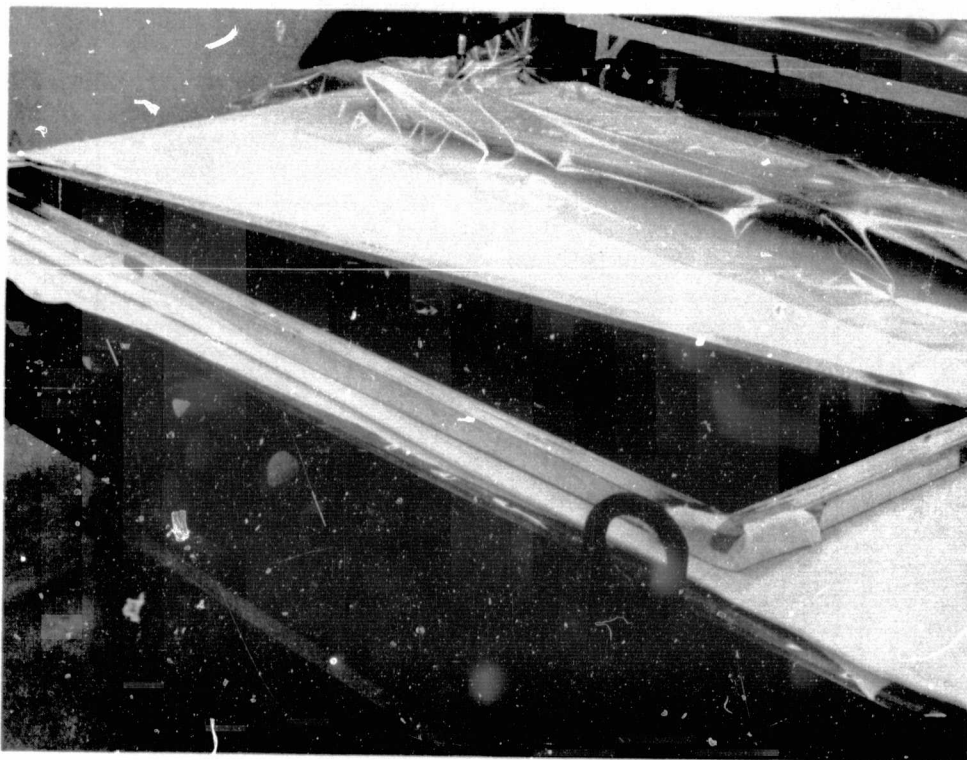


Figure 6-23. Spider Beam Assembly - Layup Tooling



Figure 6-24. Spider Beam Assembly - Bagged and Ready for Cure



Figure 6-25. Spider Cylinder Assembly - Cured Inner Skin



Figure 6-26. Spider Cylinder Assembly - Honeycomb Installation

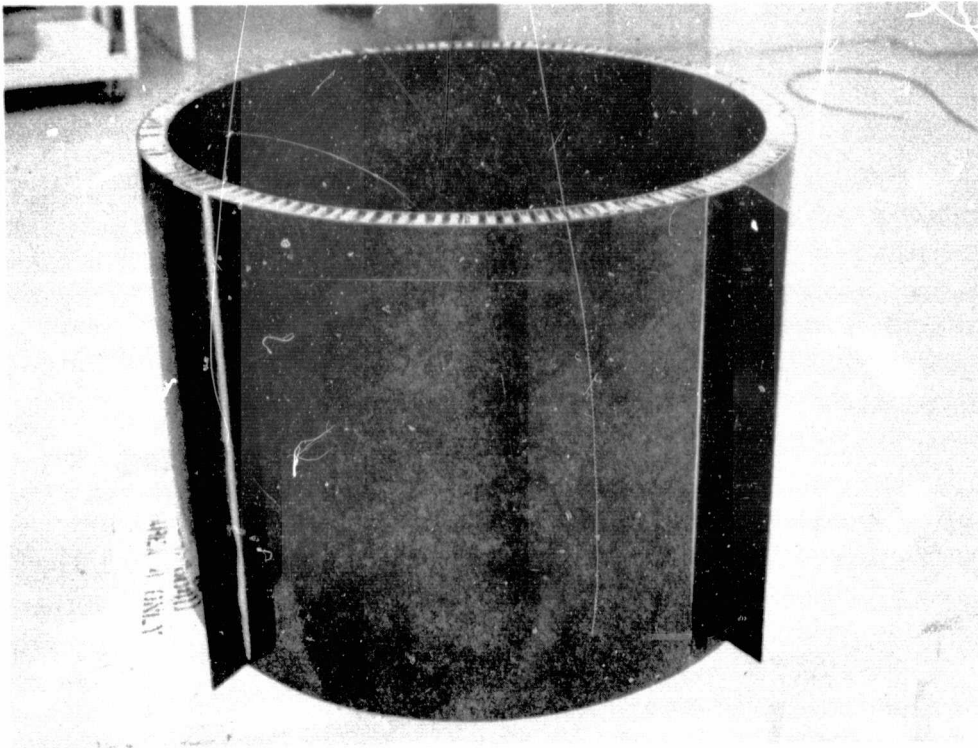


Figure 6-27. Completed Spider Cylinder Assembly

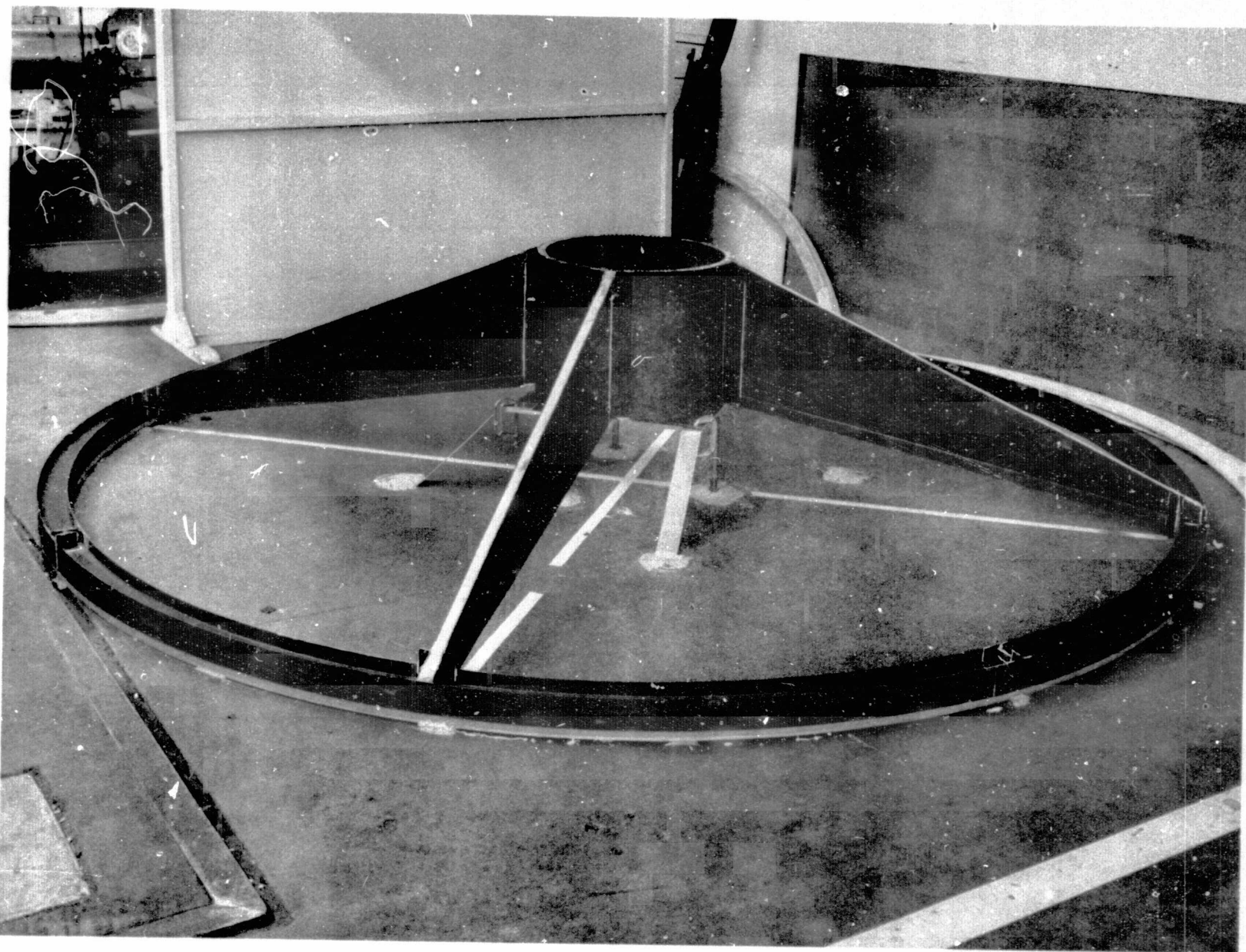


Figure 6-28. Spider Assembly Installed on Top Truss Ring

LEGEND:

- 1 INDEX GUSSETS TO PILOT HOLES IN NO. 2 RING, CLECO IN PLACE
- 2 LOCATE SPIDER ASSEMBLY ON UPPER TOOL
- 3 LOCATE DOUBLE-STRUT ASSEMBLIES USING UPPER RING PILOT HOLES
- 4 DRILL HOLES FULL SIZE THRU RING NO. 1 DISASSEMBLE, CLEAN SURFACES, APPLY ADHESIVE AND REASSEMBLE
- 5 INSTALL FASTENERS THRU RING NO. 1, TIGHTEN FOR BOND PRESSURE, ALLOW TO CURE OVERNIGHT
- 6 RAISE BAY NO. 1 SLIGHTLY AND DRILL GUSSETS ON RING NO. 2 FULL SIZE
- 7 DISASSEMBLE, CLEAN SURFACES, APPLY ADHESIVE AND REASSEMBLE
- 8 INSTALL JOINT DETAILS AND CLAMP, INSTALL FASTENERS AND TIGHTEN FOR PRESSURE, ALLOW TO CURE OVERNIGHT
- 9 RAISE BAY NO. 1 SUCH THAT RING NO. 2 IS AT TOP OF TOOL
- 10 LOCATE RING NO. 3 ON TOOL AND DOUBLE-STRUT ASSEMBLIES ON RING WITH GUSSETS FOR BAY NO. 3
- 11 DRILL HOLES FULL SIZE THRU RING AND GUSSETS
- 12 DISASSEMBLE, CLEAN SURFACES, APPLY ADHESIVE, AND BOND GUSSETS AND DOUBLE-STRUT ASSEMBLIES TO RING NO. 3, CURE OVERNIGHT
- 13 RAISE BAY NO. 1 SLIGHTLY, CLEAN BONDING SURFACES, APPLY ADHESIVE AND BOND STRUTS TO RING NO. 2, CURE OVERNIGHT
- 14 RAISE COMPLETED BAYS NO. 1 AND NO. 2 SUCH THAT RING NO. 3 IS AT TOP OF TOOL, LOCATE RING NO. 4 ON LOWER TOOL.
- 15 LOCATE DOUBLE-STRUT ASSEMBLIES ON RING NO. 4 DRILL FULL SIZE, DISASSEMBLE, CLEAN JOINT DETAILS, REASSEMBLE
- 16 APPLY ADHESIVE TO JOINT DETAILS AT RING NO. 3, CLAMP AND BOND OVERNIGHT
- 17 BOLT LOWER RING TO COMPLETE BAY NO. 3

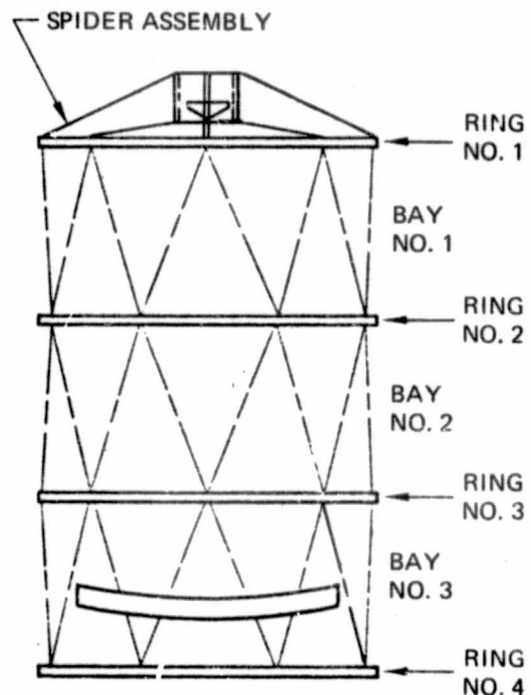


Figure 6-29. Truss Assembly Sequence

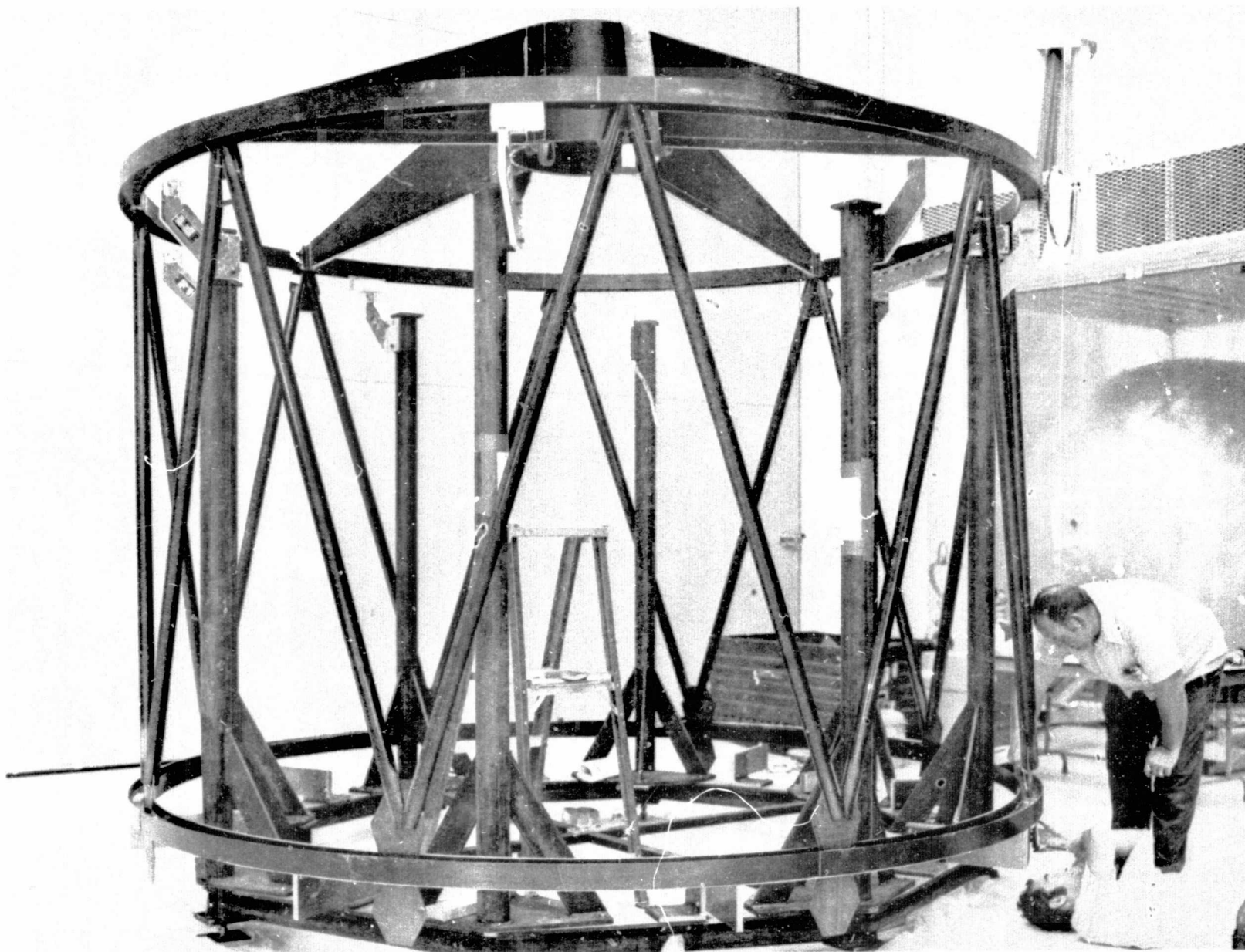


Figure 6-30. First Bay Assembly

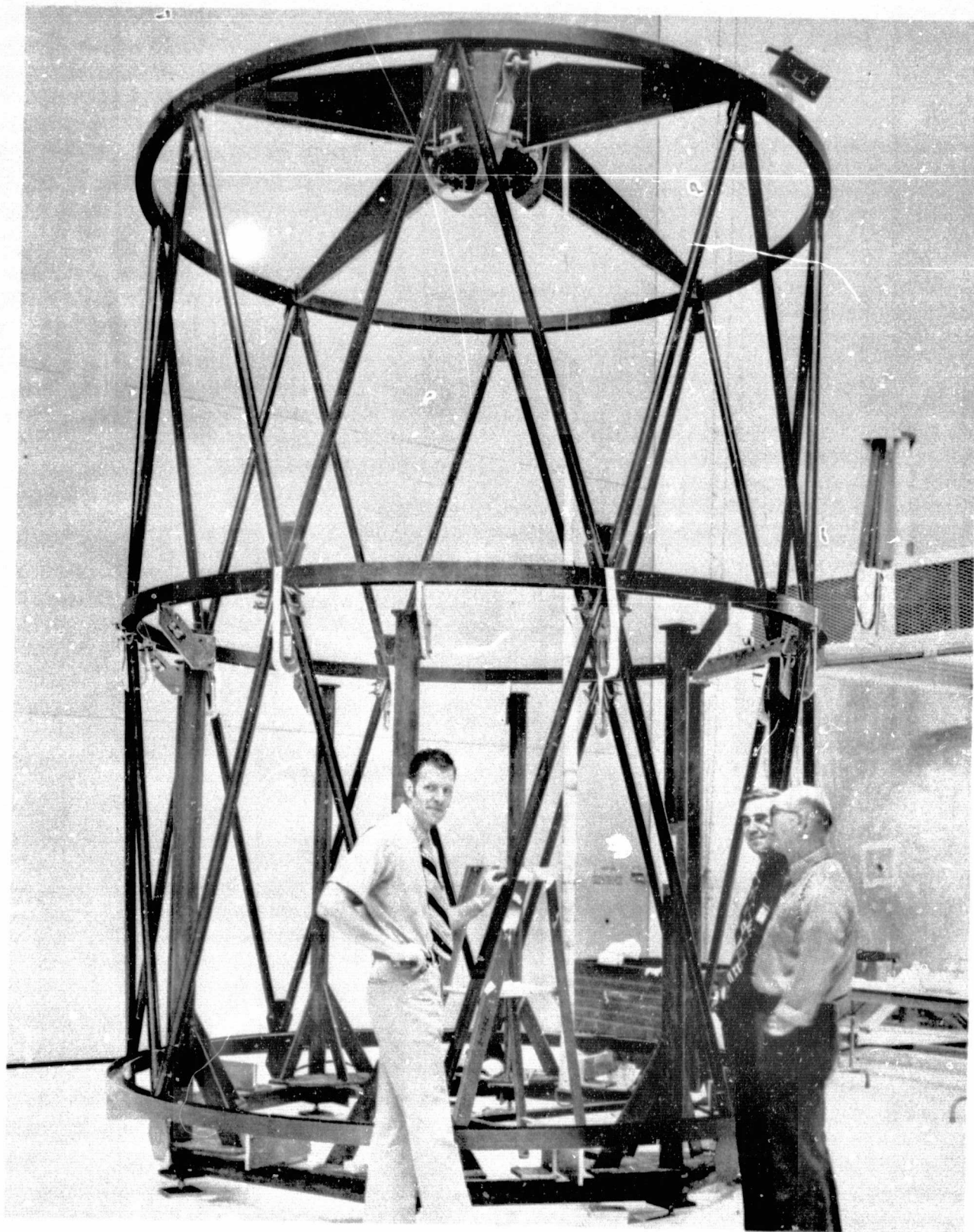


Figure 6-31. Second Bay Assembly Complete

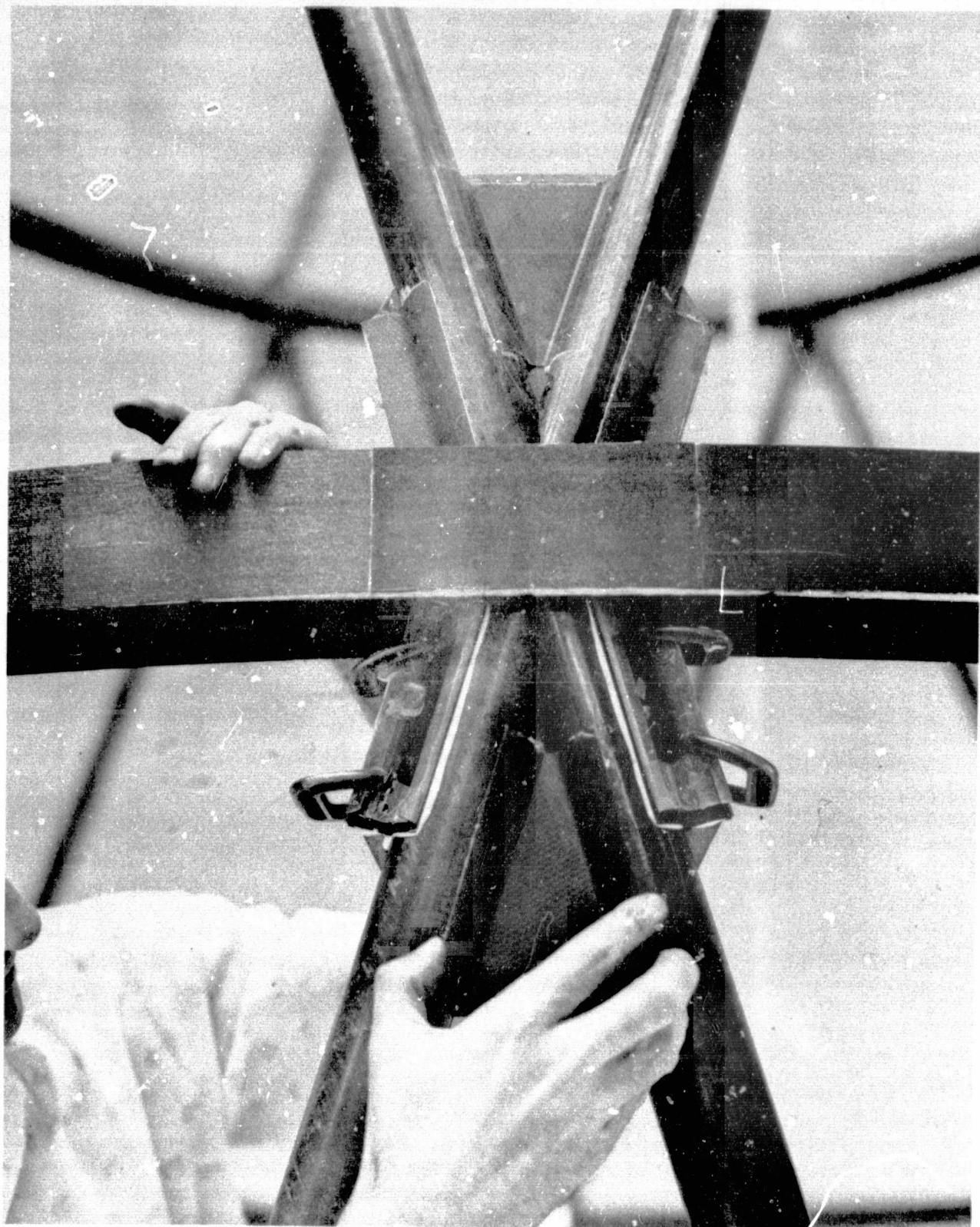


Figure 6-32. Typical Truss Joint

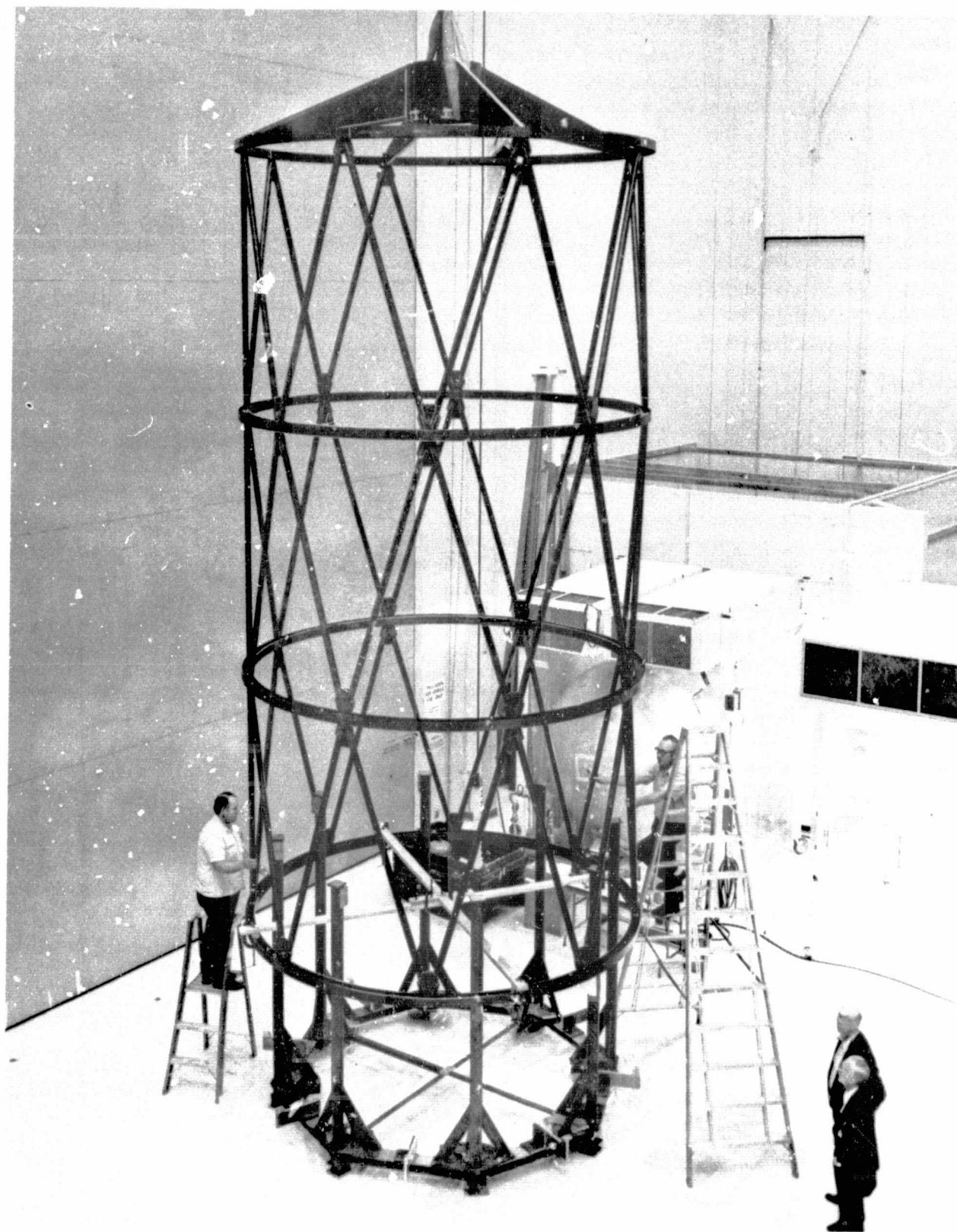


Figure 6-33. Removal of Completed Truss from Tooling



Figure 6-34. Completed Truss Assembly.

7.0 FULL-SCALE TRUSS TESTS

To establish the feasibility of the graphite/epoxy metering truss concept full-scale tests were performed. Testing was performed to determine truss stiffnesses, dynamic characteristics, and thermal distortion behavior. The test data obtained was also used to verify the analysis. Three major tests were performed in the following sequence; a static load test, a modal survey test and a thermal vacuum test.

7.1 STATIC LOAD TEST

The graphite/epoxy truss was subjected to static loads to determine its axial, bending and torsional stiffnesses. The truss was subjected to separately applied axial and side bending limit loads and a selected torsional load. The design crash loads, 9 g axial and 4 1/2 g lateral, were reduced by a 1.4 ultimate load factor to obtain limit loads.

Test Set-Up

The metering truss was attached to a welded steel ring fixture at its base. Attachments were made at the eight strut joint locations. The four bolts at each of these locations were installed using load indicating washers to control the torque during their installation. The steel base ring fixture was attached to laboratory floor rails with twenty-two 2.54 cm (1 in) diameter steel bolts.

The vertical load system, located on the longitudinal axis of the truss assembly, consisted of a pipe column, hydraulic actuator, load cell interfacing with the secondary mirror support (spider cylinder). This system reacted loads into the base ring fixture.

The bending and torsion loads were applied to the truss at its upper ring. The associated loading system consisted of a pair of hydraulic actuators, load cells and interfacing linkage between the upper truss ring and a load reaction fixture. To apply the side loads the two actuators were operated in the same direction and for the torsional loads they were operated opposite directions. The reaction structure consisted of two steel "H" section columns supported laterally.

A schematic of the test set-up is shown in Figure 7-1, and the actual set-up is shown in Figure 7-2. The attachment of the base of the truss to the steel base ring fixture is shown in Figure 7-3. Attachments of the steel base ring fixtures to the floor are also shown. A close-up of the attachment of the truss base to the fixture is shown in Figure 7-4. The installation torque of the bolts shown passing thru the truss base ring into the adapter fittings were controlled by the use of load indicating washers. Figure 7-5 shows one of the fittings installed on the top truss ring for introducing side bending loads and torsion. Figure 7-6 shows the load actuator pumps used for applying load during test.

Instrumentation

The axial, bending, and torsional loads were measured with load cells located in-line with the actuators (see Figure 7-1). Twenty-two electrical deflection indicators (EDI's) were attached to the truss at locations shown in Figure 7-7 to measure longitudinal, lateral and torsional deflections.

A multi-frame type structure was assembled and mounted to the base ring test fixture with three bolts. This assembly provided a reference for the EDI's for the full height of the truss. The three point attachment scheme provided a common reference plane for both the truss and the multi-frame instrumentation tower. Figures 7-2, -3 and -7 show the location and installation of this tower.

Test Procedure

The truss was subjected to separately applied side, torsion and axial loads. The loads were applied in 20% load increments with data recorded at each increment up to 100% and at 60% and 0% on the way down. The maximum loads attained were:

- 1) side bending--- total lateral load of 430 lb applied at the top truss ring;
- 2) torsion-- opposing lateral loads of 131.1 pounds each applied at the top truss ring;
- 3) axial-- a maximum load of 803.6 pounds applied at the secondary mirror mounting plane.

Test Data

A summary of the test data for: 1) the side load bending condition is shown in Table 7-1, 2) the torsion load condition is shown in Table 7-2, and 3) the axial load condition in Table 7-3.

In the side bending load test the EDI's were rezeroed after 20% load was applied. This was performed because of the truss distortion caused during the connection

of the actuators. In the following tests the EDI's were zeroed before and after the actuators were connected.

In the side bending load test the maximum deflections were developed in the top ring of the truss as expected. The magnitudes of the deflections showed that loads were applied evenly. The magnitudes at the 60% levels both as load was being increased and as load was being reduced were the same showing the truss was responding elastically.

In the torsion load test maximum deflection was again experienced at the top ring where load was being applied. The magnitudes of the readings of the EDI's on this ring (No's 7 & 8) showed there was some lateral motion of the truss. Again the readings of these EDI's were the same at the 60% levels both as loads were increased and reduced indicating that hysteresis effects or test peculiarities were not introduced.

In the axial load test load was introduced at the spider cylinder. By far, the bulk of the vertical deflections occurred in the spider assembly. Insignificant (non-measurable) deflections occurred between the truss upper ring and its base. The deflections at EDI's 1 and 2 located in the spider cylinder were the same at 20% levels as load was being increased and decreased and also at the 60% levels as load was increased and decreased. Again this showed that the truss was acting elastically.

Test Results

Side bending and axial limit loads as well as a selected torsional load were applied to the metering truss. The truss successfully carried these loads

without undesirable deformations occurring. Truss deflections were measured during the three test conditions. These data will be reduced to establish the truss spring rates and will be discussed along with analysis correlations in Section 7.4.

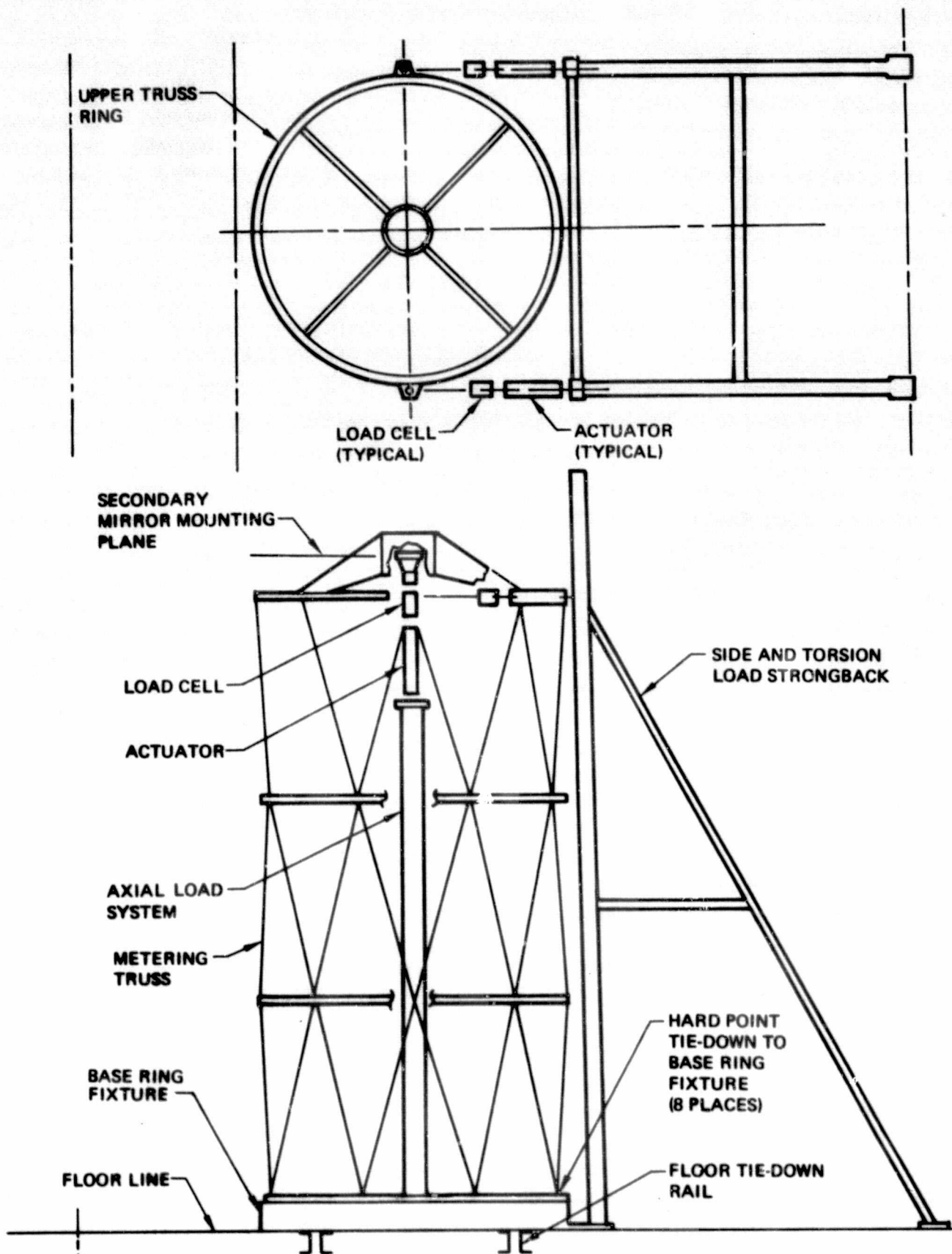


Figure 7.1. Static Load Test Setup—Schematic



Figure 7-2. Static Load Test Setup



Figure 7-3. Static Load Test - Base Attachment

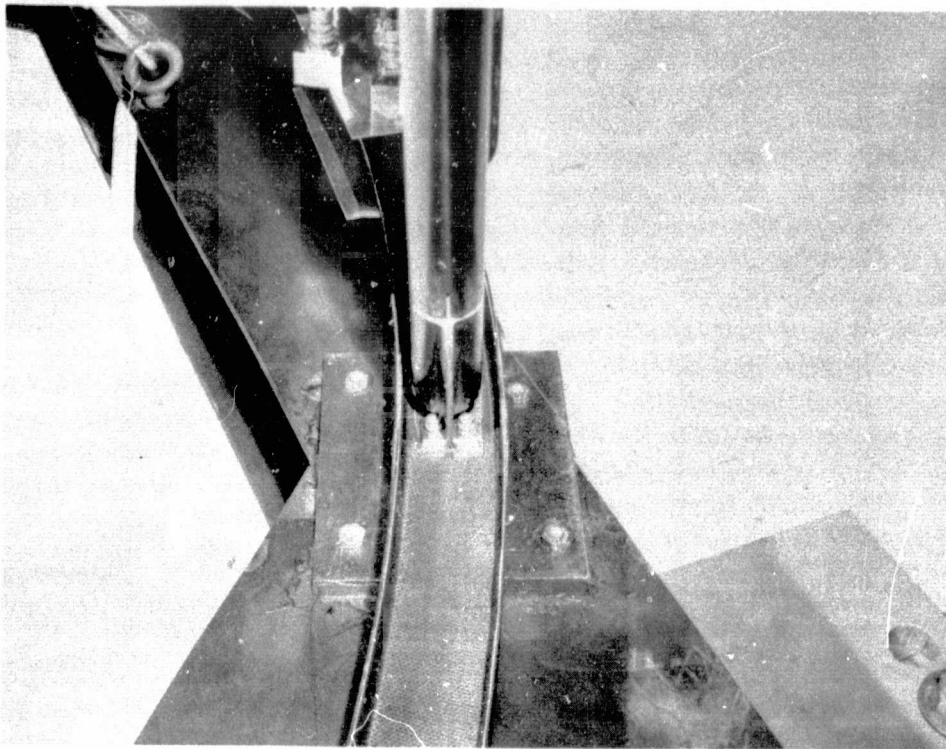


Figure 7-4. Static Load Test - Base Attachment Close-up

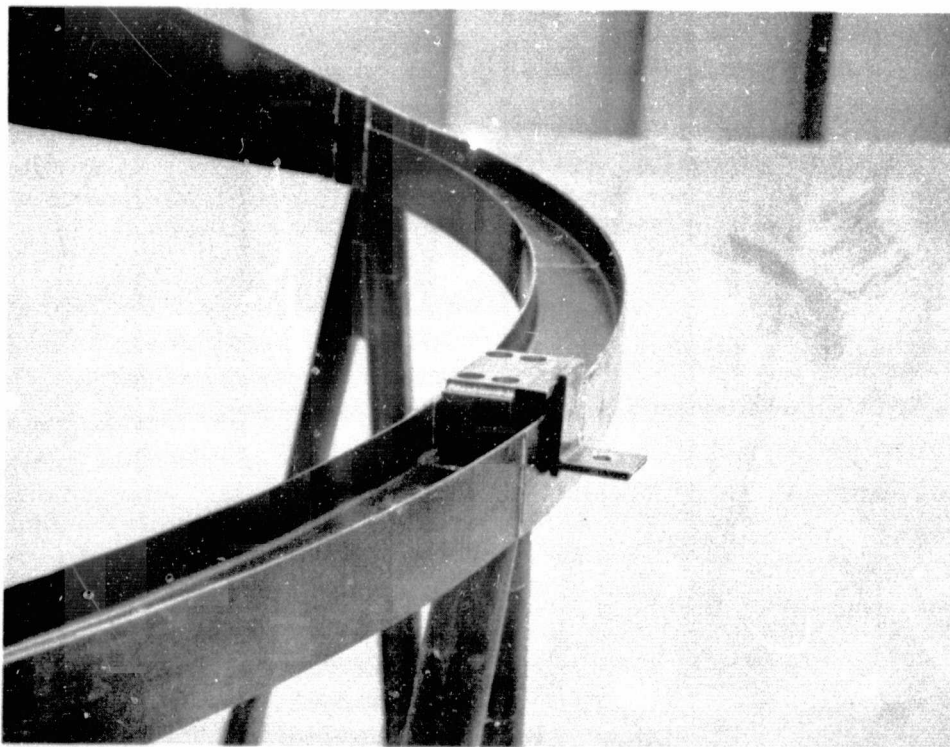


Figure 7-5. Static Load Test - Load Introduction Fitting

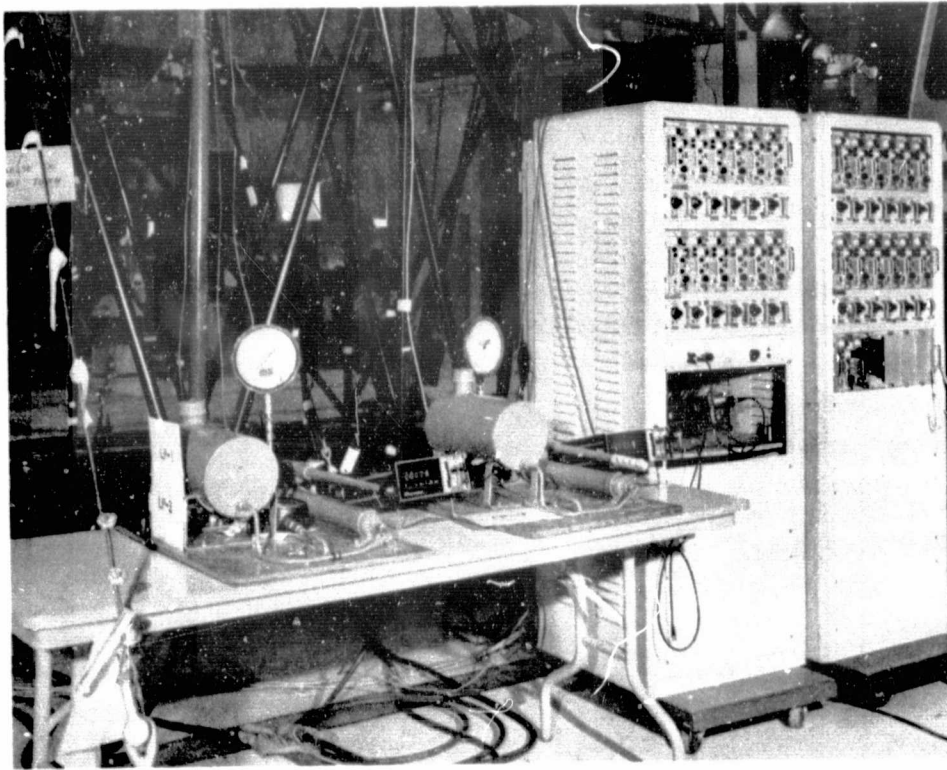


Figure 7-6. Static Load Test - Load Actuator Pumps

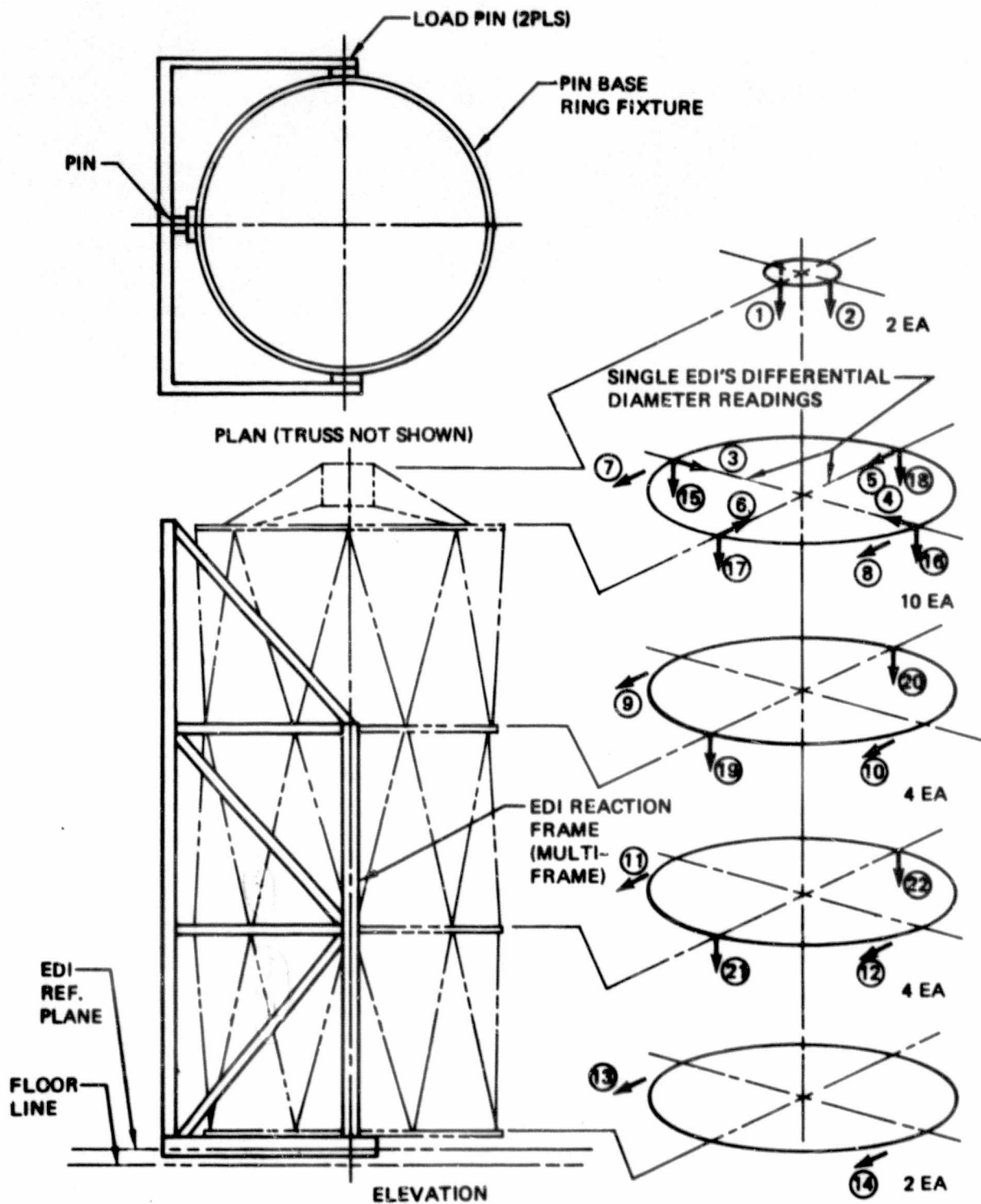
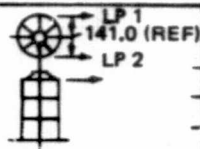


Figure 7-7. EDI Reaction Structure and EDI Locations

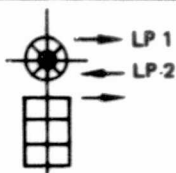
Table 7-1. Side Load Condition LST Metering Truss Static Load Test Data



% Load	Load (lbs)			Deflection (in.) x 10 ⁻³																					
	LP 1	LP 2	LP 3	1	2	3	4	5	6	7	8	9	10	11	12	13	14	15	16	17	18	19	20	21	22
20	43.2	43.3	—	0.0	0.0	0.0	0.0	0.0	0.0	0.0	0.0	0.0	0.0	0.0	0.0	0.0	0.0	0.0	0.0	0.0	0.0	0.0	0.0	0.0	0.0
40	87.2	87.4	—	0.4	0.0	0.0	0.4	0.0	0.0	8.0	9.0	4.4	4.8	0.4	0.0			0.0	0.4	0.0	1.2	0.0	0.4	0.4	0.4
60	126.8	128.3	—	0.0	0.0	0.0	0.8	0.4	0.4	16.0	16.0	8.8	9.2	0.8	0.8			0.4	0.4	0.0	1.2	0.0	0.4	1.2	0.8
80	171.5	171.6	—	0.0	0.4	0.4	1.2	0.4	0.4	24.0	26.0	13.2	13.6	2.4	1.6			0.4	0.4	0.4	2.0	0.0	1.2	2.0	1.2
100	215.0	215.0	—	0.4	0.4	0.4	1.6	0.4	0.8	32.0	33.0	17.6	18.4	3.6	3.6			0.8	0.8	0.8	2.8	0.0	1.6	2.8	1.6
80	126.0	127.8	—	0.0	0.4	0.4	1.2	0.4	0.4	15.0	17.0	8.0	9.2	3.6	3.6			0.8	0.4	0.4	1.6		0.4	1.6	0.8
0	15.2	8.5	—	0.4	0.4	0.4	0.4	0.4	0.0	0.4	5.0	2.0	2.8	0.4	0.4			0.8	0.0	0.0	0.8	0.0	0.0	0.4	0.0
0	—	—	—	0.4	0.4	1.2	1.2	0.4	1.6	0.8	26.0	3.2	3.2	0.4	0.4	0.0	0.0	2.0	2.0	0.0	0.4	0.0	0.0	0.4	0.0
Notes:				Data adjusted to zero at 20% load to compensate for disturbance of the EDI frame while connecting the load actuators.																					
Zero data readings with load actuators connected.																									
Zero data readings with load actuators disconnected.																									

EDI's 13 & 14 were defective and were replaced for the balance of the tests.

100



% Load	Load (lbs)			Deflection (in.) x 10 ⁻³																					
	LP 1	LP 2	LP 3	1	2	3	4	5	6	7	8	9	10	11	12	13	14	15	16	17	18	19	20	21	22
0	4.6	2.8		0.0	0.0	0.0	0.0	0.0	0.0	3.0	35.0	1.2	0.0	0.0	0.0	0.0	0.0	8.0	1.2	0.4	0.0	1.2	2.0	1.2	0.4
60	79.8	79.8		0.0	0.0	0.0	0.0	0.0	0.0	8.0	40.0	4.4	2.8	0.0	0.0	0.0	0.0	8.0	1.2	0.4	0.0	1.2	2.0	1.2	0.4
80	105.6	105.6		0.0	0.0	0.0	0.0	0.0	0.0	9.0	43.0	5.2	3.6	0.0	0.0	0.0	0.0	8.0	1.2	0.4	0.0	1.2	2.0	1.2	0.4
100	130.2	130.8		0.0	0.0	0.0	0.0	0.0	0.0	11.0	45.0	6.4	4.8	0.0	0.0	0.0	0.0	8.0	1.2	0.4	0.0	1.2	2.0	1.6	0.4
80	79.0	78.7		0.0	0.0	0.0	0.0	0.0	0.0	7.0	10.0	4.0	2.8	0.0	0.0	0.0	0.0	8.0	1.2	0.4	0.0	1.2	2.0	1.6	0.4
0	4.7	2.5		0.0	0.0	0.0	0.0	0.0	0.4	2.0	34.0	1.2	0.0	0.0	0.0	0.0	0.0	8.4	1.2	0.4	0.0	1.2	2.0	1.2	0.4
0	—	—	—	0.0	0.0	0.8	0.8	0.4	0.0	2.0	34.0	1.2	0.0	0.0	0.0	0.0	0.0	6.0	0.0	0.0	0.0	1.2	2.4	1.6	0.4
2	Zero data readings with load actuators connected.																								
1	Zero data readings with load actuators disconnected.																								



Table 7-3. Axial Compression Load Condition LST Metering Truss Static Load Test Data



% Load	Load (lbs)			Deflection (in.) $\times 10^{-3}$																					
	LP 1	LP 2	LP 3	1	2	3	4	5	6	7	8	9	10	11	12	13	14	15	16	17	18	19	20	21	22
0	—	—	—	0.0	0.0	0.0	0.0	0.0	0.0	0.0	0.0	0.0	0.0	0.0	0.0	0.0	0.0	0.0	0.0	0.0	0.0	0.0	0.0	0.0	0.0
0	—	—	70.0	0.0	0.0	7.6	0.0	0.0	0.0	0.0	0.0	0.0	0.0	0.0	0.0	0.0	0.0	0.0	0.0	0.0	0.0	0.0	0.0	0.0	0.0
20	—	—	161.0	10.8	10.0	10.4	1.6	3.6	4.0	0.0	0.0	0.0	0.0	0.0	0.0	0.0	0.0	0.0	0.0	0.0	0.0	0.4	0.0	0.0	0.0
40	—	—	321.0	21.6	20.8	13.6	5.2	8.0	8.0	0.0	0.0	0.0	0.0	0.0	0.0	0.0	0.0	0.0	0.0	0.0	0.0	0.4	0.0	0.0	0.0
60	—	—	482.0	32.0	32.4	17.2	8.4	12.4	12.4	1.0	0.0	0.0	0.0	0.0	0.0	0.0	0.0	0.0	0.0	0.0	0.0	0.8	0.4	0.0	0.4
80	—	—	645.0	43.2	43.2	20.4	12.0	16.4	16.8	1.0	0.0	0.0	0.0	0.0	0.0	0.0	0.0	0.0	0.0	0.0	0.0	0.8	0.4	0.0	0.4
100	—	—	803.0	54.0	54.4	24.4	15.2	20.4	20.8	2.0	0.0	0.0	0.0	0.0	0.0	0.0	0.0	0.0	0.0	0.0	0.0	0.8	0.8	0.0	0.4
80	—	—	483.0	32.8	32.8	17.6	8.8	12.8	12.8	1.0	0.0	0.0	0.0	0.0	0.0	0.0	0.0	0.0	0.0	0.0	0.0	0.4	0.4	0.0	0.4
20	—	—	162.0	11.6	11.2	10.8	2.0	5.6	4.8	0.0	0.0	0.0	0.0	0.0	0.0	0.0	0.0	0.0	0.0	0.0	0.0	0.0	0.4	0.0	0.0
0	—	—	70.0	1.6	0.4	7.6	0.0	0.4	0.8	0.0	0.0	0.0	0.0	0.0	0.0	0.0	0.0	0.0	0.0	0.0	0.0	0.4	0.0	0.0	0.0
0	—	—	—	1.6	0.0	8.0	0.0	0.8	3.6	0.0	0.0	0.0	0.0	0.0	0.0	0.0	0.0	0.0	0.0	0.0	0.0	0.4	0.0	0.0	0.0
Zero data readings load activators connected.																									
Zero data readings load actuators disconnected.																									

7.2 DYNAMIC TEST

The truss was subjected to a dynamic test to identify and measure the truss first and second cantilevered bending mode frequencies, damping and mode shapes. The truss was bolted to the floor at its base ring in the same manner described in the static test. The strong back towers used in the static test were modified and used to support two electromagnetic vibrators with attached voice coils which were used to apply exciting forces to the truss structure.

Test Set-Up

The metering truss remained mounted on the same base ring fixture used in the static test. The static test strong back towers were modified to support two vibrators at the truss upper ring elevation. The vibrators had a force rating of 25 pounds. Each had a phase reversal and a decay switch. A force switch was installed between the vibrator voice coil and the test article to measure the force input. A 125 pound steel plate was mounted in the spider cylinder to simulate the mass of the secondary mirror assembly.

A schematic of the modal survey test set-up is shown in Figure 7-8. The actual set-up is shown in the photo in Figure 7-9. As shown, the vibrators were installed in line with two of the spider beams which were rotated 90° from each other. The vibrators were installed at the top truss ring elevation on the strong back columns as shown in Figure 7-9. Thirty accelerometers were installed at ten locations on the truss. The accelerometer wires were supported by the center load column as shown in Figure 7-10. Also shown in this figure is the 125 pound secondary mirror mass simulation plate installed

in the spider cylinder. A Modal Survey Analysis System (MSAS) was used on line during the test to compute the transfer functions of the acceleration over force and to normalize the accelerometer signals for mode shape data. This equipment along with signal conditioning electronics is shown in Figure 7-11.

Instrumentation

Instrumentation for the modal survey test consisted of one kip binocular type force transducer to measure input to the test article, Endevco Model 221-D accelerometers to measure truss response, and transducer signal conditioning equipment. Thirty accelerometers located at ten locations (3 axis measurements) were used to measure the response of the truss structure. The location of these accelerometers are shown in Figure 7-12. In addition, a roving accelerometer was also used to measure structural response at various points and in establishing mode shapes. The accelerometers had a frequency range of 10 Hz to 2000 Hz and the capability of measuring accelerations from 0.05 G to 100 G's.

Test Procedure

Vibration mode frequencies and damping were obtained by sweeping the frequency of the calibration force and analyzing the response acceleration of the truss. The frequency was swept from 10 to 50 Hz. Results from the MSAS were plotted and indicated that three vibration modes in this frequency range. The first bending mode, an ovaling mode and a second bending mode. By force vectoring, a second first bending mode was located at approximately 0.2 Hz below the first located mode. The frequencies and damping were obtained for three different input force levels and also by free vibration decay.

Test Data

Vibration mode frequencies and damping were obtained from MSAS plots which indicated three vibration modes in the 10 to 50 Hz frequency range. The first bending mode was at 16 Hz, an ovaling mode at 28 Hz, and a second bending mode at 39 Hz. A second first bending mode was located by force vectoring at approximately 0.2 Hz below the first mode.

Table 7-4 summarizes the results obtained for three different input force levels. Table 7-5 summarizes the frequency and damping obtained from oscillograph recordings of the free vibration decay.

A fixture evaluation was made and revealed motion of the base fixture and floor of the test area. It should be noted that damping at the low magnitudes in this test may be influenced by how well the truss is cantilevered. In view of the motion of the mounting points, the damping data was suspected to be high. Additional testing was therefore performed on the truss under more controlled conditions under contract NAS8-31314, "Space Telescope Support Systems Module Definition Study." A summary of this work is included in Appendix A.

Test Results

Test results showed that the first mode resonant frequency was in excess of the design requirement of 15 Hz minimum. The correlation of the test results with analysis will be discussed in Section 7.4.

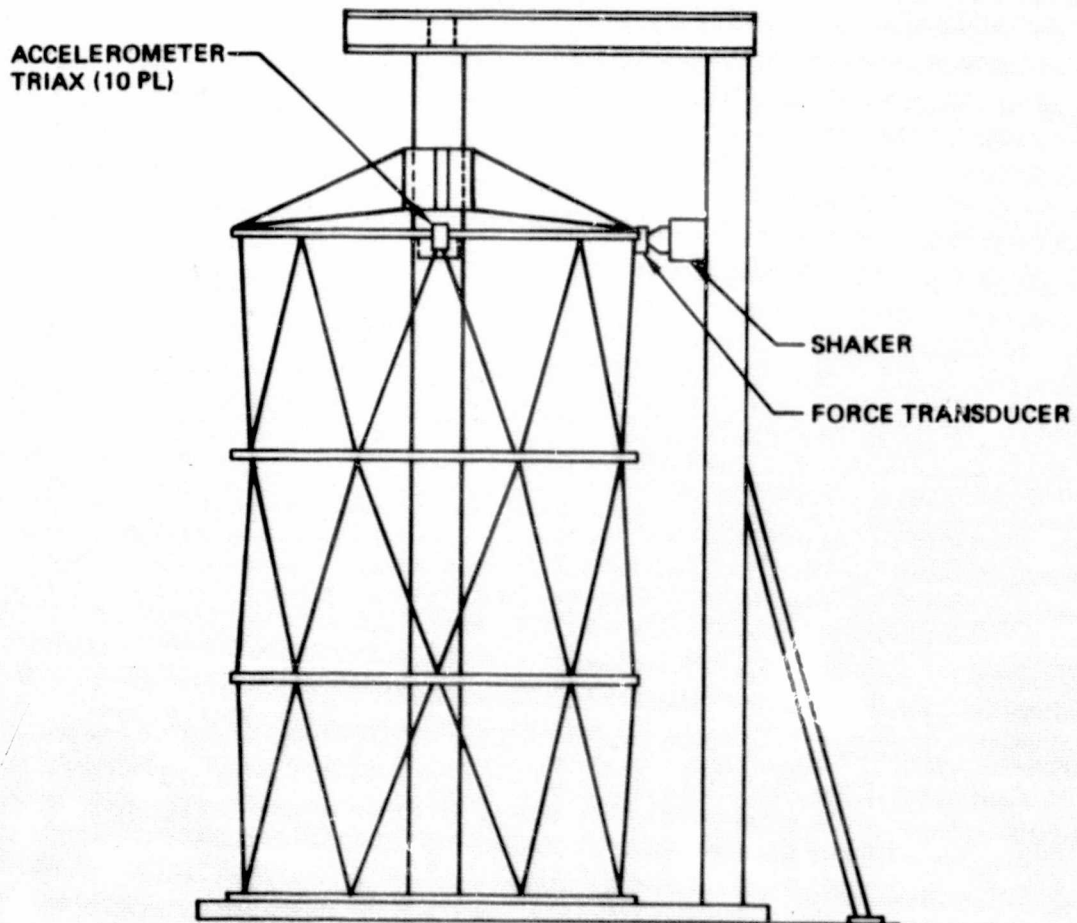
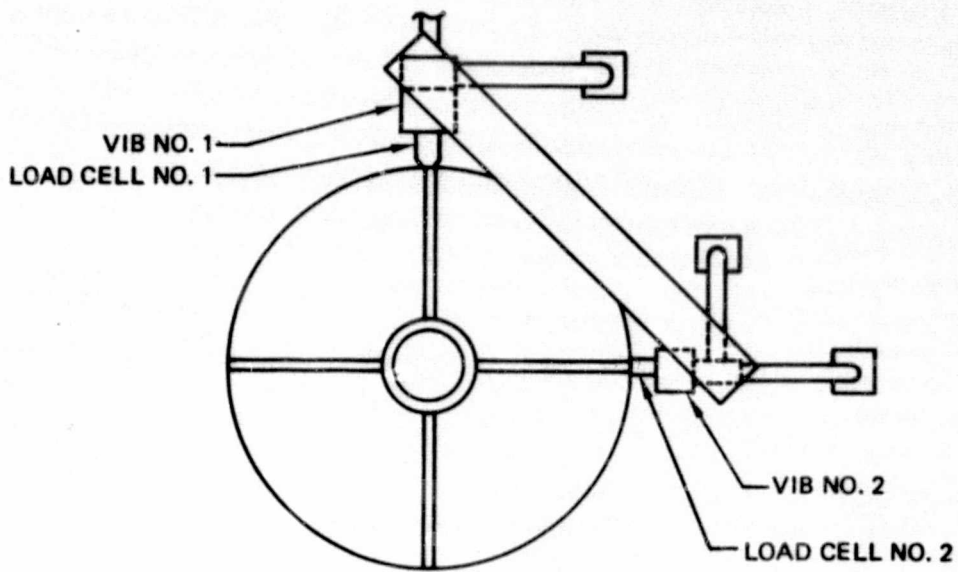


Figure 7-8. Modal Survey Test Set-Up



Figure 7-9. Modal Survey Test Setup .

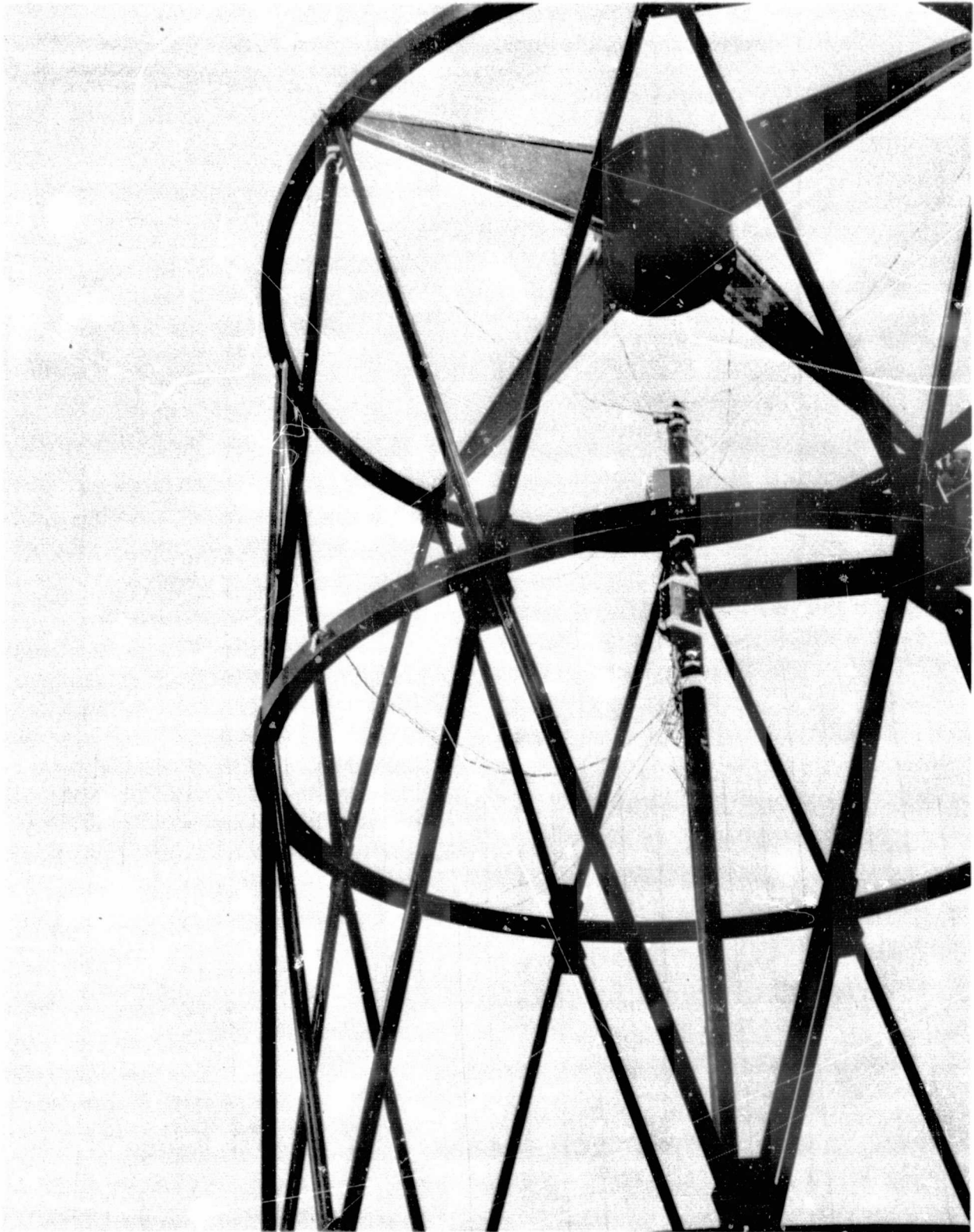


Figure 7-10. Modal Survey Test - Mass Plate and Instrumentation

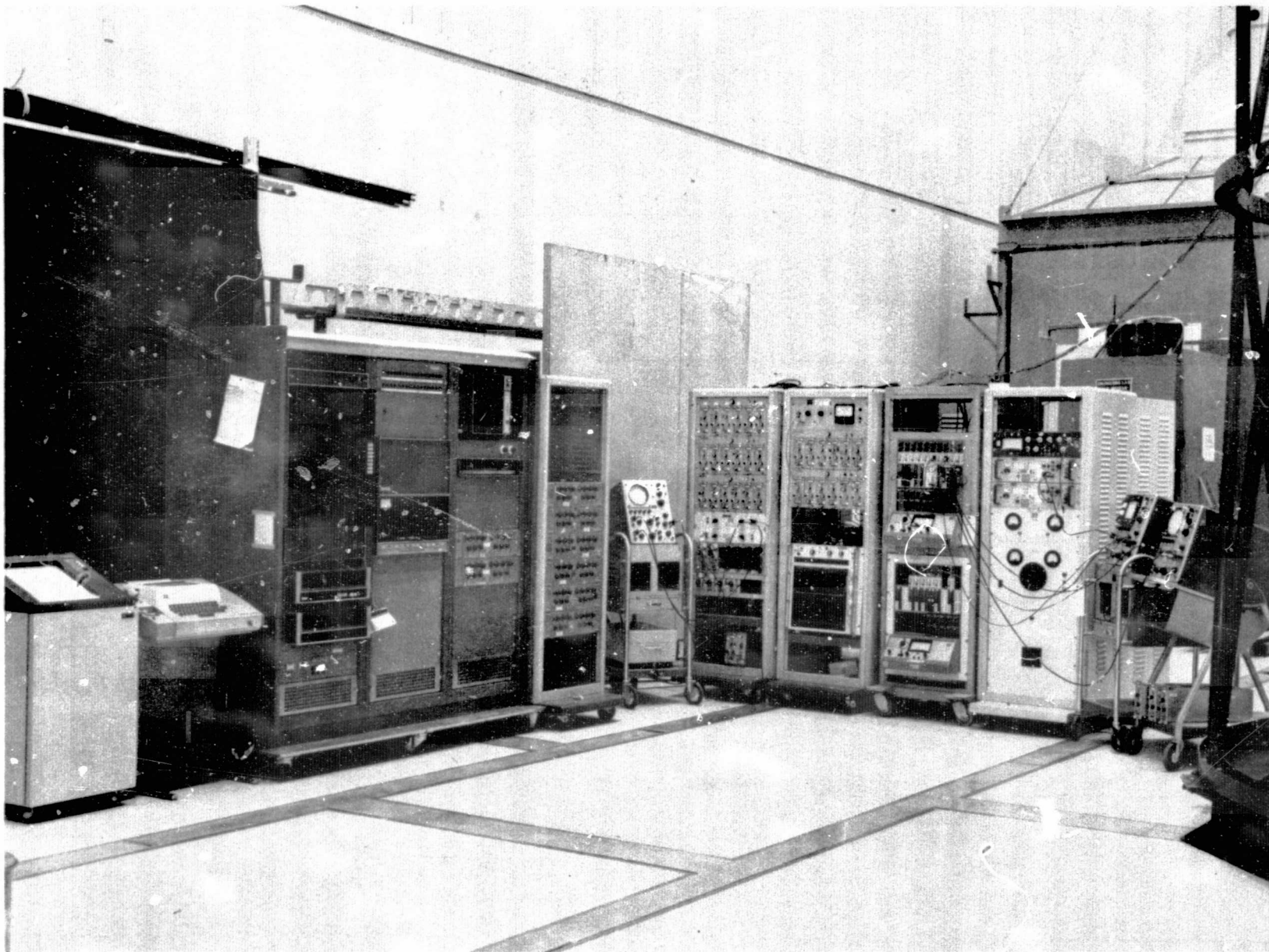


Figure 7-11. Modal Survey Test - Support Equipment

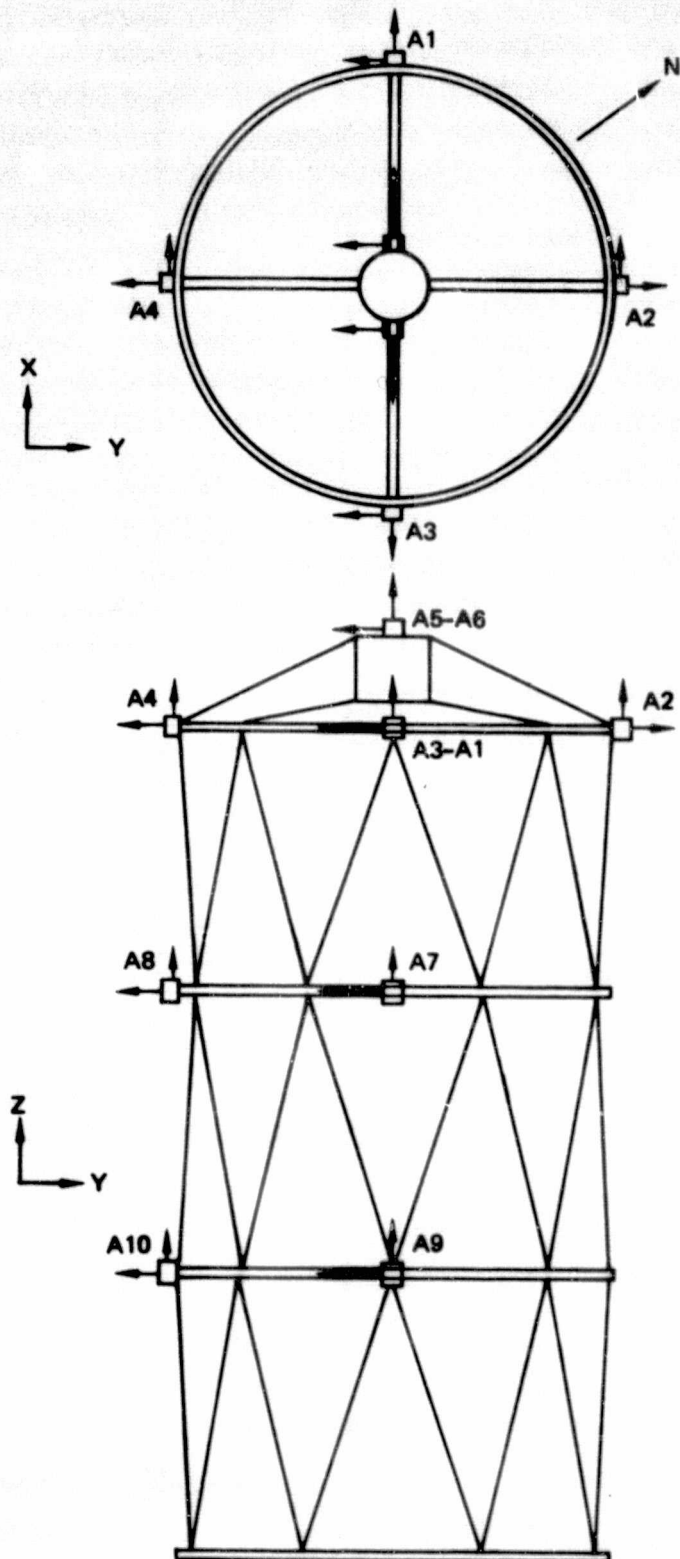


Figure 7-12. Modal Survey Test Accelerometer Location

Table 7-4. Modal Survey Test-Force Input-Frequency and Damping Data

	First bend	Ring	Second bend
Input force N (lbs)	1.38 (0.31)	3.17 (0.71)	3.16 (0.71)
Frequency (Hz)	16.194	28.13	39.62
Damping (Nyq)	0.0049	0.0094	0.0063
Force N (lbs)	3.02 (0.69)	4.45 (1.00)	4.45 (1.00)
Frequency (Hz)	16.175	28.13	39.58
Damping (Nyq)	0.0062	0.0099	0.0091
Force N (lbs)	4.45 (1.00)	0.64 (0.14)	0.64 (0.14)
Frequency (Hz)	16.176	28.13	39.62
Damping (Nyq)	0.0062	0.011	0.010

Table 7-5. Modal Survey Test — Free Vibration Decay Frequency and Damping Data

	First bend	Ring	Second bend
Input force N (lbs)	6.7 (1.5)	22.2 (5)	22.2 (5)
Frequency (decay) (Hz)	16.01	28.05	39.37
Damping	0.0076	0.0094	0.008
Input force N (lbs)	2.2 (0.5)	▷	13.3 (3)
Frequency (decay) (Hz)	16.18		39.34
Damping	0.0086		0.0086
Input force N (lbs)	4.45 (1.0)	▷	31.1 (7)
Frequency (decay) (Hz)	16.21		39.29
Damping	0.0077		0.0098

Frequency and damping by free vibration decay method.

▷ Unable to determine.

7.3 THERMAL-VACUUM TEST

The truss was tested under thermal-vacuum conditions to establish its dimensional stability characteristics. The truss was placed in a 50,000 ft³ vacuum chamber in an inverted position (Figure 7-13). A laser interferometer was mounted on the secondary mirror support cylinder to measure dimensional changes due to thermal perturbations. Truss temperature distributions were established which simulated a service condition. These temperatures were changed and the resulting dimensional changes measured. This sequence was repeated for a second service condition. In both cases the truss deflections remained within the design dimensional stability budget.

Test Set-Up

The truss was lowered into the 50,000 cubic foot vacuum chamber with the overhead crane as shown in Figure 7-14. This chamber, which is completely LN₂ shrouded is 39 ft in diameter and 49 ft high. It is mounted on a million pound seismic mass to provide a dynamic isolator (Figure 7-15). The LN₂ shrouds operate at a temperature of -314°F and are painted with a flat black paint. The chamber was rough pumped with a mechanical roughing and chain blowing system. After the initial pump down, pumping was accomplished with the LN₂ shrouds, ion-pumps, and cryodynes to provide a clean low vibration environment during the critical portions of the test.

The truss was supported in an inverted position using the same base ring used in the static and dynamic tests. The base ring was supported on the chamber hardpoints (Figure 7-16). The truss was blocked up using three short columns to provide room for the spider assembly beams. The top of the columns

incorporated nylon block supports to interface the truss ring (Figure 7-17). This arrangement permitted free independent movement of the truss ring and no resistance to differential thermal growth between the truss and the support.

The truss assembly was instrumented with resistance heaters and thermocouples and then covered with one layer of Mylar aluminized on both sides. In previous work during the development of the heater designs it was determined that this single layer of aluminized mylar was needed to reduce the emittance of the structure and minimize temperature gradients. Previous tests also showed that the bulky steel fixturing may cause "hot spots" in the chamber during test. To minimize radiation from these areas the fixturing was also covered with multi-layer insulation as shown in Figure 7-18. Figure 7-19 shows another view of truss in the vacuum chamber with the aluminized mylar covering just prior to test.

Previous tests had also determined that the desired cold temperature could not be attained in the secondary mirror support cylinder. This was caused by the heat pump effect of the interferometer box which was held at 74°F and was coupled thru its supports to the cylinder. A LN_2 cold finger was therefore inserted in the center of the cylinder to drive its temperature down. This proved not very effective as shown by temperature data obtained during test.

Deflection measurements were made during thermal distortion tests with a seven-channel laser interferometer. The interferometer was used to measure decenter, despace and tilt displacements of the primary mirror end ring relative to the secondary mirror support structure.

The seven channel laser interferometer consisting of seven modified Twyman-Green interferometers in parallel, where the optical length of the reference arm was modulated with a piezoelectric element. A 1 cm corner reflector was mounted at each point displacement was measured. The reflectors returned the beam to the detector array (Figure 7-20).

The signal and reference laser beams were demodulated by the square law detectors to produce electrical harmonics of the modulating frequency. The fundamental and second harmonic components were used to determine the direction of movement.

The output of the direction sensing logic changes state every 90 degrees of optical phase, so there are four counts per fringe. Since the optical path was folded, the resolution element was $\lambda/8$, or approximately 3.1 millionths of an inch.

The laser interferometer was mounted in a hermetically sealed box which was mounted on the secondary mirror support structure. The box was mounted thru four flexible stand-offs which eliminated the transmittal of bending moments to the sensitive interferometer base. Three of these flexible mounts continued up from the base plate of the box to provide support for the interferometer. This minimized transmittal of bending resulting from pressure distortion of the hermetic box.

The temperature of the box was carefully controlled throughout the test. It was wrapped with multilayer insulation. Dry gaseous nitrogen introduced at

1 atmosphere pressure and heated to a controlled temperature was circulated and then vented outside. Four thermocouples were monitored in the box. They were located at the box base plate, interferometer plate, cover of the box and GN_2 input tube. During test the four temperatures were highly stable and the interferometer base plate temperature remained within $\pm 1/2^\circ\text{F}$ when perturbing the truss temperatures.

Instrumentation

Low watt density strip heaters were bonded to all elements of the metering truss with double backed Kapton tape. One hundred and sixty-eight chromel constantan thermocouples were installed on the truss for thermal zone control and temperature distribution read-out. Eight copper constantan were installed on interferometer assembly for its temperature control. Deflection measurements were made with a laser interferometer mounted in a temperature controlled box, purged with nitrogen gas and maintained at atmospheric pressure. Three retroreflectors were installed on the base ring of the truss and were used as reference points for the deflection readouts.

Low watt density strip heaters were bonded to the assembled metering truss with double backed Kapton tape. Chromel constantan thermocouples were attached for temperature control and measurement. All elements of the truss were then wrapped with one layer of aluminized mylar. The truss was layed down on its side to provide easy accessability for the heater and T/C installation as shown in Figure 7-21. Typical installed heaters for both the struts and rings are shown in Figure 7-22.

The axial gradient test conditions were achieved by dividing the 3 sets of tubular members into 3 control zones, each ring into 1 control zone, and the secondary mirror support structure into 2 zones. This results in a total of 9 control zones. All zones covered 360° of the truss circumference. The circumferential gradient test conditions was achieved in much the same way. In this case, however, the individual zones covered only 180° of the truss circumference.

The heater zones for the axial and circumferential temperature gradients are shown in Figure 7-23 and 7-24. Switching of the heater zone control from the axial gradient mode to the circumferential gradient mode was accomplished exterior to the chamber, eliminating the requirement for vacuum break between test conditions.

Each heater zone contained a control thermocouple mounted on a heater, one adjacent to a heater and numerous T/C's to obtain temperature distribution. Temperature control was achieved by dissipating electrical power to the strip heaters. Power dissipation was regulated by computer control of the power supply for each temperature control zone.

Deflection measurements were made during the thermal distortion tests with a 7 beam laser interferometer. The interferometer measured the movement of three corner reflectors mounted on the truss base ring. The reflectors were mounted at 120° spacing around the ring in stainless steel containers. These containers were mounted with a single screw located at the reflector reference surface.

The pointing mirrors of the interferometer were aimed at the corner reflectors just prior to the installation of the truss in the chamber (Figure 7-25). This was repeated in the chamber and also after the cover of the hermetic box was temporarily positioned. Distortion of the beam paths due to the optical windows in the cover proved insignificant.

Test Procedure

The vacuum chamber was sealed and pumped to a pressure of less than 1 torr. A nitrogen purge of the interferometer box was established and temperature control initiated. Recorded interferometer temperature and displacement data and repeated every hour.

Maintained pressure below 10 torr for more than 9 hours.

Reduced chamber pressure to less than 1×10^{-5} torr and started cooling walls to -290°F .

As each truss zone reached its target temperature, heaters were energized to maintain target temperature.

The above process was continued until Condition 1 was achieved. Condition 1 temperatures are shown in Table 7-6 and Figure 7-26. After all temperature zones had attained target temperatures the interferometer data were recorded at half hour intervals until they indicated stability had been reached.

Nominally this took another 2 hours. Condition 1 stability was established 23 hours and 35 minutes after the test started.

Rezeroed the interferometer and raised all target temperatures 10°F. Interferometer readings were taken at hour intervals. Temperature data and interferometer data showed stabilized Condition 1A was reached 3 hours after the start of the perturbation.

The target temperatures were reduced 10°F to the Condition 1 temperature distribution. A stable Condition 1 was achieved 5 hours later.

Target temperatures were increased 10°F and the interferometer was rezeroed. A stabilized Condition 1A was achieved 4 1/2 hours after start of perturbation as indicated by both temperature and interferometer data.

Adjusted the target temperatures of each zone to Condition 2 temperature as shown in Table 7-6 and Figure 7-26. A stabilized Condition 2 was established 10 1/2 hours after its target temperatures were inserted in the controlling SDS 910 computer.

The Condition 2A temperature, which raised one half of the truss temperature 10°F as shown in Table 7-6 and Figure 7-24, were programmed into the computer. The interferometer was rezeroed. A stable Condition 2A was reached 3 1/2 hours later.

After the first radial temperature perturbation was complete, the target temperature were changed to the Condition 2 distribution. A stabilized condition was achieved in 4 1/2 hours. The Condition 2 to 2A perturbation was repeated. The interferometer was zeroed after the new target temperatures were programmed. It took 3 1/2 hours to achieve a stable Condition 2A.

Test Data

Truss temperature data was recorded on magnetic tape by the controlling SDS 910 computer every 5 min. All data were also listed on a line printer at the same time. Sixty selected channels were also displayed on remote TV screens which were updated every 10 seconds.

Typical temperature distributions and resulting temperature perturbations are shown in Figures 7-27 and -28. Figure 7-27 shows the truss thermocouple locations. Condition 1A temperatures achieved during the first perturbation, and the resulting changes in temperatures achieved during this perturbation. As shown, the 10°F axial perturbation was achieved a relatively uniform manner. The average temperature change throughout the truss was 9.90°F. Figure 7-28 shows the thermocouple locations, Condition 2A temperatures achieved during the first radial perturbation and temperature changes achieved during this perturbation. The target temperatures in the support cylinder were changed plus 5°F and actual temperature changes averaged this amount. The average temperature change on the half that was perturbed was 9.29°F.

In addition to obtaining truss temperatures, 8 thermocouples were used to obtain the interferometer box and its stand off support temperatures. Since the interferometer measurements were very sensitive to these temperature changes, more accurate copper constantan thermocouples were used. In addition, they used their own ice water reference and were read with a voltmeter.

Deflection measurements were made with a 7 beam laser interferometer during the thermal distortion tests. Deflections were based on the movement of

retroreflectors mounted on the truss base ring. Two of the retroreflectors were tracked by 3 beams each and a third reflector by one beam. The despace, decenter and tilt of the truss were based on the movement of the two reflectors that were tracked by three beams. Interferometer data were recorded by a line printer. These data were recorded at half hour intervals during the critical portions of the test and was used to determine when stabilized temperatures were achieved as well as to establish truss deflections. Ten sets of data were obtained during each recording. Scatter was small and within anticipated sine wave movements of the truss due to its vibration.

Data obtained from the digital readout of the laser interferometer were multiplied by 3.1×10^{-6} in. to establish dimensional movements. These data were then input into directional cosine equations to obtain the despace decenter and tilt of the retroreflectors.

The direction cosine equations were based on the truss geometry and location of the retroreflectors. The equations used are shown in Table 7-7. Their solution was performed on a programmable desk computer using matrix algebra.

A summary of the truss deflections is shown in Table 7-8. The measured data were converted to despace, decenter and tilt of the truss using direction cosine equations.

Test Results

Condition 1 and Condition 2 temperature distributions were attained in all areas except for the secondary mirror support. Due to the heat short through

the interferometer supports temperatures in this ring were higher than anticipated. More important, all temperature perturbations which were the source of the truss distortions were attained within $.55^{\circ}\text{C}$ (1°F).

A summary of the measured despace, decenter and tilt of the truss is shown in Table 7-8. The deflection of the truss was corrected for both the resistance heaters and change in temperature of the interferometer box supports for the critical despace condition. In all tests, two axial and two radial temperature perturbations the truss distortions were within the design budgets.

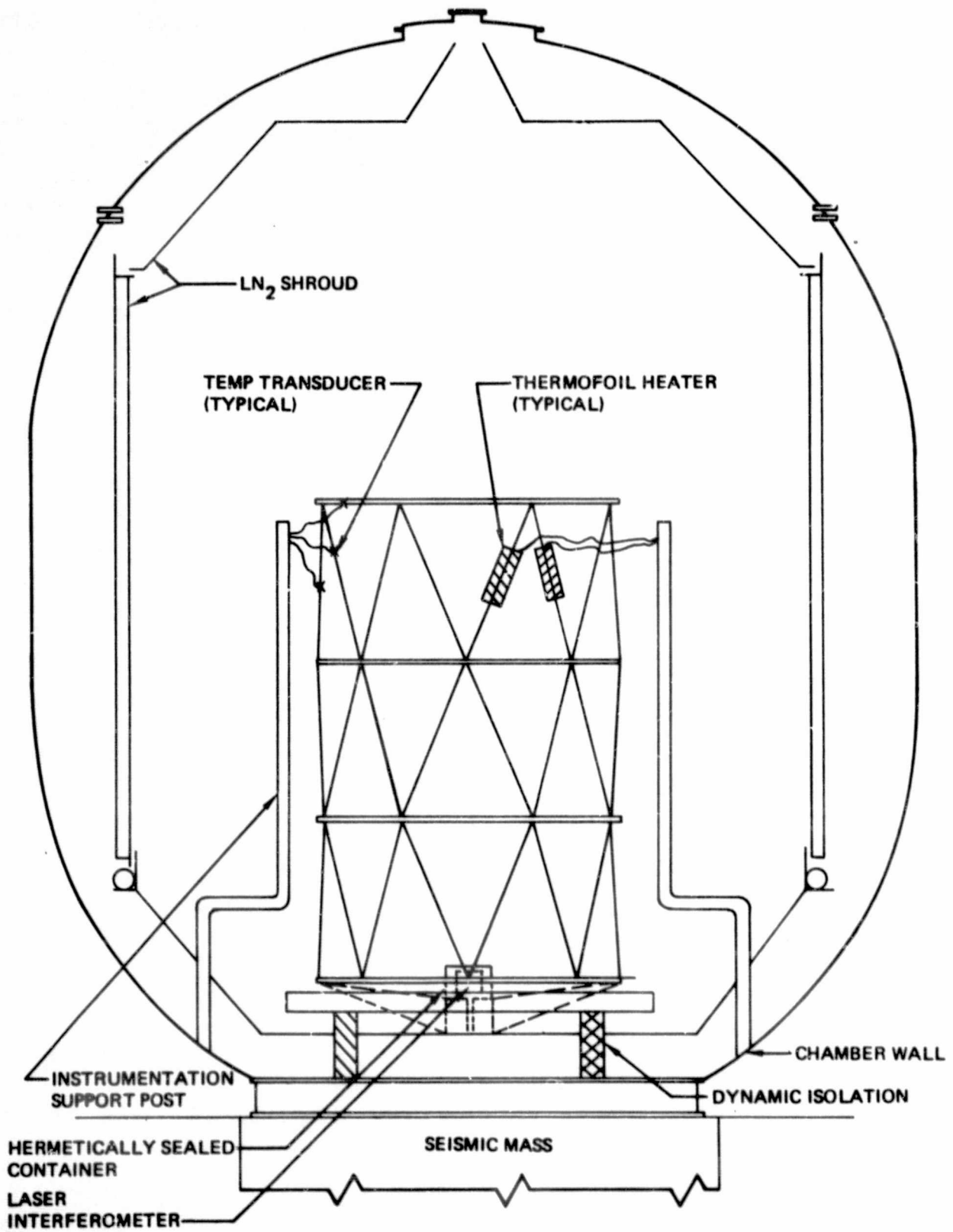


Figure 7-13. Thermal-Vacuum Test—Setup Schematic

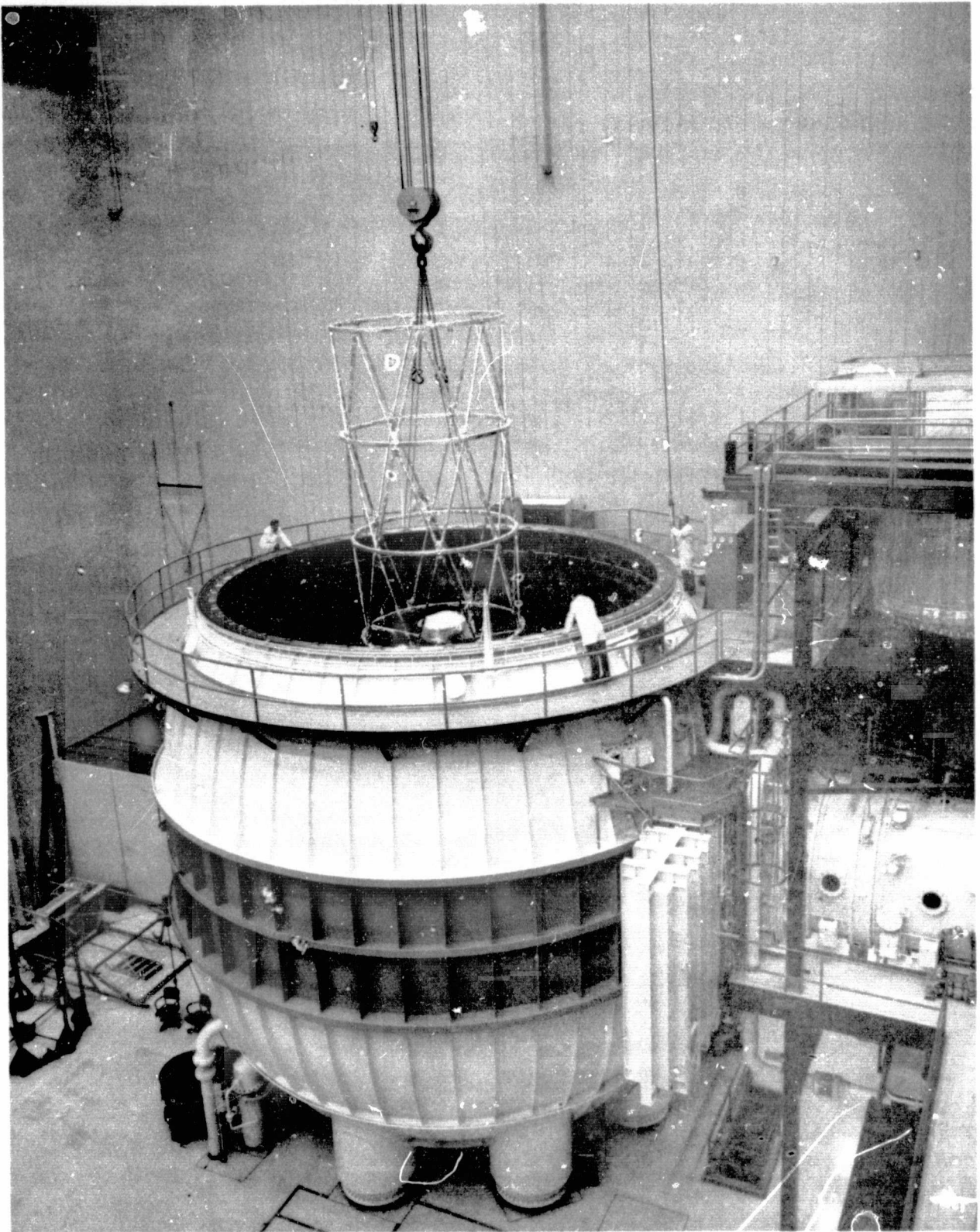


Figure 7-14. Thermal - Vacuum Test - Truss Installation in Vacuum Chamber

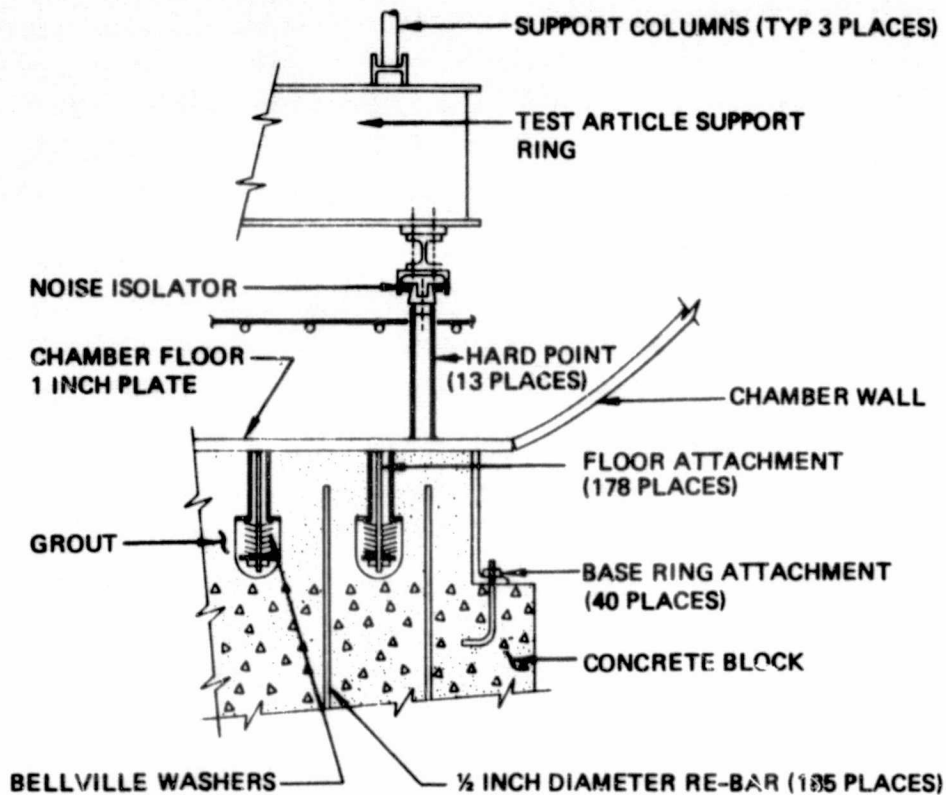


Figure 7-16. Thermal-Vacuum Test-Support Ring Installation

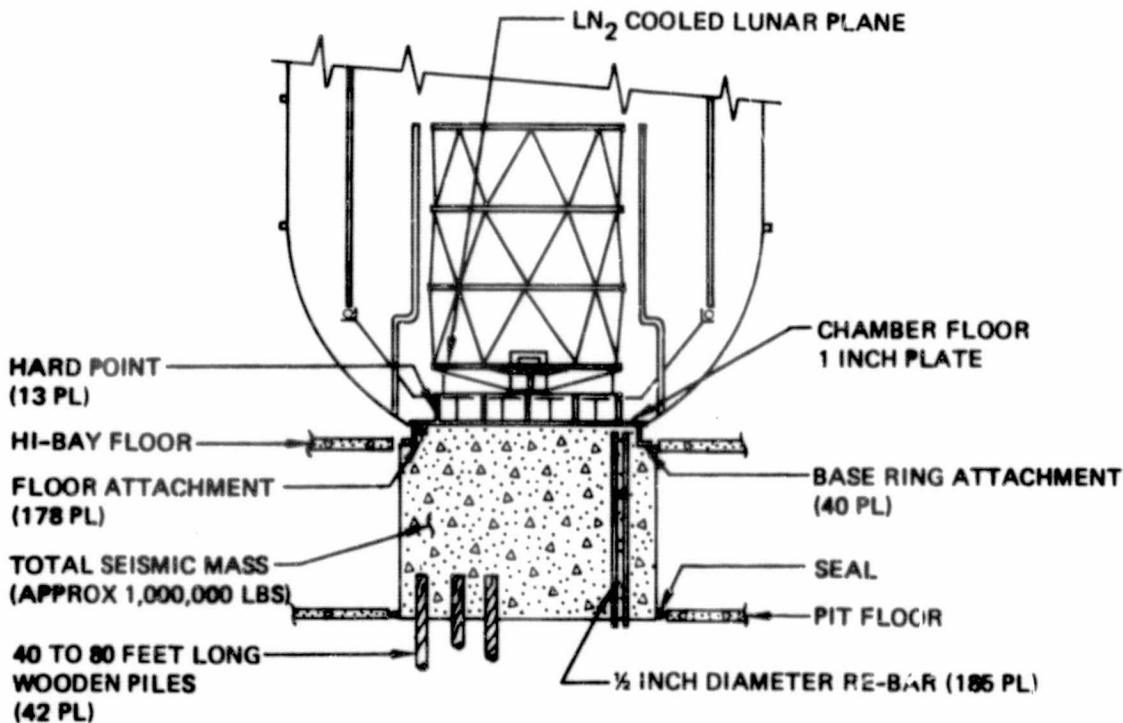


Figure 7-15. Space Chamber - Schematic

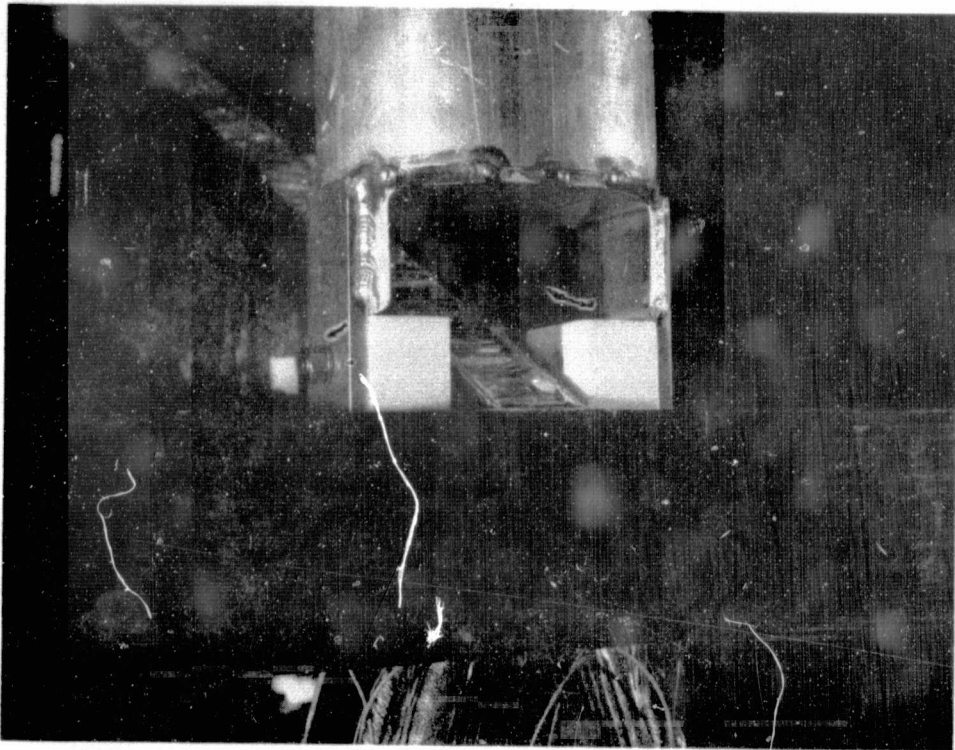


Figure 7-17. Thermal - Vacuum Test - Nylon Block Supports

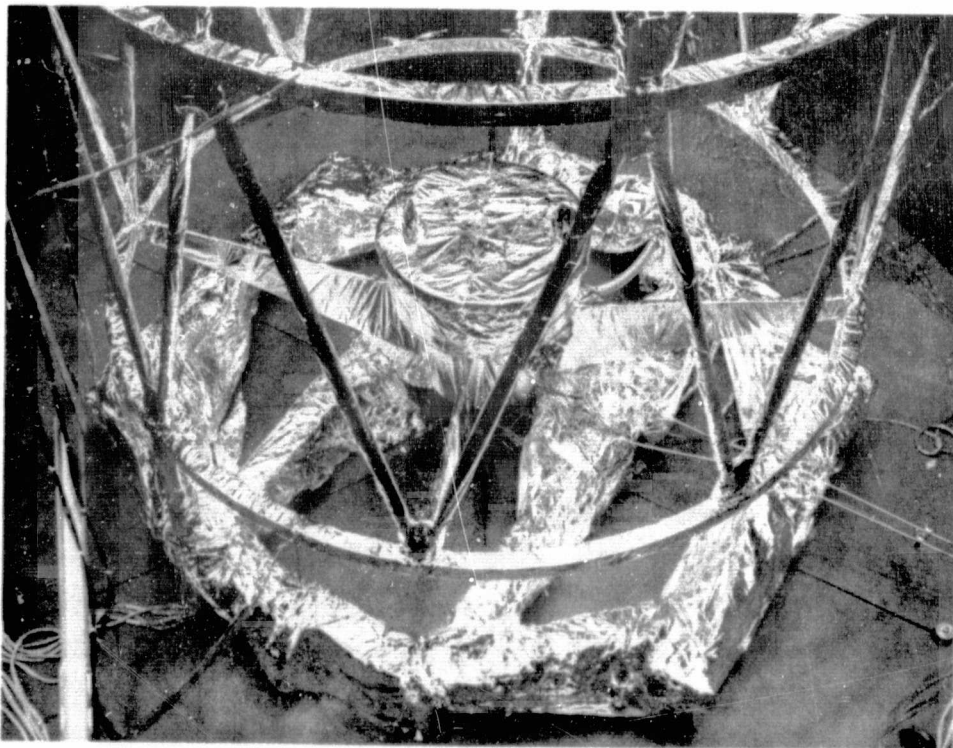


Figure 7-18. Truss and Fixturing Covered with Aluminized Mylar for Test

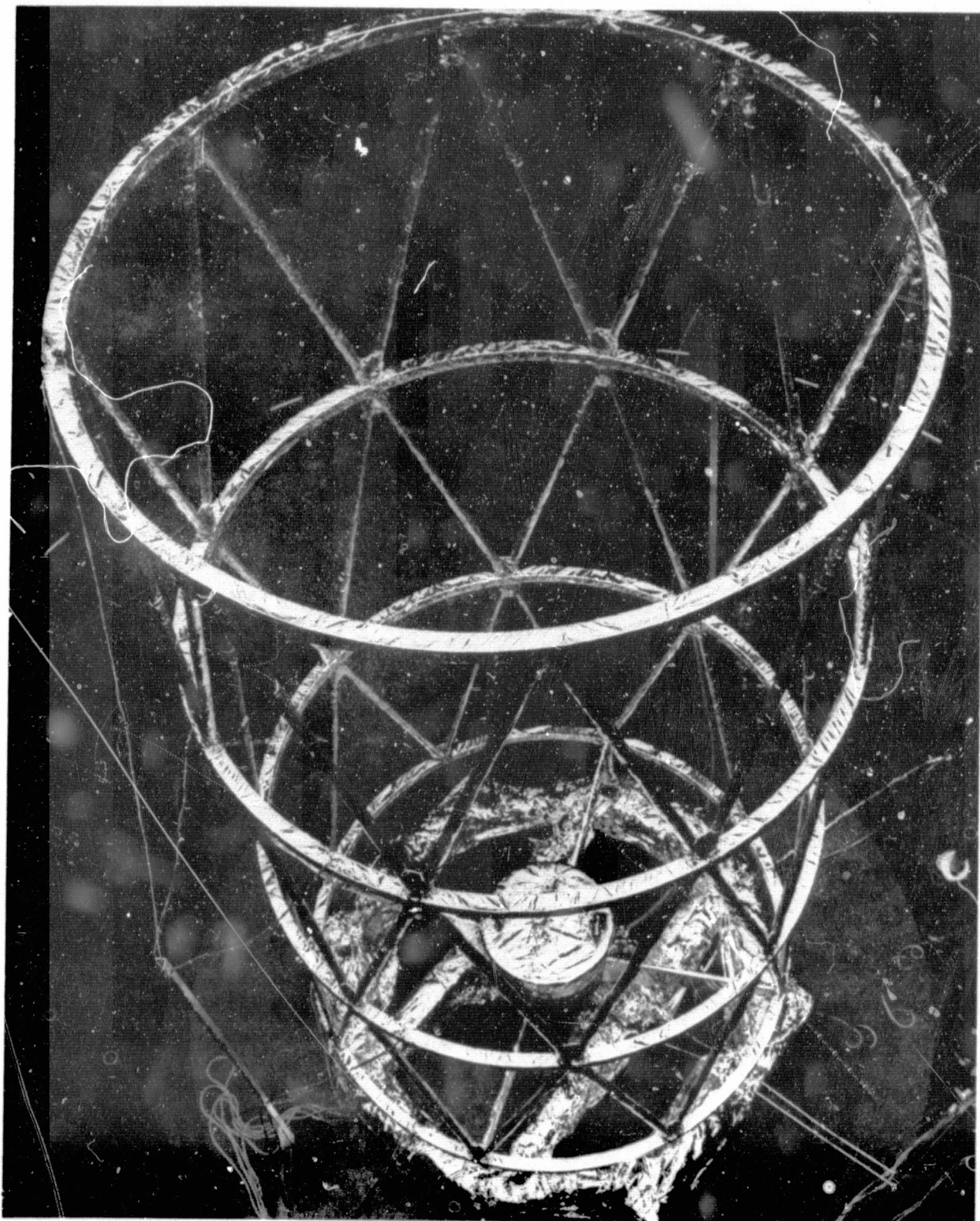


Figure 7-19. Truss in Space Chamber Prior to Test

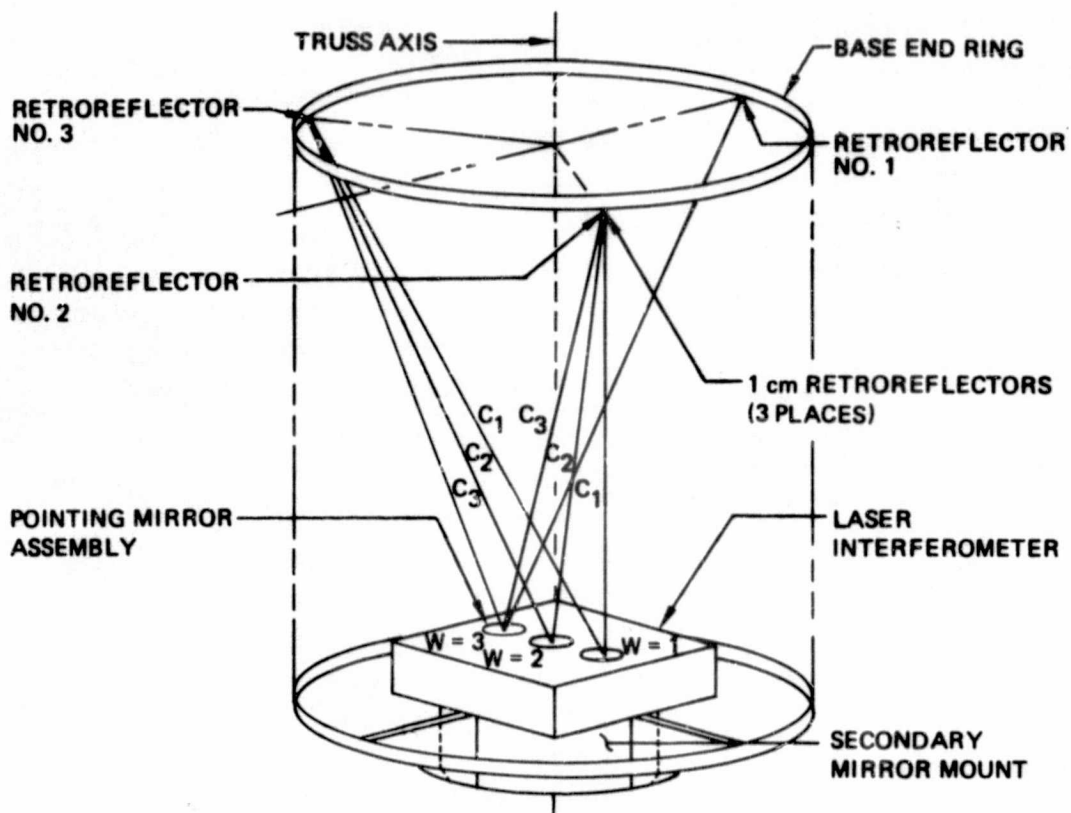


Figure 7-20. Distortion Measurement Geometry

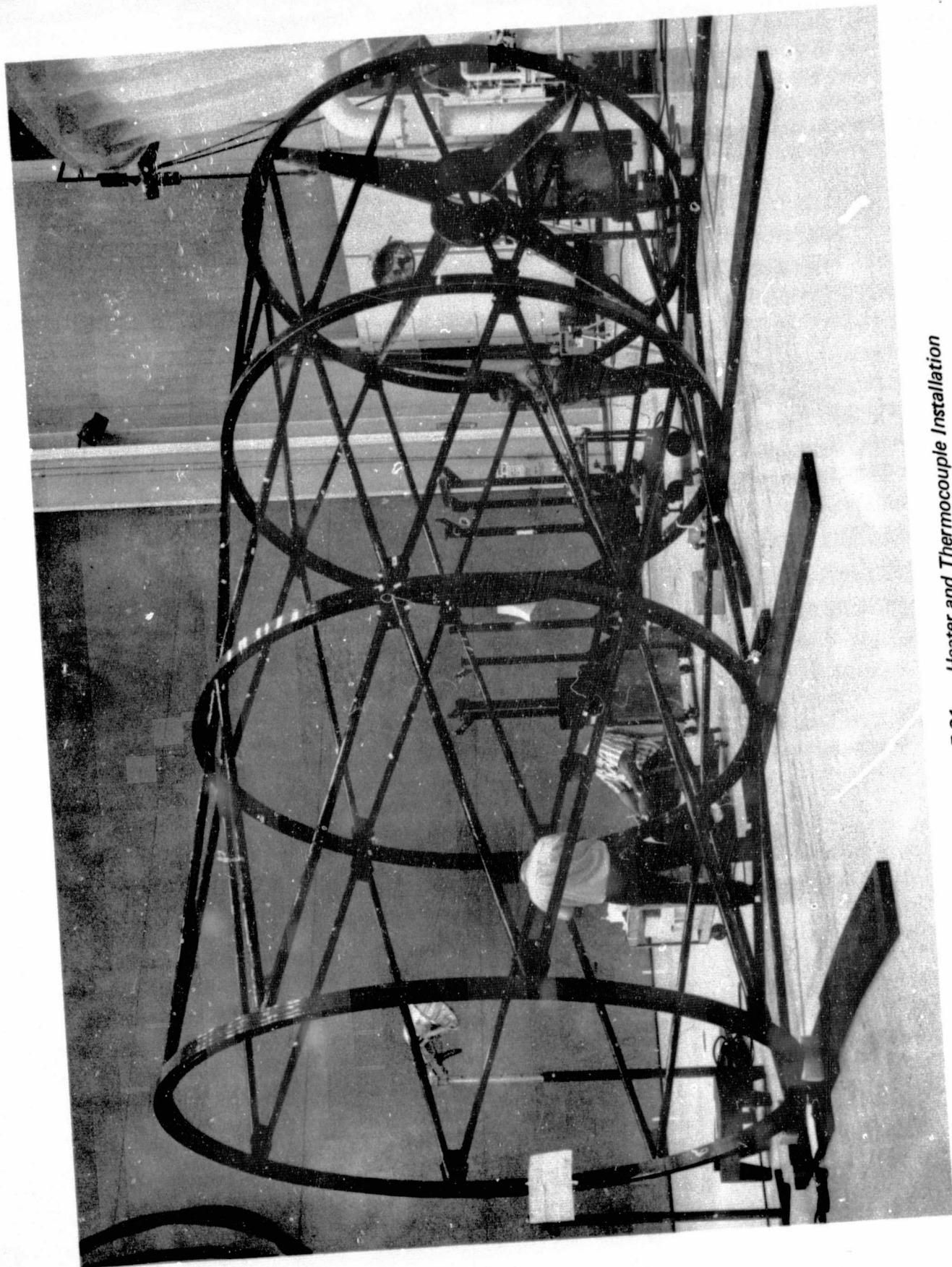


Figure 7-21. Heater and Thermocouple Installation

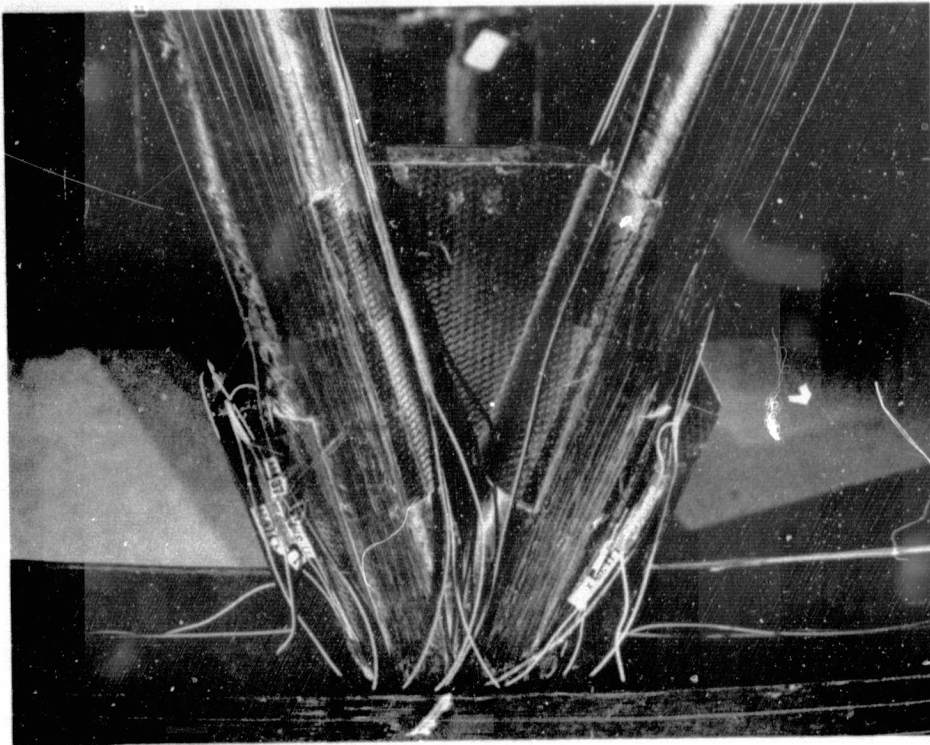


Figure 7-22. Typical Resistant Heater Installation

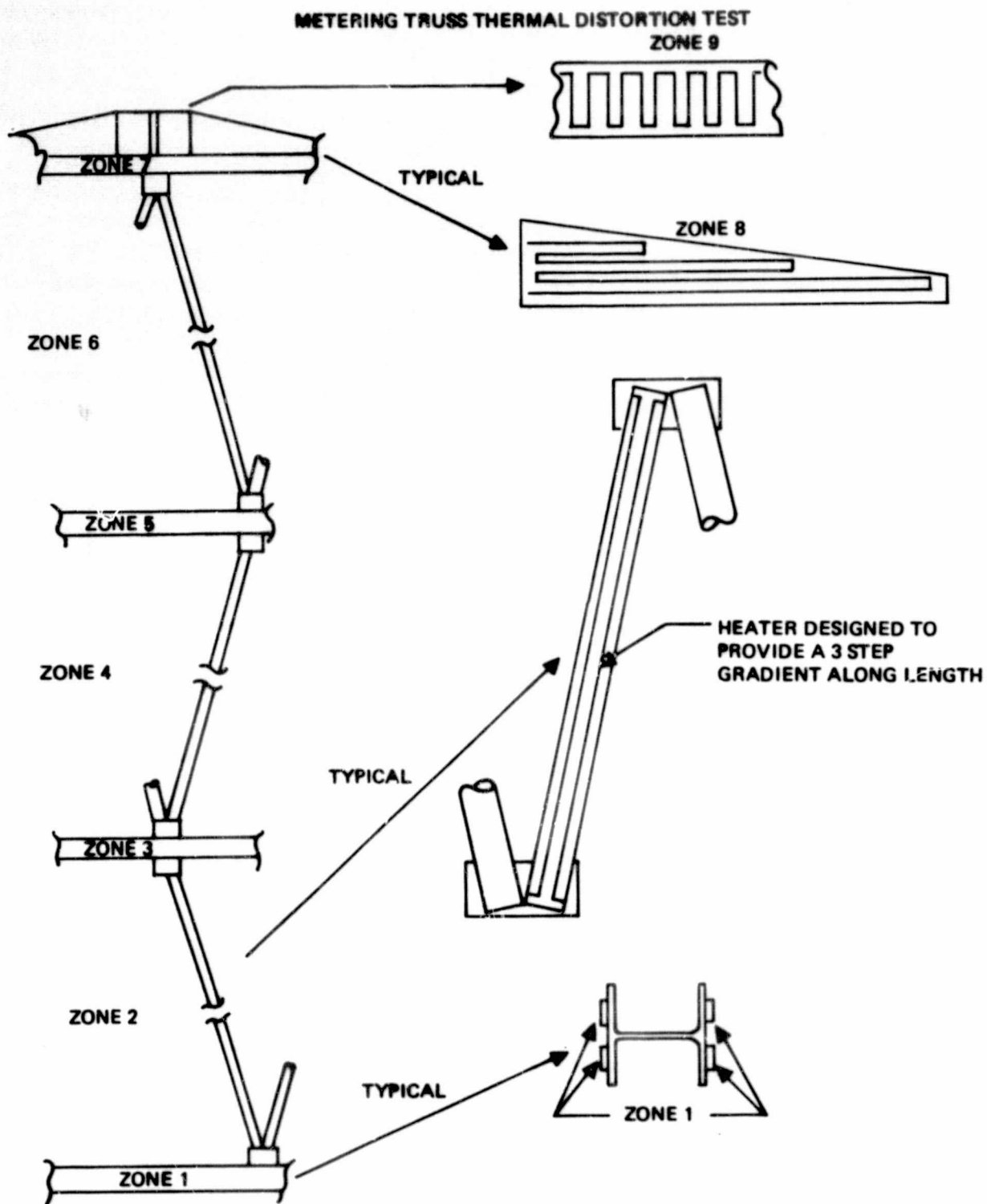


Figure 7-23. Axial Temperature Perturbation - Control Zones

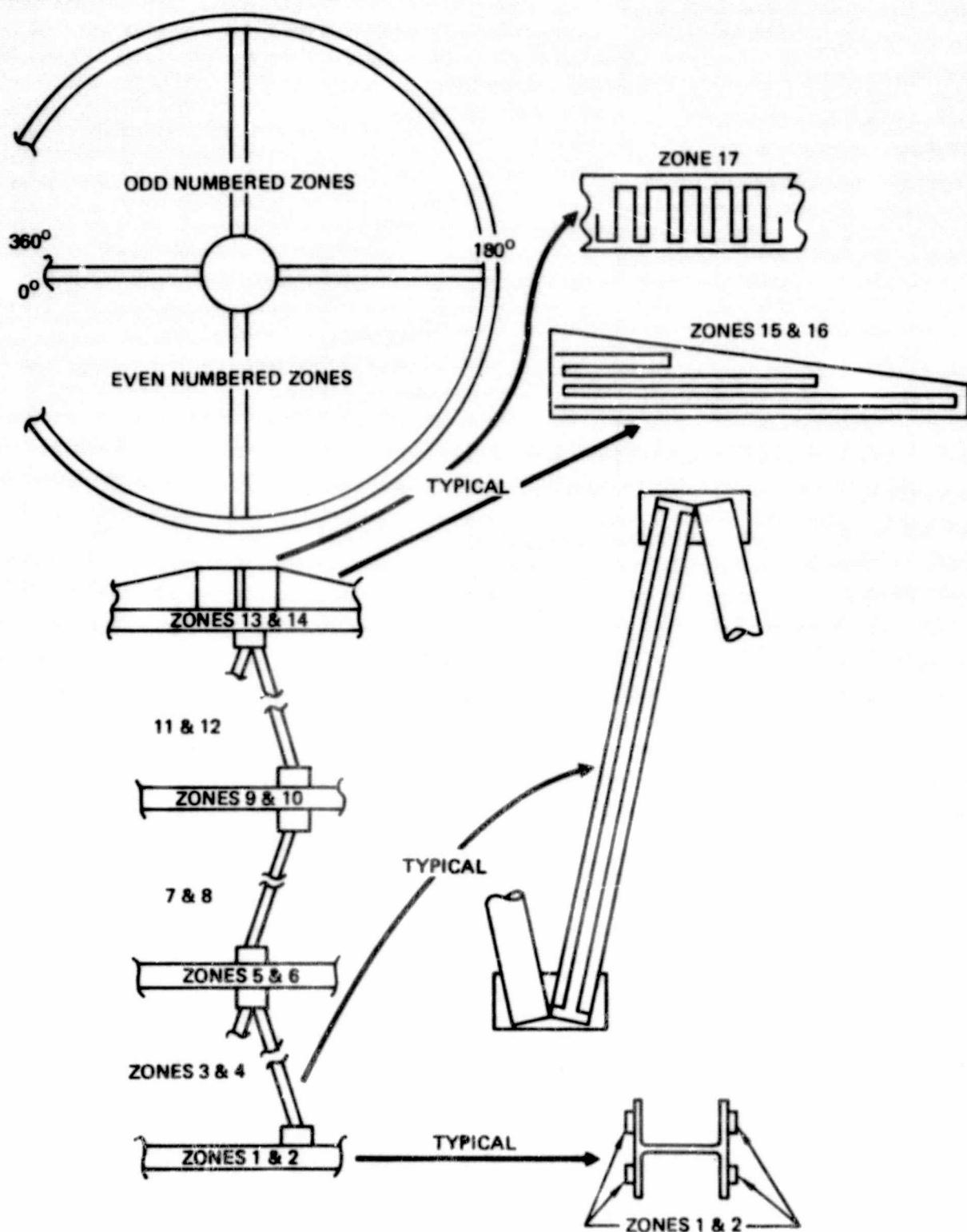


Figure 7-24. Radial Temperature Perturbation - Control Zones

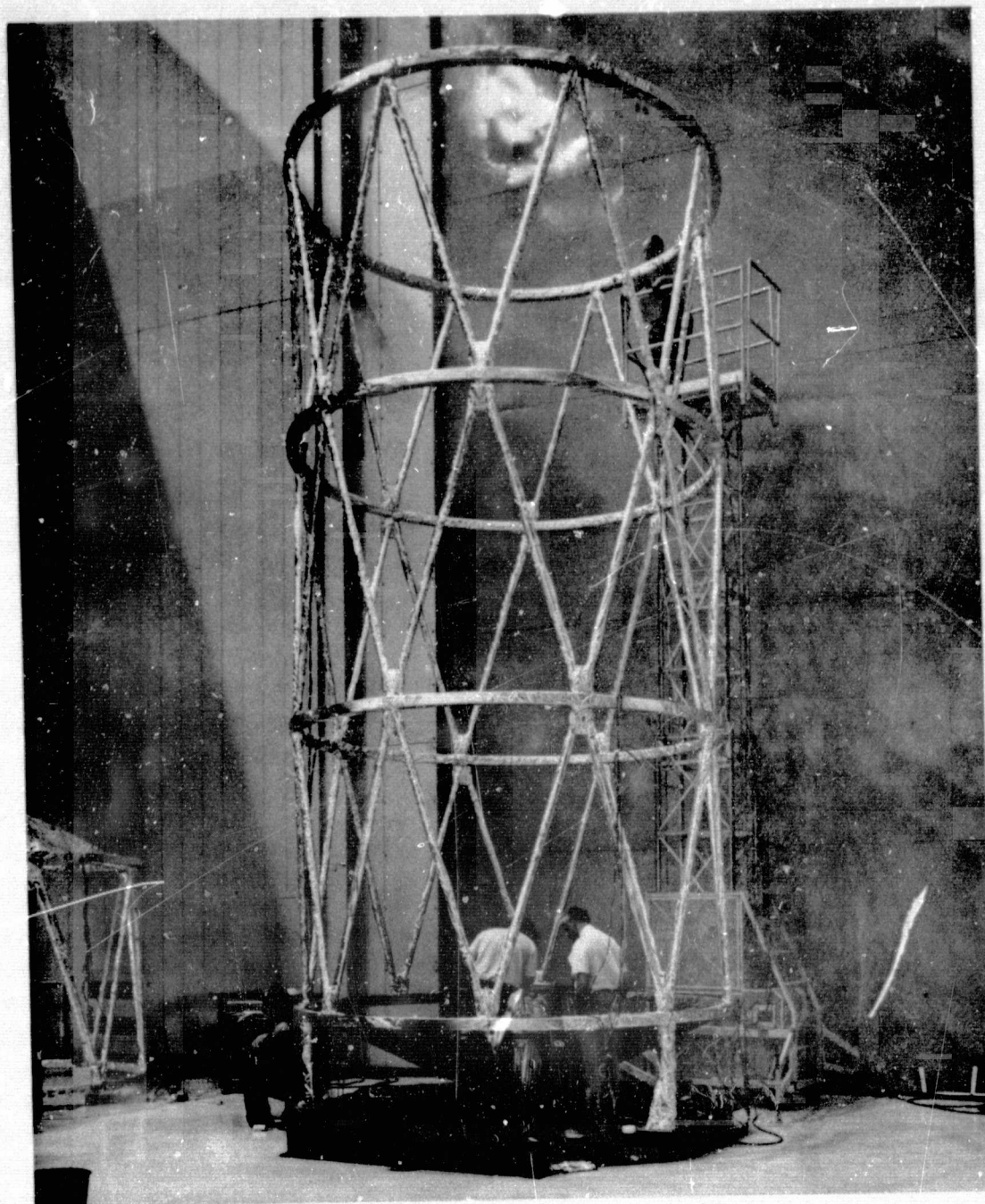
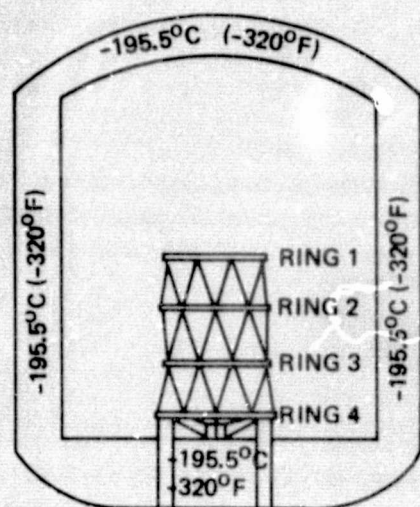


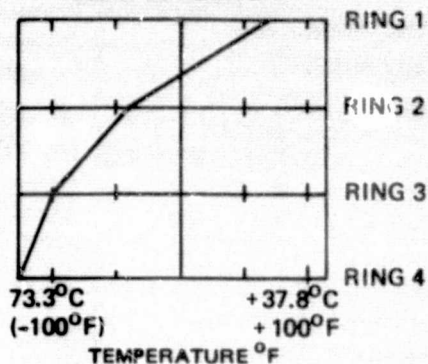
Figure 7-25. Adjustment of Interferometer Pointing Mirrors

Table 7-6. Thermal-Vacuum Test-Target Temperature

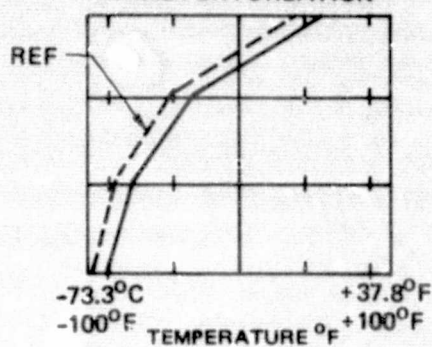
Temperature control zone and heater	Control t/c number	Target temperatures (°F)			
		Condition 1	Condition 1A	Condition 2	Condition 2A
1	149	70	80	80	90
2	150	70	80	80	80
3-1	151	8	16	—	—
3-2	151	—	—	42	52
4-1	152	8	16	—	—
4-2	152	—	—	42	42
5	153	- 40	- 30	0	10
6	154	- 40	- 30	0	0
7-1	155	- 68	- 58	—	—
7-2	155	—	—	- 20	- 10
8-1	156	- 68	- 58	—	—
8-2	156	—	—	- 20	- 20
9	157	- 100	- 90	- 40	- 30
10	158	- 100	- 90	- 40	- 40
11-1	159	- 110	- 100	—	—
11-2	159	—	—	- 40	- 30
12-1	160	- 110	- 100	—	—
12-2	160	—	—	- 40	- 40
13	161	- 120	- 110	- 40	- 30
14	162	- 120	- 110	- 40	—
15-1	163	- 80	- 70	- 40	- 30
15-2	167	- 80	- 70	- 40	- 30
16-3	164	- 80	- 70	- 40	- 30
16-4	168	- 80	- 70	- 40	- 30
17	165	- 90	- 50	- 40	- 35
18	166	- 80	- 50	- 40	- 35



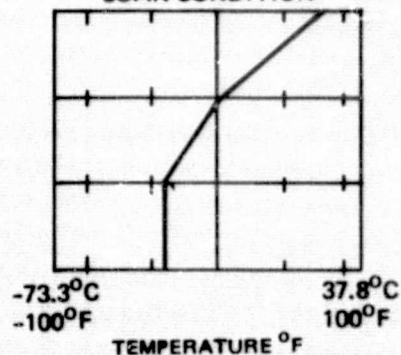
FIRST SELECTED SOAK CONDITION



AXIAL PERTURBATION



SECOND SELECTED SOAK CONDITION



CIRCUMFERENTIAL PERTURBATION

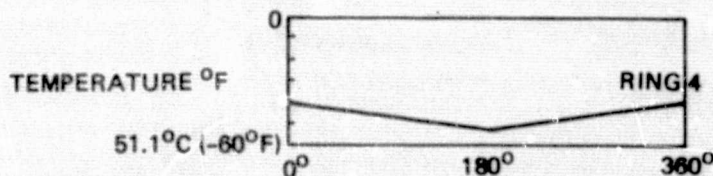
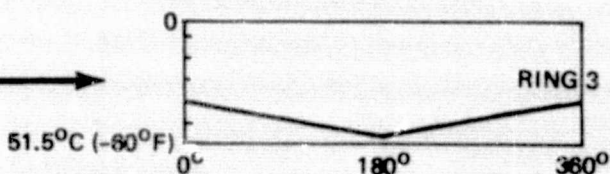
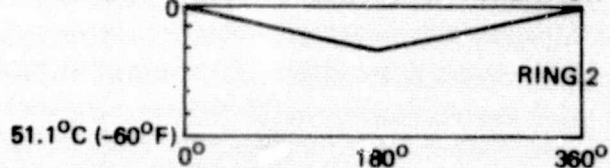


Figure 7-26. Test Temperature Distributions

- (X) THERMOCOUPLE LOCATIONS
 X TEMPERATURE CHANGE BETWEEN CONDITIONS 1 AND 1A ($^{\circ}$ F)

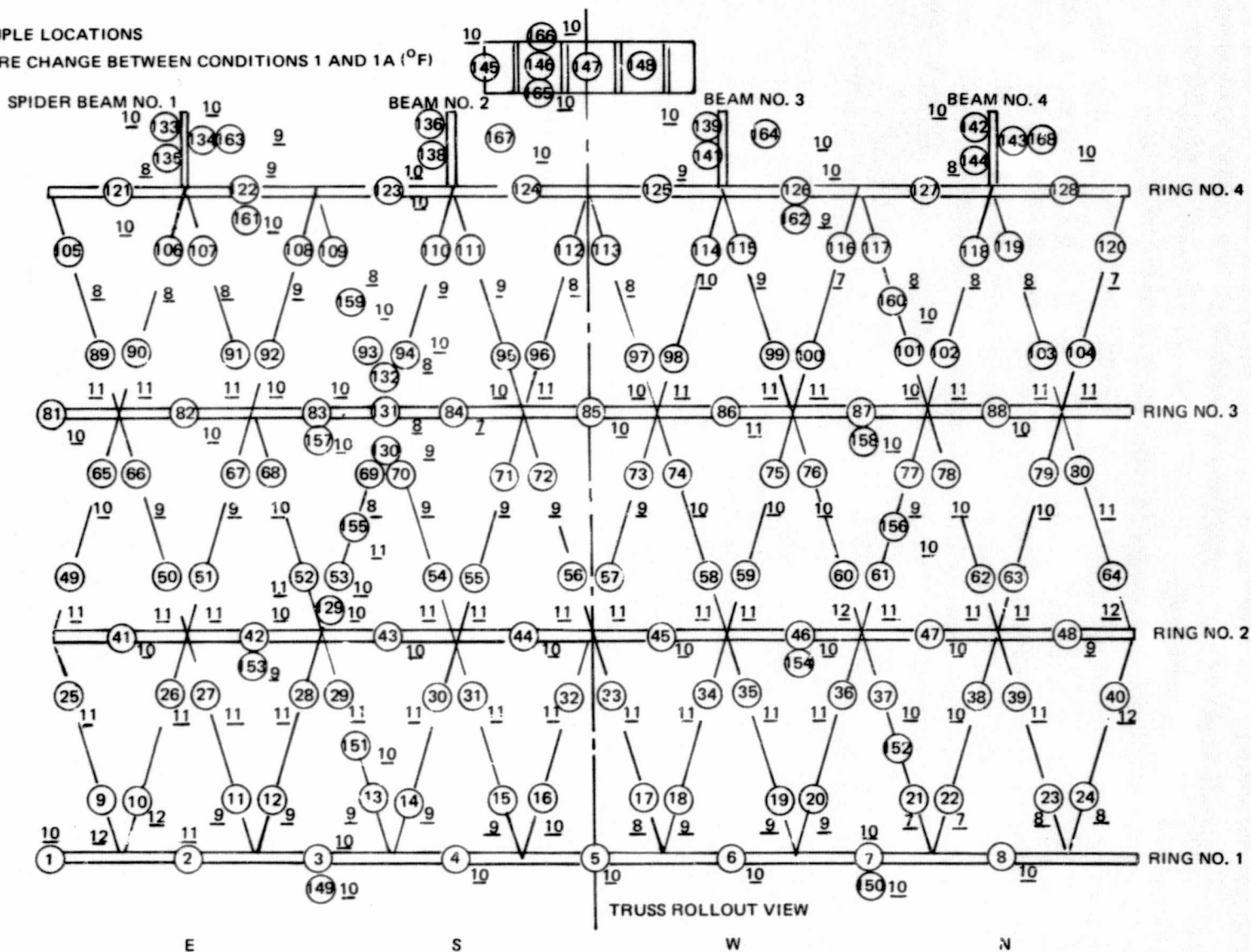


Figure 7-27. Typical Axial Temperature Perturbation

X TEMPERATURE CHANGE BETWEEN CONDITIONS 2 AND 2A (°F)

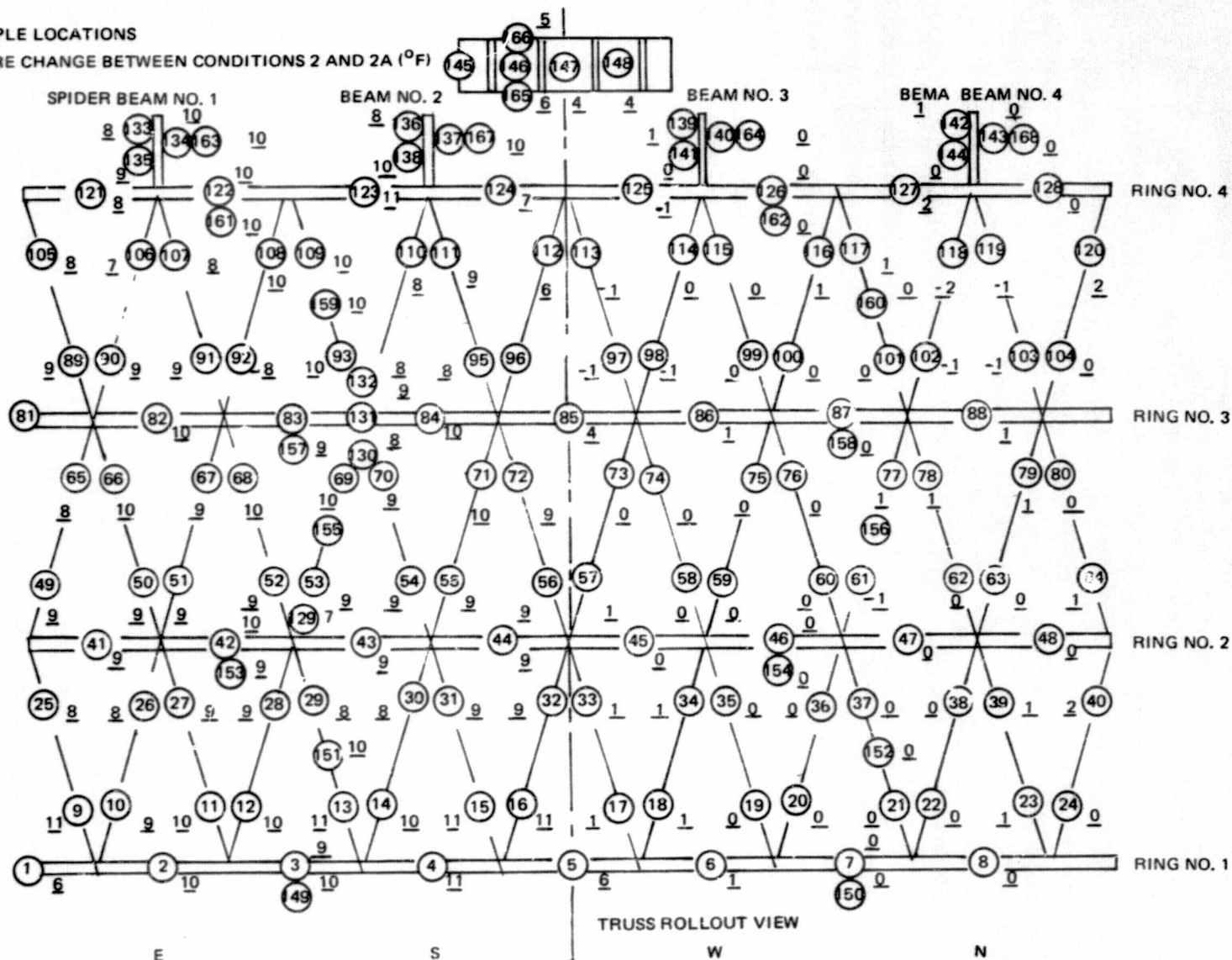


Figure 7-28. Typical Radial Temperature Perturbation

Table 7-7. Thermal-Vacuum Test-Data Reduction Equations

RETROREFLECTOR NO. 3

WINDOW NUMBER	①	$-0.183\ 795\ 802\ x + 0.202\ 073\ 174\ y + 0.985\ 576\ 218\ z = C_1$
	②	$-0.126\ 279\ 371\ x + 0.203\ 199\ 878\ y + 0.970\ 980\ 000\ z = C_2$
	③	$-0.145\ 685\ 719\ x + 0.184\ 188\ 466\ y + 0.972\ 038\ 401\ z = C_3$

RETROREFLECTOR NO. 2

WINDOW NUMBER	①	$-0.162\ 989\ 436\ x + 0.223\ 909\ 351\ y + 0.980\ 882\ 816\ z = C_1$
	②	$-0.125\ 658\ 758\ x + 0.225\ 145\ 600\ y + 0.986\ 188\ 045\ z = C_2$
	③	$-0.143\ 785\ 773\ x + 0.242\ 566\ 326\ y + 0.959\ 425\ 782\ z = C_3$

C_x Δ DISTANCE BETWEEN WINDOW AND REFLECTOR

x, y, z MOVEMENT OF RETROREFLECTOR FROM ORIGINAL POSITION.

Note: See Figure 7-18

REPRODUCIBILITY OF THE
ORIGINAL PAGE IS POOR

Table 7-8. Thermal-Vacuum Test-Truss Deflection Summary

	10°F Axial perturbation		10°F Radial perturbation	
	1st	2nd	1st	2nd
Despace (inches)				
Test	0.330×10^{-4}	0.901×10^{-4}	-0.454×10^{-4}	-0.778×10^{-4}
Heater correction	1.048×10^{-4}	1.048×10^{-4}	0.524×10^{-4}	0.524×10^{-4}
Support correction	-0.156×10^{-4}	-0.331×10^{-4}	-0.331×10^{-4}	-0.195×10^{-4}
Total	1.222×10^{-4}	1.618×10^{-4}	-0.261×10^{-4}	-0.449×10^{-4}
Budget	$\pm 2.67 \times 10^{-4}$	$\pm 2.67 \times 10^{-4}$	$\pm 2.67 \times 10^{-4}$	$\pm 2.67 \times 10^{-4}$
Decenter (inches)				
Test	0.303×10^{-3}	0.320×10^{-3}	1.0×10^{-3}	0.32×10^{-3}
Budget	1.33×10^{-3}	1.33×10^{-3}	1.33×10^{-3}	1.33×10^{-3}
Tilt (degrees)				
Test	3.43×10^{-10}	1.058×10^{-4}	3.753×10^{-4}	3.269×10^{-4}
Budget	9.36×10^{-4}	9.36×10^{-4}	9.36×10^{-4}	9.36×10^{-4}

Budget adjusted for $\Delta T = 10^\circ F$

$$\text{Despace} = 80 \mu \text{ in.} \left(\frac{10}{3} \right) = 2.67 \times 10^{-4}$$

$$\text{Decenter} = 400 \mu \text{ in.} \left(\frac{10}{3} \right) = 1.33 \times 10^{-3}$$

7.4 TEST - ANALYSES CORRELATION

Static Test

The lateral, torsional and axial stiffnesses of the truss were determined both analytically and experimentally. The analytical determinations were based on a NASTRAN model as described in Section 4.0. The lateral and torsional stiffnesses were based on deflections obtained when loading the truss at its upper ring in the same manner as loads were introduced in the static test. The axial stiffness was based on deflection obtained when loads were applied at the secondary mirror support cylinder.

A summary of the truss analytical and test deflections are shown in Table 7-9. The predicted analytical lateral and torsional deflections agreed reasonably well with the test data. The axial deflections were highly sensitive to the motion of the spider assembly. This in turn was very sensitive to the joint fixities at the ends of the spider beams. Analysis were performed in which both ends of the beams were pinned and results showed an unrealistic amount of spider assembly movement. Computer runs were made in which the large ends of the beams were fixed and the smaller ends were pinned and fixed. This change in fixity did not change the axial deflection of the truss significantly. Several NASTRAN runs were made to establish the effect of the inner spider joint stiffness on the axial deflection of the truss. In these analysis the smaller ends of the beams were fixed to the upper truss ring. Figure 7-29 summarizes this data. By using the measured axial test deflection this data shows a joint stiffness of 0.6%. This stiffness was used in the dynamic test analysis.

Dynamic Test

A dynamic analysis was made of the truss. The NASTRAN model used assumed the same joint fixity between the spider beams and cylinder as determined in the static axial load test (Figure 7-29). All of the other truss joints were fixed. A comparison of the analytical results and data obtained from the dynamic test is shown in Table 7-10. As shown, the theoretical results compared very well with the test data. The critical first mode bonding frequencies were within 2% of the actual values.

Thermal-Vacuum Test

A NASTRAN analysis was made of the truss to determine the deflections caused by temperature change. This analysis used the CTE's of the truss details established in the element tests and the fixity of the joint between the spider beams and secondary mirror support cylinder that provided a best-fit to the static axial load test data. The NASTRAN results were compared to the critical thermal-vacuum test results as shown in Table 7-11. In these comparisons the thru-the-thickness growths at the joints were not included. Growth at the joints drove the base ring of the truss away from the interferometer. The analysis determined the change in length between the truss base ring and the center (mid-height) of the cylinder. Growth due to temperature between the center of the cylinder and its edge where the interferometer was supported drove the interferometer toward the truss base ring. This growth was equal to the thru-the-thickness joint growths and therefore nullified its effect.

In the thermal-vacuum test the truss shortened 14.2×10^{-5} inches as a result of the 10°F rise in temperature. The analysis predicted a growth of 22.9×10^{-5}

inches. This error represents a large percentage of the design budget, therefore additional NASTRAN runs were made to establish a better technique for modeling the truss and improving its performance prediction. In all the analysis the three bays of the truss increased in length approximately 26×10^{-5} inches. This growth was due to the positive CTE's used in the analysis. Since they were based on actual test data, we are confident that this portion of the analysis is accurate. This strongly indicates that the overall shortening the truss experienced during test was caused by the flattening of the spider assembly as a result of the 10°F change. The amount of flattening is very sensitive to 1) the relative CTE's of the spider beams and the upper truss ring which provides the spider assembly support, and 2) the degree of fixity of the joint between the spider beams and secondary mirror mounting cylinder.

Several analyses were performed to establish the amount of vertical movement of the spider assembly as a function of the CTE of the beams. In these runs the fixity of the joints at the ends of the beams were held constant; fixed at the smaller ends and the fixity obtain with the best match in the static test (0.58%) at the larger ends. The initial analysis assumed a CTE based on the unidirectional material in the chords being smeared evenly over the depth of the beam. This produced a reduction in the height of the spider assembly of 19.8×10^{-5} and an overall truss growth of 17.7×10^{-5} inches. The beam CTE was then changed to $-0.3 \text{ in/in/}^{\circ}\text{F}$ to match the chord CTE. This may be more representative of the beam thermal growth characteristics since the chords are much stiffer than the webs. The results of this analysis reduced the overall truss growth to 5.3×10^{-5} inches. In this series of

analysis the CTE of the beams were changed to an unrealistic CTE of -0.7 in/in/ $^{\circ}\text{F}$ before the analysis results bracketed the test results. A summary of this data is shown in Table 7-12.

Another series of NASTRAN analysis were performed to determine the sensitivity of the vertical movement of the truss as a result of a 10°F change, and as a function of the joint stiffness between the spider beams and the secondary mirror support cylinder. In these analysis the CTE of the spider beams were held constant at 0.049 in/in/ $^{\circ}\text{F}$. Figure 7-29 shows that the vertical movement caused by an axial load is highly dependent on this joint stiffness. In the area in which the joint stiffness made a best match with the static test data, the slope of the curve shown is very steep and small changes in fixity can cause large variations in vertical movement. Analysis showed the same sensitivity to the joint stiffness existed when the truss temperature was changed. When the joint fixity that permitted the best match of the static test was used (0.58%) the truss grew 22.92×10^{-5} inches when the temperature was changed 10°F . When this stiffness was cut in half to 0.29% the vertical movement was cut in half for the same condition. When the joint was changed less than one half percent to a pinned design the truss shortened 49.7×10^{-5} inches. In the thermal vacuum test the truss shortened 14.2×10^{-5} inches which is bracketed by the analyses using 0 joint stiffness and 0.29% joint stiffness. With this degree of sensitivity this joint must be well characterized to permit accurate predictions of the vertical movement of the truss when undergoing temperature changes. A summary of the data developed in this study is shown in Table 7-13.

The critical truss deflections for the 10°F radial temperature changes were decenter and tilt. The decenter analysis was within 11.6×10^{-5} inches of the results obtained in the thermal vacuum test which is 8.6% of the design budget. The tilt analysis is within 1.5×10^{-4} degrees of the results obtained in the truss test. This is 16% of the design budget.

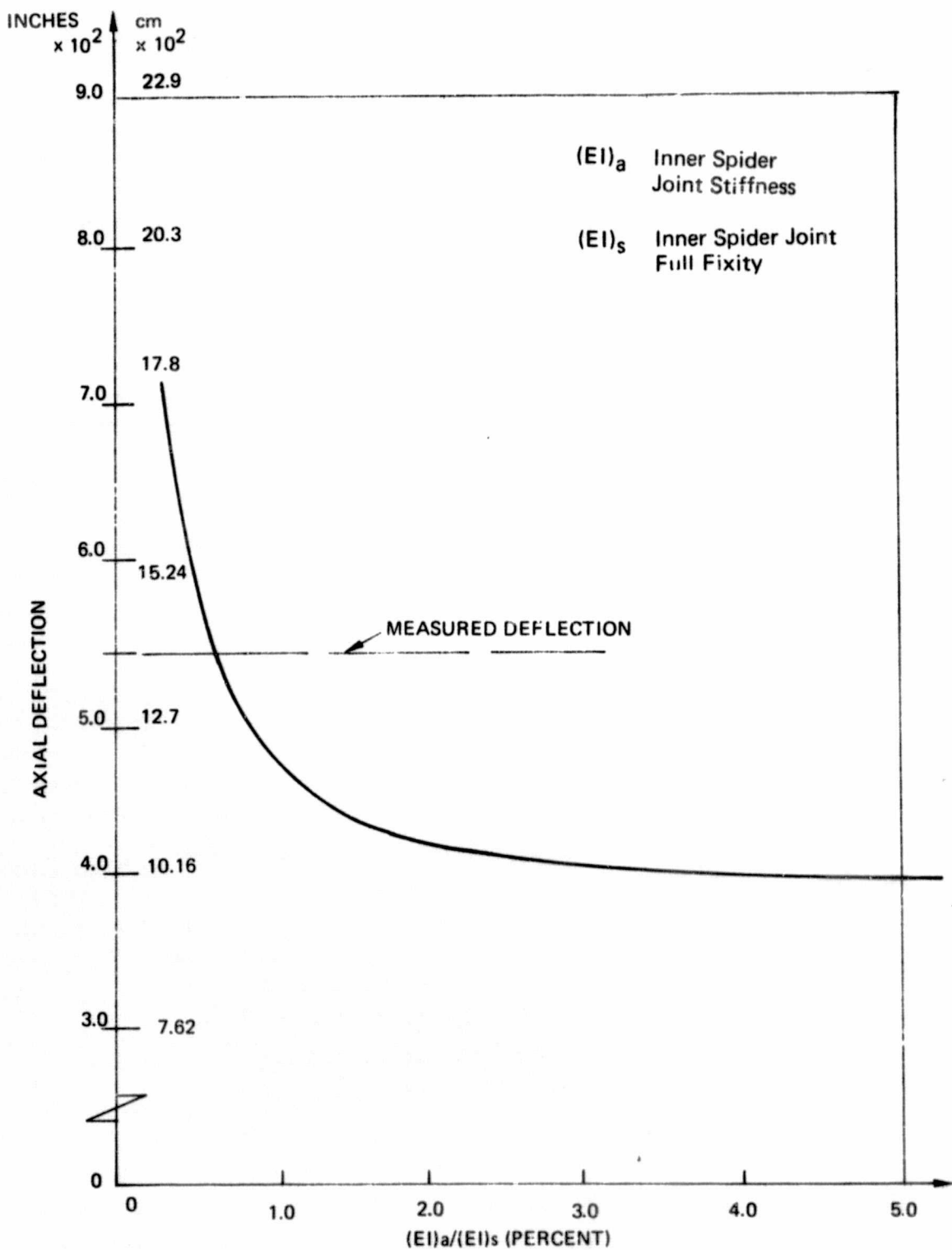


Figure 7-29. Effect of Inner Spider Joint Stiffness on Static Axial Deflection

Table 7-9. Static Test — Analysis Correlations

EDI number	Lateral cm (in.) $\times 10^{-3}$		Torsion cm (in.) $\times 10^{-3}$		Axial cm (in.) $\times 10^{-3}$	
	Test	Analysis	Test	Analysis	Test	Analysis**
1					-135* (-53.2)	-138 (-54.4)
2					-138* (-54.2)	-138 (-54.4)
Ave.					(-136) (-53.7)	(-54.4)
7	82.3* (32.4)	98.8 (38.9)	21.6* (8.5)	21.3 (8.4)		
8	96.5* (38.0)	98.8 (38.9)	-26.7* (-10.5)	-21.3 (-8.4)		
Ave.	89.4 (35.2)	98.8 (38.9)	± 24.1 (± 9.5)	± 21.3 (± 8.4)		

* Adjusted for zero data readings with load actuators connected.

** Stiffness of joint between speder cylinder and speder beams were adjusted to provide axial deflection match. This joint stiffness is used in modal and thermal distortion analysis.

Table 7-10. Dynamic Test—Analysis Correlations

Mode	Calc. freq (Hz) *	Meas. freq (Hz)	Description
1	16.5	16.2	First bending (Z)
2	16.5	16.2	First bending (Y)
3	29.1	—	Longitudinal
4	31.9	28.1	Ring ovaling
5	34.0	—	Torsion
6	44.2	39.6	Second bending (Z)
7	44.2	39.6	Second bending (Y)

* Based on NASTRAN model with best agreement to static deflection test results.

Table 7-11. Thermal--Vacuum Test--Analysis Correlations

	Condition	Nastran analysis	Test data (1)
Despace cm x 10 ⁻⁵ (in. x 10 ⁻⁵)	10°F Axial	58.2 (22.9)	-36.1 (-14.2)
Decenter cm x 10 ⁻⁵ (in. x 10 ⁻⁵)	10°F Radial	138.2 (54.4)	167.6 (66.0)
Tilt degrees x 10 ⁻⁴	10°F Radial	2.0	(2) 3.5

(1) Ave of two tests

(2) Based on two retroreflectors

Table 7-12. Spider Beam CTE Vs Axial Truss Deflection

		Axial movement for a $\Delta T = 10^{\circ}F$	
	Beam CTE $\mu\epsilon/^{\circ}C$ ($\mu\epsilon/^{\circ}F$)	Spider assy cm (in.) $\times 10^{-5}$	Total Truss cm (in.) $\times 10^{-5}$
	-1.26 (-0.7)	-126.2 (-49.7)	-37.3 (-14.7)
Test			-36.1 (-14.2)
	-0.54 (-0.3) (Chord CTE)	-81.8 (-32.2)	13.5 (5.3)
	0.09 (Smeared laminate (0.051) CTE)	-50.3 (-19.8)	45.1 (17.75)

Table 7-13. Spider Beam/Cylinder Joint Stiffness Vs Axial Truss Deflection

		Axial movement	
	Joint stiffness	Spider assy cm (in.) $\times 10^{-5}$	Total Truss cm (in.) $\times 10^{-5}$
	Rigid joints	-21.9 (-8.61)	73.4 (28.9)
	*Best fit (0.58%)	-37.2 (-14.64)	58.2 (22.92)
	1/2 Best fit (0.29%)	-65.8 (-25.9)	29.7 (11.7)
Test			-36.1 (-14.2)
	Pinned	-219.7 (-86.5)	-126.2 (-49.7)

+ Growth
- Shorten

* Best fit with static test results
Beam CTE constant = 0.049

8.0 CONCLUSIONS AND RECOMMENDATIONS

Conclusions

The results obtained in this program have demonstrated the following:

- o The graphite/epoxy metering truss concept will successfully perform to the requirements of the LST.
- o A graphite/epoxy metering truss will perform in a predictable manner. Accurate characterization of the thermal physical properties and joint fixities of the spider assembly is necessary to obtain improved analysis/test correlations.
- o The use of resistance heaters and a layer of aluminized mylar on the truss assembly during the thermal-vacuum test provided excellent control of the structural temperature distributions.
- o Element tests have demonstrated the ability to attain "near zero" CTE characteristics in truss details.
- o Element tests highly representative of the assembly details must be tested prior to finalizing the design and manufacturing processes.
- o Sophisticated measuring devices and techniques such as the use of the multi-beam laser interferometer and linear differential transformer extensometers are necessary to provide the measurement resolutions needed to show design compliance.
- o The high degree of commonality of detail parts in the truss design provides a structure that can be produced in a cost effective manner. The simplicity and producibility of the one bay assembly tool used in fabricating the truss was successfully demonstrated.

Recommendations

The following recommendations are made to improve the performance of the truss and/or obtain additional data to demonstrate full compliance with LST requirements.

- o Incorporate gusset plates in the joints that pass through a slot in the ring webs to eliminate through-the-thickness thermal growths.
- o Conduct CTE tests on typical truss joints.
- o Perform design, analysis and test investigations to improve the dimensional stability and performance predictability of the secondary mirror support structure.
- o Perform element tests to obtain mission environmental response and long-term operational effects such as:
 - 1) Dimensional change due to moisture content change.
 - 2) Moisture cycling effects on properties.
 - 3) Thermal cycling effects on properties.
- o Conduct tests on each of the truss tubes to establish CTE repeatability.
- o Fabricate a graphite/epoxy metering truss based on the present LST design which utilizes a 2.4 meter diameter primary mirror. Perform static, dynamic and thermal-vacuum evaluation tests. Incorporate it in an engineering model containing associated subsystems. Perform dynamic and thermal-vacuum tests with this model to obtain interrelated subsystem responses.

APPENDIX A

GRAPHITE/EPOXY METERING TRUSS DAMPING TESTS

Structural damping measurements were obtained in the first and second bending modes during dynamic tests of the graphite/epoxy metering truss performed under Contract NAS8-29825. Because of the extreme sensitivity of the image motion amplitude to structural damping these results were of immediate interest for the analysis of Large Telescope performance. In review of the measurements it was felt that the damping data was high and was influenced by the motion of floor and mounting ring which were monitored during the tests. Since structural damping was not the primary objective of the initial dynamics tests it was decided to perform additional truss tests to obtain damping values under more controlled conditions. The truss was mounted in a new location in which dynamic measurements were made and found to be relatively free of background noise. In the new test set-up the adapter fittings attached to the base ring of the truss were bonded and bolted directly to the floor. The floor in this area consisted of a 3-foot thick reinforced concrete slab.

Tests were also performed to assess air damping effects. A 2 inch diameter graphite/epoxy tube 36 inches long was used in these tests.

The results of the truss damping tests and air damping tests are shown in Tables A-1 and A-2. Table A-1 gives the structural damping versus amplitude data for six metering truss modes. Table A-2 gives the results of the graphite/epoxy specimen tests in the vacuum chamber to assess air damping

effects. The metering truss test results indicate that the structural damping in the low amplitude range of interest is at least 3 times greater than the conservative value ($g = .001$) assumed before test data were available. The specimen test results show that air damping is negligible as expected, so that no correction of the metering truss data for air damping is required.

Discussion of Results

The data given in Table A-1 are plotted on semi-log paper in Figure A-1 to facilitate examining the structural damping trends over a large amplitude range. The lowest amplitudes shown approach the range of critical image motion amplitudes. The .0036 arc seconds of image motion allocated to vibration is equivalent to approximately .00008 inches double amplitude lateral displacement of the secondary mirror. Extrapolation of the well defined trends in Figure A-1 to this amplitude is not unreasonable, especially in view of the relatively flat nature of the curves at low amplitudes.

Figure A-2 shows the minimum measured structural damping for each of the six modes plotted versus frequency. The four lowest frequency modes are identified as lateral, axial, or torsion modes. The two higher frequency modes are not identified, since the instrumentation was not extensive enough to determine mode shape. The two higher frequency modes were excited by lateral forcing. If we assume they are actually higher order lateral modes, a fairly consistent trend of increasing damping with increasing frequency is apparent for lateral modes. Similar trends would be expected for axial and torsion modes. Based on this assumption, an estimated lower bound on damping versus

frequency for all modes was constructed as shown in Figure A-2. The lower bound is sufficiently below the data points to allow for extrapolation to .00008 inches double amplitude as well as errors due to scatter in the data. The only data point close to the boundary is the torsion mode. As shown in Figure A-1, this mode shows a very smooth trend with little apparent scatter; and the data in this mode extend almost down to .00008 inches double amplitude.

The graphite/epoxy specimen test results given in Table A-2 indicate the effect of air-damping is negligible. At all three pressures, damping appears to increase slightly at very low amplitudes. No explanation for this trend has been found. One would expect either no variation or a decrease in damping as amplitude decreased. For the present it is assumed that damping is actually constant in this amplitude range. The mean and standard deviation of the damping data for each pressure condition are tabulated below. The computations were based on the analyzer data, not decay data.

<u>Pressure</u> <u>mm Hg</u>	<u>Mean Structural</u> <u>Damping, g</u>	<u>Standard Deviation, σ</u>
755	.00293	.00032
375	.00300	.00035
<10	.00289	.00040

The air-damping predicted by Stokes' theory for the test condition is $g = .00005$. The difference of the mean damping in air and in vacuum from the above table is $g = .00004$. This is consistent with the theory but should not be taken as an accurate measure since the scatter is large in comparison ($\sigma = .00032$ to $.00040$).

The frequency in the specimen test was above the desired range of 16 to 100 Hz. The predicted free-free frequency, including the effect of the shaker and accelerometer masses, was 345.7 Hz compared to the measured frequency of 338 Hz. The specimen was supported by soft springs at the nodes. The maximum transverse velocity ranged from .095 to 1.82 in/sec. This covered the same maximum velocity range as that obtained in the 16.56 Hz lateral mode in the metering truss test (.094 to 1.74 in/sec). The air damping forces were therefore comparable.

The mean damping measured in the specimen tests ($g \approx .0029$) is probably a good measure of the material damping for this graphite epoxy material. Other structural damping mechanisms such as joint damping were not present in the simple tube specimen, and air damping was shown to be negligible. This tends to enhance the confidence in the selection of $g = .003$ for a lower bound on structural damping for the metering truss as indicated in Figure A-2.

TABLE A-1

METERING TRUSS STRUCTURAL DAMPING
TEST DATA SHEET

<u>MODE</u>	<u>FREQUENCY Hz</u>	<u>DOUBLE AMPLITUDE DISPLACEMENT INCHES</u>	<u>STRUCTURAL DAMPING g</u>	<u>REMARKS</u>
First Bending	16.556	.0335	.00396	Run 19
	16.580	.0189	.00407	Run 15
	16.560	.0093	.00408	Run 16
	16.566	.0019	.00386	Run 18
	16.570	.0018	.00368	Run 17
Second Bending	39.506	.0069	.00585	Run 20
	39.513	.0032	.00569	Run 21
	39.519	.0017	.00569	Run 22
	39.519	.0010	.00580	Run 23
80 Hz (Lateral Forcing)	79.850	.0044	.00626	Run 31
	79.875	.0024	.00576	Run 28
	79.900	.0015	.00573	Run 29
	79.950	.0008	.00575	Run 30
	79.875	.0005	.00635	Run 27
106 Hz (Lateral Forcing)	105.93	.0018	.00660	Run 42
	106.00	.0010	.00755	Run 41
	106.03	.0005	.00660	Run 43

<u>MODE</u>	<u>FREQUENCY Hz</u>	<u>DOUBLE AMPLITUDE DISPLACEMENT INCHES</u>	<u>STRUCTURAL DAMPING g</u>	<u>REMARKS</u>
Torsion	50.900	.0042	.00393	Run 33
	50.888	.0037	.00400	Run 34
	50.881	.0017	.00378	Run 35
	50.900	.00095	.00351	Run 36
	50.913	.00098	.00341	Run 37
	50.913	.00011	.00329	Run 39
Axial	28.050	.01243	.00870	Run 45
	28.050	.00546	.00744	Run 44
	28.063	.00273	.00713	Run 46
	28.112	.00139	.00667	Run 47
	28.063	.00075	.00686	Run 48
	28.063	.00025	.00646	Run 49

TABLE A-2

SPECIMEN SECTION STRUCTURAL DAMPING
TEST DATA SHEET

<u>MODE</u>	<u>FREQUENCY</u> <u>Hz</u>	<u>DOUBLE</u> <u>AMPLITUDE</u> <u>DISPLACEMENT</u> <u>INCHES</u>	<u>STRUCTURAL</u> <u>DAMPING</u> <u>g</u>	<u>CHAMBER</u> <u>PRESSURE</u> <u>mm Hg</u>	<u>DAMPING</u> <u>(BY DECAY)</u> <u>g</u>
	337.50	.00172	.00280	755	.00237
	337.44	.00086	.00280	755	.00246
	337.44	.00043	.00267	755	.00265
	337.50	.00017	.00284	755	.00319
	337.41	.00009	.00356	755	.00329
	338.00	.00009	.00355	375	.00333
	338.13	.00017	.00322	375	.00324
	338.00	.00043	.00290	375	.00279
	337.94	.00086	.00257	375	.00282
	338.00	.00171	.00275	375	.00239
	338.63	.00171	.00266	<10	.00227
	338.72	.00085	.00233	<10	.00243
	338.56	.00043	.00295	<10	.00268
	338.56	.00017	.00354	<10	.00297
	338.50	.00009	.00295	<10	.00286

STRUCTURAL DAMPING $g = 2C/C_c$
SHEET

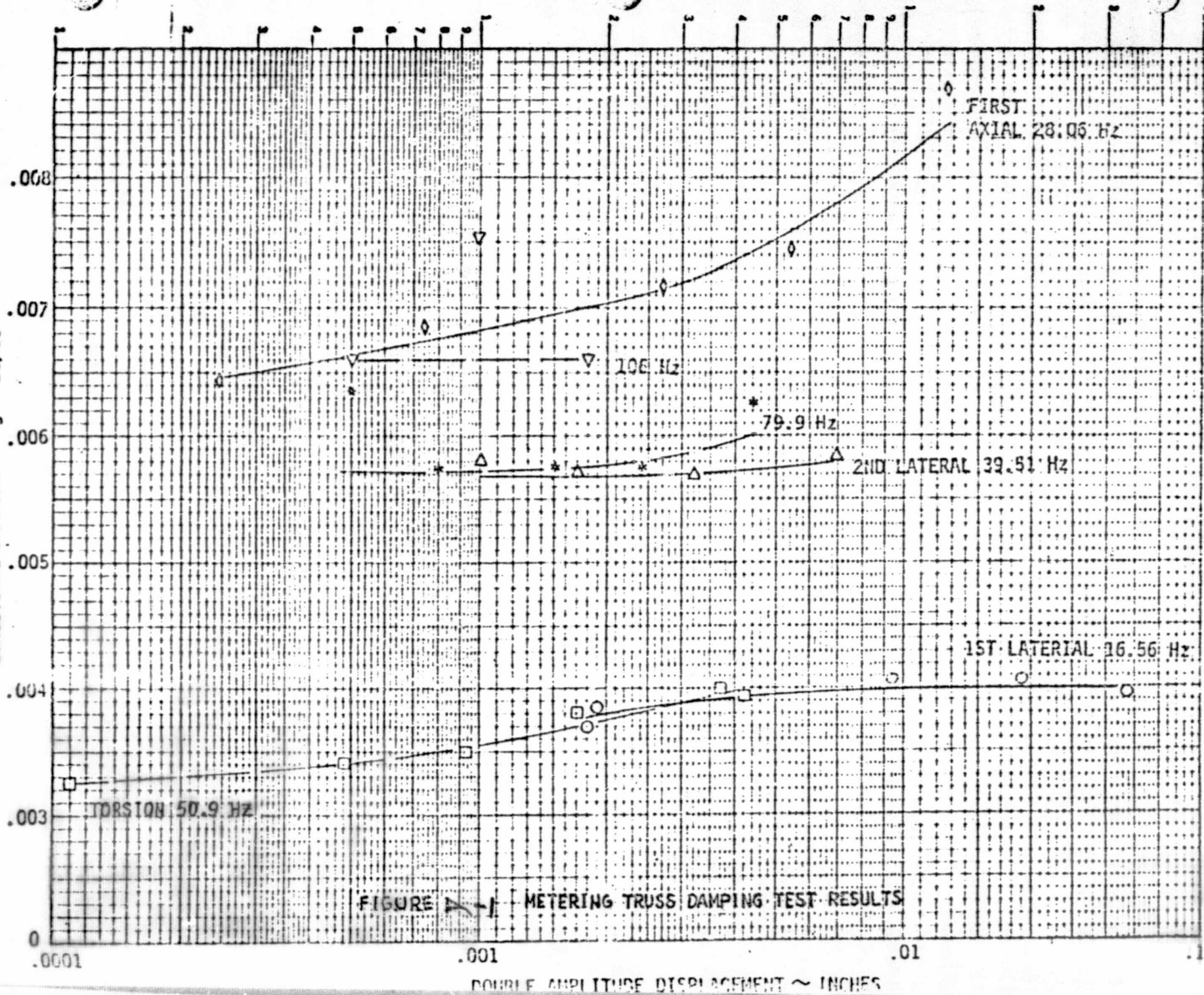


FIGURE 1-1 METERING TRUSS DAMPING TEST RESULTS

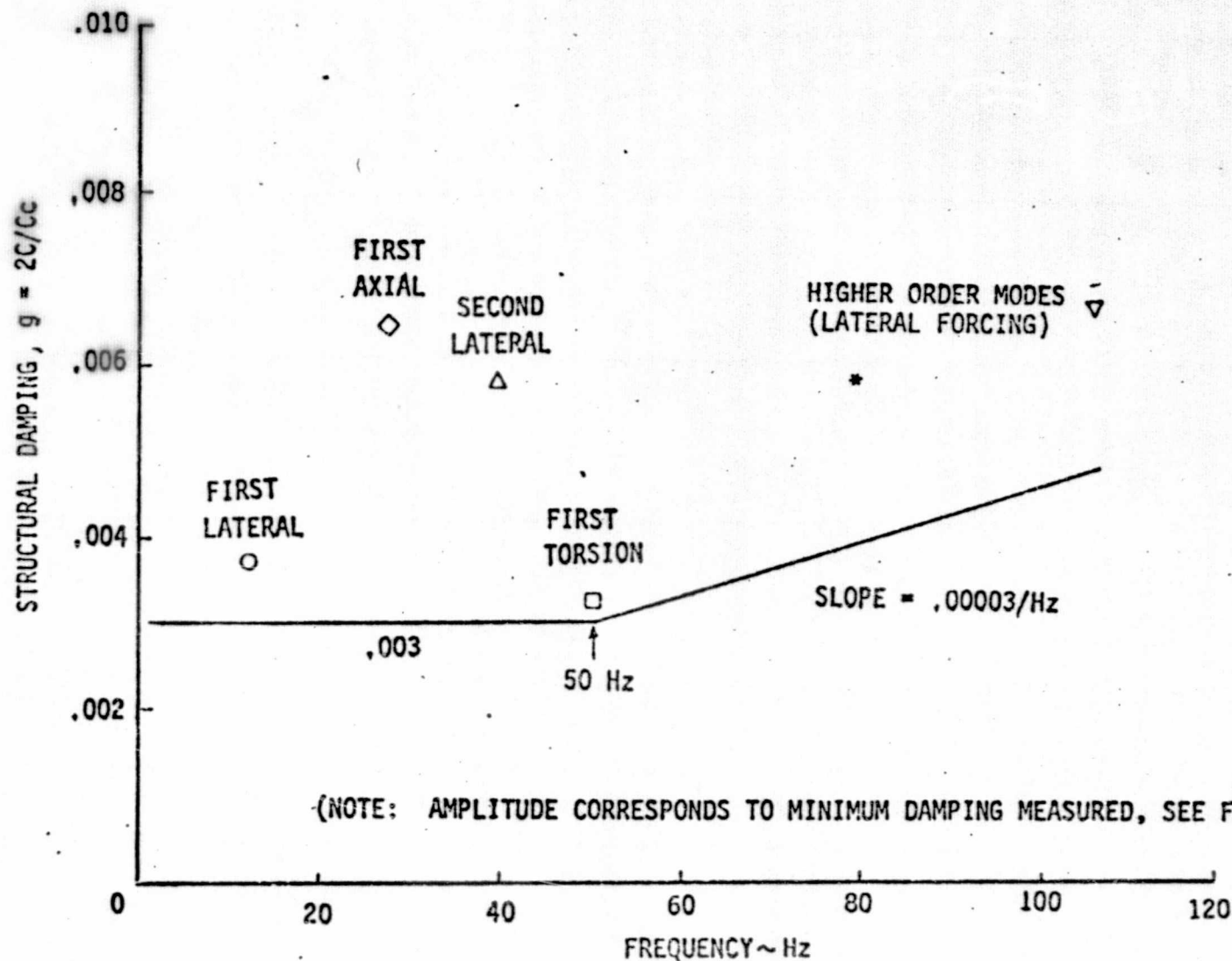


FIGURE A-2.

METERING TRUSS DAMPING VS FREQUENCY

REPRODUCIBILITY OF THE
ORIGINAL PAGE IS POOR